A study of pressure fluctuations caused by vortex breakdown

by

Artur Jerzy Jaworski

This thesis is submitted for the
degree of Doctor of Philosophy (PhD)
of the University of London
and for the Diploma of Imperial College (DIC)

1996

Department of Aeronautics
Imperial College of Science, Technology and Medicine
London SW7

ABSTRACT

This thesis describes an experimental investigation of pressure fluctuations caused by vortex breakdown. Using two simple experimental arrangements, i.e. a *vortex tube* and a *delta wing*, a detailed spectral mapping of the pressure and velocity fluctuations downstream of the breakdown is obtained. It is suggested that a spiral vortical structure, emerging from the initial burst, is directly responsible for the appearance of the quasi-periodic pressure and velocity fluctuations in the breakdown wake. It is shown that the strongest pressure fluctuations are confined to a restricted radial range, but persist some distance downstream. The highest excitation level is present within the vortex, approximately at the point of axial velocity profile inflection. The diameter based on the radial location of this point is proposed as an appropriate scaling length to characterise the quasi-periodic fluctuations. The vortex breakdown is found not to be susceptible to small periodic perturbations imposed upstream. A simple frequency parameter based on the proposed length scale and free stream velocity is suggested for early design studies of aircraft for estimating the frequency of aerodynamic loads due to breakdown. Some recommendations are made to reduce the buffet excitation on the airframe components.

ACKNOWLEDGEMENTS

I would like to express my deep thanks to Professor John Harvey and Professor Dennis Mabey for the direct supervision of this project. Their guidance, support, encouragement and patience were invaluable factors in completing the experiments. The final form of this thesis is undoubtedly a fruit of long hours they spent on correcting and discussing the text. I am greatly indebted to the Head of Department, Professor Peter Bearman, for his understanding and generosity both in terms of human resources and financial means given to this project.

I would like to thank the Polish Air Force Association in Great Britain for their sponsorship and financial support throughout my studies. I am grateful beyond words to Mr Andrzej Jeziorski for the fatherly watch he kept over me during my entire stay in the United Kingdom.

The team of technicians led by Mr Ernest Turner deserves special thanks for a creative attitude during planning, producing, and assembly of the vortex tube apparatus and wing models. Contributions from Mr Alan Smith, Mr Ian James, Mr Harry Engler, Mr Bruno Collini and Mr Joseph Megyesi were vital for the research, but frankly, it is hard to point out a single person in the team, who *was not* involved in the project.

Mr John Coles, without whom the tunnel tests would not have been possible, will always occupy a special place in my memories. Not often one can meet a person giving not only his time but also his heart to the work to such an extent as him.

The flow visualisations were made thanks to Mr John O'Leary. His tremendous sense of humour, great photographic skills, and ability to make difficult things easy were equally important for successful results.

The electrical and electronic equipment, necessary for the experiments, was assembled by the Electrical Services led by Mr Clive Mott. Great credit must be given to Mr Roger Serpell and Mr Russel Carter for solving numerous practical problems emerging during the experiments. The digital processing of video images and photographs was possible thanks to the help offered by Mr John Wye.

I would like also take the opportunity to thank all members of the clerical staff for their kindness and every-day help throughout my entire studies. Mrs Roslee Fairhurst, Miss Sarah Payton and Miss Tilly Hill deserve a particular mention.

LIST OF CONTENTS

LIST OF FIGURES AND TABLES

SYMBOLS AND ABBREVIATIONS

Latin symbols:

b	wing span, [m],
	thickness of axial velocity profile, [m],
c	wing root chord, [m],
$\bar{c}$	mean aerodynamic chord, [m],
C_D	drag coefficient, [-],
C_L	lift coefficient, [-],
C_M	pitching moment coefficient, [-],
C_N	normal force coefficient, [-],
D	diameter, length scale, [m],
f	frequency, [Hz],
F	Froude number, [-],
h	total pressure (equation 2.19 and following), [m^2/s^2]
H	height, [m],
	total pressure, [Pa],
K	pitching rate or reduced pitching frequency, [deg] or [-],
L	length scale (e.g. total aircraft length), [m],
n	frequency parameter, [-],
p	static pressure, [Pa],
$\overline{p}$	RMS level of pressure fluctuations, [Pa],
q	dynamic pressure, [Pa],
	swirl parameter, [-],
Q	flow rate, [m^3/s],
r	radial co-ordinate, [m],
R	correlation function, [-],
	(reference) radius, [m],
Re	Reynolds number, [-],
Ro	Rossby number, [-],

s wing semispan, [m],

S flow force, [m],

S_n spectral density (normalised), [1/Hz],

t time, [s],

u radial velocity, [m/s],

U tunnel speed, [m/s],

v tangential velocity, [m/s],

V reference swirl velocity, [m/s],

w axial velocity, [m/s],

$\overline{w}$ RMS value of velocity fluctuations, [m/s],

W reference axial velocity (confined vortices), [m/s],

x streamwise (chordwise) co-ordinate, [m],

y spanwise co-ordinate, [m],

Greek symbols:

α angle of incidence, [deg],

β angle of yaw, [deg],

γ swirl angle, [deg],

Γ circulation, [m^2/s],

δ radius of vortex core, [m],

ζ axial vorticity, [1/s],

η azimuthal component of vorticity, [1/s],

θ azimuthal co-ordinate, [deg],

Λ sweep angle, [deg],

ν kinematic viscosity, [m^2/s],

ρ density, [kg/m^3],

τ swirling ratio, [-],

ψ stream function, [m^3/s],

Ω angular velocity, [rad/s],

circulation number, [-],

Abbreviations:

L	Long choke
M	Medium choke
S	Short choke
LM	Large Model (delta wing)
SM	Small Model (delta wing)
P	Pressure measurements
V	Velocity measurements
LEX	Leading edge EXtension
PIV	Particle Image Velocimetry
PTV	Particle Tracking Velocimetry
TLEB	Tangential Leading Edge Blowing

CHAPTER I

INTRODUCTION

In very broad terms vortex breakdown can be defined as an abrupt change in the structure of an axisymmetric swirling flow which leads to a substantial increase in unsteadiness. Generally it is associated with a rapid retardation of the axial velocity near the axis and corresponding divergence of the streamlines (see, for example, figure 2.1 - page 21). The phenomenon of vortex breakdown was discovered nearly 40 years ago, but despite many theoretical, experimental and numerical investigations its nature is not understood fully, and none of the existing theories gained a general acceptance.

Vortex breakdown is witnessed in many situations, for example, on slender wings at high incidence, in wing-tip vortices (Leibovich-1978), in swirling flows through pipes, nozzles and diffusers (Hall-1972), in the draft tubes of water turbines, in the outlet casings of axial turbines and compressors (Escudier-1988), and in a Ranque-Hilsch refrigeration tube (Escudier-1987), but it can also be *applied* for flame stabilisation in furnaces and combustion chambers as a fluid dynamical flame holder (Escudier-1988).

The occurrence of the vortex breakdown has serious implications for aircraft with highly swept or slender delta wings. Slender wings are used for efficient supersonic flight, but are also attractive for the high-incidence-low-speed regime

during landing and take-off. An excellent review of the benefits of slender wings for combat aircraft is given by Polhamus (1984). In the high incidence regime the shear layers separating from the leading edges roll up and create *leading-edge vortices* which induce areas of low pressure and thus provide additional lift. However, in some circumstances (explained in chapter 2), the leading edge vortices undergo breakdown. This leads to a sudden deterioration of aircraft aerodynamic performance.

Vortex breakdown has significant adverse effects on both the static and the dynamic aerodynamic characteristics. It has been found to be responsible, for example, for loss of lift and for introducing unsteadiness in rolling and pitching moments, which results in poor control over the aircraft. It is also a source of the large scale coherent structures which emerge in the breakdown wake and manifest their presence by the quasi-periodic oscillations of pressure and velocity fields. This feature of the post breakdown flow fields is the cause of the buffet excitation on the wings and fins of some modern highly manoeuvrable aircraft (such as F-18) at high angles of attack. The excitation may cause fatigue problems and thus seriously shorten the lifetime of some vital components of the aircraft.

It is worth noting that vortex breakdown is not always considered as an undesirable effect. The wing-tip vortices shed by large transport aircraft constitute a potential danger for light aircraft especially during take-off and landing. Here, encouraging vortex breakdown can destabilise the flow and is an attractive mechanism for reducing the strength of the large vortical structures.

* * *

The subject of the present research is a study of the quasi-periodic features of the vortex breakdown flow field. It was known, from previous investigations, that the excitation spectra on fins due to vortex breakdown, measured on advanced combat aircraft (e.g. the F-18), have sharp peaks at a frequency which varies from configuration to configuration. For a given configuration the frequency f for peaks in the fin buffet excitation spectra can be correlated by the expression (Mabey-1991):

$$\frac{f\bar{\bar{c}}}{U}\sin(\alpha) = const\,, \tag{1.1}$$

where $\bar{\bar{c}}$, U and α, are mean aerodynamic chord, free stream velocity and angle of incidence, respectively. The constant in equation (1.1) varies from 0.1 to 0.8 for various configurations. Such a wide variation implies that $\bar{\bar{c}}$ is not the length which controls the phenomenon, and correlation (1.1) appears to be unhelpful for early design studies.

The objective of this research was to investigate the physics underlying the appearance of the quasi-periodic fluctuations in the breakdown wake, chiefly by the techniques of spectral mapping of the pressure and velocity fields. This has been done using a vortex tube and a delta wing, which represent the simplest, but also the most widely different, test cases known to the author. The ultimate goal was to identify the controlling length parameter, say D, and to suggest a more appropriate frequency parameter n, characterising the breakdown-related fluctuations:

$$n = \frac{fD}{U} = const\,. \tag{1.2}$$

Hopefully this would be constant for all airframe configurations.

The author would like to contribute to the understanding of the physics of the vortex breakdown and to establish a suitable criterion (1.2) for design studies which utilize measured or predicted values of D.

CHAPTER 2

LITERATURE REVIEW OF THE VORTEX BREAKDOWN PHENOMENON

Early experimental observations of the vortex breakdown were made in the late fifties. The credit for the first well documented one is usually given to Peckham and Atkinson (1957). Discussing the tests on a gothic wing of aspect ratio 1.0 they reported that after the wing reached a certain critical angle of incidence the condensation trail, indicating the core of the leading-edge vortex, 'appeared to "bell-out" before disappearing', which in turn suggested that 'the geometry of the rolling-up process varies'.

Since the vortex breakdown phenomenon had very serious implications in the field of aeronautics, it is quite understandable that a great many experiments were conducted during flight tests, on aircraft models or just simplified configurations like delta wings. However, this type of investigation is unlikely to give a clear insight into the physical mechanisms governing the breakdown because of an extremely complex structure of the flow field. For this reason the experiments by Harvey (1962), who investigated the swirling flow in the so-called "vortex tube", were undoubtedly the greatest breakthrough in experimental investigations, permitting observation of the breakdown 'in vitro'. In his apparatus the azimuthal velocity was introduced by a set

of adjustable "swirl vanes", placed upstream of the cylindrical test section. The idea was applied later by many researchers and vortex tube experiments constitute also a major part of current work.

Extensive experiments in conjunction with the theoretical work resulted in several theories of vortex breakdown. The well-known theories are: hydrodynamic instability, theory of conjugate states, boundary layer separation analogy, wave theories, theory based on vorticity dynamics. The main difficulty in obtaining the generally accepted theory lies in the fact that vortex breakdown is a highly non-linear process, and each of the above mentioned theories is able to pick up only some of the aspects while ignoring others, thus oversimplifying the phenomenon.

Recent advances in computer technology (increasing computational power) have allowed the investigators to seek explanations of the breakdown from numerical solutions. The great advantage is obviously the ability to introduce numerical models that are far more complicated (including direct numerical simulation) than the 'simple' theories mentioned above.

2.1. Physical description of the vortex breakdown

Generally speaking the vortex breakdown phenomenon (often referred to as vortex bursting or breaking-up of the vortex) can be described as an abrupt change in the structure of the core of an axisymmetric flow which, before the breakdown, had a large amount of swirl. The changes in the character of the flow consist of:

- pronounced (and in some sense unexpected) retardation of the flow along the axis which takes place within axial distance of about one core diameter.
- divergence of the stream surfaces (often described as swelling) near the axis of the flow.
- stagnation of the flow due to the retardation and appearance of a region of reversed flow (taking the axisymmetric or asymmetric forms) on the vortex axis

and a change to highly unsteady flow (which coincides with the transition to turbulent flow in the breakdown wake).

Figures 2.1 and 2.2 show schematically the process of vortex breakdown which can be commonly observed in cylindrical or slightly diverging ducts. The flow upstream of the breakdown can be divided into two regions: viscous core with a strong nearly rigid-body rotation, and an irrotational flow surrounding the core with a near uniform distribution of axial velocity and much smaller swirl component compared with the core (see figure 2.1, cross-section $x=x_1$). In most situations, for example on slender wings and in many vortex generators, the axial component of velocity has a considerable overshoot (as shown in figure 2.1), although this is not crucial for the breakdown occurrence (breakdown has been observed for flat and wake-like profiles). Most important of all, the changes in the swirl velocity distribution are confined within a small radial distance from the vortex axis (corresponding roughly to the viscous core). During the breakdown the flow field undergoes a dramatic change: the axial velocity acquires a wide wake-like profile while the tangential velocity distribution becomes flatter with the maximum value placed further outwards in relation to the vortex axis then before the breakdown (cross-section $x=x_2$). The flow undergoing the breakdown behaves as if meeting a body of revolution placed on the axis of the vortex. Dye introduced into the centre reveals a zone of stagnant and recirculating fluid around which the fluid elements outside the axis are forced to flow (figure 2.1). Downstream of the recirculation region the flow becomes unsteady and often indicates the onset of turbulence.

In the existing literature, the vortex breakdown is broadly referred to as a *transition*. This, however, is rather awkward if not erroneous, since the breakdown is mistakenly associated with the transition from the laminar to the turbulent flow. Thus a better term describing vortex breakdown is a *change*. Vortex breakdown takes place in some sense independently from the state of the flow. The simplest examples are:

- the breakdown over swept wings of an aircraft where the flow both upstream and downstream of breakdown is turbulent; however downstream the flow is more *unsteady* and of *higher* level of turbulence.

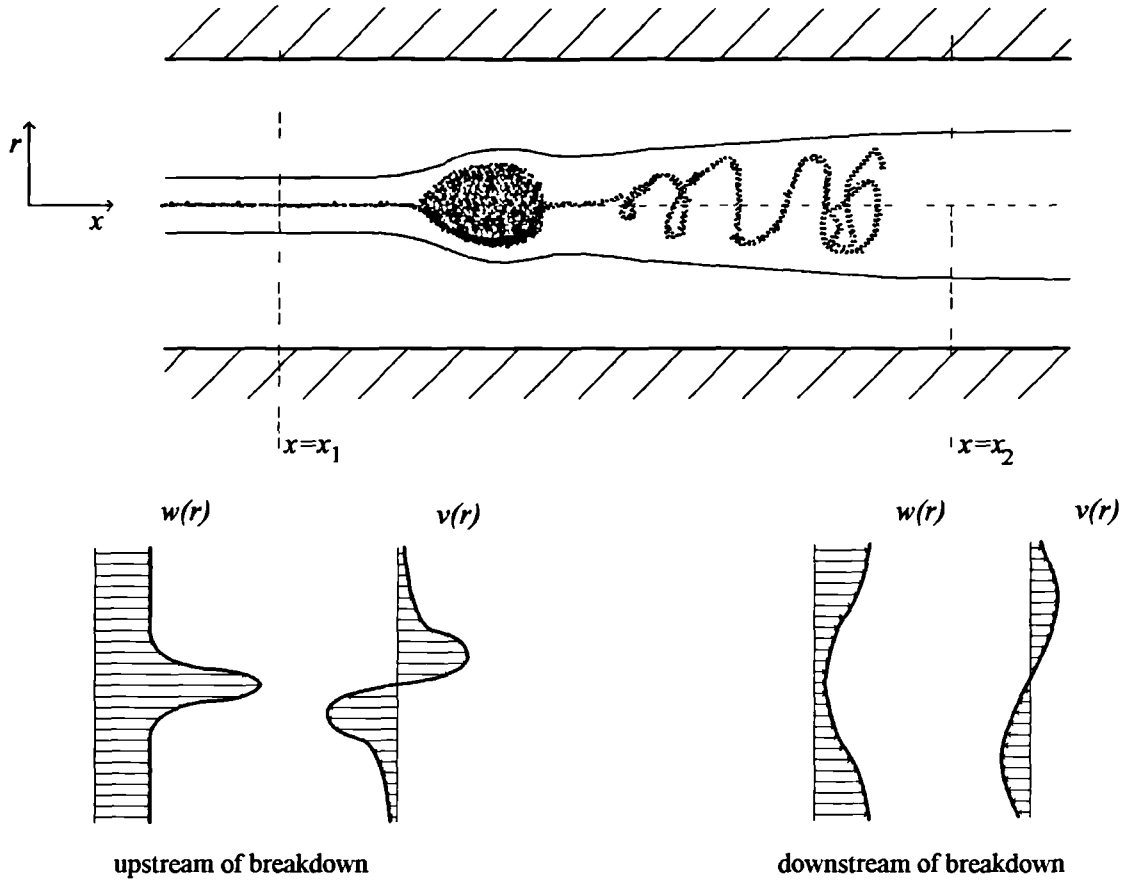

Figure 2.1. Vortex breakdown in the tube. Dots indicate dye introduced into the vortex axis. *w(r)* and *v(r)* are the axial and the swirl velocities, respectively.

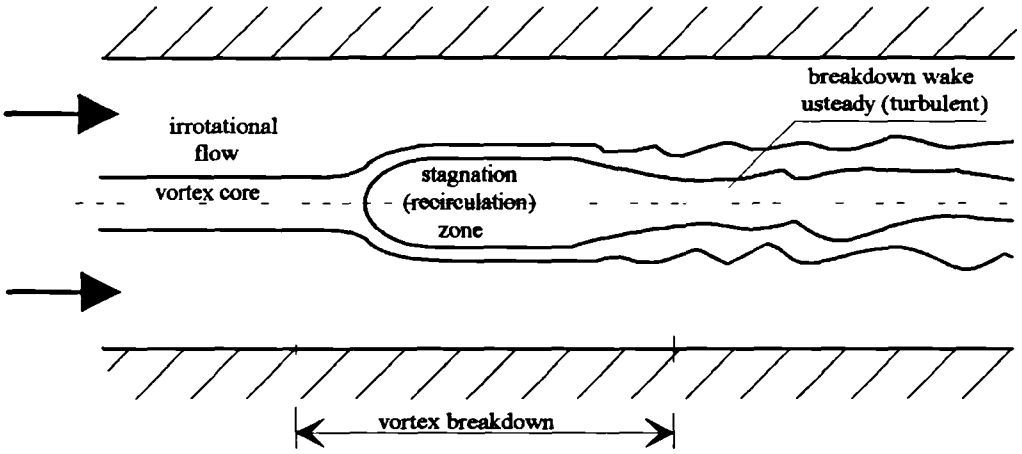

Figure 2.2. Idealised process of vortex breakdown in a cylindrical tube.

- the breakdown on a delta wing model at low speed (e.g. the one in figure 2.7a, discussed later), where the flow upstream and some distance downstream of stagnation point is laminar. However the *unsteadiness* due to the occurrence of breakdown leads eventually to the onset of turbulence. This kind of experiment conducted under laboratory conditions (often at extremely low speeds, required for good visualisation) frequently exhibits transition to turbulent flow at the same time as the breakdown and hence can be 'blamed' for the misconception mentioned above.

2.2. Vortex breakdown in aeronautics

It should be emphasised that vortical motions and their breakdown are only one of the specific topics in a much broader area of three-dimensional separating flows with vorticity induced by separation lines oblique to the free stream, as discussed in the short yet comprehensive review given by Peake and Tobak (1983). The understanding of such flows is limited and in many cases only qualitative. The main difficulties are mutual interactions between several vortical motions (originating, say, at different places on the body of an aircraft) and their unsteadiness both in space and time. Flow visualisation showing interactions of vortical motions is given by Erickson and Gilbert (1983). Currently even the most sophisticated numerical methods, although very instructive from the viewpoint of understanding, fail to predict all of the flow features in a comprehensive manner. Hence the following review has to be very limited and fragmentary and often offers more illustrative information rather than theoretical considerations.

2.2.1. Physics of the flow past delta wings - basic topics

Hall (1961, 1966b), Legendre (1966), and Küchemann (1978) and more recently Hoeijmakers (1990) outlined some basic features of the flow past delta wings. When the wing is set at an angle of incidence the flow separates on a sharp (or

relatively sharp, considering the wing dimensions) leading edge and forms a free shear layer (figure 2.3.). The separation process is responsible for creating large amounts of vorticity which can be regarded as a vortex sheet originating at the separation line.

The shear layer (in other words, the vortex sheet) curves and rolls up, with its intersection with a plane normal to the wing forming a spiral. The identity of discrete layers is lost due to the viscous effects, and the velocity profiles in the inner part of the spiral become nearly axisymmetric. Fluid particles typically follow paths originating at the leading edge and spiral along the vortex axis (figure 2.4). The rolled-up vortex sheets form the so-called 'core', the concept being somewhat arbitrary. It is possible to define it (Leibovich 1983,1984) as the region containing most of the vorticity or the region where the flow is nearly axisymmetric.

The radius of the 'core' grows in the axial direction. The circulation about the core increases approximately linearly with distance along the axis due to continuous feeding of vorticity into the region of the core[1]. At the same time the axial component of velocity near the axis increases because of a continuous drop in pressure due to increasing vorticity of the core. The maximum axial velocity exceeds the free stream velocity by a factor of 2 to 5, according to different measurements. Legendre (1966) reports that this very high velocity along the axis of the core is likely to tend to infinity for vanishing viscosity.

It is worth noting that, according to many observations, there is no significant influence of the Reynolds number on the size of the core. However the size of the 'viscous subcore' (where the viscosity of the fluid plays an important role) decreases with increasing Reynolds number. The axis of the core is located about one core diameter above the lifting surface.

The adverse pressure gradient in the region of the wing just outboard of the centre of the leading-edge vortex core causes a secondary separation. The free shear layer which originates at the secondary separation line also rolls-up in a manner

[1] This is true for straight edged wings. The gothic or ogive wings are not discussed here.

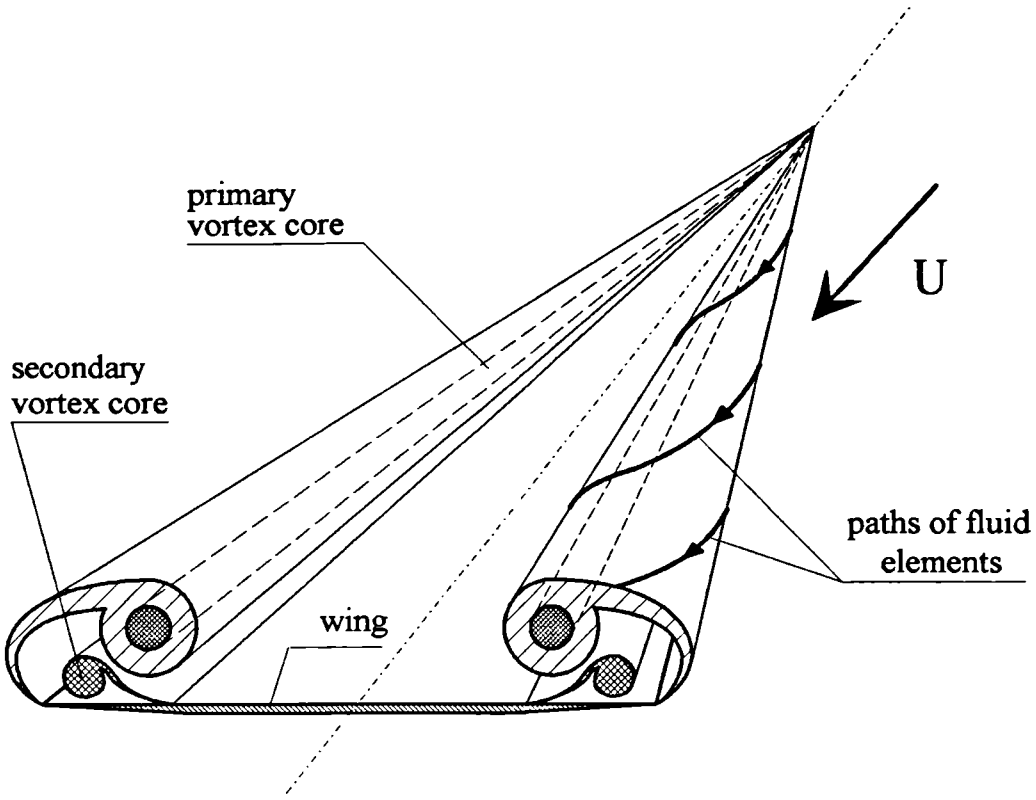

Figure 2.3. Formation of the leading edge vortex on a delta wing.

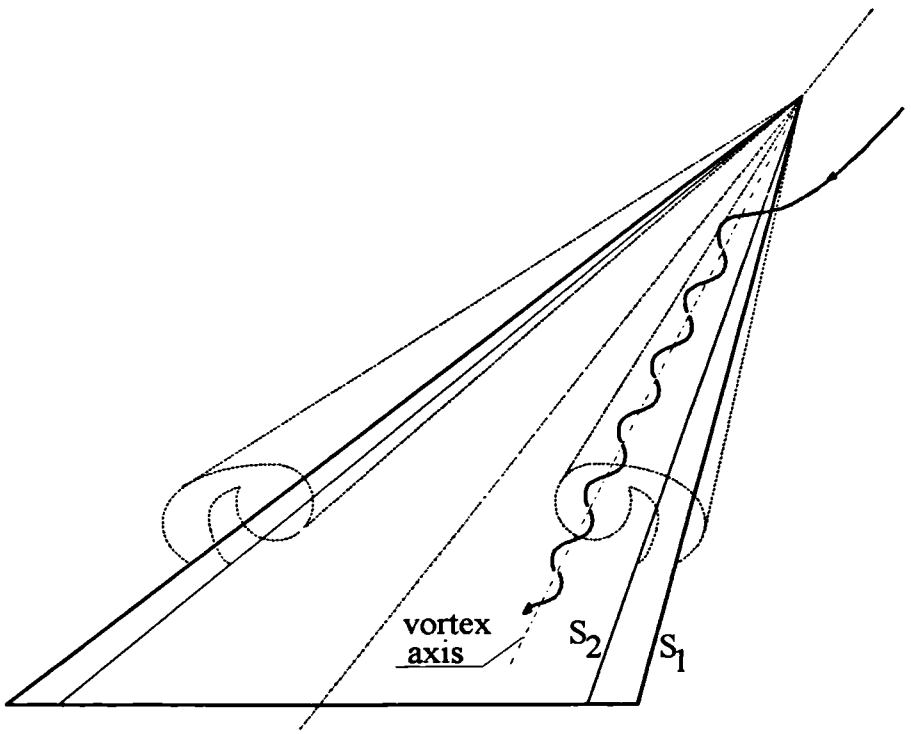

Figure 2.4. Helical path of the fluid element entering the vortex structure, S_1, S_2 - primary and secondary separation lines.

similar to the leading-edge primary vortex, the only difference being the opposite sign of vorticity. Secondary separation becomes more important (Hoeijmakers-1990) for wings at smaller incidence or with lower sweep angles. Del Frate *et al.* (1990) report the existence of 'tertiary' separation lines on F-18 HARV leading edge extension (LEX). Similarly Agrawal *et al.* (1990) report tertiary vortices over delta wings in some numerical solutions of the Navier-Stokes equations. Nelson and Visser (1990) showed that the secondary vortices can burst in the same way as primary ones.

2.2.2. Early observations of the vortex breakdown on slender wings

As can be easily seen from the phenomenological definition given in 2.1 and the description given in 2.2.1 the flow past slender wings at large angles of incidence is likely to undergo vortex breakdown because of

large amounts of swirl. Thus vortex breakdown was observed by Peckham and Atkinson (1957) and soon after became a subject of extensive experimental research.

The credit for one of the most comprehensive and illuminating experimental investigations must be given to Lambourne and Bryer (1962), hence their work is often referenced in this review. Figure 2.5 of their photograph (which can be today regarded as "classic") shows the laminar vortex breakdown at low Reynolds number over a delta wing with the sweep angle of 65° placed in the water tunnel at the speed of 2 in./sec. The axial filament reveals two apparently different types of breakdown - spiral and bubble-like (more information on breakdown 'modes' is given in 2.4.1.).

By means of a ciné film they established that the axial flow suddenly decelerated, deflected and performed a few turns of a regular whirling motion then finally underwent a transition to turbulence. Figure 2.6, based on the findings, shows the axial velocity of the fluid element on the vortex centreline. The high slope at the beginning of the curve corresponds to the conditions upstream of the burst. In fact the

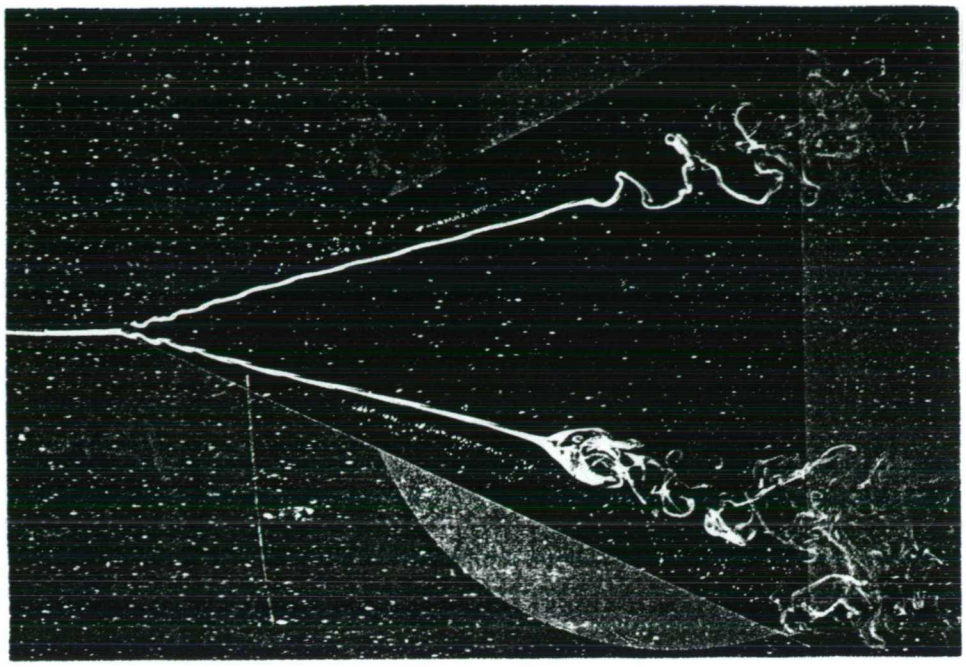

Figure 2.5. Vortex breakdown on 65^{O} sweep delta wing. From Lambourne and Bryer (1962).

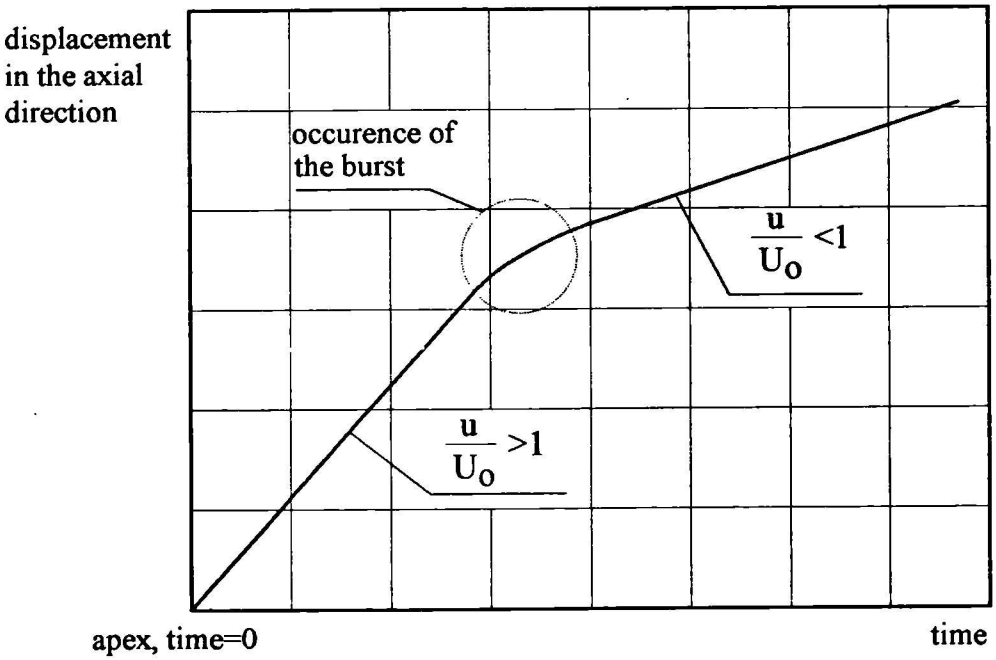

Figure 2.6. Axial velocity of the fluid element on vortex centreline for bursting conditions. Based upon Lambourne and Bryer (1962).

overshoot in the velocity was 1.63 and 2.48 for Reynolds numbers based on root chord[2] 1.2×10^4 and 3×10^4 respectively. The kink in the curve is an indication of a

[2] i.e. $Re = Uc/\nu$, where U, c and ν are the free stream velocity, delta wing root chord and fluid viscosity, respectively.

rapid deceleration and consequent burst. Then the axial velocity decreases achieving the values 0.55 and 0.83 of the free stream for the mentioned Reynolds numbers.

Figure 2.7 shows a detailed photograph of the burst (a), together with the interpretative sketch of its structure (b). The dye filament, which takes the form of

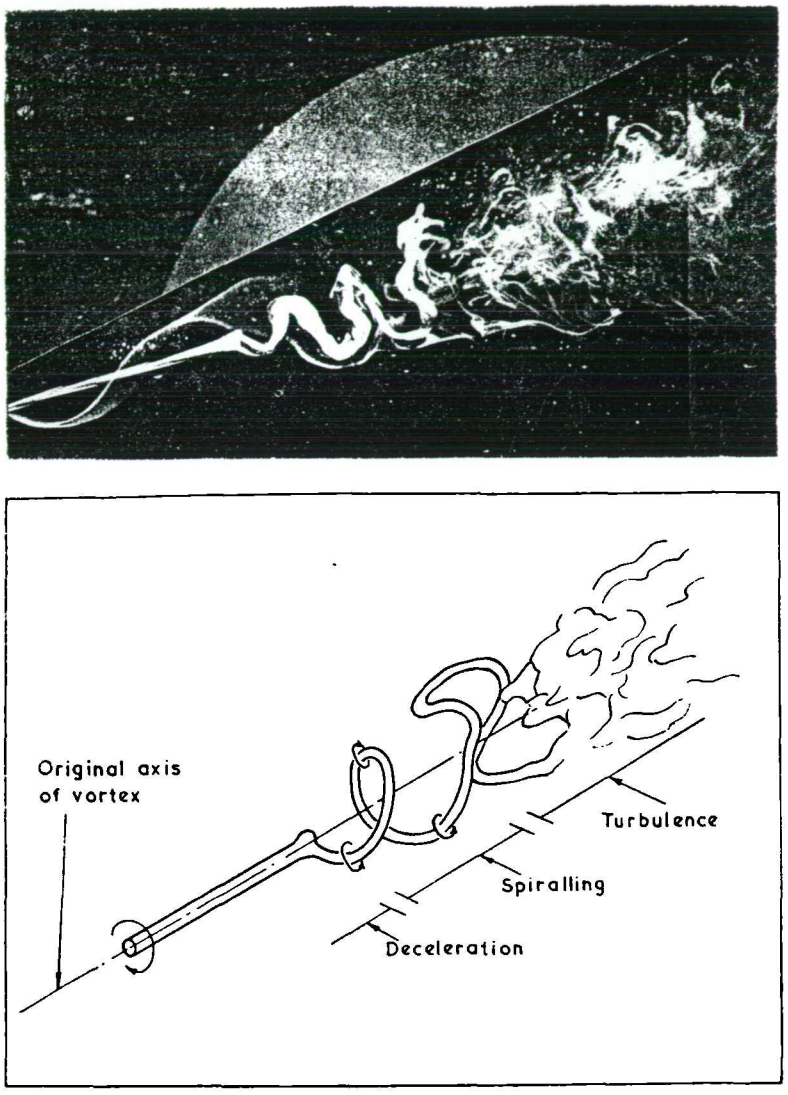

Figure 2.7. Vortex breakdown: a- photograph of spiral breakdown, b- interpretative sketch.

a conical spiral, is rotating 'bodily' about the original vortex axis and has the same sense of rotation as the laminar vortex, whereas the sense of the spiral itself is opposite. The material particles are rotating around the spiral filament in a sense consistent with the reversed flow existing inside the coils of the spiral and at the same time preserving the sense of rotation from before the burst. The rotation about the

spiral explains the dragging of the fluid from downstream within the spiral coils and the formation of the stagnant region.

The work of Lambourne and Bryer (1962) mentioned previously and investigations by Elle (1961), Peckham(1961), Wentz and Kohlman (1969) and many others established the influence of the wing geometry and its orientation in reference to the free stream flow on the occurrence and the position of vortex burst (some quantities that appear in the considerations are pointed out in figure 2.8). According to the observations vortex burst exhibits the following properties:

- For a given wing the position of the vortex breakdown depends on the angle of attack. The higher the incidence the earlier the burst tends to appear. For small angles of incidence the burst can take place downstream of the wing's trailing edge or even not to appear if the leading-edge vortex is not strong enough. Increasing the angle of attack leads to the earlier burst, but after some critical angle is exceeded the structure of the leading-edge vortex is replaced by a bluff body type vortex shedding (for a detailed considerations see Rediniotis *et al.*-1993).
- For a given angle of incidence the burst takes place earlier on the wing with lower sweep angle (figure 2.9).
- When the wing is yawed the vortex breakdown occurs earlier on the advancing side whereas on the retreating side it is delayed. Peckham (1961) and Elle (1961) report that the change in yaw of about 1-2 degrees changes the patterns of flow radically on the two sides of the wing (figure 2.10).

It is possible to obtain some empirical correlations of burst position as a function of, for example, sweep angle and incidence, but they are usually of limited value and results by individual investigators seem to contradict each other (e.g. Lambourne and Bryer-1962 and Elle-1961), the differences often being attributed to the unknown interference of the test rigs (e.g. different blockage and turbulence levels of the tunnels and various support mechanisms) or simply to a subjective

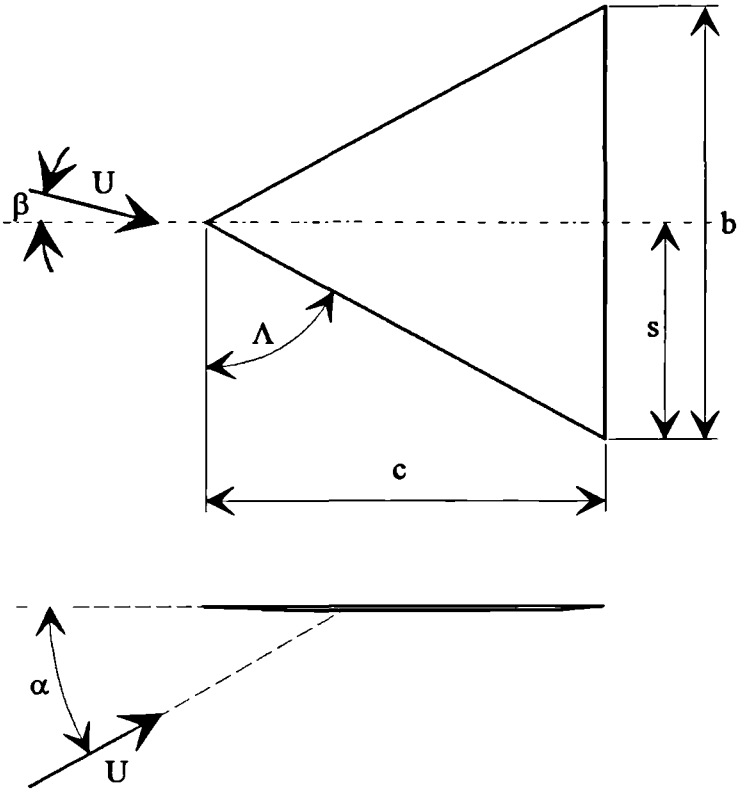

Λ - sweep angle
b - wing span
s - wing semi-span
c - root chord
α - angle of attack
β - angle of yaw
U - free stream velocity

Figure 2.8. Geometry and orientation of a delta wing in relation to external flow.

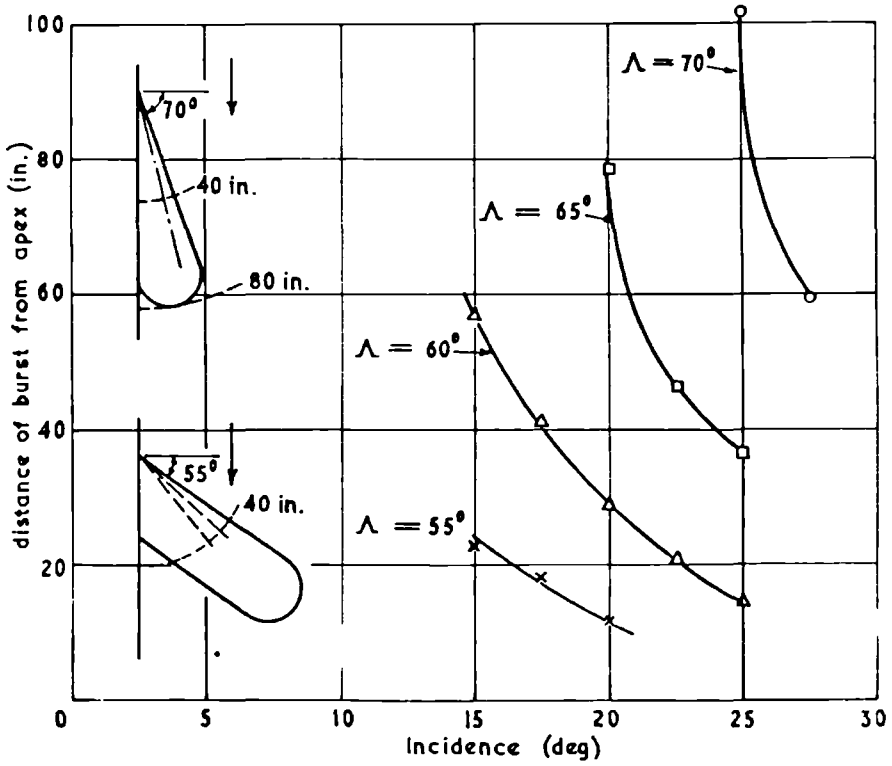

Figure 2.9. Variation of burst position with incidence and sweep angle. From Lambourne and Bryer (1962).

judgement of an investigator who determines the location of the burst from flow visualisation.

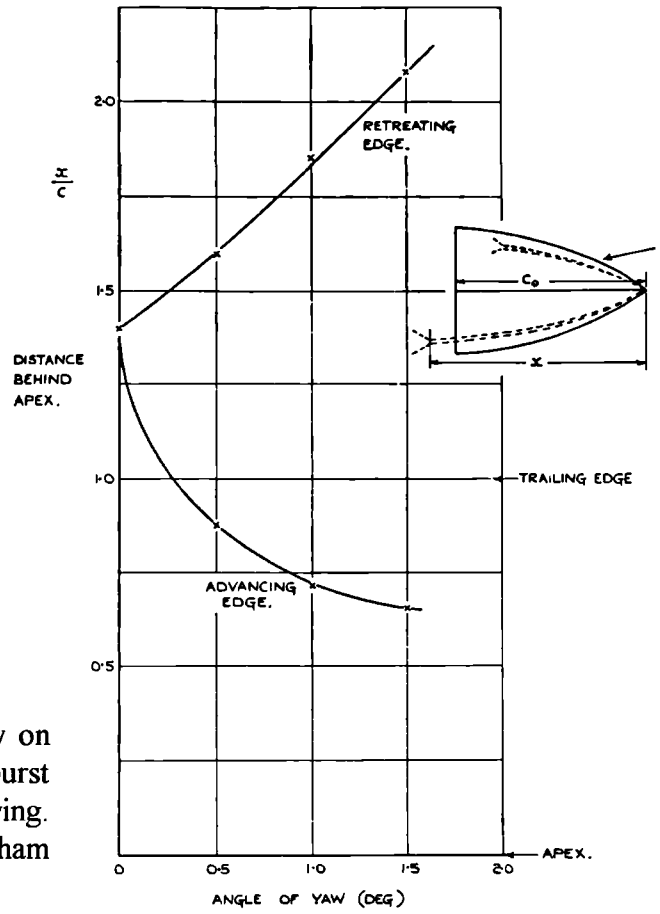

Figure 2.10. Influence of yaw on the position of burst on a slender wing. From Peckham (1961).

Lambourne and Bryer (1962) collected the data for delta wings of 65° sweep angle for the Reynolds number based on root chord $0.01\times10^6 < Re < 4.6\times10^6$ and concluded that the position of the breakdown is practically unaffected by the magnitude of the Reynolds number - the variations in *Re* being imposed by changing velocity, testing geometrically similar models and using fluids of different viscosity (e.g. wind and water tunnels).

One of the features of the vortex breakdown, important for any measurements performed by means of external probes, is its hypersensitivity to bodies introduced into the vortex core. The objects introduced into an otherwise unburst core cause premature breakdown, sometimes well ahead of them. Thus extreme care should be taken during the experiments incorporating 'physical' probes. They should be as small as possible or some of the experimental conditions should be changed to take into account their undesired influence.

2.2.3. Aerodynamic characteristics and vortex breakdown

One of the well-known and favourable effects of using slender wings is the appearance of leading-edge vortices at high angles of incidence, which generate increased lift. The strength of these vortices increases with angle of attack, so that they become a dominant and steady flow feature. The acceleration of the flow in these vortices significantly affects the pressure distribution on the wing by creating regions of low pressure, directly beneath the vortex core, which are usually referred to as "suction peaks". It is this phenomenon that is mainly responsible for an increased lift due to the vortex flow, the so-called 'vortex' or 'non-linear' lift. As a typical example, Wentz and Kohlman (1969) reported that for a delta wing with 75° sweep, vortex lift amounts to 50% of total lift (at about 25° incidence). Nelson and Visser (1990) give a figure of 30% which is attributable to the vortex lift.

A stable vortex with an orderly structure can persist, depending on the sweep angle, up to attitudes as high as 25° to 35°, the limit being the onset of large scale vortex breakdown taking place above the wing. Bursting of the vortex leads to an increase in the cross-sectional area of the vortex core and a decrease of the axial and tangential velocities. This causes loss of lift and reduction of nose-down pitching moment (Nelson and Visser-1990). The evolution of the magnitude of the 'suction peaks' due to breakdown is well documented by Lambourne and Bryer (1962). Greenwell and Wood (1992) developed a simple technique for detecting the position of the burst. Their model was a point vortex over an infinite plate, inducing a suction peak. They associated the burst occurrence with changes in 'half-width' of suction peaks.

Figure 2.11, based somewhat on the results by Wentz and Kohlman (1969) for the wing of 65° sweep, shows the lift of the wing obtained from the Polhamus' (1966) suction analogy, experiments, and by calculating only the 'potential' component of the Polhamus' total lift. The obvious shortcoming of the Polhamus'

theory is that it does not take into account the breakdown phenomenon[3].

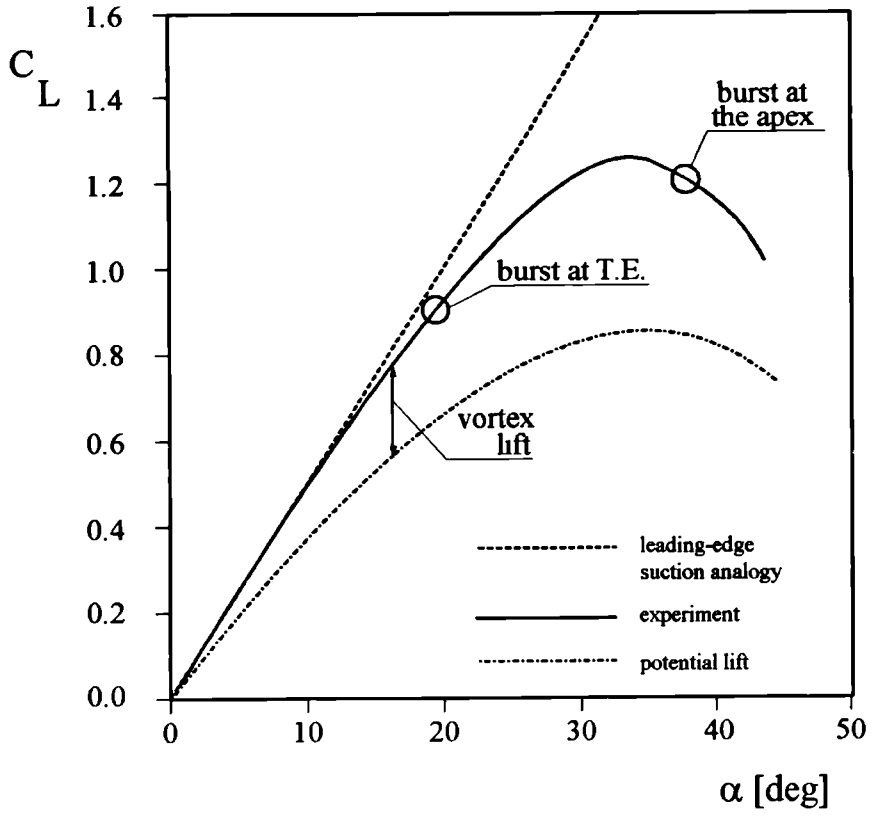

Figure 2.11.Lift characteristics for a 65° sweep delta wing obtained from Polhamus' suction analogy, experiments and potential calculations. Based upon Wentz and Kohlman (1969).

Figure 2.12, modified from Escudier (1988), shows the lift (C_L), drag (C_D) and pitching moment ($-C_M$) coefficients undergoing a sudden deterioration due to the onset of the vortex breakdown. During take-off and landing very often conditions arise when the flight regime involves sideslip. Naturally in this case the positions of bursts on the port side and the starboard side of an aircraft are different, and roughly speaking the 'lifts' for each side differ thus leading to an unexpected rolling moment. These phenomena cause unsteadiness and poor control over the aircraft and may have adverse effects on flight safety.

A number of investigations (e.g. Rao-1990, Shah *et al.*-1990, Brown *et al.* -

[3] In addition the Polhamus' lift is higher than the experimental lift even before the breakdown appears over the wing (say in the range of incidence between 10° and 18°), which is probably attributable to the complicated behaviour of the flow near the trailing edge.

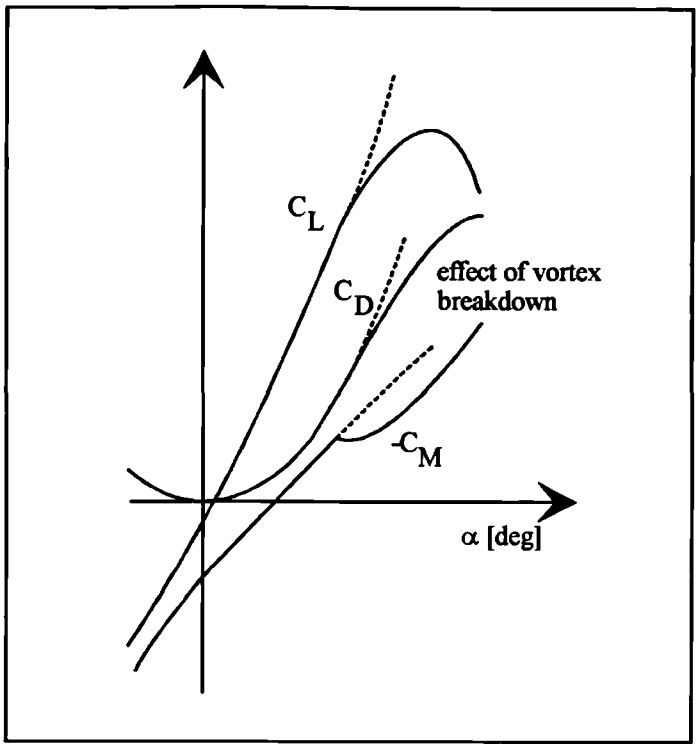

Figure 2.12. An example of the influence of vortex breakdown on deterioration of wing's aerodynamic characteristics. From Escudier (1988).

1990, Lee *et al.*-1990, Lee and Brown-1990, Mabey-1991, Wood and Bean-1993) indicate that the occurrence of the vortex breakdown has serious implications for fin buffeting for advanced, highly manoeuvrable combat aircraft. One typical example is the twin-fin configuration of the F-18 fighter (figure 2.13). Here one of the most important features is the appearance of Leading edge EXtensions (LEX). The main objective of introducing LEX was to increase the maximum lift coefficient (beyond that which could be obtained without LEX). The rolled-up vortex that originates at LEX apex induces a high flow velocity on the suction side enhancing the lift (in the same manner as for delta wings), thus the maximum lift coefficient is shifted to higher angles of attack (Erickson and Gilbert-1983, Shah *et al.*-1990); an example is given in figure 2.14.

The extensive wind tunnel and flight tests show that vertical fin buffeting occurs for angles of incidence for which the fins are "immersed" in the turbulent, energetic wake of the burst LEX vortex. The accelerations experienced by fins are reaching 500 g (Mabey-1991), this in turn leads to severe fatigue problems and thus

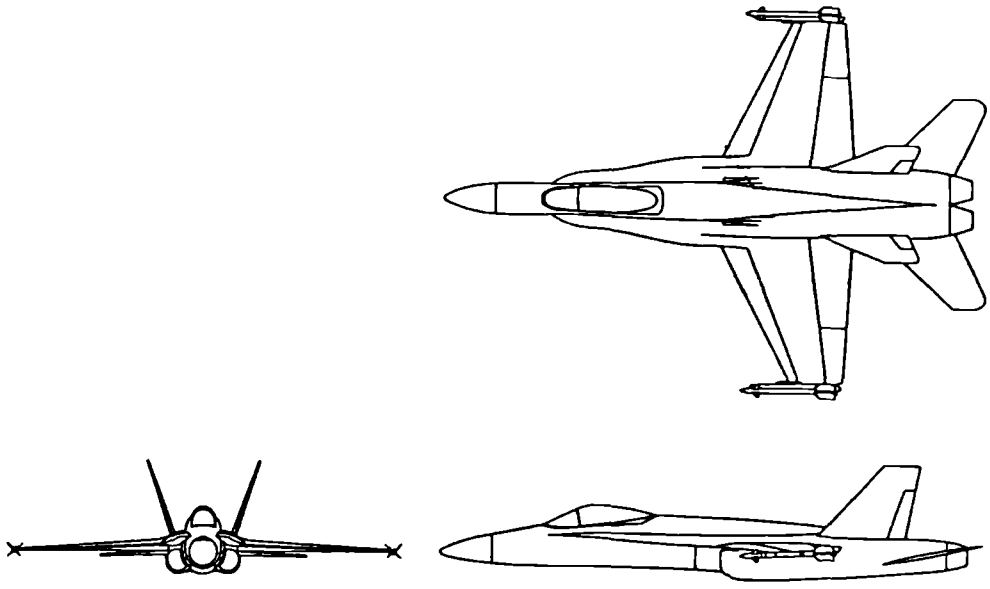

Figure 2.13.A twin-fin F-18 configuration with LEX. From Shah *et. al.* (1990).

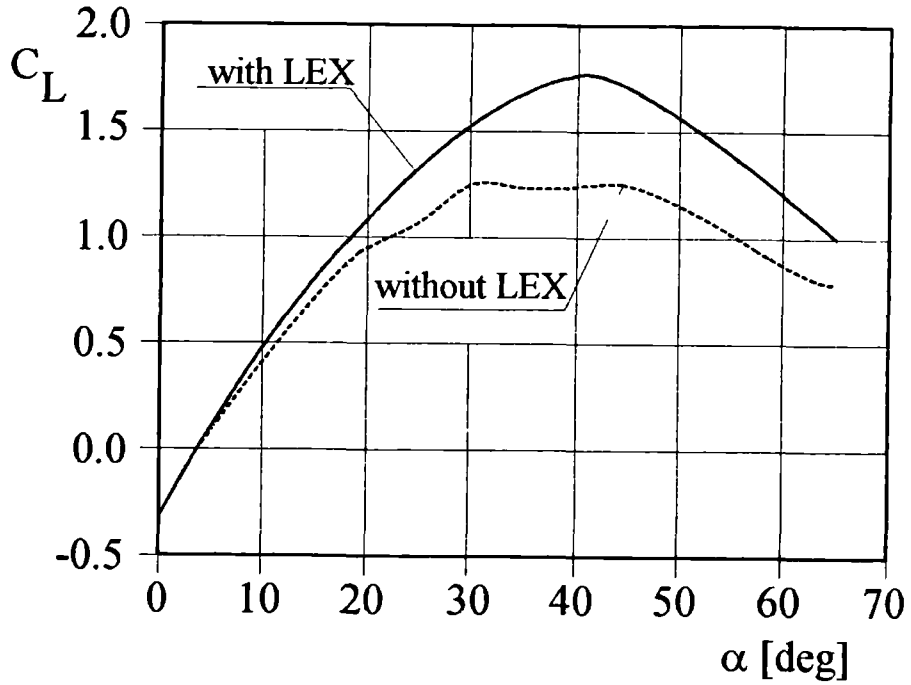

Figure 2.14.The influence of LEX on lift coefficient of an F-18 fighter. From Shah *et. al.* (1990).

shortens the life-time of fins. Figure 2.15 presents schematically the mechanism of the buffet excitation on fins for a combat aircraft, whereas figure 2.16 shows a photograph of the in-flight breakdown of the LEX vortex (the coherent structures, just downstream of burst point, are clearly visible).

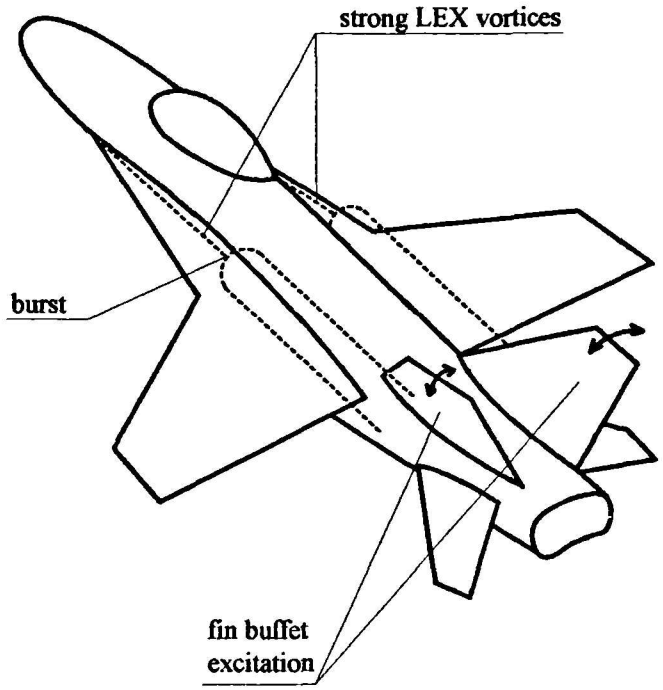

Figure 2.15.Mechanism of the buffet excitation of fins on modern combat aircraft.

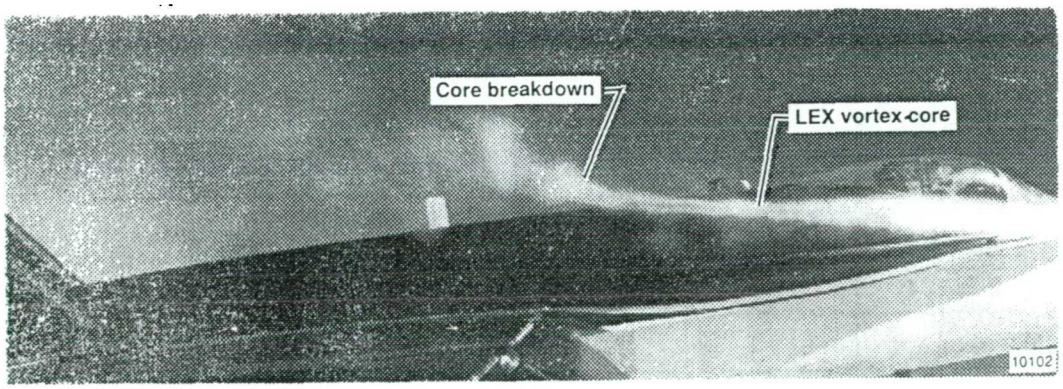

Figure 2.16.Flight visualisation of the LEX vortex burst. Del Frate *et al.* (1990).

Mabey (1991) found that the maximum fin buffeting occurs for $\alpha=23^{\circ}$, while the vortex burst position is at about $x/L=0.65$ (figure 2.17). This position is well upstream of the fin. Hence he suggests that although the local buffet excitation may be small at burst it reaches a maximum some short distance downstream where the vortex core is enlarged. Consistent with this hypothesis, as will be shown later in the thesis, the maxima in excitation spectra appear somewhat downstream of breakdown origin. Another interesting feature, found by Mabey (1991), which fully supports the

hypothesis of breakdown induced buffeting, is the behaviour of the buffet excitation while changing the aircraft's sideslip, which acts as an apparent change in the sweep of the LEX.

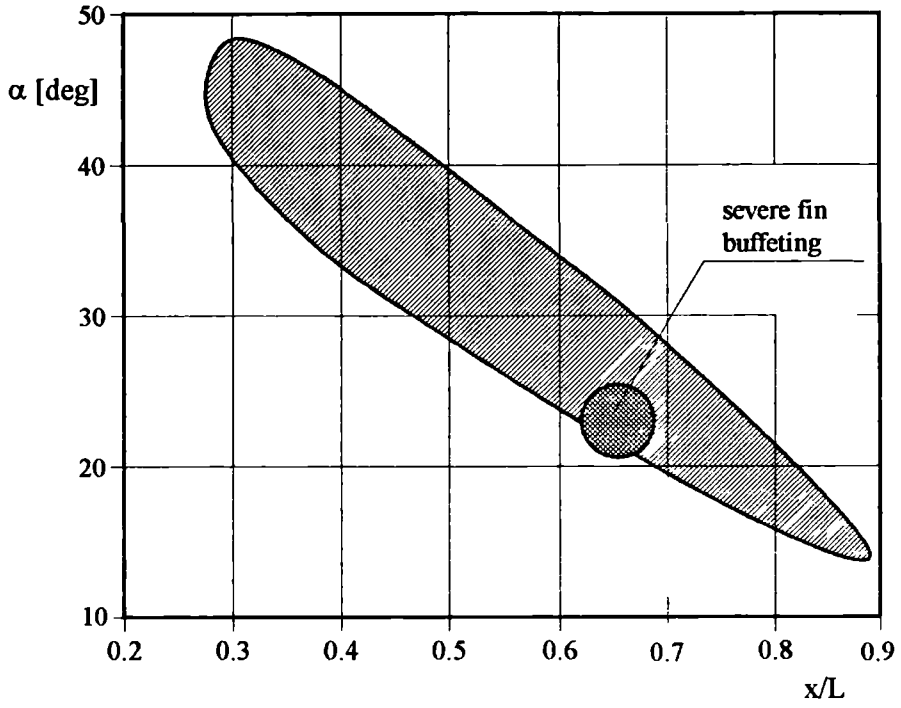

Figure 2.17.Streamwise position of the burst as a function of incidence. The region reflects the scatter of different measurements. x/L=0.2 and x/L=0.9 correspond to LEX apex and fin trailing edge, respectively. Based upon Mabey (1991).

Wood and Bean (1993), Gursul (1994), Hubner and Komerath (1994,1995), showed that the breakdown wake (perhaps at least before changing to fully disorganised flow) indicates the presence of large quasi-periodic structures, identified in pressure and velocity spectra as well-defined 'peaks'. Figure 2.18 (Gursul-1994) shows the power spectrum of the pressure transducer signal, obtained for 70° sweep delta wing by means of the transducer mounted flush on the wing's suction surface, which is characterised by a sharp peak at about f=40 Hz.

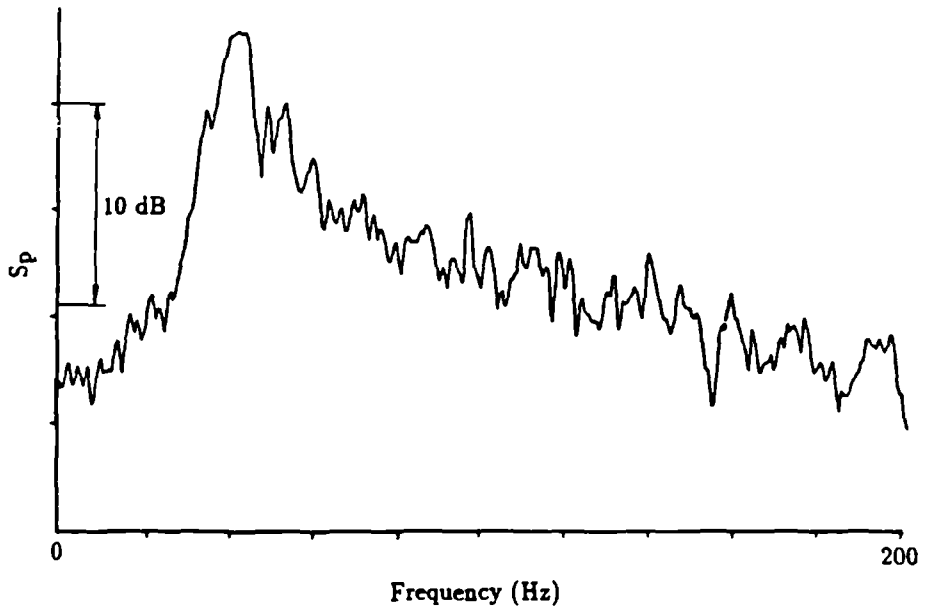

Figure 2.18.Spectrum of pressure fluctuations at x/c=0.89, y/s=0.42 for α=35.5^0, Λ=70^0. From Gursul (1994).

2.2.4. Behaviour of the burst under unsteady conditions

The behaviour of the vortex breakdown in unsteady conditions was the subject of many investigations, one of the first being Lambourne and Bryer (1962). More recent studies are Cunningham and den Boer (1990), Hanff and Ericsson (1990), Miau *et al.* (1992), Magness *et al.* (1993), Soltani and Bragg (1993), Towfighi and Rockwell (1993), Gursul and Yang (1994) and many others.

Lambourne and Bryer (1962), during their water tunnel tests, observed the influence of altering the flow velocity on the position of burst. They reported that sudden acceleration of the flow resulted in a forward motion of the burst and then a gradual return to the original place when the flow approached the new steady value. Deceleration had exactly the opposite effect (i.e. movement downstream and then a gradual regaining of the original position).

Many experiments on dynamic behaviour of the burst were conducted on wings with imposed pitching motion. Pitching is usually set either as a periodic oscillation of the angle of attack or as a so-called 'ramp' pitching motion (either

linear or sinusoidal increase or decrease of incidence). The non-dimensional quantity associated with pitching - reduced pitching rate - usually takes the following form:

$$K = \frac{(d\alpha/dt)\, c}{2\, U} \qquad (2.1)$$

where α - angle of incidence [rad], c - root chord [m], U - free stream velocity [m/s], and can be regarded as a ratio of characteristic velocity associated with angular displacement ($c(d\alpha/dt)/2$) to the free stream velocity (U) [4]. Experiments are usually conducted for values of K up to 2.

Experiments with periodic pitch indicate that there is a phase delay between the oscillatory motion of the wing and the corresponding change in position of the burst (figure 2.19). Gursul and Yang (1994) report that this delay depends mainly on the reduced frequency (pitching rate for periodic oscillation) K, and can reach 180° (figure 2.20). This means the burst position shifts to the apex while the incidence decreases and vice versa, which is exactly opposite to the static behaviour.

Miau *et al.* (1992) investigated the 'ramp' pitching influence on vortex development and burst by using a set of delta wings with different sweeps (Λ=59°, 63.4°, 67°, 70°) and applied a low reduced pitching rate between 0.01 and 0.04. During the pitching-up motion they observed the delay in appearance of breakdown in relation to steady-state and identified its two sources: firstly, the time delay of order (c/U) which is required for the flow to respond to the changes in pitch; secondly, the delay (occurring for rather low sweeps and high K) which they attributed to suppression of the primary vortex by exaggerated development of secondary separation region during the transient manoeuvre. For pitching-down motion only the first delay was found. In this investigation the instantaneous velocity field was obtained by LDA techniques.

[4] The dimension of K is [deg] or [rad] depending on units of α. K should involve some characteristic angle to be dimensionless. For a periodic motion, however, ($d\alpha/dt$) is replaced by frequency. Thus K is non-dimensional.

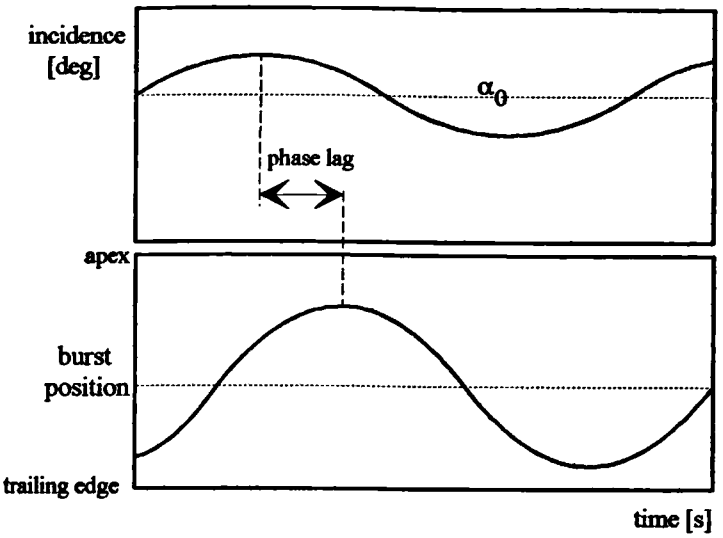

Figure 2.19.Phase lag between wing oscillation and corresponding burst position. From Gursul and Yang (1994).

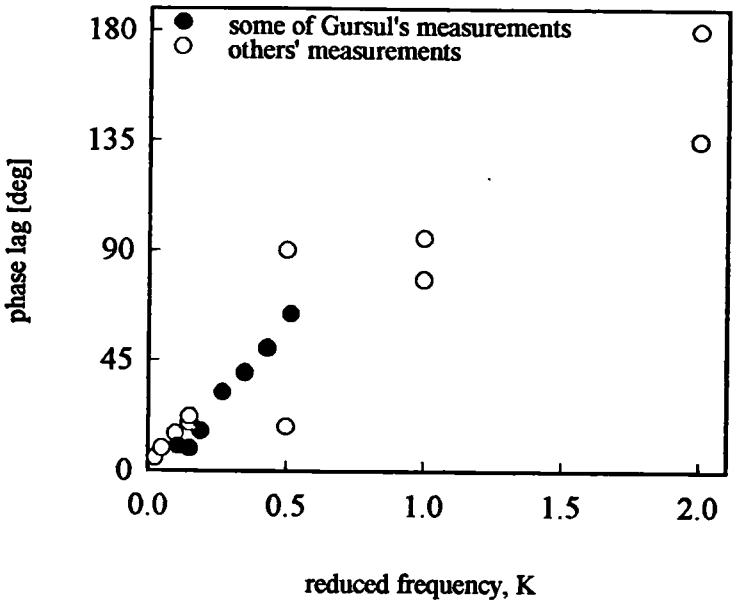

Figure 2.20.Phase lag as a function of reduced frequency, $\Lambda=70^0$. From Gursul and Yang (1994).

The phase delays described can be expressed as hysteresis loops if, say, α is plotted against breakdown position (or an aerodynamic force coefficient). Soltani and Bragg (1993) show an example of the hysteresis of normal force coefficient[5] when a 70^o sweep delta is performing an oscillatory pitching motion with extremes $\alpha=0^o$ and

[5] Some more detailed measurements of forces and moments, including the hysteresis phenomena, on a straked delta wing can be found in Cunningham and den Boer (1990)

55° (figure 2.21). The pitching-up motion produces an overshoot in C_N, while pitching down is responsible for a deficit in relation to static values. They point out that the magnitude of these effects depends strongly on the reduced frequency and the mean values of angle of attack. The transient manoeuvre has been also observed by means of PIV techniques (Magness *et al.*-1993, Towfighi and Rockwell-1993, Lin and Rockwell-1995).

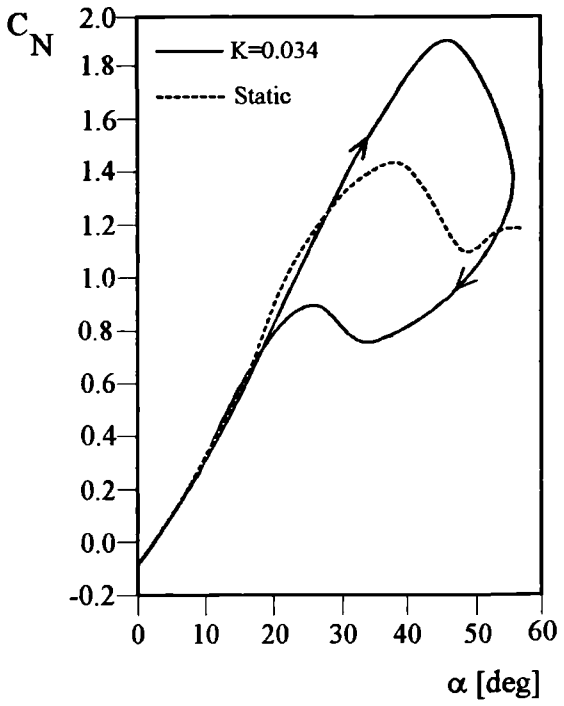

Figure 2.21. Comparison of static and dynamic normal force coefficient, $\Lambda=70^0$. From Soltani and Bragg (1993)

2.2.5. Vortex breakdown control

As shown earlier, vortex breakdown has adverse effects on both dynamic and static aerodynamic characteristics, for example, causing undesired effects in lift, pitching and rolling moments and also shortening the life of aircraft components due to fatigue processes (e.g. fins of F-18). The question of controlling vortex breakdown has been addressed by many researchers (e.g. Gersten *et al.*-1985, Rao-1990, Gu *et al.*-1993, Bean *et al.*-1993 and many others), the aim being to develop measures to manipulate dominant vortical flow structures. Different techniques were proposed, which can be divided into:

- passive controls; adding elements like: LEX-fence, strakes, dorsal root extensions

etc. which help, for example, fix or couple (decouple) vortical motions.

- active controls; e.g. blowing or suction, which, roughly speaking, may be regarded as an attempt to delay/eliminate vortex bursting, by changing the balance between axial and swirl components within the vortex; or moving leading edge flaps.

Figure 2.22 shows some examples of passive (dorsal root extension - *a*) and active controls (hinged LEX in a and TLEB - *b*) giving fin buffet attenuation. Tangential Leading Edge Blowing (TLEB) affects the vortex equilibrium condition by controlling the location of the separation point.

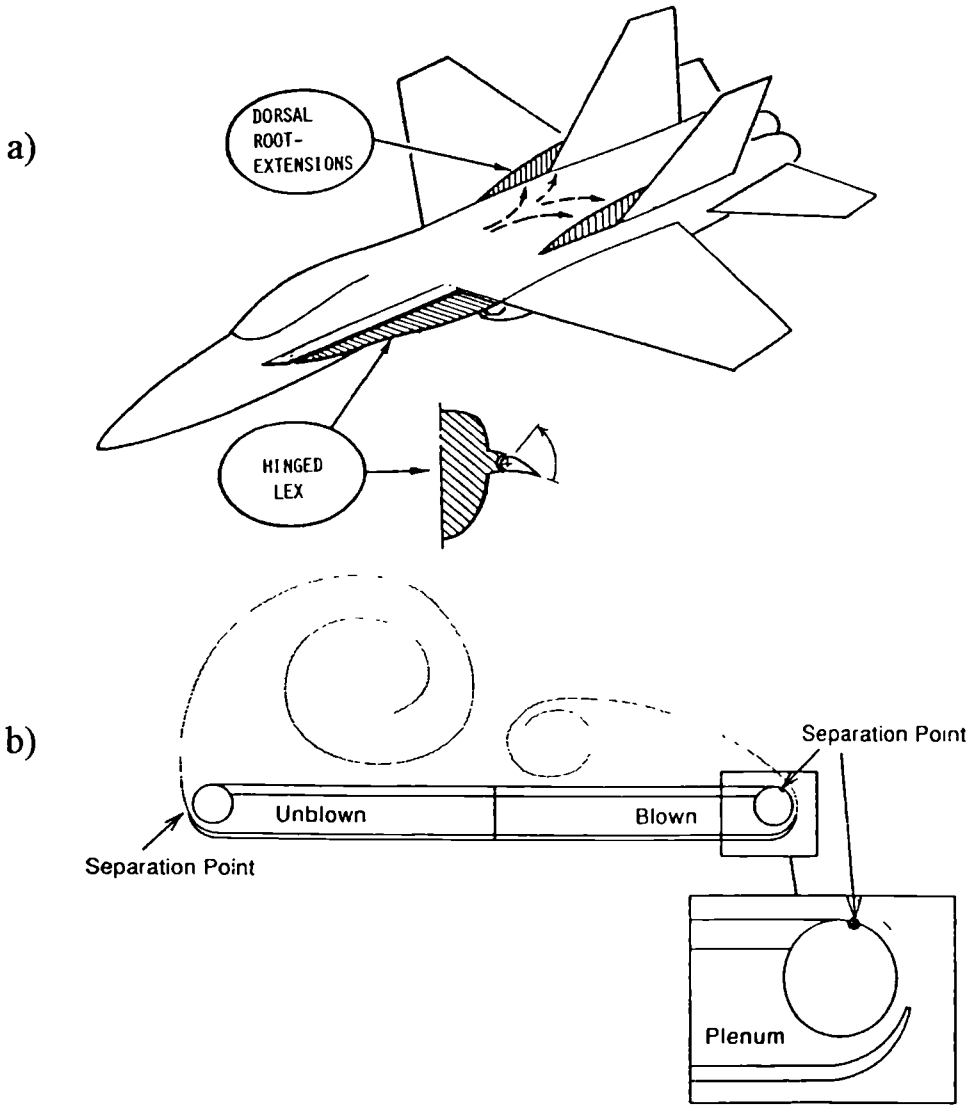

Figure 2.22.Examples of passive and active controls for attenuation of fin buffet by means of: a- hinged LEX and dorsal root extension, from Rao (1990); b- tangential leading edge blowing (TLEB), from Bean *et al.* (1993).

2.3. Devices for simulation of the vortex breakdown

Vortex breakdown has serious implications in the field of aeronautics. However even the simplest experimental configurations, like delta wings, do not provide a satisfactory control over the phenomenon. The dependence of the vortex axis location on angle of attack and the hypersensitivity of the burst to the presence of probes illustrate the difficulties met by researchers. Therefore the simulation of the phenomenon in different devices was necessary to understand its general features. The designs of these vortex generators differ and the following sections discuss various vortex breakdown simulations.

2.3.1. Vortex tube

Harvey (1960,1962) conducted a series of experiments in a device called the 'vortex tube'. The detailed design is described in the paper by Titchener and Tylor-Russel (1956), who investigated the growth of vortices in turbulent flow. Figure 2.23

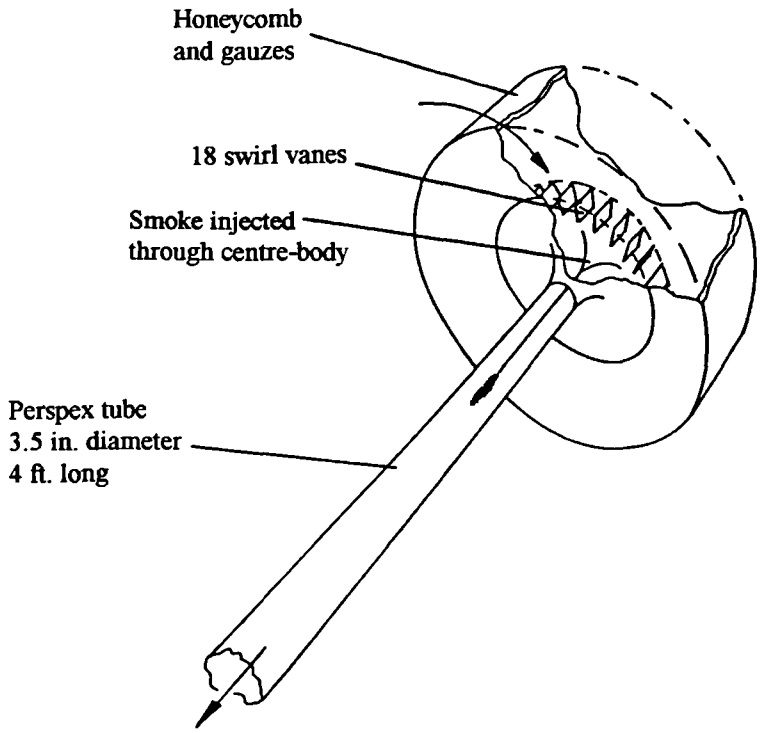

Figure 2.23. Vortex tube arrangement used by Harvey (1960,1962).

shows the vortex tube arrangement used by Harvey. The apparatus consists of a Perspex tube serving as a test section and a carefully designed air intake. The air, which is drawn through the apparatus by means of the fan located at the downstream end (not shown in figure 2.23), passes the set of swirl vanes and acquires the tangential component of the velocity. Then it is turned through an annular channel created by an outer curved wall and a centre-body, and finally reaches the cylindrical test section. The gauzes and honeycomb covering the intake provide steady laminar flow conditions and reduce the influence of the ambient pressure fields. The screen at the downstream end produces a significant pressure drop and thus stabilises the flow in the test section.

The vortex core is created by the shedding of the centre-body boundary layer. The low centre-line pressure leads to the formation of an axial velocity jet just downstream of the centre-body. The size of the core can be changed by suction or blowing through the slot located at the centre-body. Outside the core, up to the outer boundary layer on the tube wall, the flow is irrotational and the circulation is approximately constant for all radii.

Similar arrangements to the one described were used by many other investigators: Lambourne and Bryer (1962), Kirkpatrick (1965), Sarpkaya (1970,1971,1974), Faler and Lebovich (1978), Garg and Leibovich (1979), Escudier and Keller (1985a, 1985b). Figure 2.24 shows the experimental set-up utilised by Sarpkaya, who conducted his experiments in water. The test sections, unlike Harvey's, were slightly diverging tubes with the semi-angle of divergence up to 4.30^{o}. Another variation of the vortex tube is the device used by Brücker and Althaus (1992,1995) and Brücker (1993). Here the complicated design of swirl vanes and bell-mouth inlet is replaced by a set of 12 guide vanes arranged about the centre-line (figure 2.25). The vanes are fixed at an angle of 45^{o} and the only controlling parameter is the flow rate. The choke is introduced inside the test section to provide an adverse pressure gradient. In this type of arrangement the axial velocity profile has a wake-like distribution, unlike the previous ones.

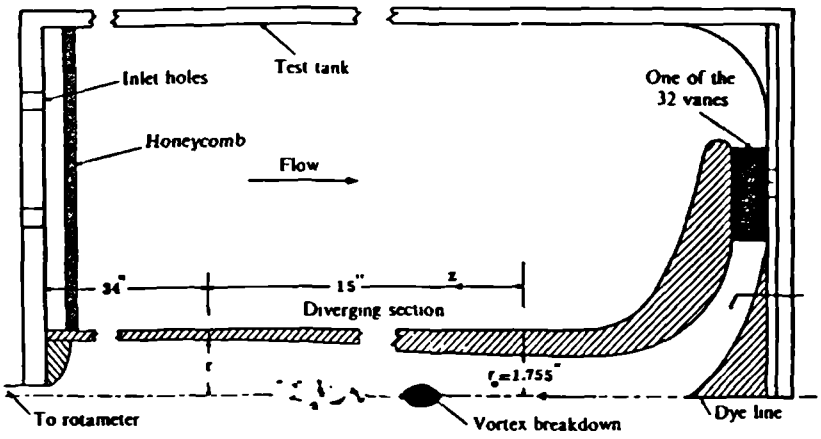

Figure 2.24.Apparatus with slightly diverging test section for water experiments by Sarpkaya (1970,1971,1974).

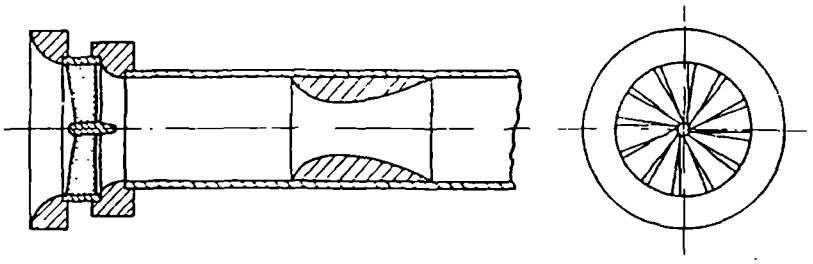

Figure 2.25.Water channel used by Brücker and Althaus (1992,1995) and Brücker (1993), with star-like guide vane arrangement.

It is worth emphasising certain differences between the leading-edge vortices and the vortices obtained in the vortex tube generators. Firstly, in the leading-edge vortex on slender wings the vorticity is fed in a continuous manner, thus allowing the vortex to strengthen. In the vortex tube, however, after the swirl is imparted to the flow there is little change in its character until the vortex bursts. Secondly, the feeding of vorticity to the leading-edge vortex spoils the axial symmetry of the flow. By using the axisymmetrical geometry of the vortex tube the asymmetries appearing in leading-edge vortices are removed. The most important difference between delta wing and vortex tube experiment, from the practical point of view, is the ability of the latter to change the circulation and the adverse pressure gradient independently within a certain range. Thus the vortex tube arrangement is more convenient in controlling and investigating the breakdown.

2.3.2. Tangential inlet vortex generator

Escudier *et al.* (1980) and Escudier and Zehnder (1982) employed a configuration in which the vortex is generated by an inflow jet tangential to the wall of a cylindrical cavity (figure 2.26). The vortex core is produced by the rolling-up of the shear layer shed at the slot exit[6]. In this sense the process may be comparable

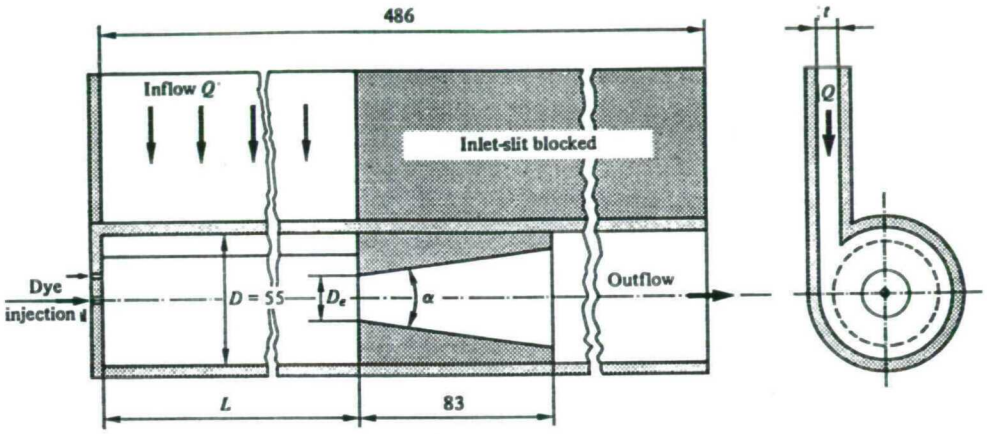

Figure 2.26. Tangential inlet vortex generator (slit tube) employed by Escudier *et al.* (1980) and Escudier and Zehnder (1982).

to the formation of the leading-edge vortex on slender wings, but here the adverse pressure gradient can be varied independently by the diverging nozzle. Escudier (1988) points out certain drawbacks of the configuration: firstly, the flow is

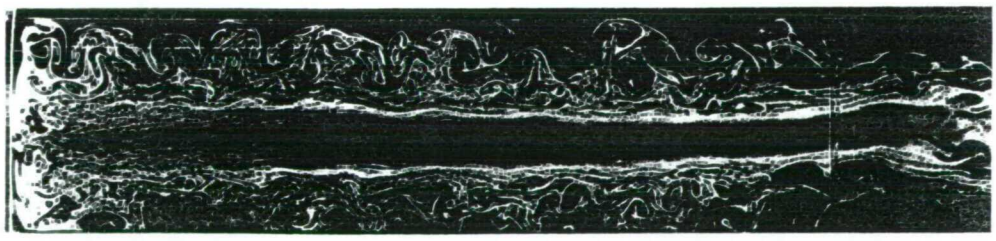

Figure 2.27. An example of Taylor-Görtler vortices in a jet-driven vortex flow. From Escudier (1988).

[6] The contribution of vorticity from the endwall boundary is practically negligible, unlike in the vortex tube, where the vortex core is created by the shedding of the centre-body boundary layer.

significantly influenced by Taylor-Görtler vortices which form on the tube wall (figure 2.27), and secondly, the flow in the generator section is slightly asymmetrical.

2.3.3. Rotating circular pipe

Suematsu *et al.* (1986a, 1986b) employed the apparatus shown in figure 28a. Here, the working fluid (water), contained in the constant head tank (1), passes through a honeycomb (2) and enters an acrylic pipe (3) of internal diameter 58.6 mm and length 0.6 m. The induction motor (8) drives the pipe, so that it rotates about the centre-line. The porous material (4) (polyurethane foam 40 mm thick), inserted at the beginning of test section, rotates with the pipe, thus the swirl velocity profile

a) b)

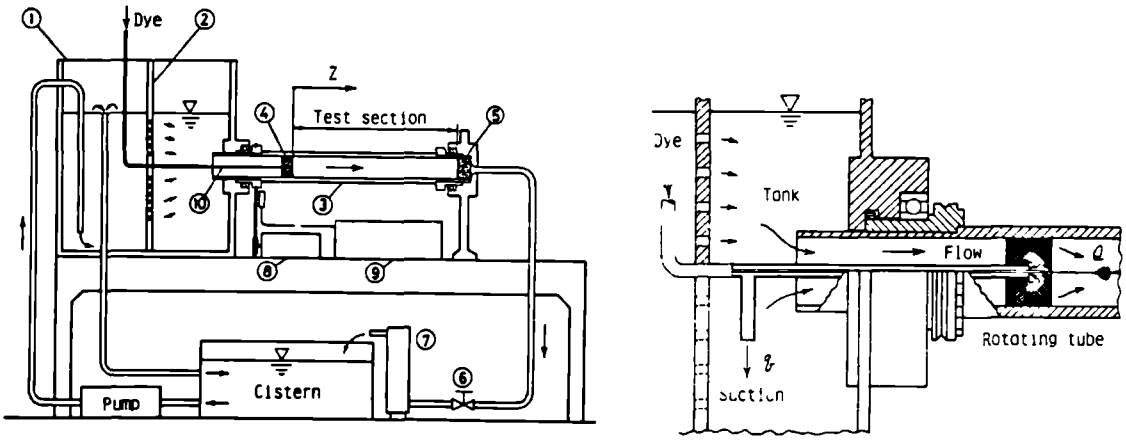

Figure 2.28. Apparatus used by Suematsu *et al.* (1986a, 1986b); a- design: 1 - constant head tank, 2 - honeycomb, 3 - circular pipe, 4,5 - filters, 6 - valve, 7 - rotameter, 8 - motor, 9 - optical tachometer, 10 - dye leading tube; b - suction applied to the vortex centre.

corresponds to solid body rotation, whereas the axial velocity profile is roughly uniform. The fluid leaving the test section passes through the filter (5), valve (6) and rotameter (7) and is discharged to the cistern. The flow is visualised by injecting a

dye through the tube (10) into the centre of rotating pipe. Optional test sections can be introduced in the form of slightly diverging or converging pipes. The flow conditions can be changed also by applying suction within the porous material (figure 2.28b).

2.3.4. Vortices generated in cylindrical containers

Escudier (1984), following earlier German experiments, employed a configuration (figure 2.29) completely different to ones discussed so far. Here the vortex is generated inside a vertical circular cylinder filled with liquid (in his experiments glycerine/water mixture) by means of a rotating endwall. The physics of this confined flow is given, for example, by Lopez and Perry (1992). The rotating endwall creates the Ekman boundary layer which, due to centrifugal forces, acts like a pump sending the fluid outwards and drawing it down from above. The fluid moving outwards meets the tank's side wall and then spirals upwards. The flow is turned once again when it reaches the upper endwall and finally separates from the upper endwall at its centre, thus forming a central vortex which returns the fluid

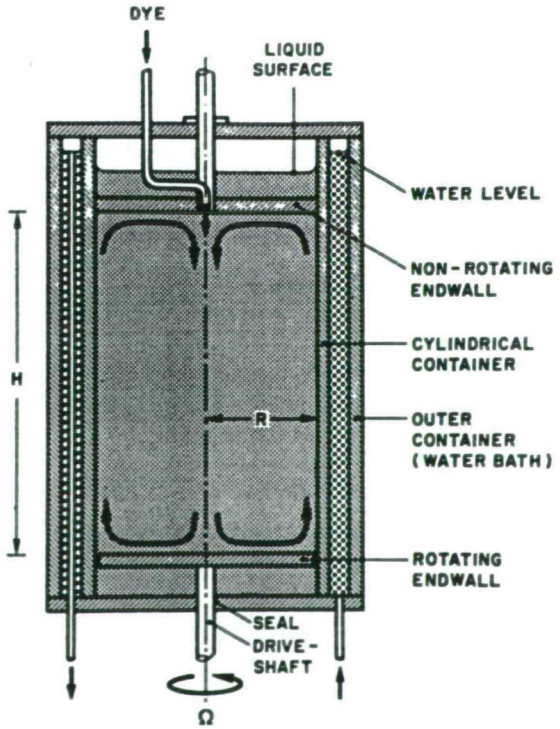

Figure 2.29. Schematic diagram of the experimental arrangement used by Escudier (1984). R=95 mm, H-adjustable, investigated range: $1.0<H/R<3.5$.

downwards towards the Ekman layer. Depending on experimental conditions this central vortex can break down.

The unquestionable advantages of this unusual arrangement are practically perfectly axisymmetric vortex and a limited number of governing parameters (namely the rotational Reynolds number $Re=\Omega R^2/\nu$ and H/R - the cylinder aspect ratio[7]). In addition the simple boundaries make the comparison between experiments and numerical calculations easy and reliable.

Spohn *et al.* (1993) used an apparatus working on the same principle (figure 2.30a), but replaced the upper endwall by a free surface. Thus it is possible to change the aspect ratio H/R continuously by changing the liquid level in the apparatus. However the presence of the free surface changes somewhat the flow patterns originally observed by Escudier (1984).

Granger (1993) described a vortex generator in the form of the cylindrical tank in which the vortex is created by tangential injection of water along the inner surface through numerous orifices, while the axial flow is imposed by a sink in the middle of the bottom endwall (figure 2.30b). Maxworthy *et al.* (1983) conducted experiments in a *rotating tank* with axial motion imposed by a suction tube mounted in the upper endwall (figure 2.30c).

a)

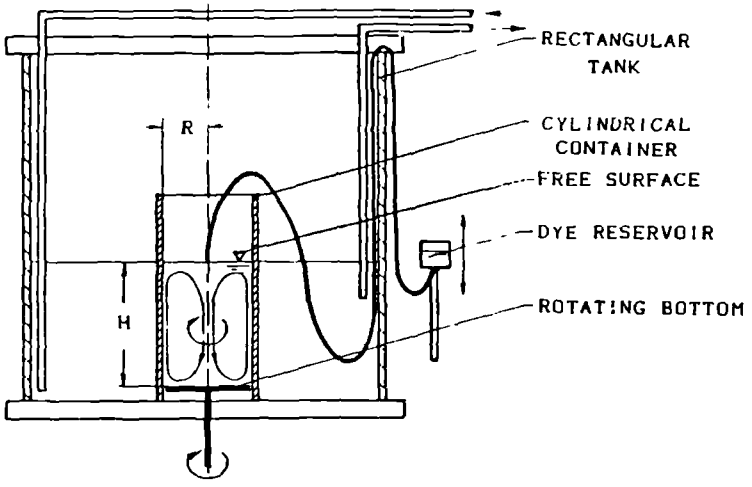

Figure 2.30.*(continued on the next page)*

[7] Here Ω, R, H and ν are the angular velocity of the endwall, radius and height of the cylinder and fluid viscosity, respectively.

b)

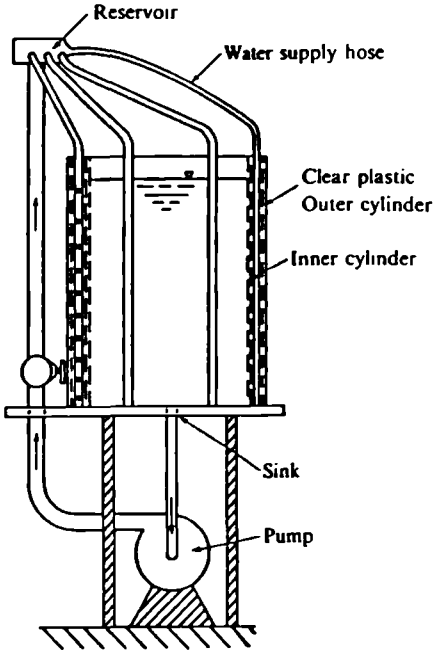

c)

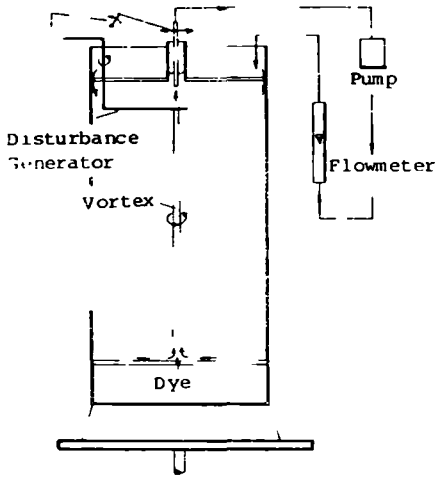

Figure 2.30.Other designs of cylindrical containers; a- by Spohn *et al.* (1993), R=55 mm, H-adjustable, investigated range: $0.5<H/R<4$; b- by Granger (1993), dimensions of outer cylinder: D=0.58m, H=1.22m; c- by Maxworthy *et al.* (1983)

2.3.5. Experiments with free vortices

The devices described in sections 2.3.1 through 2.3.4 generate vortices often described as 'confined' as opposed to 'free vortices' met, for example, in wind tunnel tests. The fundamental difference lies in the interaction of the vortex with the boundaries of the apparatus (which may be strong, for example, in the vortex tube, but negligible in wind or water tunnel tests).

Delta wings in the water or wind tunnel, described in section 2.2 , are naturally the simplest generators of free vortices. Staufenbiel and Helming (1985) employed a rectangular wing of aerodynamic cross section for creating a wing-tip vortex which was in turn subjected to different pressure gradients by capturing it in a nozzle/diffuser system (figure 2.31). Pagan and Molton (1990) used the arrangement

shown in figure 2.32. Here two airfoils are attached to a central sting which can be used for air blowing. This allows independent control over the swirl and axial velocity profiles. The vortex enters the air intake of two parallel plates with adjustable flaps at the downstream end. By adjusting the flaps to change the pressure gradient in front of the intake, it is possible to control the breakdown position (which always remains in front of the intake).

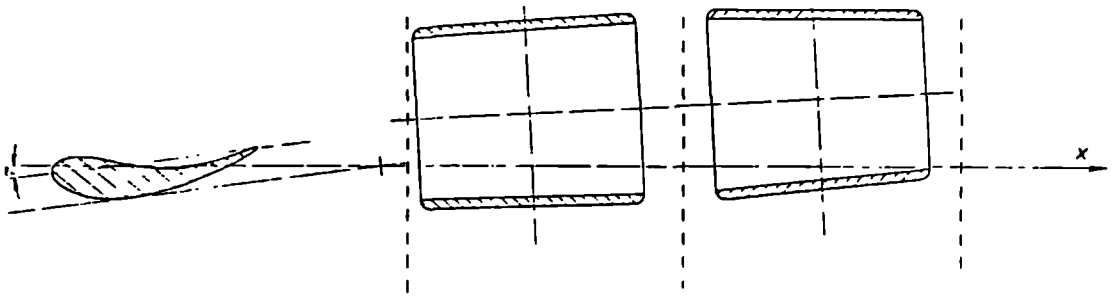

Figure 2.31.A diagram of a set-up used by Staufenbiel and Helming (1985).

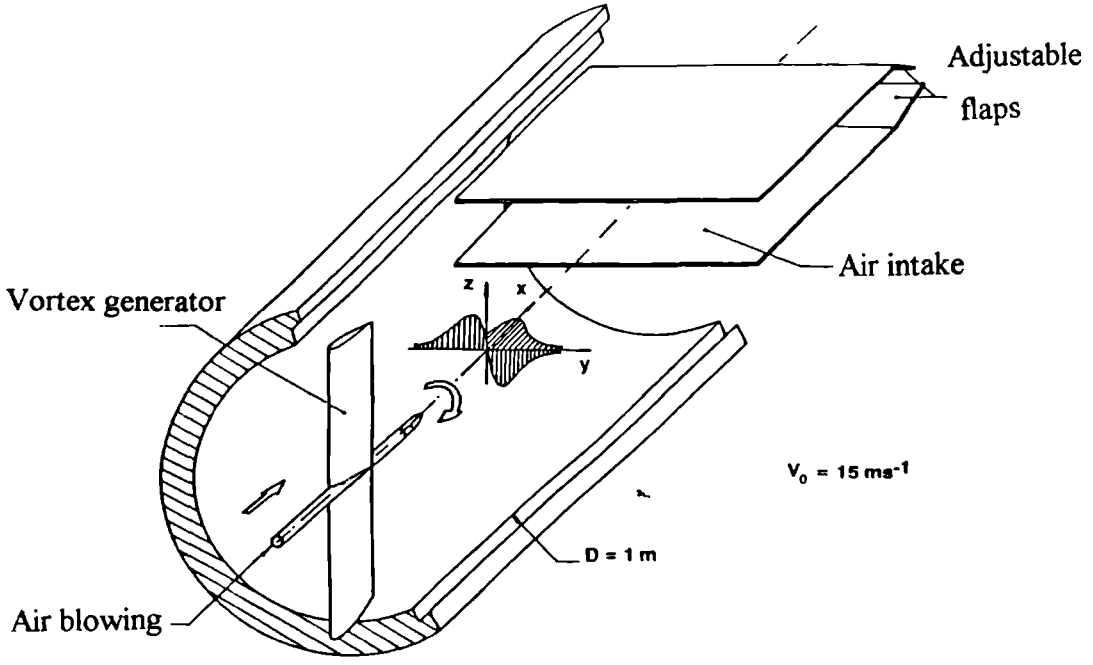

Figure 2.32.An experimental arrangement with axial blowing and pressure gradient control by Pagan and Molton (1990).

2.4. Experimental investigations of vortex breakdown

A short phenomenological description of vortex breakdown's fundamental features was given briefly in section 2.1 to outline the primary subject of the thesis. Vortex breakdown was defined as an abrupt change in the structure of the core of an axisymmetrical flow with large amounts of swirl, with three basic features which are: (1) a sudden retardation of the flow, (2) divergence of stream surfaces and (3) stagnation accompanied by flow reversal and sudden change to a very unsteady flow. Here some aspects of the phenomenon will be examined in more detail.

2.4.1. Forms of vortex breakdown

One of the most detailed investigations of the vortex breakdown were those by Sarpkaya (1970, 1971, 1974). The study, conducted with the apparatus shown in figure 2.24, mainly employed flow visualisation techniques and was concerned with the behaviour of the breakdown in response to different flow conditions (e.g. swirl intensity and axial velocity). According to his results vortex breakdown may assume three different forms (figure 2.33 a, b and c) which can be revealed by injecting dye into the vortex centre-line and gradually increasing the initial swirl.

The first to appear, once the swirl reaches some critical value, is an asymmetric form, consisting of an abrupt deceleration, kink and then deformation of the axial filament into a spiral which persists for a few turns and then finally breaks up into turbulence (figure 2.33a). This form looks similar to the one found by Lambourne and Bryer (1962), shown in figure 2.5 (upper half of the photograph). The second form, which is revealed as the swirl is increased, is also asymmetric. The axial filament decelerates and expands into a slightly curved triangular sheet taking a double-helix shape (figure 2.33b). This form of breakdown was not found within a leading-edge vortex. For larger amounts of swirl, the axial filament spreads out symmetrically at the stagnation point and the outer streamlines expand as

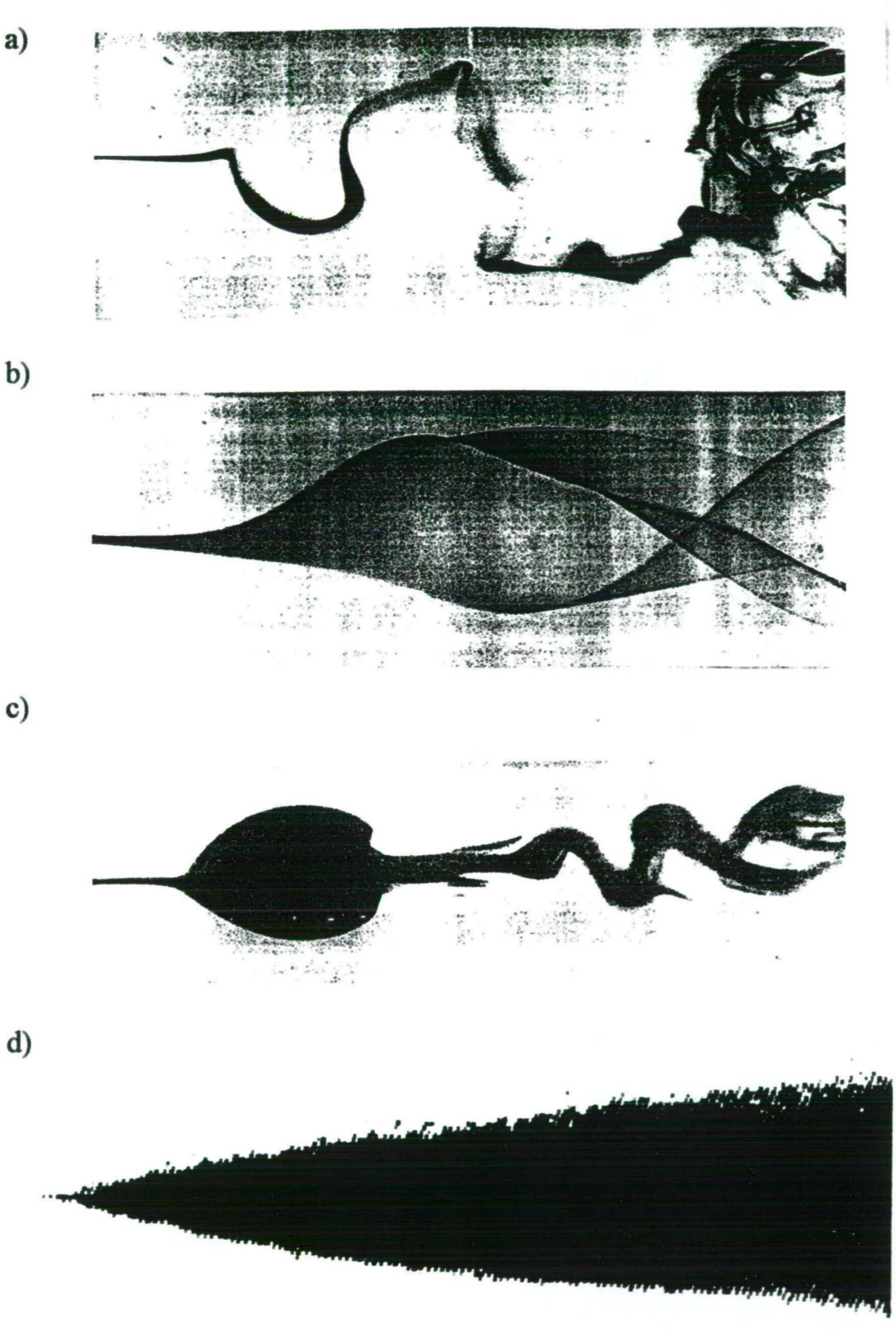

Figure 2.33.Forms of vortex breakdown found by Sarpkaya (1970,1971,1995): a-spiral form, b-double helix form, c-bubble form, d-conical form (turbulent).

if meeting a solid body. Behind the stagnation point a nearly axisymmetric bubble of recirculating fluid forms, followed usually by a few spiral turns then a transition into turbulence (figure 2.33c). This form is comparable with vortex breakdown shown in the lower half of figure 2.5.

Sarpkaya (1970,1971) put his experimental data into the graph showing different forms of vortex breakdown as a function of Reynolds number $Re=W_mD_O/\nu$ and circulation number $\Omega=\Gamma/W_mD_O$ (see section 2.4.4 for symbol explanations). The resulting map is shown in figure 2.34. The regions in the figure: I, II and III correspond to axisymmetric, spiral and double helix modes of breakdown, respectively. Region IV marks the conditions which do not lead to breakdown.

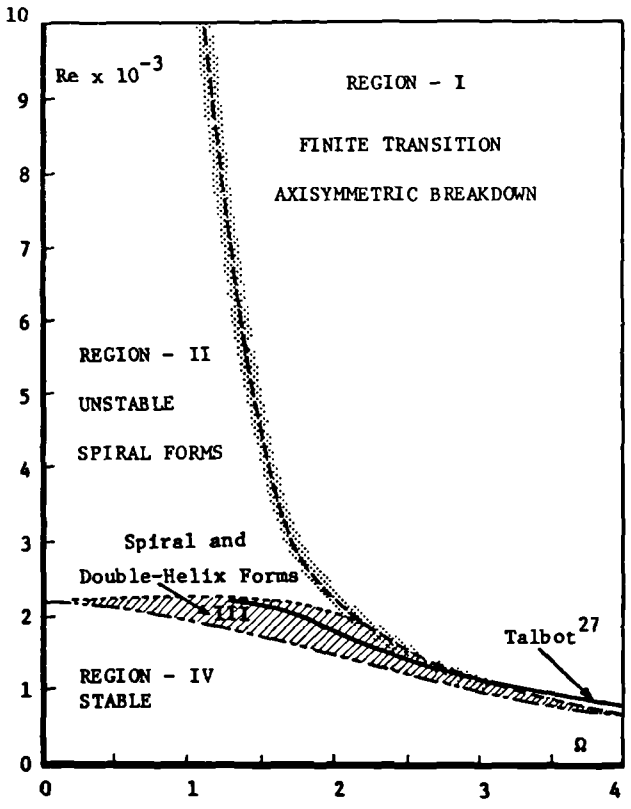

Figure 2.34. The four states of swirling flow by Sarpkaya (1971) as a function of Reynolds number Re and circulation number Ω. The conical breakdown (Re between 5×10^4 and 2.25×10^5, Ω between 0.50 and 0.77) outside the borders.

Recently Sarpkaya (1995) supplemented his early research by investigating vortex breakdown in the same apparatus at much higher Reynolds numbers (namely between 5×10^4 and 2.25×10^5 with corresponding circulation number 0.77 and 0.50). The form of breakdown, which he observed, is characterised by the

appearance of a small bubble-like structure which is itself almost an integral part of the turbulent wake. The higher the Reynolds number the more the bubble and the wake 'unite', finally forming a 'turbulent cone' (figure 2.33d). The originality of this observation may however be questioned. This 'form' of breakdown is commonly found on slender wings at high Reynolds numbers (compare the remarks in section 2.1). The current investigations, using correlation techniques in the wake, suggest that this form of breakdown is a turbulent 'version' of spiral mode. This might be even inferred by 'extrapolation' of figure 2.34 beyond its borders (for much higher Reynolds numbers and fairly small circulation numbers[8]).

Faler and Leibovich (1977) conducted experiments using a copy of Sarpkaya's apparatus. They proposed a more detailed classification of different types (or 'modes') of the breakdown phenomenon based on the development of the axial filament: (0) axisymmetric bubble, nearly closed, followed by spiralling flow and transition to turbulence, (1) also axisymmetric, but with open end, and an immediate transition to turbulence, (2) spiral type, (3) starts with a spiral, but exhibits shearing and rapidly becomes disorganised, (4) flattened bubble, open at its downstream extremity, (5) double helix mode, (6) the axial filament shears into the tape and departs off the axis but the structure is steady or very slowly rotating in a laboratory frame of reference. The results were presented in the form of 'map' (figure 2.35) showing the occurrence of these different modes (although in a different way than by Sarpkaya). The authors admit there are some differences in the conditions at which the particular modes appear (comparing to Sarpkaya's results), but the general trends are maintained.

In practical situations two forms of breakdown are most often observed: the spiral and the bubble-like forms. The first one is common for leading edge vortices, whereas the second is more likely to appear in confined axisymmetrical vortices,

[8] It is worth mentioning that the Reynolds numbers for the current vortex tube experiments were of order of 1×10^5 (falling roughly in the middle of Sarpkaya's -1995). The estimated circulation number was about 0.8 (also quite close). Most of Sarpkaya's qualitative and quantitative findings were confirmed in the course of present research.

although both forms may interchange.

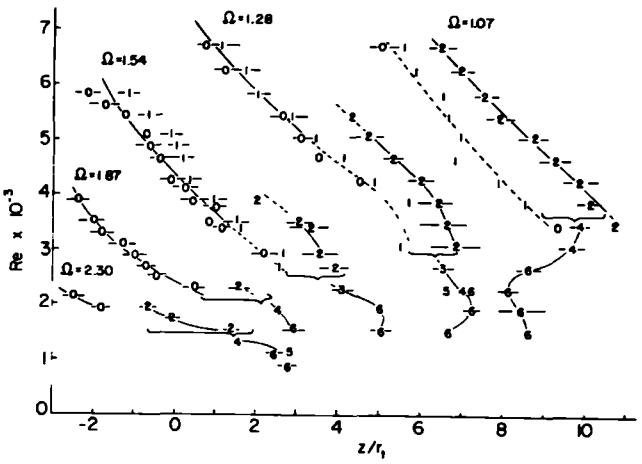

Figure 2.35.A 'map' of different breakdown modes by Faler and Leibovich (1977). The type of disturbance (0-6) and its mean axial location vs. *Re* for five values of Ω.

It is a matter of controversy whether the different modes of breakdown are distinctive forms or just different aspects of the same phenomenon. It could be argued that the appearance of the two forms is due to differences in the way the dye is injected into the vortex. However Leibovich (1983,1984) suggests that the spiral and bubble forms are indeed different and gives at least two pieces of evidence to support his view. Firstly, the measured values of the core expansion ratio (i.e. ratio of the core diameter in the wake to the core diameter in the approach flow) associated with the bubble form are significantly larger than those for spiral type. Secondly, as noted by Sarpkaya, when the flow conditions change, so that the spiral form changes into the bubble, their mean axial position changes in a discontinuous manner (the bubble being located upstream of the spiral).

If these two forms of breakdown are indeed different the question arises, which of them is the fundamental one ? The experiments performed in a tank with a rotating endwall (e.g. Escudier-1984, see figure 2.29) for different rotational Reynolds numbers and aspect ratios revealed only bubble forms of breakdown (figure 2.36).

Thus the tentative conclusion may be drawn that the spiral form is rather an undesired side effect of non-axisymmetrical disturbances introduced into the

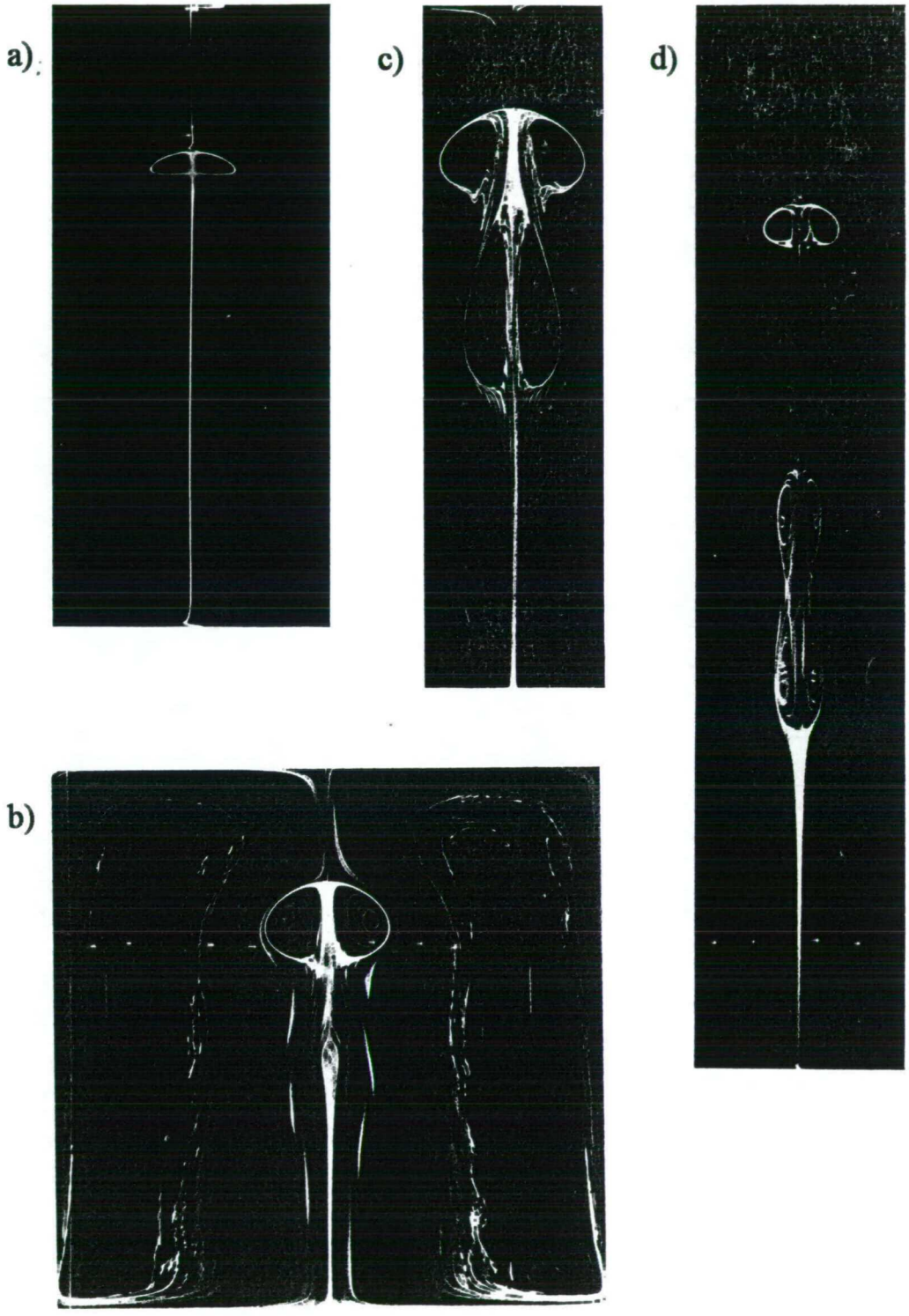

Figure 2.36. Examples of bubble forms of breakdown obtained in the cylinder with rotating endwall by Escudier (1984); a- Re=1854, H/R=1.5, b- Re=1854, H/R=2, c- Re=2494, H/R=2.5, d- Re=2752, H/R=3.25. For H/R=1.5 and 2 single bubbles present, for H/R=2.5 and 3.25 double and triple bubble forms present. The pictures obtained by a laser sheet visualisation.

experimental set-up (e.g. vortex tube) or present anyway due to asymmetries in the flow (e.g. leading edge vortex), whereas in the arrangement producing more symmetric and steady conditions only the bubble form is present.

Somewhat similar conclusions were reached by Brücker and Althaus (1992,1995) and Brücker (1993) in the three parts of their investigations, although the configuration they used was entirely different from the one used by Escudier. They employed a quasi three-dimensional instantaneous measurement technique, combining particle tracking velocimetry (PTV) with volume scanning. By this method they obtained the first quantitative experimental results of the unsteady and asymmetric interior region of a vortex breakdown (their apparatus was shown in figure 2.25). Their results show that the stationary bubble-type breakdown has a 'nearly axisymmetric, single-celled vortex ring-like distribution of circumferential vorticity'[9], whereas the spiral breakdown 'should be viewed as a result of the bubble's instability because the topological characteristics of the spiral in its front part indicate its origin from the bubble-mode'. Additionally they showed that the front stagnation point for spiral-type of breakdown is displaced from the former centre, which causes displacement of the approaching vortex core. Thus the stagnation point and deflected core rotate about their common centre. Figure 2.37 shows the transition from bubble to spiral form due to increasing the Reynolds number (based on the core diameter) from 300 to 330. Towfighi and Rockwell (1993) investigated an instantaneous structure of vortex breakdown on a delta wing by means of Particle Image Velocimetry (PIV). Their results indicate clearly the presence of the spiral mode of vortex breakdown (figure 2.38).

[9] This observation is contrary to the work of Faler and Leibovich (1978), who found a two-celled internal structure of the bubble by interpolating the LDA measurements.

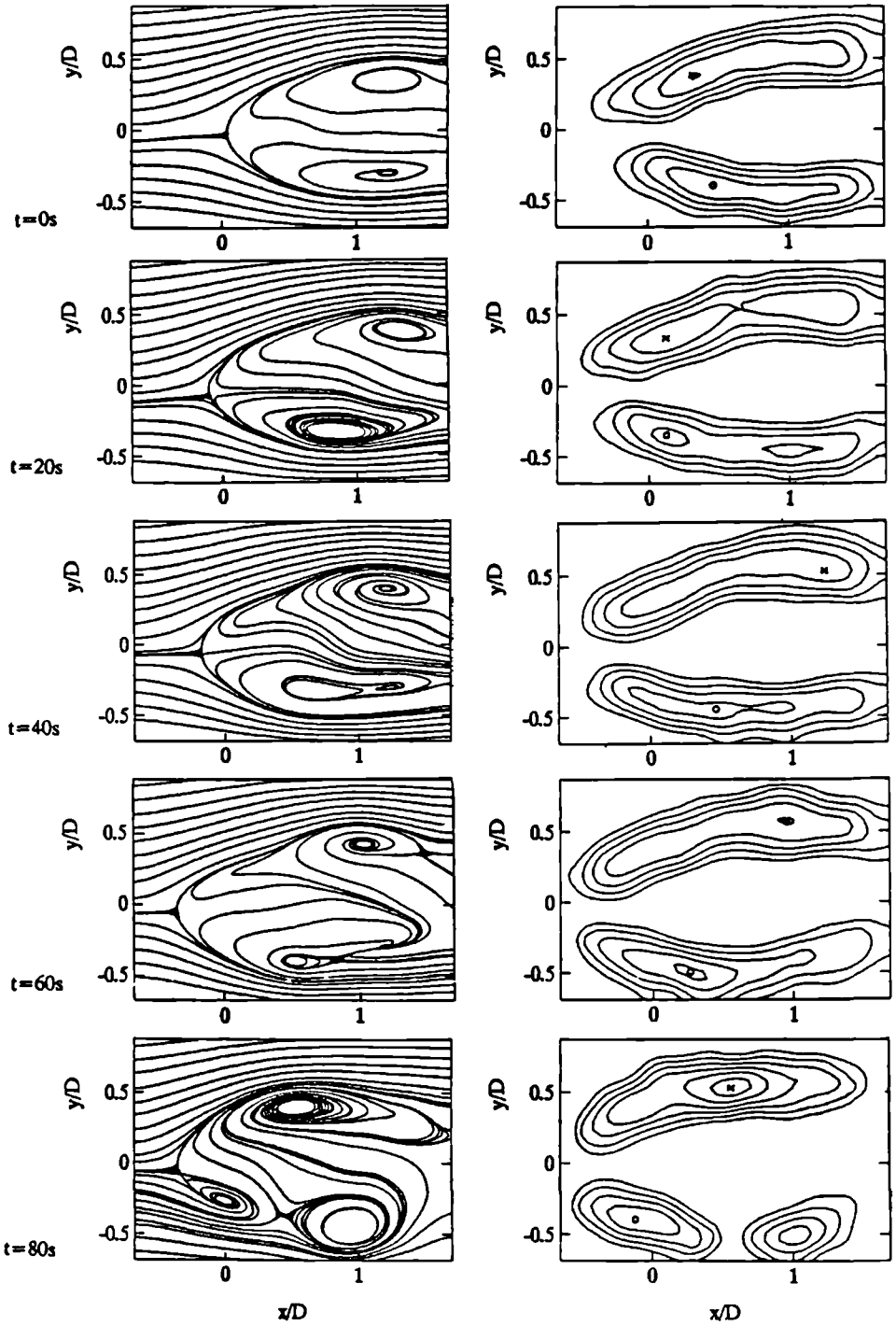

Figure 2.37. Time-dependent flow in the centre plane during the transition from bubble to spiral type of breakdown after an increase in *Re* from 300 to 330. Left: projection of streamlines in the centre plane. Right: contours of constant circumferential vorticity. From Brücker and Althaus (1995).

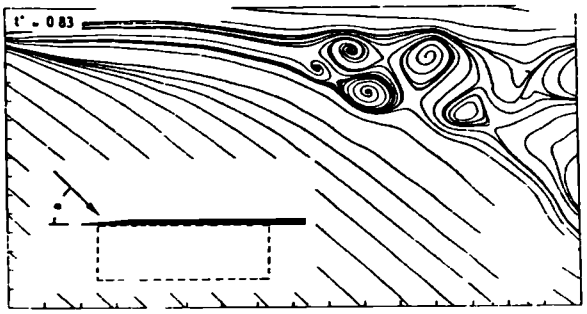

Figure 2.38. An example of instantaneous sectional streamline pattern in the plane passing through the centreline of the leading edge vortex. From Towfighi and Rockwell (1993).

2.4.2. Velocity profiles associated with vortex flows

The velocity profiles in the vortex were roughly drawn in figure 2.1. In most of the cases the axial component of velocity has an overshoot near the flow axis before the burst, however this depends very much on the kind of vortex generator used [10]. It is possible to introduce several mathematical functions for modelling the shape of these profiles.

Rankine vortex

This approximation was used by Squire (1960,1962) for his analytical solutions[11] and later by Escudier and Keller (1983, 1985a). The axial velocity component is assumed to be constant:

$$w(r)=W_O\ , \tag{2.2}$$

whereas the tangential velocity is expressed by means of two different equations depending on radial distance from the vortex axis:

$$\begin{aligned} v(r)&=\Gamma_\infty r/2\pi\delta^2 \quad , \quad \text{for } r \le \delta, \\ v(r)&=\Gamma_\infty/2\pi r \quad , \quad \text{for } r > \delta, \end{aligned} \tag{2.3}$$

[10] e.g. Brücker and Althaus (1992) reported a wake like velocity profile prior to the burst; Staufenbiel and Helming (1985) showed rather flat axial velocity profile of the wing-tip vortex.
[11] Squire's theory of vortex breakdown will be discussed later.

where δ is the radius of the vortex core i.e. the radial location with maximum swirl velocity ($V_O=\Gamma_\infty /2\pi\delta$). The distribution of swirl velocity inside the core is linear thus implying solid body rotation. Outside the core the flow is treated as an irrotational potential vortex. This shape of tangential velocity is certainly not physically correct, having discontinuous derivatives. However it is extremely useful for theoretical studies because of its simplicity.

Burger vortex

The drawbacks of the Rankine vortex representation are usually overcome by using a Burger vortex swirl velocity profile. One of the possible forms is :

$$v(r)=(\Gamma_\infty/2\pi r)[1 - \exp(-1.256\, r^2/\delta^2)] \quad , \tag{2.4}$$

where coefficients Γ_∞ and δ can be obtained from experiments by fitting methods if necessary.

The axial velocity profile accompanying the swirl velocity profile given by (2.4) usually takes the following form (Delery-1994):

$$w(r)=W_\infty + (W_O - W_\infty) \exp [-(r/b)^2] \quad , \tag{2.5}$$

where W_∞, W_O, are free stream and centre-line axial velocities respectively, and b is the thickness of the axial profile defined as the distance to the centre-line where:

$$[w(r) - W_O]/[W_\infty - W_O] = 1/e \quad , \tag{2.6}$$

(e is the base of the natural logarithm). Again, the experimental values of W_∞, W_O and b can be obtained from proper fitting methods. The axial profile given by (2.5) can be applied to both the jet- and the wake-like velocity profiles.

Other velocity profiles

Squire (1960,1962) considered a swirl velocity profile of the form:

$$[v(r)/V_O]^2=(1/t)\int_0^t y^2\,\mathrm{sech}^2(y)\,dy \qquad (2.7)$$

where $t=r^2$, and V_O - maximum swirl velocity. However this form of the expression was chosen only for the sake of simplified calculations. Escudier (1987, 1988) proposed an improved version of equation (2.4), based on his measurements in both slit-tube and vortex tube arrangements. He introduced an additional term into the Burger vortex so that:

$$v(r) = (\Gamma_\infty/2\pi r)[1 - \exp(-1.256r^2/\delta^2)] + \omega r/2 \quad . \qquad (2.8)$$

Grabowski (1974) and Grabowski and Berger (1976) in their numerical calculations used polynomial expressions for modelling the vortex flow field.

2.4.3. Vortex breakdown and pressure field

The importance of an external pressure gradient for vortex breakdown was appreciated by Lambourne and Bryer (1962). They explained the dependence of vortex burst position on incidence and sweepback of delta wings by the presence of the longitudinal pressure gradient. They concluded that 'the length of the laminar part of the vortex is extended by a reduction of the longitudinal pressure gradient'. According to Gursul and Yang (1994), for a leading edge vortex the external pressure gradient is generated by the potential flow, and it is adverse due to the existence of the trailing edge. The experiments conducted in a vortex tube (Sarpkaya-1974), a slit tube (Escudier and Zehnder-1982) or in the arrangement by Pagan and Molton (1990) all confirm the important role of an adverse pressure gradient (i.e. positive in terms of pressure changes) for occurrence of the vortex breakdown.

Generally, adverse pressure gradient imposed on vortical flow promotes the breakdown, i.e. there is a smaller amount of swirl required for the burst in the presence of an adverse pressure gradient. Delery (1994) points out that an adverse pressure gradient increases the *local swirl* number by decelerating the axial velocity component and thus precipitating vortex breakdown. Additionally, rapid divergence of the test section (e.g. Escudier and Zehnder-1982) or choke-like arrangements (as used in current investigations) cause an increase in the size of the vortex breakdown and thus the structure is better defined (figure 2.39).

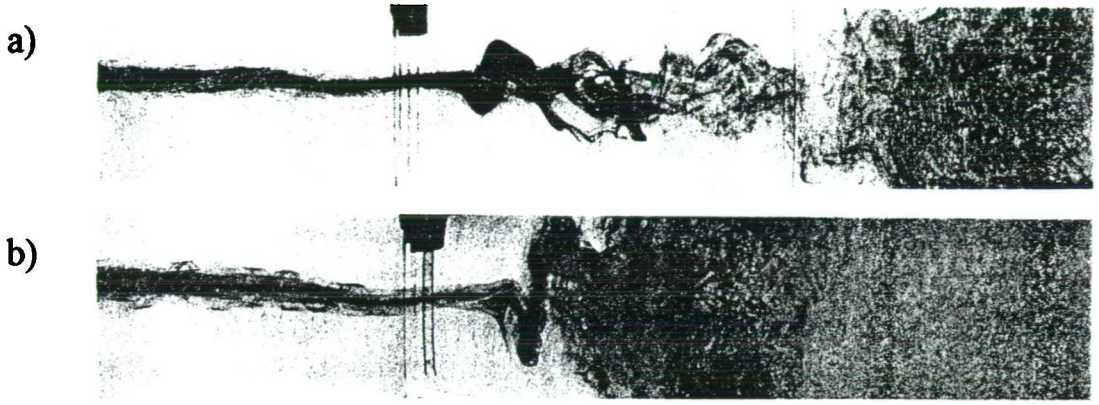

Figure 2.39.An increase of the breakdown size due to imposed adverse pressure gradient: a- cylindrical tube (Ω=2.60, *Re*=2900), b- flared tube with cone angle 20^{o} (Ω=2.03, *Re*=3800. From Escudier and Zehnder (1982).

Experiments by Harvey (1962) and Staufenbiel and Helming (1985) show that it is sometimes[12] possible to regain the pre-burst conditions if a negative pressure gradient is applied just downstream of the breakdown (say, in the form of a contraction).

An interesting feature is the pressure field inside the vortex prior to the burst. Kirkpatrick (1965) made measurements of the pressure distribution across the vortex. The accuracy of this kind of measurement may be questionable, because of probe interference. Nevertheless the pressure field suggests a significant drop in centre-line total and static pressures (figure 2.40). The static pressure loss at the axis can be as much as 4 to 5 times the dynamic pressure.

[12] for low Reynolds numbers and carefully controlled flow conditions

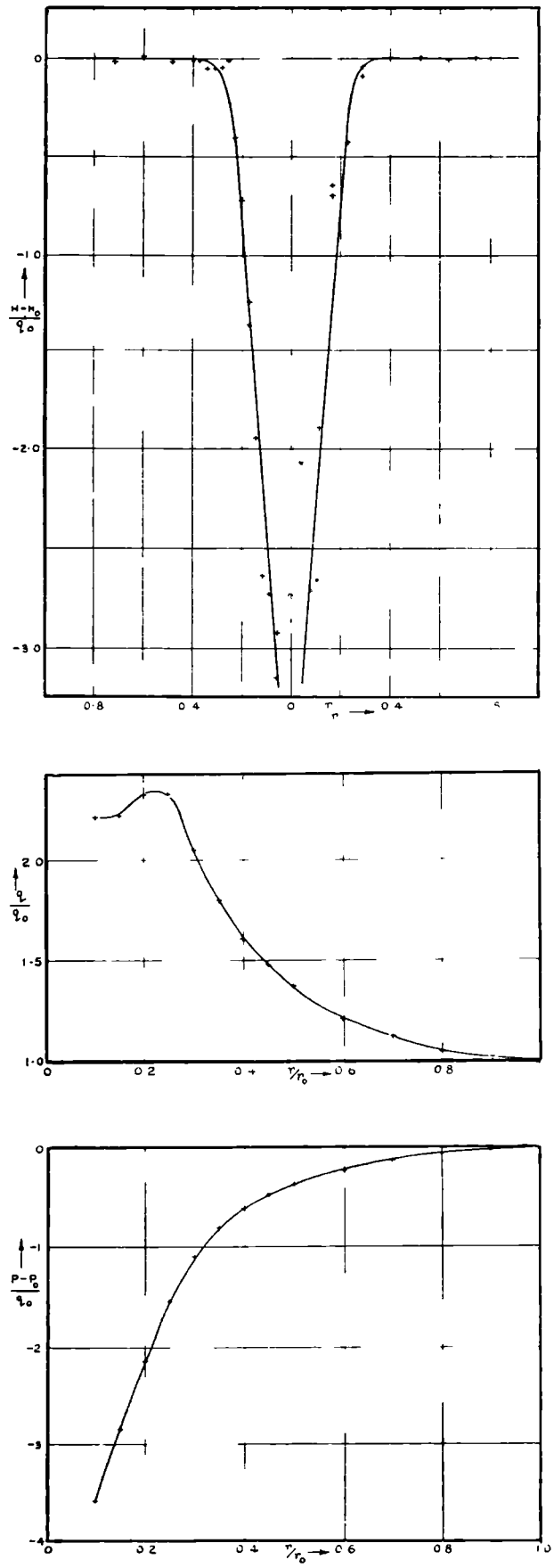

Figure 2.40. Behaviour of a- total pressure (H), b- dynamic pressure (q) , c- static pressure (p), for an unburst vortex in the cylindrical tube (from Kirkpatrick-1965). Index 'o' refers the conditions at the edge of the vortex.

2.4.4. Non-dimensional quantities and criteria for vortex breakdown.

There are a great many investigations concentrated on parametric studies of vortex breakdown. The main purpose, especially during the early studies, was to find a criterion which might be useful in predicting the occurrence of vortex breakdown or, in other words, to identify a critical state of the flow which triggers the phenomenon. Among the first quantities proposed was the *helix* or *swirl angle*, i.e. the angle between the path of spiralling fluid particles and the axis of the vortex, which can be expressed as:

$$\gamma(r)=\arctan\,[v(r)/w(r)] \quad . \tag{2.9}$$

It was measured for the first time by Harvey (1960,1962) by injecting smoke into the flow ahead of the burst (through a glass capillary about 0.12 mm in diameter) and photographing the resulting traces. The swirl angle obtained is shown in figure 2.41.

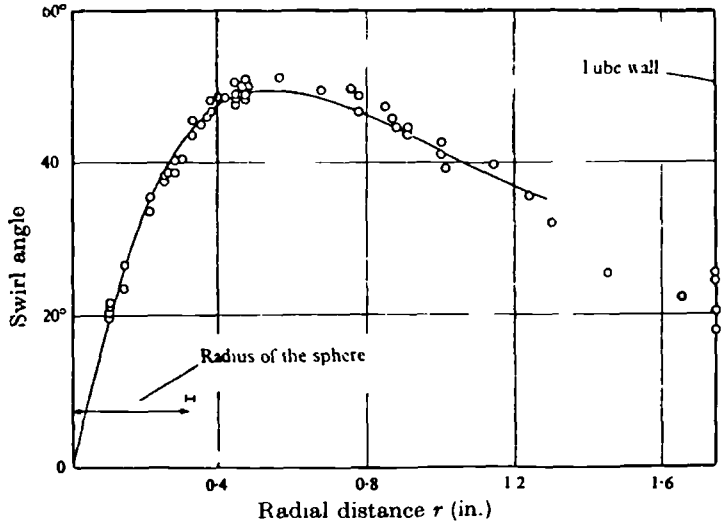

Figure 2.41.Swirl angle distribution by Harvey (1960,1962).

The maximum value of γ, corresponding to conditions leading to vortex breakdown, was 50.5° to 51.0° which was in very good agreement with Squire's (1960,1962) theoretical predictions. Later these measurements were confirmed by Sarpkaya (1970, 1971). Additionally he found that for a spiral mode the critical helix

angle is lower and varies from 38° to 45°, depending on the intensity of the circulation.

Another quantity is the *swirl parameter*. It was introduced for the first time by Squire (1960,1962) and later used by Lessen *et al.* (1974) for their inviscid theory of a trailing line vortex. The swirl parameter may be regarded as the ratio of maximum swirl velocity to the axial velocity on the centre-line (however many authors define this quantity in slightly different manner):

$$q = V_O/W_O \quad . \tag{2.10}$$

Squire (1962) found the swirl parameter to be 1.00, 1.12 or 1.20, depending on velocity profile under consideration. Hence, in order to provoke the occurrence of the vortex breakdown, the swirl velocity should be rather larger than the axial velocity. By analogy, the *swirling ratio* (Delery-1994) is defined as the maximum swirl velocity to the free stream axial velocity:

$$\tau = V_O/W_\infty \quad . \tag{2.11}$$

It is also common to use the *Rossby number* (*Ro*) which can be interpreted as an inverse of the swirl parameter. Spall *et al.* (1987) proposed that the critical value of $Ro=0.65$ for breaking-up of a wing-tip vortex, but comparisons of *Ro* for leading edge vortices were inconclusive. Robinson *et al.* (1994) suggested that the critical value of *Ro*, based on numerical Navier-Stokes and Euler calculations of the leading edge vortex,was between 0.9 and 1.4. Delery (1994) summarised the theoretical, experimental and numerical findings with respect to the Rossby number and swirl parameter, concluding that the critical value of *Ro* corresponding to breakdown is between 0.71 and 0.90 (his swirl parameter was defined slightly different than by equation 2.10).

Escudier and Zehnder (1982), Escudier (1987) and Escudier (1988) discussed the non-dimensional parameters, introduced by Sarpkaya (1970, 1971) in order to find the conditions for vortex breakdown, i.e. the Reynolds number

$$Re=W_m D_O/\nu \quad , \tag{2.12}$$

based on mean axial velocity $W_m=4Q/\pi D_O^2$ and tube diameter D_O (Q-volume flow rate), and circulation number

$$\Omega=\Gamma/W_m D_O \quad , \tag{2.13}$$

where Γ is the circulation imparted to the flow. They argued that dimensional considerations must lead to an additional parameter i.e. the ratio of the radial velocity to the tangential velocity in the inflow section:

$$R=U_{in}/V_{in} \quad . \tag{2.14}$$

They explained that this parameter was overlooked by investigators using vortex tubes similar to those by Harvey and Sarpkaya, since the term ΩR is always constant. Escudier and Zehnder (1982) proposed the criterion for the occurrence of vortex breakdown at a fixed location in the tube in the form of the following correlation:

$$Re_B \sim \Omega^{-3} R^{-1} \quad . \tag{2.15}$$

All these 'numbers' or 'criteria', attempting to predict the critical conditions leading to the occurrence of the vortex breakdown, lack generality. However they can often be used in particular situations as a 'rule of the thumb', indicating possible breakdown. The vortex breakdown phenomenon actually is too complicated to characterise by simple methods. Its prediction has to involve a full investigation of the interacting velocity and pressure fields. Thus any criterion in the form of single number must be an oversimplification of the complex reality.

2.5. Theoretical explanations of vortex breakdown

During the last 40 years the vortex breakdown phenomenon was the subject of many theoretical studies, which led to different theories for vortex breakdown. Several excellent reviews are available, the best known being papers by Brown and Lopez (1990), Delery (1994), Escudier (1988), Hall (1972) and Leibovich (1978,1983,1984)

Generally, theoretical studies are conducted assuming the fluid is inviscid. Thus they fail to predict the influence of the Reynolds number on vortex breakdown. They all agree, however, that the ratio of the swirl to the axial velocity plays an important role. They also appreciate the significance of an adverse pressure gradient in promoting and controlling the breakdown. Interestingly their findings, despite different approaches, are in good agreement with each other as well as with experimental results. The theories attempting to explain vortex breakdown can be divided into the following classes:

I. Wave-motion theories, which associate breakdown with the appearance of waves on a columnar vortex (e.g. theory of critical state, hydraulic jump or solitary waves)
II. Instability theories, which associate breakdown with amplification or decay of infinitesimally small disturbances.
III. Stagnation theories, based on examination of quasi-cylindrical Navier-Stokes equations, which associate breakdown with the failure of numerical solutions.
IV. Theories based on vorticity dynamics.

* * *

Before the specific theories are reviewed briefly, it is worthwhile first to present the basic assumptions and corresponding equations of motion for the flows under consideration.

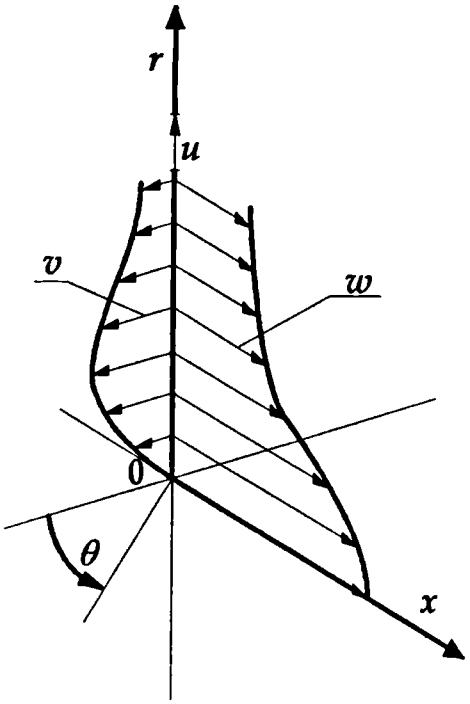

Figure 2.42.Cylindrical system of co-ordinates.

Equations of motion are considered in the cylindrical system of co-ordinates (figure 2.42) r,θ, x with corresponding velocity components u,v,w. Hall (1966b) gives full equations of motion for the axially symmetric flow of a perfect, viscous, heat conducting gas. However the assumption of steady flow for an incompressible fluid with axially symmetric velocity and pressure fields leads to considerably simpler system of Navier - Stokes equations in the following form:

$$\frac{\partial u}{\partial r}+\frac{u}{r}+\frac{\partial w}{\partial x} = 0\,, \tag{2.16a}$$

$$u\frac{\partial u}{\partial r}+w\frac{\partial u}{\partial x}-\frac{v^2}{r} = -\frac{1}{\rho}\frac{\partial p}{\partial r}+\nu(\nabla^2 u-\frac{u}{r^2})\,, \tag{2.16b}$$

$$u\frac{\partial w}{\partial r}+w\frac{\partial w}{\partial x} = -\frac{1}{\rho}\frac{\partial p}{\partial x}+\nu\nabla^2 w\,, \tag{2.16c}$$

$$u\frac{\partial v}{\partial r}+w\frac{\partial v}{\partial x}+\frac{vu}{r} = \nu(\nabla^2 v-\frac{v}{r^2})\,, \tag{2.16d}$$

where

$$\nabla^2 \equiv \frac{\partial^2}{\partial r^2} + \frac{1}{r}\frac{\partial}{\partial r} + \frac{\partial^2}{\partial x^2} \quad , \tag{2.17}$$

p, ρ, ν are the pressure, density and kinematic viscosity, respectively. The above system of equations served as a starting point for numerous investigations.

Hall (1961) proposed a solution of the system (2.16) for a leading-edge vortex. He assumed that 1) the flow is continuous, i.e. does not include the vortex sheets and is rotational in order to allow the convection of the vorticity, 2) diffusion of vorticity takes place only within a slender 'subcore'. Thus the equations were solved separately for 'outer' and 'inner' regions, for which different simplifications were possible, and then the results were matched together. In the 'outer' region the flow was assumed inviscid (but rotational) and conical, which led to a set of ordinary differential equations. Thus explicit analytical solutions were found for the velocity and pressure fields. For the 'inner' region the flow was assumed to be laminar and approximations concerning the boundary conditions, as well as simplifications analogous to the boundary-layer theory, were made. Stewartson and Hall (1963) improved the method by seeking the 'inner' solution in the form of an asymptotic expansion containing inverse powers of the logarithm of the Reynolds number. Thus they corrected the matching of the 'outer' and 'inner' solutions. The solutions obtained gave satisfactory results in terms of reproducing the velocity and pressure fields found from experiments (including an overshoot in axial velocity and a drop in pressure at the centre-line). These methods provided a useful basis for investigations of vortex breakdown.

For a steady, inviscid and incompressible axisymmetric flow, equations (2.16) take a particularly simple form. It is convenient to introduce the stream function ψ defined by:

$$u = -\frac{1}{r}\frac{\partial \psi}{\partial x} \quad , \quad w = \frac{1}{r}\frac{\partial \psi}{\partial r} \quad , \tag{2.18}$$

the total pressure: $$h = p/\rho + (u^2+v^2+w^2)/2 \quad , \tag{2.19}$$

and the circulation: $$\Gamma = rv. \tag{2.20}$$

Then system (2.16) can be reduced to the single equation:

$$\frac{\partial^2\psi}{\partial r^2} - \frac{1}{r}\frac{\partial\psi}{\partial r} + \frac{\partial^2\psi}{\partial x^2} = -\Gamma\frac{d\Gamma}{d\psi} + r^2\frac{dh}{d\psi}. \tag{2.21}$$

Here the total pressure and circulation are dependent only on the stream function. Equation (2.21) was the starting point for many analytical solutions of vortex breakdown (Squire-1960,1962, Benjamin-1961,1962,1967). By assuming that the flow is quasi-cylindrical, i.e. $\partial u/\partial x << \partial w/\partial r$, equation (2.21) can be rewritten as:

$$\frac{\partial^2\psi}{\partial r^2} - \frac{1}{r}\frac{\partial\psi}{\partial r} = -\Gamma\frac{d\Gamma}{d\psi} + r^2\frac{dh}{d\psi} \quad , \tag{2.22}$$

which can be integrated for some simple forms of $\Gamma(\psi)$ and $h(\psi)$.

Brown and Lopez (1990) investigated equation (2.16b) for a steady, inviscid, axisymmetric swirling flow i.e.

$$u\frac{\partial u}{\partial r} + w\frac{\partial u}{\partial x} = \frac{v^2}{r} - \frac{1}{\rho}\frac{\partial p}{\partial r} \tag{2.23}$$

They considered the generation of the azimuthal component of vorticity through the stretching and tilting of vortex lines:

$$\eta = \frac{\Gamma}{r}\frac{d\Gamma}{d\psi} - r\frac{dh}{d\psi} \quad , \tag{2.24}$$

where $\eta = \partial u/\partial x - \partial w/\partial r$, is the azimuthal component of vorticity.

2.5.1. Wave theories

Squire's theory of critical state

Squire (1960,1962) developed the theory of long standing waves on a cylindrical vortex motion. He was looking for conditions appropriate to the existence of standing waves in a flow field, arguing that if such waves exist, the disturbances present downstream will spread upstream and thus cause the vortex breakdown. As a starting point he used equation (2.21). He proposed that the stream function ψ consists of the stream function corresponding to the mean flow and the stream function of the disturbance i.e.

$$\psi = \psi_0 + \psi_1 \,. \tag{2.25}$$

The disturbance ψ_1 was assumed to be periodic in the stream direction

$$\psi_1 = f(r)\cos(\alpha x) \quad . \tag{2.26}$$

The three profiles of tangential velocity were investigated, each accompanied by the uniform axial velocity. These three tangential velocity profiles were equivalent to those of Rankine and Burger vortices and the one given by equation (2.7). For these three cases the infinitely long waves were found when the ratio of maximum swirl velocity V_O to the axial velocity W (which is uniform) is

$$V_O/W = \begin{cases} 1.20 \text{ for Rankine profile} \\ 1.00 \text{ for Burger profile} \\ 1.12 \text{ for the profile given by (2.7)} \end{cases}$$

giving the helix angle $\gamma = 50.2^\circ$, 45° and 48.2° respectively. The theory can be in a sense supported by the already mentioned direct measurements of the helix angle by

Harvey (1960,1962) and Sarpkaya (1970,1971).

Benjamin (1962) pointed out that the group velocity of the standing waves considered by Squire is directed downstream, so that the waves can form only in the rear of a disturbing agency and cannot propagate upstream. Hall (1972) criticised Squire's theory for the lack of explanatory power: it does not predict where and when the critical state is reached, or how the change in the structure of the core takes place. On the other hand it considers the vortex core as a flow with a possible critical state - thus introducing a new concept, which was pursued later by many investigators. Finally the criteria derived are generally accepted as valid, despite the oversimplified model.

Benjamin's theory of conjugate states

The theory by Benjamin (1961,1962,1967), supplemented later by Fraenkel (1967), offered an explanation for the vortex breakdown phenomenon as a finite transition between two dynamically conjugate states of axisymmetric swirling flow, analogous to a hydraulic jump in open-channel flow.

It is well-known that for the uniform flow of a liquid in an open channel with the flow rate Q and total head h there are two possible states. One of them is subcritical which means that the Froude number

$$F=w/(gl)^{1/2} \tag{2.27}$$

is less than unity (corresponding to larger l and smaller w) and the other is supercritical i.e. $F > 1$. Here w, l and g stand for horizontal velocity, fluid depth and acceleration of gravity respectively. The difference between these two states lies in their capability to support infinitesimal standing waves, which can occur only in subcritical flow.

The quantity often associated with the flow described is the 'flow force' which is defined as a sum of horizontal momentum flux and pressure force per unit span:

$$S = \rho\,[w^2 l + (gl)/2] \quad . \tag{2.28}$$

S can be shown to be greater for subcritical than for supercritical flow. Thus the transition from the subcritical to supercritical state must be accompanied by an external force (figure 2.43). however when the reduction in flow force is small only the train of standing waves appears. On the other hand the transition from the supercritical to subcritical state results in an increase of the flow force and this *release* of flow force is responsible for forming hydraulic jumps (figure 2.44). However, again in the 'milder' case (with Froude number only slightly greater than one) a steady wave train is established on the subcritical flow.

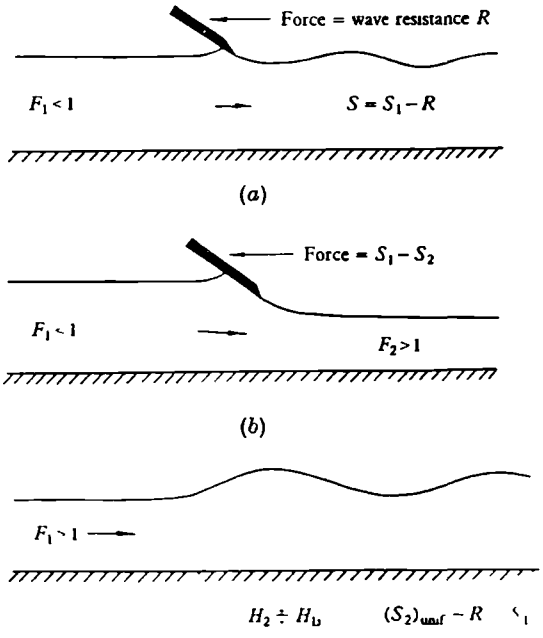

Figure 2.43. Effects of an external force exerted on subcritical flow: a-formation of the wave train, b-transition to supercritical flow. From Benjamin (1962).

Figure 2.44. Two types of hydraulic jump: a-undular, and b-dissipative with uniform flow downstream. From Benjamin (1962).

Benjamin (1962) showed that each aspect of the open channel flow has a counterpart in axisymmetric swirling flows. He investigated the cylindrical inviscid flow i.e. fulfilling equation (2.22) in a cylindrical duct of radius R. The substitution $y=r^2/2$ and introduction of the new variable $I=r^2v^2/2$ modify equation (2.22) to give

$$\frac{\partial^2\psi}{\partial y^2}=h'(y)-\frac{1}{2y}I'(y) \quad , \tag{2.29}$$

(accents denote ψ derivatives),

with boundary conditions

$$\psi=0 \qquad \text{for} \qquad y=0$$

$$\text{and} \qquad \psi=\Psi(R) \quad \text{for} \quad y=a=R^2/2 \tag{2.30}$$

Then, following Squire, the stream function is assumed to consist of a steady component, being the solution of (2.29) and a stationary axisymmetric perturbation i.e.

$$\psi(x,y)=\psi_0(y)+\varepsilon\phi(y)exp(\gamma x) \quad , \tag{2.31}$$

It can be shown that ϕ itself must be a solution of the second-order differential equation

$$\frac{d^2\phi}{dy^2}+\left[\frac{\gamma^2}{2y}-\frac{1}{w}\frac{d^2w}{dy^2}+\frac{(dI/dy)}{2y^2w^2}\right]\phi=0 \tag{2.32}$$

with kinematical boundary conditions

$$\phi(0)=\phi(R)=0 \quad . \tag{2.33}$$

Generally there is an infinite set of real eigenvalues γ_0 , γ_1 , γ_2 , ... , which allow the solutions ϕ_0 , ϕ_1 , ϕ_2 , ... of (2.32) to satisfy boundary conditions (2.33), but there is

only a limited possibility of standing waves when $\gamma^2 < 0$ (so that $\gamma = i\alpha$). Thus the state of the flow can be either supercritical when all eigenvalues γ^2 are positive with no standing waves possible or subcritical when at least the first eigenvalue gives negative γ^2. Equation (2.32) with $\gamma^2=0$ becomes the critical equation (in Squire's sense)

$$\frac{d^2\phi_c}{dy^2}+\left[-\frac{1}{w}\frac{d^2w}{dy^2}+\frac{(dI/dy)}{2y^2w^2}\right]\phi_c=0 \qquad (2.34)$$

Then it can be shown that the necessary and sufficient condition for the existence of standing waves is that ϕ_C should vanish in $0 < y < a$ at least once.

For a given state of flow, with prescribed profiles for $v(r)$ and $w(r)$ (and hence for known h and I) the corresponding stream function, say ψ_A, is a particular integral of the equation of motion (2.29). However (2.29) is a second order equation with the solution containing two arbitrary constants, and moreover there are just two boundary conditions (2.30). Thus the stream function ψ_A is one of a conjugate pair. The second, say ψ_B, is connected to the first by having the same h and I over their common stream surfaces.

By analogy to the flow force in the channel flow Benjamin introduced a similar quantity for vortical flow as follows

$$S = 2\pi\int_0^a\{p+\rho w^2\}dy \quad . \qquad (2.35)$$

By means of calculus of variation he showed that if a curve drawn in the plane (ψ,y) represents the physical flow, it must be an extremal of integral S (and moreover it is a minimum). Thus if flow A is the one for which S is a minimum, then for the conjugate flow B the flow force $S_B > S_A$, where S_B is neither minimum nor maximum. Hence in any conjugate pair of flow states, S is a minimum for one, and S

is larger (but neither minimum nor maximum) for the other (figure 2.45). The most interesting conclusion is, however, that the test for supercritical conditions based on equation (2.34) can be shown to be equivalent to the criterion that S is minimum. In addition the subcritical flow always has a larger flow force than its conjugate.

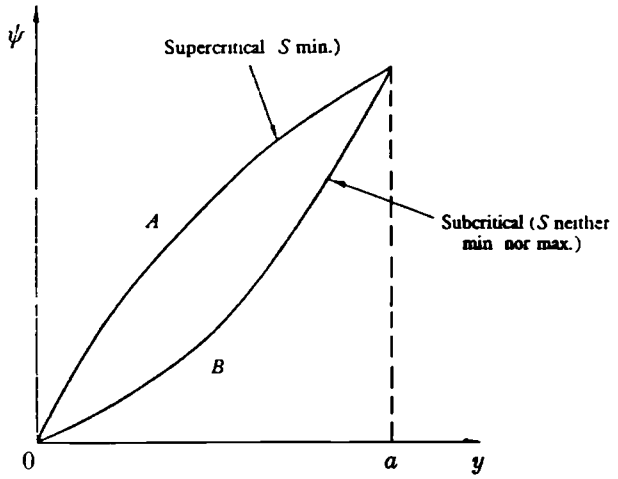

Figure 2.45.Conjugate solutions in (ψ,y) plane. From Benjamin (1962).

This reasoning led Benjamin to conclude that vortex breakdown can be explained as a 'finite amplitude' transition from a supercritical state of flow (which cannot support infinitesimal standing waves) to a subcritical state. The conjugate subcritical state has an excess of flow force, which can be released by formation of waves downstream of the transition (in the 'mild' case) or the appearance of a turbulent region (for large flow force excess). In the latter case the total head loss due to the turbulence should be accounted for by some additional hypothesis.

By analogy to the channel flow, Benjamin introduced a quantity similar to Froude number, which behaves in the same manner, i.e. it is greater than unity for supercritical flow and less than unity for subcritical flow. He considered the absolute velocities, measured positively in the direction of the flow, at which waves of extreme length propagate with the flow (c_+) and against the flow (c_-). Thus c_+ is always positive, whereas c_- may have either sign (depending on convective action of the flow). For sufficiently high convective velocity the upstream propagation of waves is not possible (supercritical flow). Thus the parameter

$$N=(c_+ + c_-) / (c_+ - c_-) \qquad (2.36)$$

specifies the supercritical ($N > 1$) and the subcritical ($N < 1$) flows.

Benjamin (1967) consolidated his ideas more explicitly by using a perturbation analysis. He showed how the subcritical flow could be represented as a small but finite perturbation of the supercritical flow. For non-dissipative transition he found the perturbation to be a solitary wave, whereas for a small amount of dissipation a wave train would emerge. He suggested that, for weak transitions, vortex breakdown is the *manifestation* of the leading wave. In contrast Squire had suggested that the existence of waves evokes the burst.

The main objection to Benjamin's theory is that vortex breakdown is far from being a small perturbation. Thus the large axial gradients of velocity, stagnation and divergence of stream surfaces cannot be explained. Although Benjamin has developed and reinterpreted Squire's idea of critical flow, his explanation gives no better results than the previous one. It is far more difficult to test on account of its mathematical complexity.

Theory of trapped waves

Randall and Leibovich (1973) proposed an extension of the theories by Squire, Benjamin and themselves, which were based on the calculation of weakly non-linear waves. They suggested that the vortex breakdown phenomenon could be explained as a large amplitude wave motion, the idea being that the small amplitude waves, generally possible in rotating fluids, are connected with waves of *arbitrary* amplitude that result from *initial* disturbances of greater strength. The mathematics of their theory are omitted here. The calculations were based on the equations of critical flow (from their earlier paper on dissipative effects on non-linear waves in rotating fluids). The inflow and boundary conditions were chosen to simulate the experiments by Sarpkaya.

They argued that the identification of breakdown as a wave motion agrees with all observations of the *transient* phenomenon. The development consists of an upstream propagation from a downstream source of disturbance. Moreover the propagation takes place within the region where the flow is subcritical, and does not continue beyond an equilibrium position upstream of which the flow is supercritical.

The behaviour of the recirculation zone was modelled by a solitary wave. This solitary wave is amplified due to the geometry of the flow (a diverging duct) and at the same time dissipated due to viscosity effects. Thus the stationary ('trapped') wave in the equilibrium position is an outcome of opposite effects of amplification and dissipation.

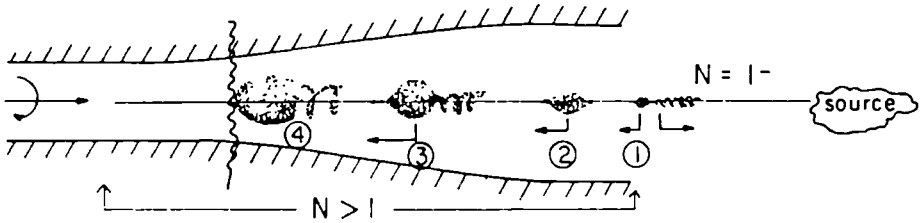

Figure 2.46.Hypothetical mechanism of the vortex breakdown according to Leibovich (1985).

The theory of trapped waves was supplemented and reinterpreted later by Leibovich (1985). The main improvement consists of taking into account the interaction between the axisymmetric and non-axisymmetric modes of breakdown. Figure 2.46 schematically shows the hypothetical mechanism for vortex breakdown of nearly critical (but supercritical) flow inside the diverging tube. Here the evolution of the breakdown can be explained in four stages:

(1) The disturbance source downstream generates waves. The long axisymmetric waves propagate upstream into a weakly supercritical flow existing at point *1* (the other axisymmetric and non-axisymmetric waves have smaller group velocity and are washed downstream).

(2) The divergence of the tube causes wave amplification and decrease in length

and at the same time the propagation speed increases (these features come from Kortweg - de Vries equation for so-called 'solitions') - the wave reaches point *2*.

(3) In the absence of any energy dissipation mechanism, the wave grows and accelerates through the diverging duct. However, if the wave becomes unstable to non-axisymmetric disturbances (as usually happens), say at point *3*, there is a 'leakage' of energy from axisymmetric to non-axisymmetric fluctuations.

(4) The instability of an axisymmetric wave can reduce the amplification rate of the advancing solition[13], so that it is captured at some location corresponding to equilibrium and thus the stationary vortex breakdown takes place (point *4*).

Figure 2.47 shows the streamlines in and near the region of reversed axial flow created by an axisymmetric solition. Ma and Leibovich (1985) applied the finite amplitude wave theory for solitary waves to model the spiral mode of vortex breakdown.

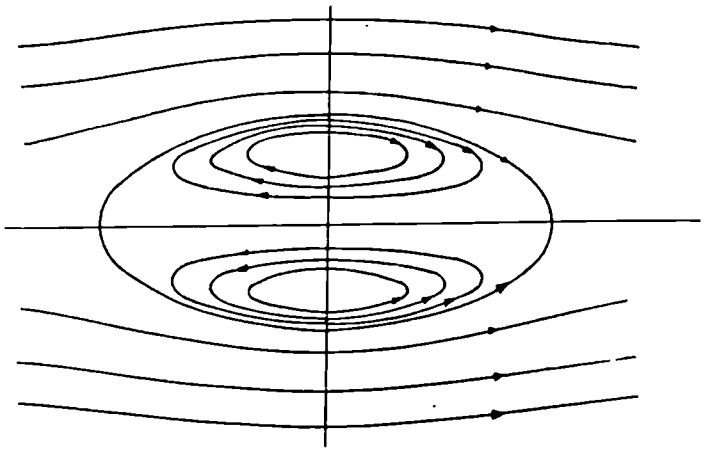

Figure 2.47.Streamlines in and near the region of reversed axial flow due to an axisymetric solition. From Leibovich (1985).

The experimental corroboration for the theoretical approaches employing the concept of solitary waves was given by Maxworthy *et al.* (1983). They obtained their results from a rotating tank with suction on the upper endwall (figure 2.30c). The disturbance was introduced by 'cutting through' the core with a thin solid rod and

[13] Leibovich (1985) defines 'solition' as a coherent waveform that propagates without change of form

cutting-off the axial flow for a moment. This disturbance was propagating within the core in the form of solitary wave. Figure 2.48 shows the photographs of axisymmetric waves on the vortex.

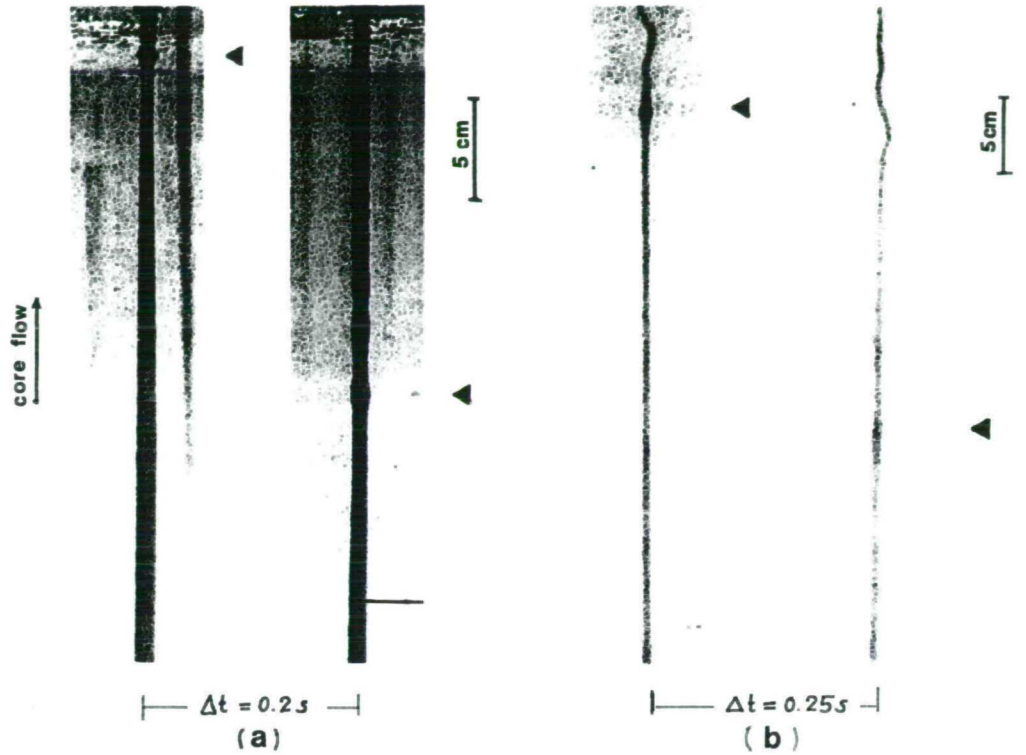

Figure 2.48.Photographs of axisymmetric waves on the vortex core: a-developing stable solitary wave, b-unstable wave. From Maxworthy *et al.* (1983).

Other wave theories

Escudier and Keller (1983,1985a) and Escudier (1988) proposed to look upon the vortex breakdown as a two-stage transition (figure 2.49 gives the photograph and interpretative sketch). The first stage is an isentropic transition to an intermediate flow state which consists of a central stagnant cavity, separated from an outer irrotational flow by a layer of rotational fluid. After the first stage of transition the flow is still supercritical. The second transition can be regarded essentially as a hydraulic jump from the intermediate supercritical to the final subcritical state. They also suggested that the probable explanation for the occurrence of the various spiral forms of breakdown is the instability and subsequent roll-up of the thin rotational

layer of the fluid between the stagnant zone and the outer irrotational flow.

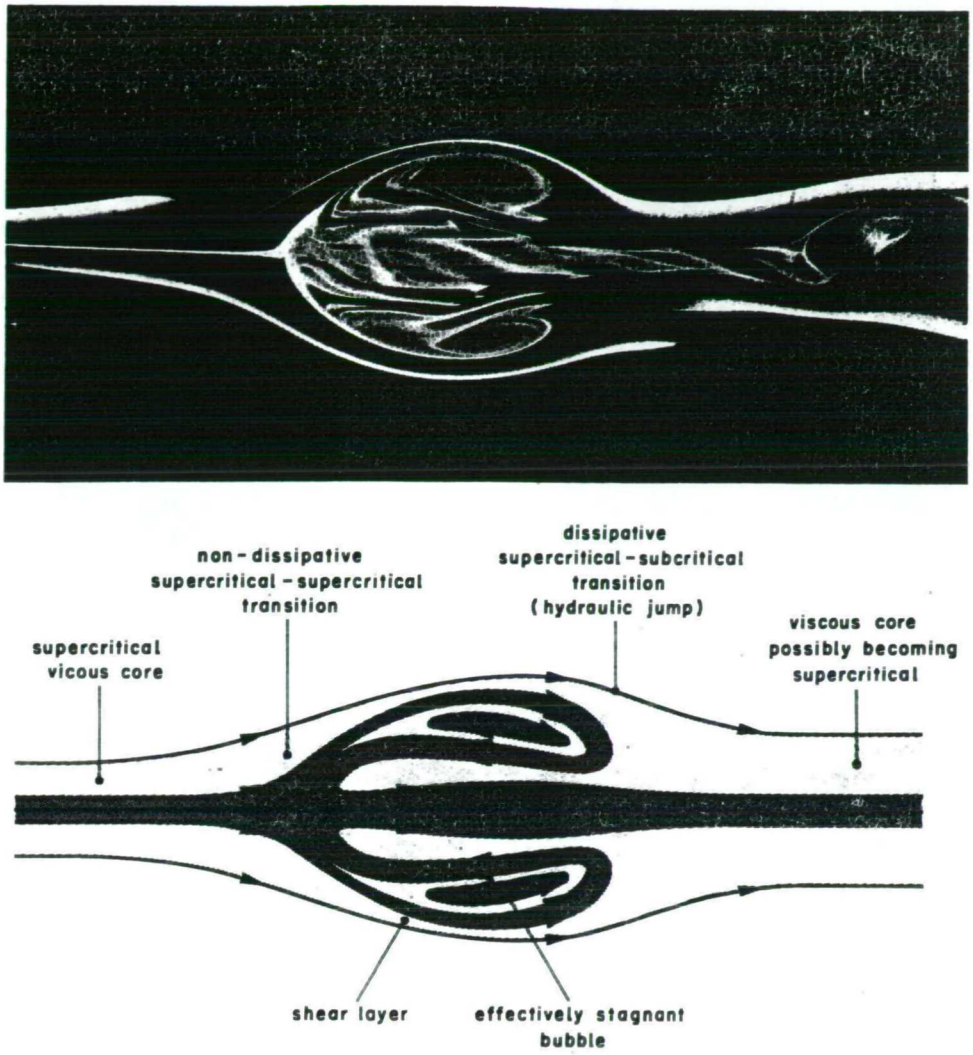

Figure 2.49. An interpretation of the vortex breakdown as a two-stage transition according to Escudier (1988). Reynolds number based on tube diameter Re=960.

The pressure spectra, obtained during the current research, at locations corresponding roughly to this thin rotational layer, exhibit 'broad band peaks', (presumably indicating the layer's presence), which then are replaced downstream by 'sharp-peaked' spectra (probable roll-up and spiralling). This might in a sense support Escudier's (1988) explanations, but cannot serve as a proof. The hypothesis itself is rather speculative and in fact does not explain the breakdown mechanism nor does it give any applicable criteria. Hence it represents no advance in previous theories (e.g. by Squire or Benjamin).

* * *

Suematsu and Ito (1981) and Suematsu *et al.* (1982) developed a theoretical explanation of vortex breakdown in a pipe. The mathematical model assumed a uniform axial velocity and the fluid's rigid rotation[14]. The inertial waves occurring were found to play a significant role in vortex breakdown. The earlier of their two papers dealt with stationary breakdown whereas the later one took into account the time dependent features of the breakdown.

The following assumptions were made: (1) the fluid is incompressible and inviscid, (2) the primary flow is cylindrical with $v(r)$ and $w(r)$ being given functions, (3) the velocity variations of disturbance are small compared with $v(r)$ and $w(r)$. Thus the flow can be expressed as a sum of a mean flow and disturbance components in the following form

$$\begin{aligned} u &= U_m(r) + u_d = U(r)exp[-i(m\theta+kx)+\lambda t], \\ v &= V_m(r) + v_d = V_m(r) + V(r)exp[-i(m\theta+kx)+\lambda t], \\ w &= W_m(r) + w_d = W_m(r) + W(r)\, exp[-i(m\theta+kx)+\lambda t], \\ p &= p_m(r) + p_d = p_0 + \rho\int_0^r \{[V_m(r)]^2/r\}dr + P(r)\, exp[-i(m\theta+kx)+\lambda t], \end{aligned} \tag{2.37}$$

where u, v and w are the velocity components in the cylindrical system r, θ and x; p is pressure and p_0 is the mean pressure on the centre-line; indices 'm' and 'd' correspond to mean distributions and disturbance components, respectively; $U(r)$, $V(r)$ and $W(r)$ are complex functions of r; λ a complex number, k a real number and m a positive integer (including zero). The expressions in equations (2.37) are substituted into the Euler equations of motion. The mean axial velocity is assumed uniform e.g. $W_m(r)=W_0=const.$ The mean circumferential velocity is $V_m(r)=\Omega r$,

[14] this type of flow occurs in pipe rotating about its axis. The example of physical realisation of this flow was given in section 2.3.3.

$\Omega=const>0$. After considerable transformations and assuming that λ is purely imaginary i.e. $\lambda=in$ (n real) the disturbance can be expressed in the following form:

$$\begin{aligned} u_d &= U \sin(nt-m\theta-kx) = AF_1 \sin(nt-m\theta-kx), \\ v_d &= V \cos(nt-m\theta-kx) = AF_2 \cos(nt-m\theta-kx), \\ w_d &= W \cos(nt-m\theta-kx) = AF_3 \cos(nt-m\theta-kx), \\ p_d &= P \cos(nt-m\theta-kx) = AF_4 \cos(nt-m\theta-kx), \end{aligned} \tag{2.38}$$

where A is an arbitrary constant indicating the amplitude of the disturbance and functions F_1 to F_4 are the explicit analytical expressions involving the co-ordinate r, Bessel functions of r and constants k, m, n, Ω and W_0.

Although the theoretical considerations are valid only for small disturbances, the results obtained are extended for finite amplitudes, in order to calculate the streamlines or velocity profiles of the flow field. Figure 2.50 shows the different modes of breakdown (regarded as a standing wave i.e. $n=0$) for $m=0,1$ and 2. Interestingly the streamlines reproduce qualitatively three modes of vortex breakdown (i.e. bubble, spiral and double helix). Moreover the superposition of modes $m=0$ and $m=2$ yields a streamline pattern corresponding to type 4 of breakdown mode of Faler and Leibovich (1977) i.e. the flattened bubble (figure 2.50d). Similar considerations are possible for unsteady breakdowns, i.e. $n\neq0$ (Suematsu *et al.*-1982) and also give good agreement with breakdown observations.

The strength of the model described lies undoubtedly in its capability to predict some of the breakdown features by using fairly simple assumptions (cylindrical flow, rigid body rotation). An apparent shortcoming, is the extension of the solution for small perturbations to large amplitude perturbations made in the similar manner as Leibovich (1985). However, it should be noted that later tests in a rotating tube (Suematsu *et al.*-1986a,1986b) show strikingly good agreement with the theoretical predictions.

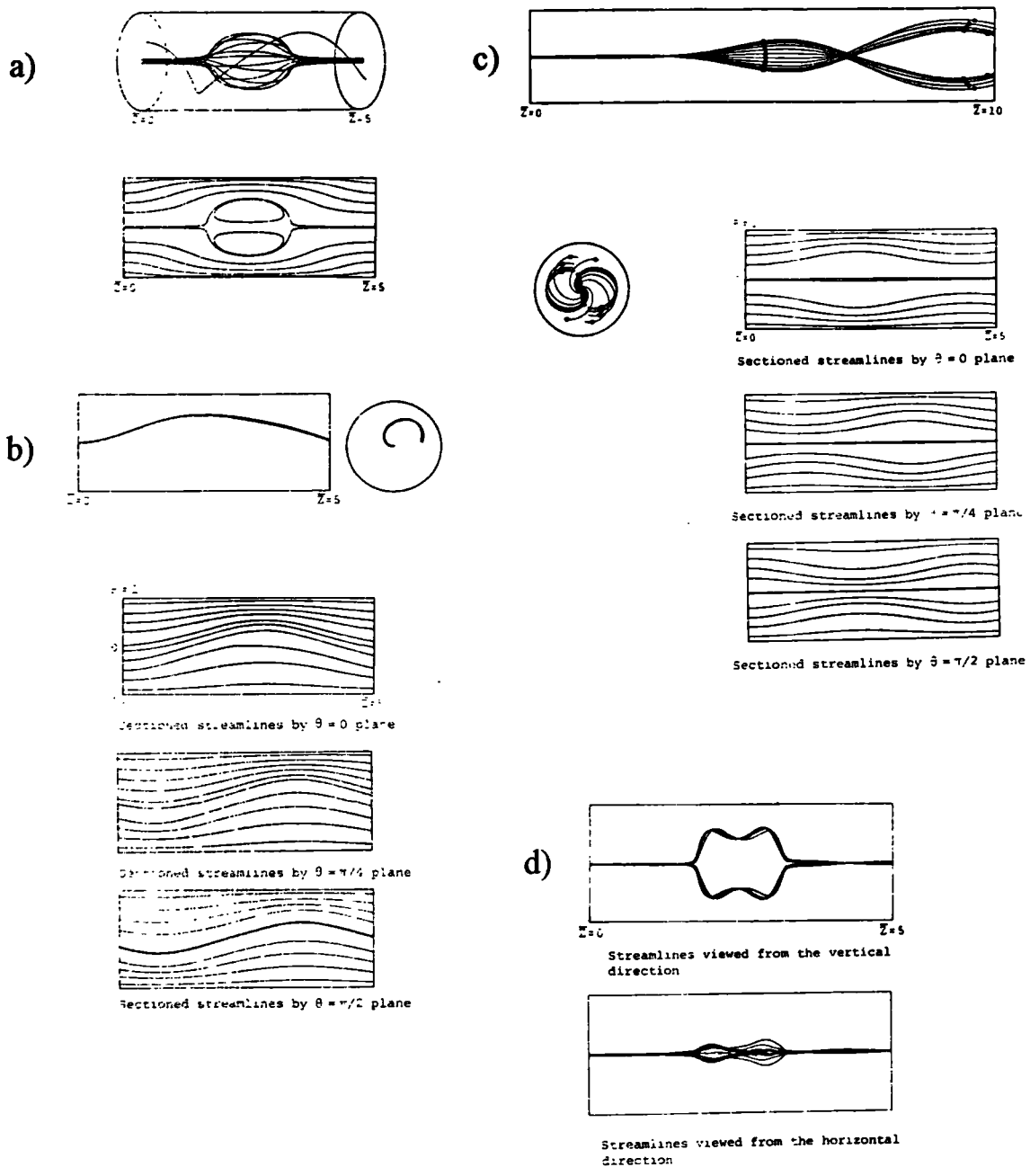

Figure 2.50.Different modes of stationary breakdown obtained by Suematsu and Ito (1981): a- s=0 mode (streamlines and sectioned streamlines), b- s=1 mode (streamlines and sectioned streamlines by θ=0, θ=π/4, θ=π/2 planes), c- s=2 mode (streamlines and sectioned streamlines by θ=0, θ=π/4, θ=π/2 planes), d- superposition of s=0 and s=2 modes giving the type 4 of Faler and Leibovich-1977 (streamlines viewed from vertical and horizontal directions).

2.5.2. Instability theories

The stability (or instability) theories treat vortex breakdown in a manner similar to the transition from laminar to turbulent flow[15]. Thus the possible amplification or decay of infinitesimally small disturbances imposed on the mean flow is investigated. These theories are based on a linear stability analysis applied to the axisymmetric laminar Navier-Stokes equations and seek for solutions in the following form[16] (Delery-1994):

$$\begin{bmatrix} u \\ v \\ w \end{bmatrix} = \begin{bmatrix} 0 \\ V_m \\ W_m \end{bmatrix} + \begin{bmatrix} U \\ V \\ W \end{bmatrix} exp[\, i\,(kx+m\theta)+\lambda t] \qquad (2.39)$$

where $[0, V_m, W_m]$ is the cylindrical mean flow, $[U,V,W]$ the amplitude of perturbation, k a real number, m an integer ($m=0$ indicates axisymmetric perturbation and $m\neq 0$ spiral one) and λ a complex number. If the real part of λ is negative, the flow is stable. Otherwise it is unstable. The appearance of unstable modes is associated with breakdown.

Ludwieg[17] derived a criterion for the instability of the helical flow in the thin annulus to spiral disturbances in the following form:

$$(1-h)(1-h^2) - (5/3-h)\,g^2 < 0 \quad , \qquad (2.40)$$

---

[15] Here the breakdown *is* treated as if it was directly related to the *transition* between laminar and turbulent flow, at least from the point of view of mathematics applied (compare remarks in section 2.1.).

[16] There are many alternative ways of writing the argument of the *exp* function. Here , unlike Suematsu, it is not preceded by minus sign. Lessen *et al.* (1974) and Lessen and Paillet (1974) express the perturbation as:

$$[U,V,W,P] = [F(r), iG(r), H(r), P(r)]\; exp\,[i\,(kx + m\theta - kct)],$$

where k and m are axial and azimuthal wave numbers and c is the complex phase velocity (clearly this case deals also with pressure disturbance). There is no attempt made in this thesis to unify the notation.

[17] Reported here after Hall (1972), Leibovich (1978), Escudier(1988), Delery(1994) and others

where $g \equiv (r/v)\ (dw/dr)$ and $h \equiv (r/v)\ (dv/dr)$. He suggested that after the onset of instability, spiral disturbances could amplify, induce the asymmetry in the vortex core and thus lead to stagnation. Ludweig's analysis does not, however, depend on the mode of disturbance and deals with an irrelevant physical model.

Leibovich and Stewartson (1983) investigated the inviscid instability of columnar vortex flows in unbounded domains to three-dimensional perturbations. The flow was found unstable if

$$v\ (d\Omega/dr)\ [\ (d\Omega/dr)\ (d\Gamma/dr) + (dw/dr)^2\ ] < 0 \quad , \tag{2.41}$$

where $\Omega = v/r$ and $\Gamma = vr$. Stewartson (1982) extended these investigations for flows with $\mathrm{Re} >> 1$ with disturbances of large azimuthal wave numbers. Leibovich (1983,1984) outlines a few more criteria for stability of a columnar vortex derived by different authors.

Lessen *et al.* (1974) investigated the stability to non-axisymmetric disturbances of a trailing vortex given by the velocity profiles[18]:

$$\begin{aligned} w &= q[1-exp(-r^2)]/r \quad , \\ v &= exp(-r^2) \quad , \end{aligned} \tag{2.42}$$

which is a non-dimensional form of the Burger vortex given by equations (2.4) and (2.5) - commonly called q-vortex; q is the swirl parameter i.e. the ratio of maximum swirl velocity to maximum axial velocity. The disturbances considered are of the form

$$exp[i\ (kx+m\theta-kct)] \quad , \tag{2.43}$$

and were found to die out quickly for a small value of q if $m=1$. However for negative values of m (i.e. with helical wave paths opposite in sense to the wake rotation) the growth rate increases and then decreases with respect to axial wave

[18] In their mathematical (and numerical) investigations the units are not important. The parameter q is sufficient for changing the strength of the vortex.

number k. Table2.1 gives the maximum growth rates for the six values of m investigated together with values of k and q corresponding to these growth rates. Figure 2.51 shows the growth rate (i.e. the product of axial wave number and imaginary part of phase speed) for q=0.8 and m = -1, ... , -6.

m	growth rate	k	q
-1	0.1470	0.30	0.32
-2	0.3138	1.20	0.70
-3	0.3544	1.70	0.79
-4	0.3777	2.15	0.82
-5	0.3912	2.60	0.83
-6	0.4008	3.20	0.83

Table 2.1. Maximum growth rates of non-axisymmetrical instabilities, from Lessen *et al.* (1974)

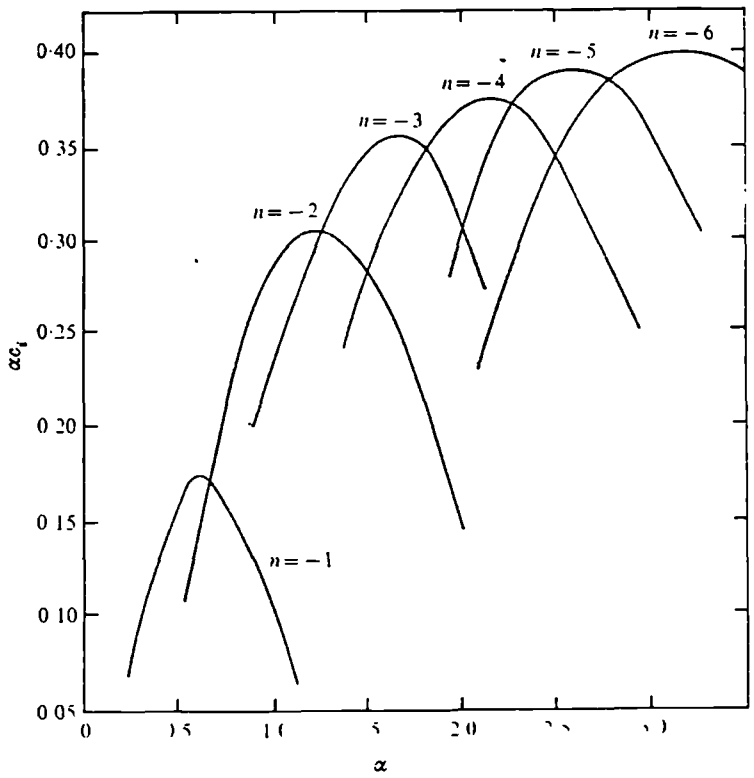

Figure 2.51.The growth rate of non-axisymmetrical instabilities for q = 0.8 and m = -1,..., -6. From Lessen *et al.* (1974).

The flow becomes completely stabilised, that is all wavelengths become damped, for q slightly greater than 1.5 [19]. Lessen and Paillet (1974) also considered the viscous effects in a similar stability analysis.

More recently Khorrami (1991) investigated the viscous modes of instability in trailing vortices. The inviscid results of Lessen *et al.* (1974) were confirmed and moreover the two viscous modes of instability were revealed: axisymmetrc ($m=0$) and asymmetric ($m=1$). However the growth rates corresponding to these modes were found to be orders of magnitude smaller than the inviscid modes.

Kribus and Leibovich (1994) studied the linear stability of strongly non-linear waves to three-dimensional perturbations. They showed that the most unstable are the perturbations with azimuthal wave number $m=\pm1$, which is consistent with the experimental results of Garg and Leibovich (1979). Additionally the results showed that the sense of rotation of the helical streaklines is not always the same, but depends on the basic flow (non-rotating patterns being also possible). This may explain some of the contradictory experimental results obtained in different investigations.

The experimental results by Garg and Leibovich (1979) suggest that the flow upstream of the breakdown is stable to non-axisymmetric disturbances (since q is much greater than 1.5, the limit found by Lessen *et.al.*-1974). This hypothesis supports the view that vortex breakdown *is not* a consequence of the instability.

According to Escudier (1988), there are also other indications denying the instability as a direct cause of breakdown:

- In carefully controlled conditions (e.g. in cylindrical container) only the axisymmetric form of breakdown is present. Since it is generally accepted that the vortex flows are much more stable to axisymmetric than non-axisymmetric disturbances, the bubble form is unlikely to be a consequence of instability of the approach flow.

[19] This may apparently contradict the results by Squire. However the analysis by Lessen *et.al.* (1974) investigates the stability to non-axisymmetric disturbances. The result means only that prior to the burst the flow is stable to these instabilities. This does not contradict the Squire's results, since he dealt only with axisymmetric perturbations.

- Breakdown appears as a sudden change (like a shock wave or hydraulic jump). There is no evidence of continuous growth typical for hydrodynamic instability.
- The spiral and bubble modes of breakdown were found to interchange under apparently steady conditions. Thus the instability explanation of spiral breakdown would imply that the destabilised flow may somehow stabilise itself to permit the formation of the bubble form. Such a process seems unlikely unless the conditions are transient.

Although instability may not cause the vortex breakdown, numerous investigations confirm that instability plays an important role in the wake of breakdown (where, say, q is smaller than 1.5, according to Lessen *et al.*-1974). It is responsible for producing the helical patterns (coherent structures) which determine quasi-periodic behaviour of the flow field.

2.5.3. Stagnation theories

One of the generally accepted features of vortex breakdown is stagnation of the flow due to the retardation (compare section 2.1). A number of theoretical investigations explored this property of vortex breakdown. The idea was to examine (mostly by numerical methods) the quasi-cylindrical Navier-Stokes equations, which in a sense resemble the two-dimensional boundary layer equations. It is well known that for a boundary layer, separation is predicted at or near the point where the actual numerical calculations fail. Similarly it was found that for certain upstream conditions the numerical solutions of the quasi-cylindrical Navier-Stokes equations could not be continued beyond some point downstream because of the appearance of appreciable axial gradients (preceding the actual breakdown, as it is believed).

The concept was developed in the successive papers by Hall (1966a, 1967, 1972). The equations of motions considered by Hall (1972) were those given by the

system of equations (2.16), but simplified to account for quasi-cylindrical flow i.e.

$$\frac{\partial u}{\partial r}+\frac{u}{r}+\frac{\partial w}{\partial x}=0, \tag{2.44a}$$

$$\frac{v^2}{r}=-\frac{1}{\rho}\frac{\partial p}{\partial r}, \tag{2.44b}$$

$$u\frac{\partial v}{\partial r}+w\frac{\partial v}{\partial x}+\frac{vu}{r}=\nu\left(\frac{\partial^2 v}{\partial r^2}+\frac{1}{r}\frac{\partial v}{\partial r}-\frac{v}{r^2}\right), \tag{2.44c}$$

$$u\frac{\partial w}{\partial r}+w\frac{\partial w}{\partial x}=-\frac{1}{\rho}\frac{\partial p}{\partial x}+\nu\left(\frac{\partial^2 w}{\partial r^2}+\frac{1}{r}\frac{\partial w}{\partial r}\right), \tag{2.44d}$$

with boundary conditions on the axis of symmetry ($r=0$): $u = v = \partial w/\partial r = 0$ and a condition (for example a prescribed pressure distribution) at the edge $r=R(x)$. The solution of the system of equations (2.44) can be calculated by proceeding step by step in the axial direction starting from some point (say $x=x_0$) where the initial velocity distributions $v=v_0(r)$ and $w=w_0(r)$ are prescribed.

Hall (1966a) made numerical calculations for the conditions corresponding to the experimental set-up and inlet conditions measured by Kirkpatrick (1965) and obtained good agreement. The computation came to a halt close to the position of the experimental breakdown.

The physical mechanism for retardation of the flow can be deduced from equation (2.44b). After integration (Hall-1972) one obtains:

$$\left(\frac{\partial p}{\partial x}\right)_{r=0}-\left(\frac{\partial p}{\partial x}\right)=-\int_0^r \frac{\partial}{\partial x}\left(\frac{\rho v^2}{r}\right)dr, \tag{2.45}$$

which means that the pressure gradient along the axis varies across the core and this variation depends on swirl. Comparing the orders of magnitude of the variables the

following relationship can be drawn

$$\left(\frac{\partial p}{\partial x}\right)_{r=0} - \left(\frac{\partial p}{\partial x}\right)_{r=R} \propto \rho \alpha \Gamma^2/R^3 \tag{2.46}$$

where α is the order of magnitude of the divergence of the stream (u/v), and Γ and R are the orders of magnitude of circulation and core radius, respectively. Relation (2.46) shows that generally the axial pressure gradient is much more influenced by swirl effects (quadratic dependence) than the actual divergence of the streamlines (linear dependence). Hence the retardation along the core of the axis is larger than that along the outside. Krause (1983,1985) made a similar analysis and obtained some more general results in the form of integral relations (solved numerically) containing radial, axial and circumferential components of velocity and radial derivatives of the latter. The observations by Hall were confirmed, but additionally the contribution of viscous forces to the initiation of vortex breakdown was considered. It was found that in the absence of an external pressure gradient the viscous forces eventually lead to breakdown. However even if a relatively small external gradient is imposed, it becomes the dominating feature controlling the breakdown. Thus the viscous effects become less important.

Similar numerical analyses to that of Hall were conducted by Bossel (1969, 1971) and Mager (1972). Their common property was the appearance of singularities, as it is believed, preceding the burst. Bossel (1969), however, attempted to overcome the failure of numerical solutions by dividing the computational domain into several regions with different sets of governing equations.

Randall and L-eibovich (1973) pointed out that the analogy with boundary layer separation is inappropriate. The approximation signals breakdown correctly only because it simulates the change of the flow from supercritical towards critical. Hence the possibility of upstream wave propagation is introduced into the

physics. They argued that a similar failure would occur in a step-by-step calculation in a supersonic duct, if the flow was driven towards sonic conditions. Thus the criterion based on the possibility of wave propagation is actually more general.

2.5.4. Vorticity dynamics theory

Brown and Lopez (1990) considered the vortex breakdown phenomenon from the point of view of the generation of the azimuthal component of vorticity through the stretching and tilting of vortex lines. The starting point for their considerations was equation (2.24), repeated here for convenience:

$$\eta = \frac{\Gamma}{r}\frac{d\Gamma}{d\psi} - r\frac{dh}{d\psi} \quad ,$$

which describes steady, inviscid, axisymmetric flow (η is the azimuthal component of vorticity). They considered the curve C in the plane (r,x), given by relation $r=\sigma(x)$, chosen such that the stream function is constant on C i.e. $\psi(r,x)=\psi_1$ (figure 2.52).

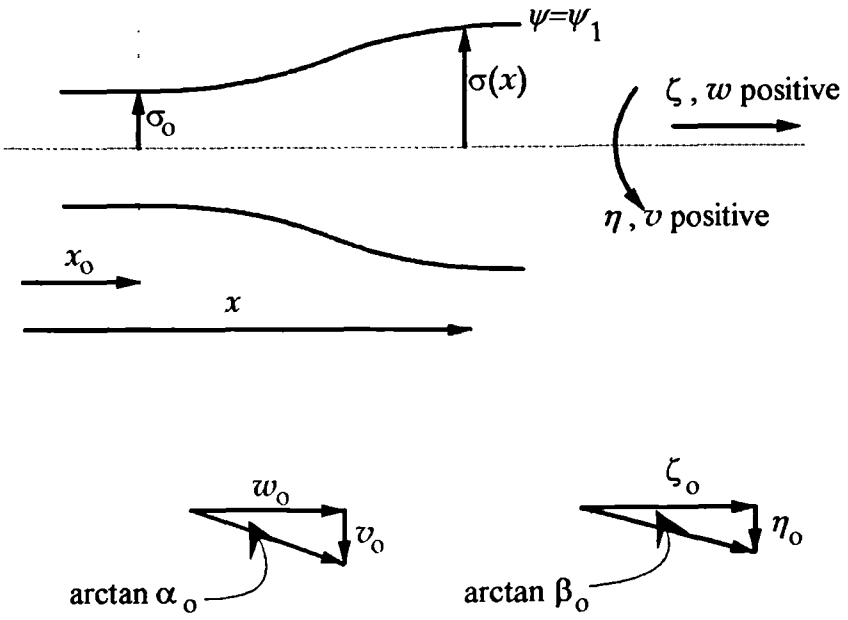

Figure 2.52. System of co-ordinates and some quantities used in theoretical investigation by Brown and Lopez (1990).

Then on C

$$\eta(x) = \Gamma(\psi_1)\,\Gamma'(\psi_1)/\,\sigma - \sigma\, h'(\psi_1) \quad , \tag{2.47}$$

$$d\psi = 0 \quad \text{and} \quad u = w\sigma'(x) \quad ; \tag{2.48}$$

or on a stream surface

$$\eta(x) = A/\,\sigma - B\,\sigma \tag{2.49}$$

and

$$d\eta = -(A/\,\sigma^2 + B)d\sigma \tag{2.50}$$

where $A=\Gamma(\psi_1)\,\Gamma'(\psi_1)$ and $B=h'(\psi_1)$. Next they assumed that at certain location x_0 and on particular stream surface $\psi=\psi_1$ the stream surface radius σ_0 is known, together with azimuthal and axial components of both the velocity and vorticity: v_0 , w_0 , η_0 and ζ_0 . Then constants A and B can be expressed as:

$$A=\sigma_0\, v_0\, \zeta_0 / w_0 ;$$

if $\eta_0 \neq 0$ then

$$B= (\eta_0/\sigma_0)\,[\,(v_0\zeta_0) / (w_0\eta_0) \; - \; 1\,] ,$$

and if $\eta_0 = 0$ then

$$B=(v_0\zeta_0) / (\sigma_0 w_0) .$$

Hence equation (2.49) takes form:

$$\eta = \alpha_0\zeta_0\left(\frac{\sigma_0}{\sigma} - \frac{\sigma}{\sigma_0}\right) \qquad \text{for } \eta_0 = 0$$

$$\frac{\eta}{\eta_0} = \frac{\sigma_0}{\sigma}\left(\frac{\alpha_0}{\beta_0}\right) - \frac{\sigma}{\sigma_0}\left(\frac{\alpha_0}{\beta_0} - 1\right) \qquad \text{for } \eta_0 \neq 0 \tag{2.51}$$

where $\alpha_0 = v_0/w_0$ and $\beta_0 = \eta_0/\zeta_0$ are the tangents for the helix angles of the velocity and vorticity, respectively. Hence the increase of the azimuthal vorticity on the stream surface depends merely on the ratio of helix angles α_0 and β_0 on the surface at x_0 and the ratio of surface radii at x_0 and x.

Brown and Lopez (1990) made the hypothesis that the necessary condition to bring axial velocity to zero (which triggers breakdown) is the development of a negative azimuthal component of vorticity. The Biot-Savart law for an axisymmetric flow field leads to the following relation between axial velocity (or more precisely rotational component of axial velocity) on the centre line and vorticity field:

$$w(0,x) = \frac{1}{2}\int_{-\infty}^{\infty}\int_{0}^{\infty} \frac{\sigma^2 \eta(\sigma, x')}{[\sigma^2 + (x - x')^2]^{3/2}} d\sigma\, dx' \cdot \qquad (2.52)$$

This implies that the velocity on the axis due to vorticity will be zero or negative at some x only if $\eta(\sigma, x')$ is negative in some region (other terms in the integral are everywhere positive). In addition it must be the *local* azimuthal vorticity since the influence of the far-field vorticity decreases as $(x - x')^3$.

By plotting equation (2.51) in co-ordinates (σ/σ_0 , η/η_0) with α_0/β_0 as a parameter (figure 2.53) it may be inferred that the production of negative azimuthal vorticity is possible only if $\alpha_0/\beta_0 > 1$. This can be regarded as a necessary condition for vortex breakdown.

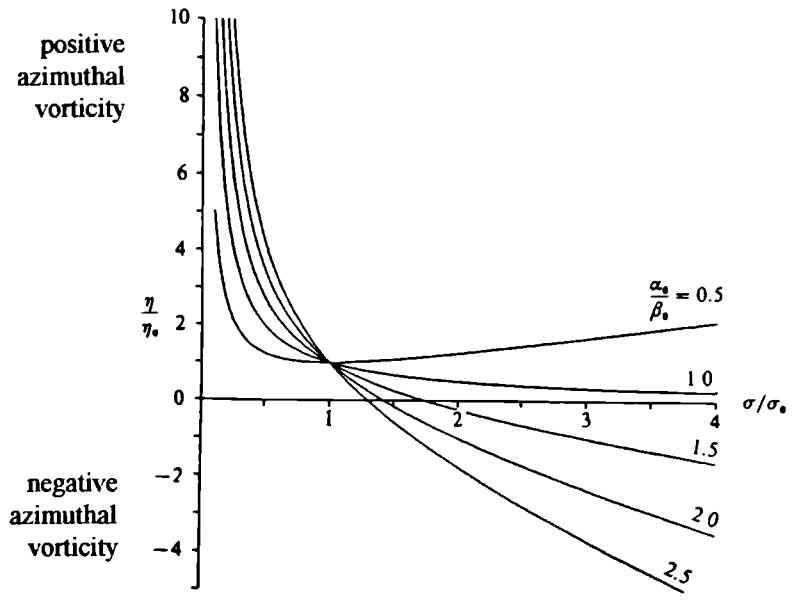

Figure 2.53.Plot of the equation (2.51) in co-ordinates ($\sigma/\sigma_0, \eta/\eta_0$) with α_0/β_0 as a parameter. From Brown and Lopez (1990).

The rapid divergence of the stream surfaces in the breakdown region can be explained on the basis of equation (2.51) as follows.

- The development of negative azimuthal vorticity on stream surfaces induces a negative axial velocity on the axis.
- This, by continuity, leads to the increase of stream surface radius.
- The increased radius induces a further increase in negative azimuthal vorticity.

The latter again leads to effects given in the first point. Hence the breakdown may be seen as a 'positive feedback'. However it is rather a consequence of compatibility between velocity and vorticity fields. The mechanism described clearly needs an *initial* divergence of the stream surfaces. This is, according to numerical simulations conducted by Lopez (1990) and Brown and Lopez (1990), provided by the action of viscous forces. These initiate the reduction in the azimuthal velocity and vorticity, which results in stretching and tilting of axial vorticity. However, the inviscid mechanism given by equation (2.51) later takes control over the phenomenon and plays the major role. The work by Darmofal (1993) gives further insight into the vorticity dynamics in connection with vortex breakdown.

2.6. Numerical simulations of vortex breakdown

The numerical approach based on quasi-cylindrical equations, although useful from the point of view of the prediction of vortex breakdown (compare section 2.5.3), is not capable of predicting the flow in the entire domain. In the region of vortex bursting the stream surfaces diverge, large axial gradients develop, and the calculations fail. Thus no information about the flow downstream of the burst is available. Numerical solutions of the full Navier-Stokes equations are in general free from these defects. However some problems may appear between the 'parabolic' approach flow region and the 'elliptic' or 'hyperbolic' flow regions due to the breakdown and in its wake.

Among the first successful numerical solutions of the Navier-Stokes equations for a laminar incompressible axisymmetric flow in a circular duct were those obtained by Kopecky and Torrance (1973). The problem was formulated in terms of the stream function ψ, azimuthal vorticity η and circulation Γ ; an explicit finite difference procedure was used to integrate the time dependent transport equations. The approach flow was assumed as a Burger vortex with uniform axial velocity. Grabowski (1974) and Grabowski and Berger (1976) solved a similar problem in terms of 'primitive' variables by using an artificial compressibility method. The inlet velocity profiles were in polynomial forms (as those used by Mager-1972), the axial velocity having jet-like or wake-like profiles. More recently Brown and Lopez (1990) obtained the time-dependent numerical solutions of the Navier-Stokes equations by methods outlined in a paper by Lopez (1990).

Generally these simulations are consistent with each other. For some combinations of the flow parameters, patterns with a recirculating zone (single- or two-celled) resembling an axisymmetric 'bubble' are obtained. Similarly the basic features of breakdown like, for example, the maximum swirl angle, are reproduced correctly[20]. However there are some weaknesses. The vortex burst migrates upstream until it reaches the upstream boundary[21], so that no steady state location some distance from the 'inlet' of the computational domain is achieved. In addition the solutions indicate breakdown regardless of state of the upstream flow (subcritical or supercritical). Finally, the assumption of axisymmetric motion does not allow the computation of the detailed structure of breakdown (which includes non-axisymmetric effects).

Shi (1985) solved the complete Navier-Stokes equations for incompressible and axisymmetric but unsteady flow. He examined an isolated axisymmetric, concentrated, vortex embedded in an unbounded uniform flow with a constant

[20] e.g. 44.17 to 49.95° in Grabowski's-1974 solutions and 42° to 56° in Darmofal's-1993
[21] unless some external pressure gradient is imposed (as, for example, in Darmofal-1993)

circulation. Due to the problem formulation no solutions were obtained when the flow was subcritical. For appropriate combinations of flow parameters the solution exhibits quasi-periodicity after some time. A new cell generated at the front of the breakdown bubble grows gradually and moves downstream with the main flow. Then merges with another cell previously generated into a large one and goes downstream. This phenomenon is periodic and resembles the shedding of vortex rings.

Nakamura *et al.* (1983) conducted a numerical simulation of vortex breakdown by using the vortex filament method. The vortex region was represented by multiple filaments, with the axial velocity component induced by a spiral winding of the filaments. The axisymmetric and spiral types of breakdown are reproduced by introducing to the flow axisymmetric and three-dimensional disturbances, respectively.

Lopez (1990) and Lopez and Perry (1992) solved the time dependent Navier-Stokes equations for flow confined in cylinder with a rotating endwall, modelling the experimental set-up by Escudier (1984) - figure 2.29. They obtained excellent agreement with the experimental results, perhaps due to well defined and simple boundary conditions.

The study of Berger and Erlebacher (1992) addresses the question of breakdown migration to the initial computational cell. They derived a modified set of governing differential equations for swirling flows, which produce a stagnation point, whose location depends on the core Reynolds number, the flow divergence, the swirl velocity and the strength of the vortex.

A review of the numerical methods o simulating vortical flows in aeronautics is given by Hoeijmakers (1990). Two dominating techniques are the numerical solution of the Euler and Navier-Stokes equations. The latter are believed to be more accurate (e.g. in predicting massive separation regions, vortex core structure[22], shock-boundary layer interactions etc.) but also more laborious to

[22] The Euler methods usually overestimate the expansion of the vortex due to the primary separation because they do not encounter the viscosity responsible for secondary and tertiary separation.

compute. However both methods are equally effective in predicting the onset of the vortex breakdown[23] (see, for example, Agrawal *et al.*-1990&1992, Robinson *et al.*-1994).

The onset and hysteresis of vortex breakdown above a 75° sweep delta wing at low Reynolds numbers were investigated by Visbal (1994,1995). He solved the full unsteady, three-dimensional Navier-Stokes equations. Vortex breakdown was found to emerge in the wing's near wake as a nearly-axisymmetric bubble. The bubble was growing as it was propagating upstream over the wing. Then it transformed into a rotating spiral, after loosing the stability to asymmetric disturbances.

2.7. Background of the present research.

The direct motivation for the present experimental investigation was the study by Professor Dennis G. Mabey at DRA, Bedford, on fin buffeting on an F-18 model. His interpretative hypothesis (Mabey-1991) was outlined briefly in section 2.3.3. According to this hypothesis pressure fluctuations due to breakdown are as shown in figure 2.54. Although the actual picture of the pressure fluctuations

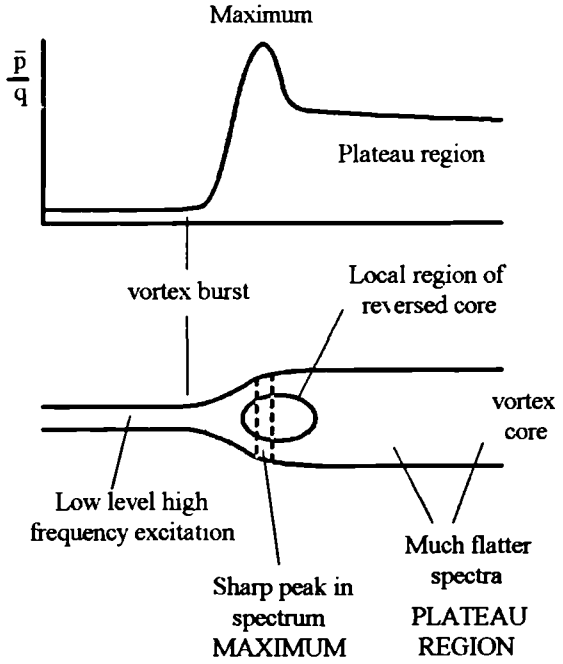

Figure 2.54.Interpretative hypothesis derived by Mabey (1991).

[23] Inviscid models are successful perhaps due to only a slight dependence of breakdown location on Re.

revealed from this study differs in detail from the one sketched, it was a good starting point.

None of the theories, briefly described in section 2.5 , have succeeded in predicting the pressure fluctuations due to the vortex burst, or how these pressure fluctuations scale with the vortex dimensions. Thus the investigations must be made either numerically as, for example, Rizk and Gee (1992), who calculated the fluctuating airloads on the vertical tail of an F-18 using Navier-Stokes equations, or experimentally, as during the present research.

Historically, the first investigation dealing with quasi-periodic phenomena caused by vortex breakdown was made by Cassidy and Falvey (1970). They employed a swirl vane arrangement and measured the unsteady pressure and velocity due to a burst vortex (figure 2.55). No attempt was made to perform the spectral analysis, nor was the proper spatial resolution achieved.

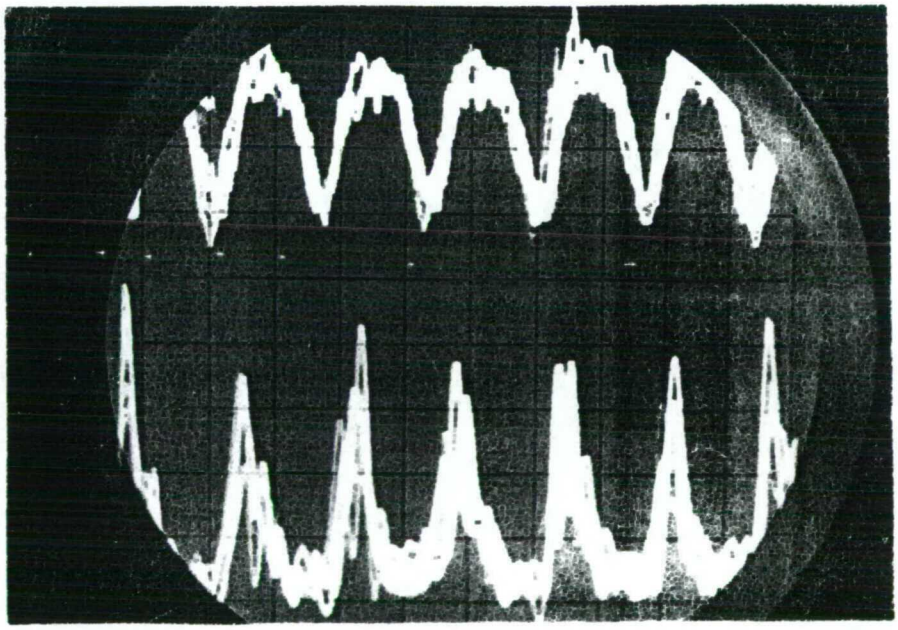

Figure 2.55. Quasi-periodic velocity (upper trace) and pressure fluctuations found by Cassidy and Falvey (1970).

Faler and Leibovich (1978) and Garg and Leibovich (1979) were using a copy of the apparatus of Sarpkaya and made LDA measurements of velocity profiles and

fluctuations accompanying the breakdown flow field. The spectra of the axial and tangential velocities measured exhibit well defined peaks. They concluded that the helical instability (i.e. m=-1) in the wake is responsible for the appearance of the coherent (periodic) oscillations. However the proper frequency parameter (dependent on the burst or wake features and not, say, on the apparatus' dimensions) was not derived. Radial traversing showed that the locations with 'highest peaks' in the spectra were somewhere near the edge of the vortex core. However no particular conclusions were drawn. Rough estimates made by the author show reasonable agreement with the present investigations. Figure 2.56 shows the spectra of axial velocity obtained by Garg and Leibovich (1979) some distance downstream of the burst (their investigations were not dealing with pressure fluctuations)

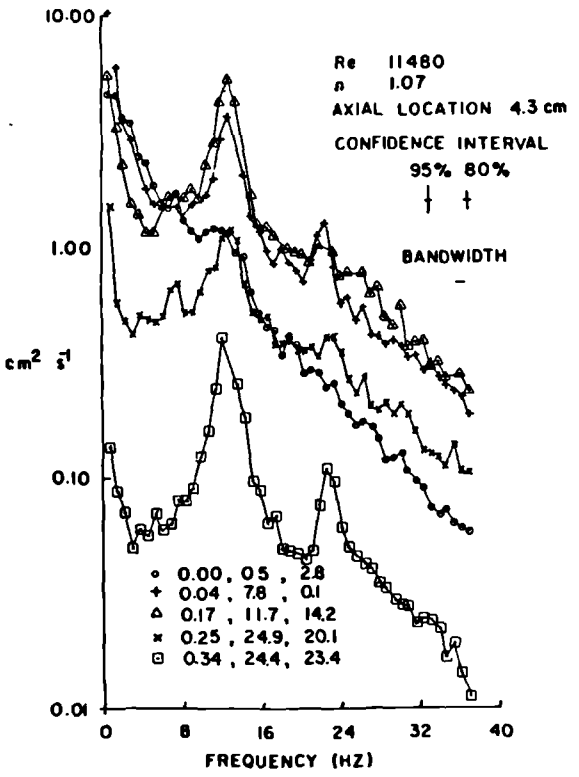

Figure 2.56. Spectra of the axial velocity in the near wake of breakdown. Axial burst location at x=2.3 cm. Lower legend gives radial location normalised by the local tube radius, mean axial velocity [cm/s] and mean swirl velocity [cm/s]. From Garg and Leibovich (1979).

Shah *et al.* (1990) investigated the vertical fin excitation, on an F-18 model, due to the vortex burst. They found that the burst LEX vortex was responsible for a sharp peak in the excitation spectra on the fin. With the LEX removed (and the strong vortex not present) the excitation was greatly reduced.

Wood and Bean (1993) performed hot-wire measurements of the flow at the trailing edge of the delta wing (in a plane perpendicular to the wing's surface), for a set of delta wings with sweep angles between 55° and 75°. A sharp peak in velocity spectra was found at locations some distance off the vortex centre-line, within the shear layer just as for Garg and Leibovich (1979). The reduced frequency parameter

$$n = (f\bar{\bar{c}}/U)\sin\alpha \tag{2.53}$$

(based on wing mean aerodynamic cord) was found constant for a given geometry, although it changed from configuration to configuration. A unique frequency parameter was not proposed. The changes in 'vortical frequency' were associated with changes in vortex core dimensions due to different sweeps and angles of attack.

Hubner and Komerath (1994,1995) conducted studies to map the spectra of the quasi-periodic structures due to the vortex burst on 59.3° cropped delta wing. The cross-spectral analysis (involving two hot-wire sensors) revealed the existence of a helical path around the core of the vortex system. The spectra of velocity fluctuations demonstrated narrow frequency bands containing the majority of the fluctuation energy. The frequency corresponding to these narrow bands was found to decrease along the vortex as the core dimension grows.

Gursul (1994) made experiments on four delta wings with sweep angles $\Lambda=60°,65°,70°$ and 75°. The coherent structures (or helical paths) were tracked by means of pressure transducers mounted flush on the wing's surface (one of the spectra was shown in figure 2.18). It was found that the dimensionless frequency

$$n=fx/U \tag{2.54}$$

is nearly constant for a given geometry (f - the dominant frequency, x - the chordwise distance from the apex, U - free stream velocity). Dimensional analysis for the four variables - Γ, f, x and U - led to the conclusion that there is a

single relation

$$fx/U = F(\Gamma/Ux) \quad , \tag{2.55}$$

where Γ is the circulation of the leading edge vortex. The circulation is then estimated by slender wing theory. The idea behind using circulation was to eliminate the variable x (the circulation is a linear function of x), thus the frequency parameter would not depend on the distance from the apex. However the weakness of this reasoning is that Γ practically does not change due to the burst (only the distribution of the vorticity is changed). Hence the frequency parameter would be present even for the pre-breakdown conditions, where there are no fluctuations.

Mabey (1995) analysed the experimental data of Gursul (1994) for 60°,65° and 75° delta wings. He proposed a reduced frequency parameter for a delta wing wake:

$$n = (fs/U)\sin\alpha = (fc\ (\cot\Lambda)/U)\sin\alpha \quad , \tag{2.56}$$

(where s is the wing's semispan) which gives the value of $n=0.25 \pm 0.02$ within a range of α corresponding to the breakdown location over the wing (but neither too close to the apex nor to the trailing edge).

Gursul and Yang (1995) used flow visualisation techniques and velocity measurements to see if there was any relation between the frequency of helical mode instability in the breakdown wake and the instantaneous location of the burst on the wing. They concluded that the changes in breakdown location occur at much lower frequencies than the frequency of the helical instability. This suggested that the burst location was not influenced by the helical instability.

Wolfe *et al.* (1995) addressed the question of the impingement of a streamwise vortex on a thin plate. Their experimental set-up is shown in figure 2.57. The objective was to relate the instantaneous structure of the breakdown flow field (monitored by PIV techniques) incident on a thin plate to the spectra of surface

pressure along the plate (measured by means of pressure transducer). By traversing the plate it was found that pressure fluctuations exhibit the sharp peaks which correspond spatially to the concentrations of azimuthal vorticity. The surface pressure spectra correspond *qualitatively* to those obtained during the present investigation and those of Wood and Bean-1993. There was a relatively low level of fluctuations near the axis of the vortex, sharp peaks at the edge of the vortex core and again low levels outside the vortex. Figure 2.58 shows the measured pressure spectra with respect to different radial locations of the transducer.

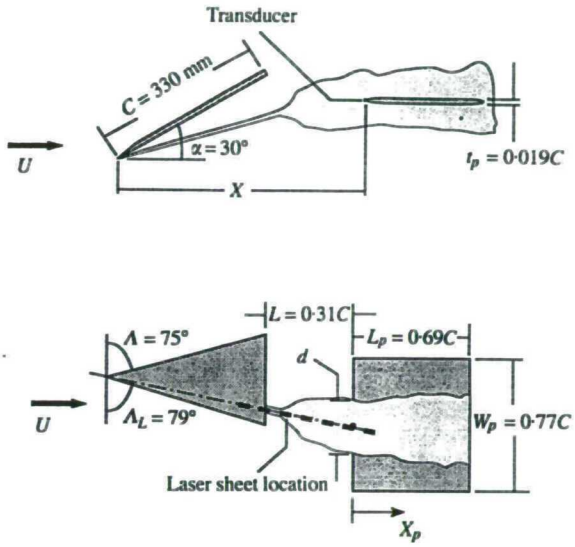

Figure 2.57.Experimental set-up of Wolfe *et al.* (1995).

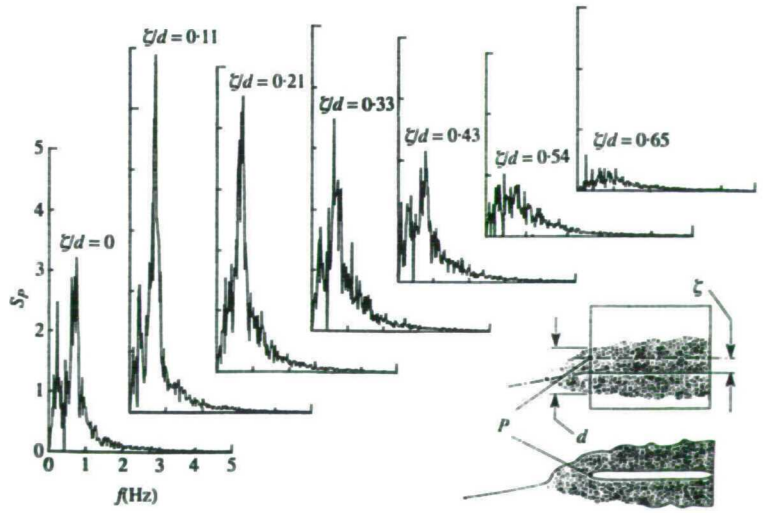

Figure 2.58.Spectra of pressure fluctuations across the vortex by Wolfe *et al.* (1995).

The thin flat plate represents a *highly* intrusive method of investigation. It is well-known (see, for example, remarks in section 2.2.2) that the vortex breakdown is strongly affected by introducing bodies into the flow. It is not clear how the plate (in fact bigger than the actual delta wing) affected the measurements. The authors themselves point out that the burst position was unsteady while traversing the plate off the axis.

Recently Canbazoglu *et al.* (1995) investigated the impingement of a broken down vortex on a fin that was mounted on a 75° delta wing model. Experiments were conducted in a water channel at low Reynolds number of about 50,000 (based on the wing root chord). One of the most important conclusions, which agrees fully with the results of present investigation, is that the regions of low and high levels of vorticity (appearing as a staggered pattern in the PIV images) coincide with the regions of low and high RMS surface pressure on the fin. In addition spectra of surface pressure fluctuations show peak values which are well correlated with regions of high fluctuating vorticity.

CHAPTER 3

EXPERIMENTAL TECHNIQUES

During this research the phenomenon of vortex breakdown was investigated by means of two distinctively different experimental configurations: a *vortex tube* and a *delta wing*. The main purpose was to compare and relate the vortex burst phenomena obtained in two widely different situations. In addition, these two configurations were believed to be the simplest realisable test cases.

The vortex tube arrangement was particularly attractive, since it provided easy and reliable control over the strength of the vortex and thus the burst location. The control over the scale of the phenomenon was possible by introducing chokes of different shapes into the test section. The versatility of the flow conditions made the apparatus an ideal tool for similarity or scale effect studies. Although the delta wing arrangement is less convenient (having for example no obvious frame of reference, stronger probe interference, etc.) it certainly models the phenomena occurring on real aircraft configurations better, by maintaining some degree of non-axisymmetry. Thus it is a valuable tool for validation and generalisation of the data obtained in the vortex tube.

This chapter contains a brief description of the experimental configurations and instrumentation used. The more detailed information (necessary for possible continuation of the research) is given in Appendix A.

3.1. The design of the vortex tube apparatus

The vortex tube apparatus was conceptually similar to the one used by Titchener and Taylor-Russell (1956) and later by Harvey (1960,1962). The main differences between those and the new apparatus were: increased diameter of the test section (to diminish possible boundary interference), introduction of a variable adverse pressure gradient (for changing the scale and growth rate of pressure disturbances) and a slightly modified air intake (smoother inflow). Here only a short technical description is given (for details see Appendix A). A general view of the apparatus is shown in figure 3.1. Its main components were: the air intake, the cylindrical test section connected to the centrifugal fan via the diffuser, and a corrugated PVC tube (for simplicity the DC motor and exhaust tubing are not shown in the figure). The apparatus was assembled and operated on the 'Mezzanine floor' at the Department of Aeronautics, Imperial College, London.

3.1.1. Air intake

The intake consisted of two 'shells', with diameter of about 1.2 m, cast in fibre glass. The castings, which were basically smooth three-dimensional surfaces of revolution, formed a radial air intake. One surface smoothly joined the wall of the test section. The other converged to the test section's centre-line via a removable centre-body. The aluminium perforated sheet rolled around the intake, and a layer of fine nylon mesh wrapped around the perforated sheet provided a pressure drop, which helped reduce the influence of the ambient conditions on the phenomenon (for example drafts in the laboratory which caused unexpected movements of the burst). An initial swirl was imparted to the flow by means of twenty guide vanes placed between the intake's castings. Flow visualisation was realised by means of the smoke generator, which fed smoke through a small tubing in the centre-body.

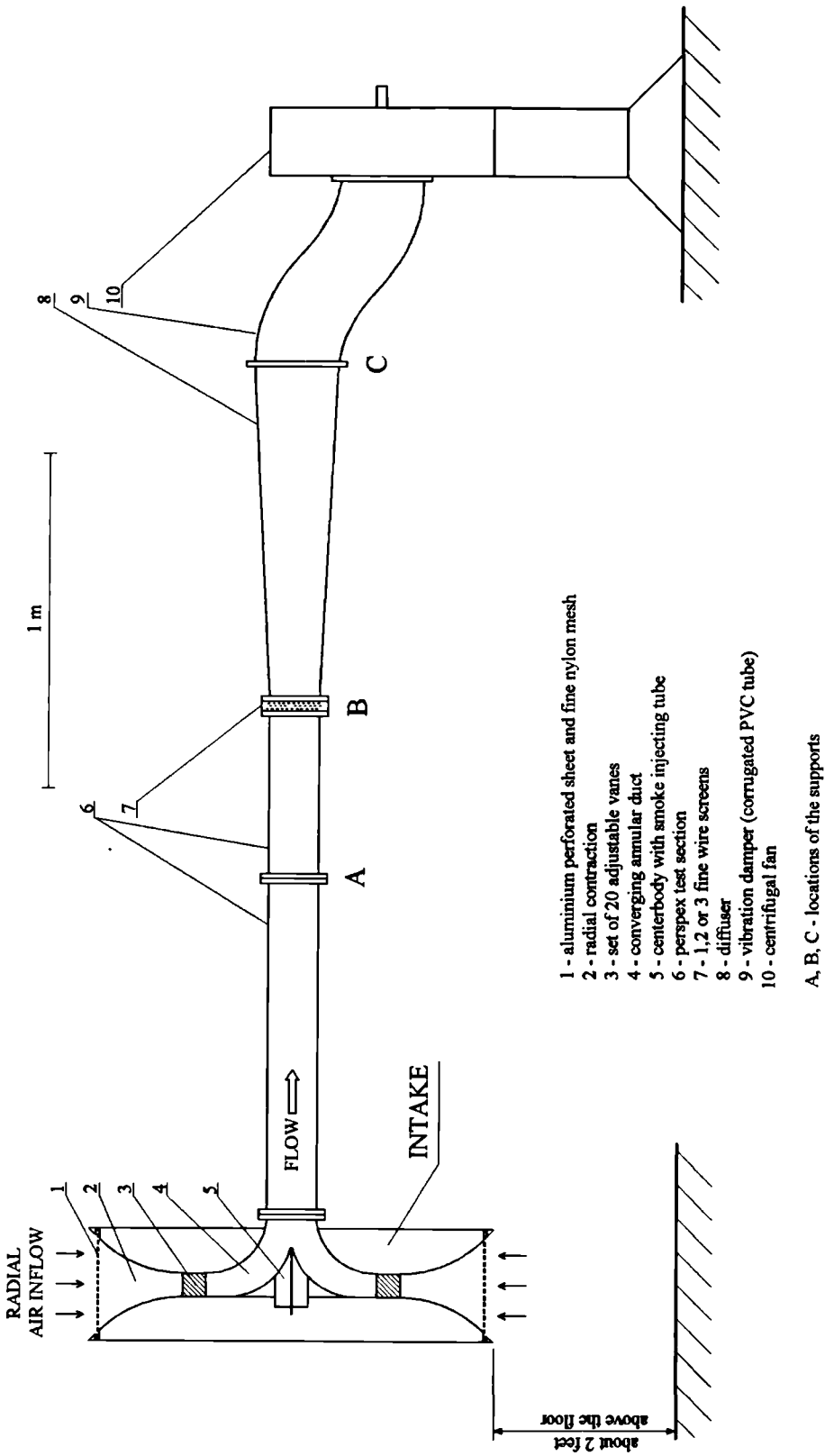

Figure 3.1. General view of the vortex tube apparatus

3.1.2. Test section

The basic test section of the apparatus consisted of a cylindrical Perspex tube. Its nominal internal diameter was 149 mm and the wall thickness was about 6 mm. It was divided into two parts; 1.0 m and 0.5 m long (figure 3.1), for easier access to the interior. A number of probe ports were placed in two meridional planes, perpendicular to each other, along the longer part of the test section (figure 3.2). The port-to-port distance along the test section was 100 mm.

Control over the location and size of the vortex breakdown was maintained by means of three chokes of different shapes slid into the test section. Figure 3.3 shows some details of these chokes (called later *short, medium* and *long*) used in the experiments. They were made of transparent, 0.25 mm thick, melanex sheets rolled-up to form conical surfaces of contractions and diffusers. The contractions' semi-angle was 7.9^{o} for all chokes. The semi-angles for the diffusers were: 10.6^{o}, 7.9^{o} and 4.7^{o}, respectively. The melanex cones were joined and supported by wooden rings (machined so that they could accommodate the cones' edges). The smallest internal diameter inside the chokes was 109 mm, which gave a contraction ratio of 0.535 relative to the test section area.

There were economic and practical reasons for using the melanex chokes, instead of chokes machined in Perspex. Manufacturing the different wooden rings was short, simple and inexpensive. This was extremely important during the initial investigations, when the appropriate shape and length of the choke had to be determined by 'cut and try' methods. The melanex cones were made by simple methods (scissors, staples and PVC tape), thus helping the departmental workshop. In addition, the test section was slightly elliptical (to within an error of about 0.5 mm). Flexible material like melanex filled the entire tube's cross-section, without the gaps that would appear with a choke of solid material. Thus the imperfections of the test section could be 'covered up'.

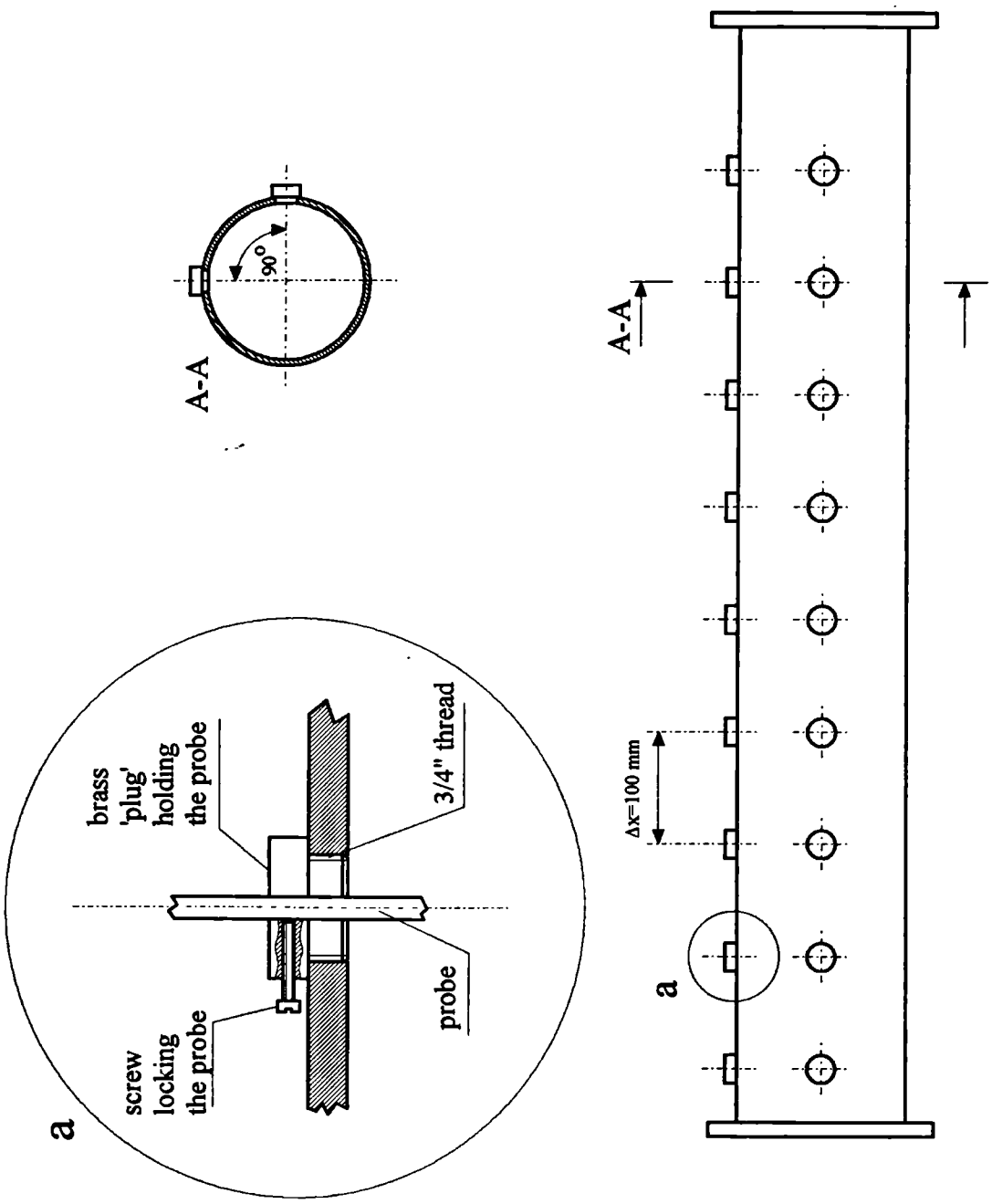

Figure 3.2. The main test section; probe port in detail.

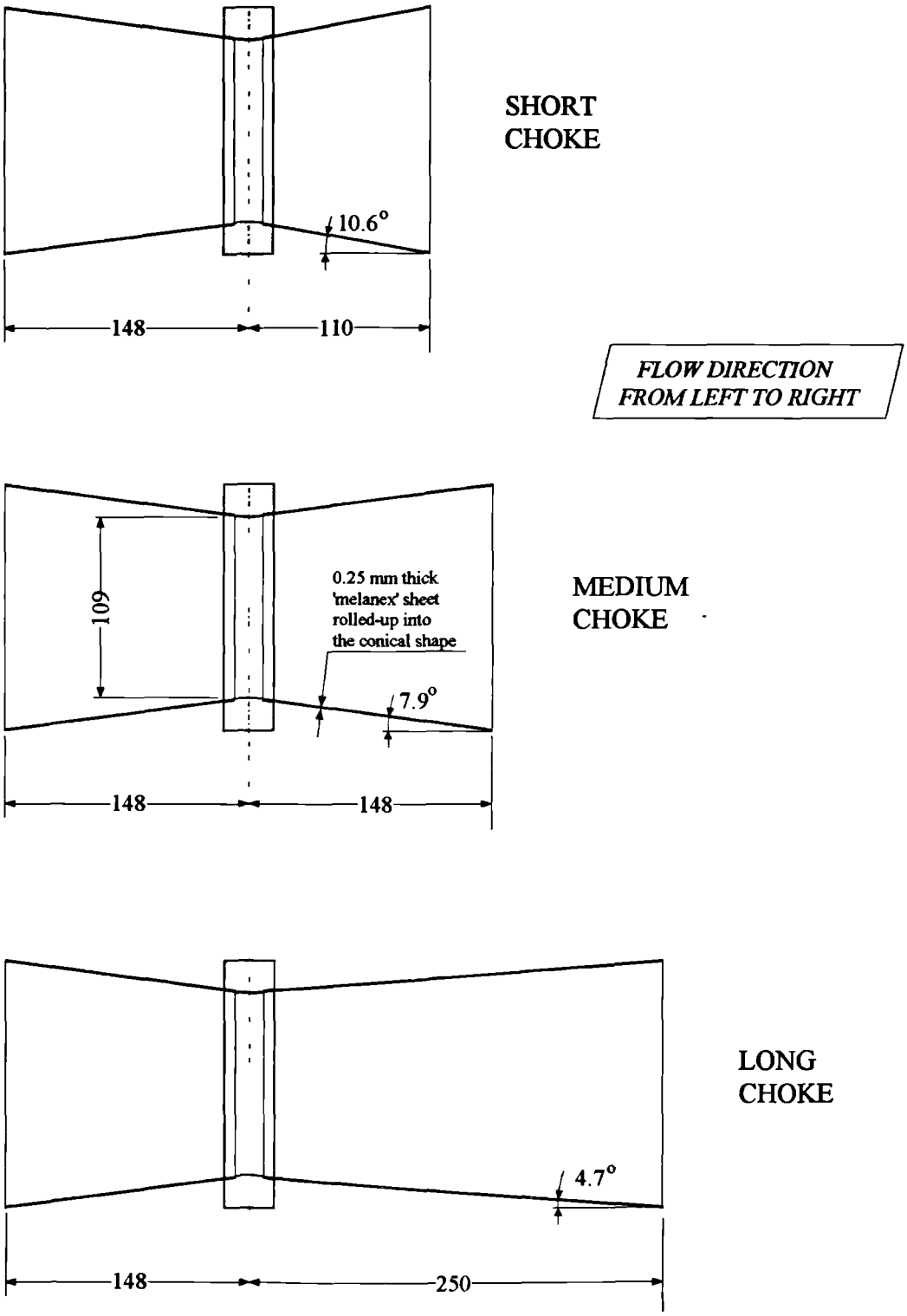

Figure 3.3. Three melanex chokes.

The interior of the chokes was reached by probes passing through a number of holes made every 10 mm (but not necessarily in the same meridional plane). Thus the streamwise resolution of measurements was obtained by sliding the choke within the range of 100 mm to allow different holes to be in front of a given port. This method was justified by the decisive role of the adverse pressure gradient - created by the choke - in determining the character of the breakdown phenomenon. The holes not used in the course of the experiment were sealed with PVC tape.

For the choke configurations described there is a possibility of separated flow occurring on the diffusers' walls. However this was not observed during the current investigation and there may be at least three reasons:

- the Reynolds number is high, e.g. comparing with Sarpkaya (1974) - thus the separations are reduced.
- the flow has a swirl component; hence the centrifugal forces prevent separation (and also in a sense the apparent semi-angle of divergence is reduced due to the spiral paths of fluid elements).
- the burst occupies the centre of the choke (as if a solid body of revolution was placed in the choke) - hence the flow cannot be considered as 'classic' flow in the diverging duct.

In fact, the only situation when the separation did occur was in the flow *without* swirl inside the shortest choke (i.e. with 10.6^{o} semi-angle).

The possible instability of the flow due to the fan operation was reduced by placing one or more fine wire screens at the downstream end of the test section to provide a significant pressure drop. The diffuser (figure 3.1) was introduced to regain some of the static pressure. The diffuser was 1 m long and joined the PVC tube (254 mm) to the test section (149 mm) - giving the divergence semi-angle of 3^{o}. The flexible PVC tube was used for damping mechanical vibrations coming from the motor and the fan, and for matching the different levels of the test section and fan inlet.

3.1.3. Flow rate control

The flow through the rig was driven by a *Tornado* centrifugal fan (Keith Blackman Ltd., S/N U67164) available in the Department. The fan was driven by a DC motor with continuous power control. The fan inlet was fixed to the rig as described in the previous section. The PVC tube, 305 mm in diameter and about 8 m long, was connected to the fan's exhaust, and the air (very often contaminated with smoke) was discharged outside the building.

The maximum flow rate through the rig (with a single wire screen at the test section's downstream end) was approximately 0.16 m^3/s, corresponding roughly to a mean axial velocity of just over 9 m/s in the test section or 17 m/s in the narrowest place of the choke. Continuous regulation of speed was used for visual observations. Generally, measurements were made for two selected speeds (one corresponding to the full capacity of the rig, the other to 60% of the maximum flow rate). Hence it proved practicable to achieve the reduced speed by putting additional wire screens at the downstream end of the test section. The configuration of the screens, giving the required reduction in the flow rate, was found at the beginning of the investigation and used throughout all experiments. This technique gave an accuracy of flow rate in the range of ± 2% (when extremes of temperature and atmospheric pressure were considered). Although this accuracy is not high, it was impractical to make a proper velocity calibration daily (using a shared fragile Betz manometer) because of the poor access to the rig (via narrow, steep stairs).

The maximum Reynolds number, based on the narrowest choke diameter and choke maximum velocity, was 0.13×10^6. The turbulence level of the flow prior to the burst cannot be characterised by a single figure, because of the jet-like profile shed from the centre-body. Generally the maximum turbulence level appeared near the vortex axis (about 15%, relative to the 'free stream' axial velocity). It quickly fell with the radial position of the probe (3% for r about 5-10 mm, less than 0.8% for r greater than 25 mm). The turbulence level increased slightly again in the boundary layer close to the tube wall (2.5%).

3.2. Delta wing experiment

The vortex breakdown experiments on delta wings were conducted in the Donald Campbell Laboratory, the Department of Aeronautics, Imperial College, London. The wind tunnel's test section was 4.5 ft wide and 4 ft high with a total length of 3.25 m. The maximum speed of the empty tunnel is about 60 m/s. The tunnel speeds, at which the phenomena were investigated, were generally about 6, 10 and 29 m/s. These, together with models of different size, gave the range of Reynolds number (based on the wing's root chord length) between 0.13×10^6 and 1.29×10^6. The maximum blockage ratio of the tunnel was 6%. The highest free stream turbulence level was less than 1.0%.

3.2.1. Models and support

The experiments were conducted with two models of a 65° sweep angle delta wing, shown in figure 3.4. This configuration was chosen as it is one of the best documented cases in vortex breakdown investigations (see chapter 2). It has also been a subject of extensive buffeting measurements in conventional and cryogenic wind tunnels. The larger model had a span of 600 mm (643.4 mm root chord) and was 8 mm thick. The smaller one, had a span of 300 mm (321.7 mm root chord), and was 3.2 mm thick. Both models were made of aluminium sheets. All three sides of the triangular plate forming the larger model were bevelled at an angle of 6°. On the smaller model only the leading edges were bevelled (this was because the probe support was located near the trailing edge). The sharp leading edges introduced the well-defined separation lines into the flow.

The models were mounted on a 2 feet long sting and additionally secured by steel wires (figure 3.5). The sting was attached to the models by means of brackets fixed to the compression side (at 0.67 of the chord for larger model and 0.85 of the

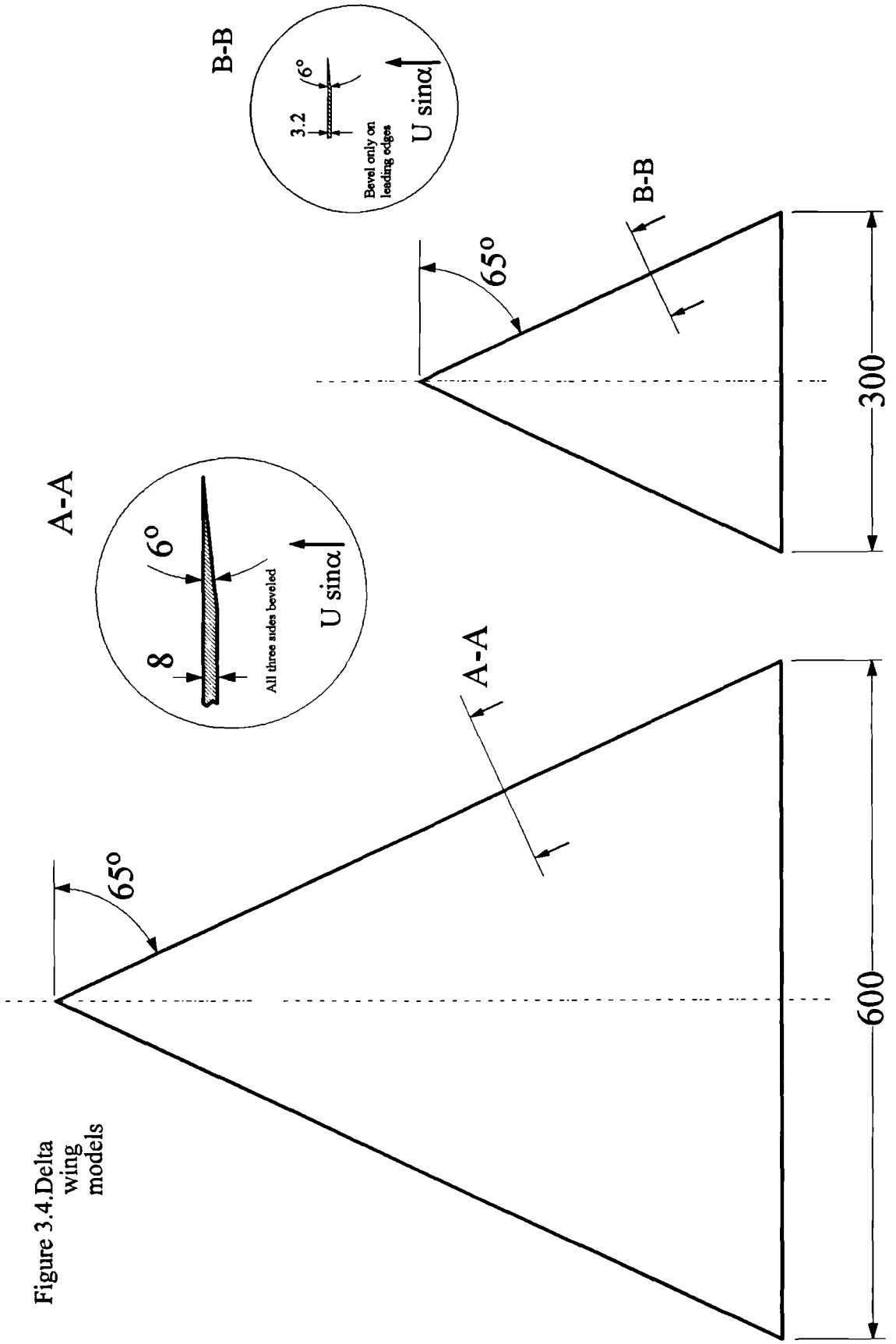

Figure 3.4.Delta wing models

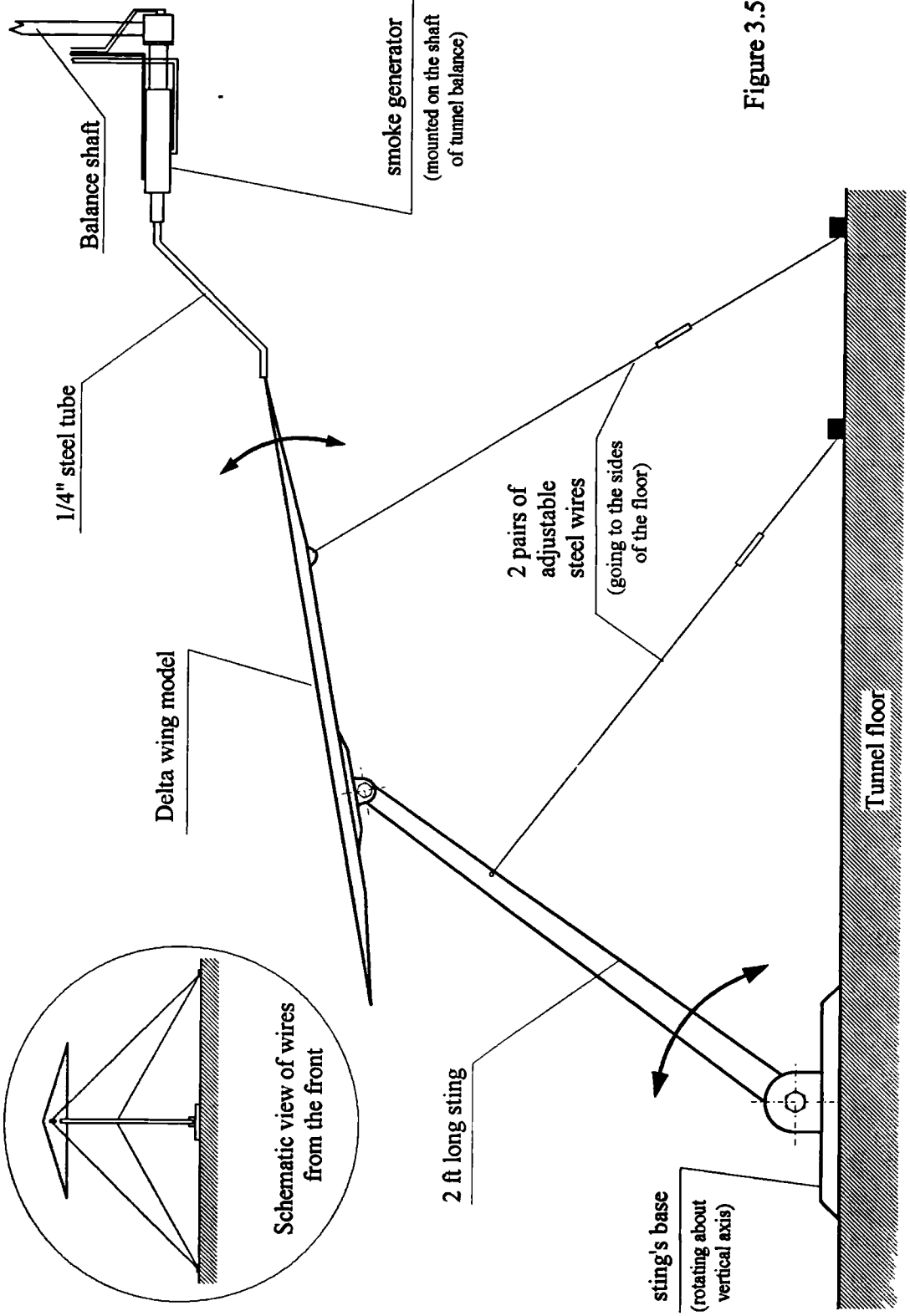

Figure 3.5.Model support and smoke generator

chord for smaller one). By adjustment, it was possible to place the models about the centre of the tunnel cross-section, for each of the angles of attack investigated. The latter was set by means of an inclinometer with an accuracy of 0.1^{o}. The best practical indication of the 'zero' yaw condition turned out to be the symmetric appearance of the vortex burst on the starboard and port sides of the model. The estimated accuracy was about 0.1^{o}.

3.2.2. Flow visualisation

The flow visualisation was provided by the same smoke generator as for the vortex tube. It was fixed to the shaft coming down from the tunnel force balance (figure 3.5). The electric power, mineral oil and compressed CO_2 were delivered to the generator from outside of the tunnel along the shaft. The smoke generator was elevated 150 mm above the wing apex level to reduce interference with the leading edge vortices being studied. The smoke was introduced to the apex by a 6.35 mm steel tube bent in two places. The CO_2 flow rate was selected to match the free stream velocity. This was easy because the smoke traces indicated shearing at unmatched flow rates.

3.2.3. Arrangement of the probes

At present the Donald Campbell wind tunnel does not have a functional traverse mechanism which could be used for positioning the probes. Therefore a simple device had to be assembled to obtain spatial distributions of measured quantities. Figure 3.6 shows the probe support mechanism (projections *a*, *b* and *c* for the smaller model arrangement, and the side view for the larger model, *d*). The mechanism, which was operated manually, consisted basically of two brass bars. The first one ('vertical'), was perpendicular to the wing. The other ('horizontal') was located over the wing's centre line, parallel to the wing. This allowed the probe (or

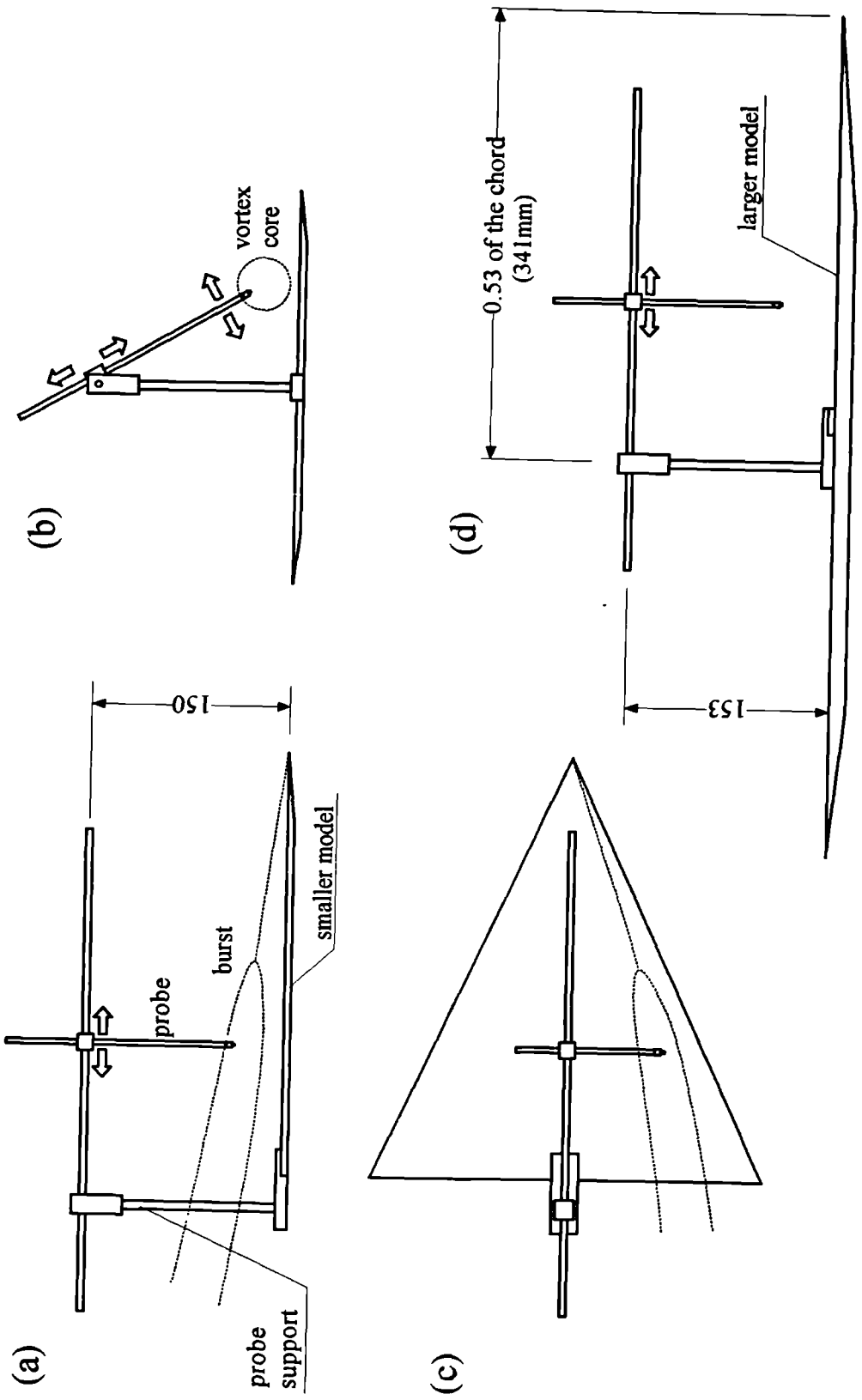

Figure 3.6.Probe support (a,b,c - three projections of the smaller model, d - side view of the bigger model.

probes) to be traversed along the vortex axis (see projection *a*) but with both the angle relative to the wing's surface, and the depth of the immersion into the vortex, variable (see projection *b*).

The vortex centre was established by hot-wire measurements looking for the smallest axial velocity. Once the centre was located, the probes (either a pressure probe or a hot-wire probe) were traversed across the vortex along the line containing the vortex centre. This allowed measurements analogous to those in the vortex tube, within the frame of reference related to the vortex, not to the wing. The vortex centre was found separately for each angle of attack and each chordwise location investigated. The procedure described assumes that the vortex can be considered as being axisymmetrical (compare discussion in section 2.2.1.).

It should be stressed that the geometry of the vortex on the delta wing is far more complicated than inside the vortex tube. In addition, the simple probe support did not provide unrestricted freedom in positioning the probe. Thus, unlike the arrangement in the vortex tube, the probes were not always strictly perpendicular to the vortex axis. Fortunately, this did not have any noticeable effect on the results.

Measurements of the excitation spectra on the wing's surface were conducted with flush mounted pressure transducers placed in holes going through the wing. The holes were made so that a close fit 'keyed' the transducer in the hole. The seal between suction and compression sides of the wing was made of 'plaster' placed around the transducer's casing from its back (i.e. from the compression side). This method was dictated by practical reasons. The holes were made 'in situ', usually directly under the vortex axis, after it was established from measurements. Hence there was no need to dismantle the set-up and insert proper transducer ports by the departmental workshop. The reference tube and cables were taped with PVC, going first towards the wing's centre line and then along the centre line towards the sting.

3.3. Instrumentation

The experiments within the current investigation comprised chiefly of measurements of fluctuating pressure and, to a lesser extent, fluctuating velocity. Thus the equipment consisted of pressure transducers and thermal anemometers (hot-wires), together with proper signal conditioning and a PC based analog to digital (A/D) converter. Clearly, considerable effort must have been deployed in the 'physical' or 'mechanical' side (the proper housings for the probes, calibration devices etc.). The data processing included fairly standard procedures such as fast Fourier transform (FFT) or correlation techniques. Some mean velocity measurements were taken with a conventional pressure probe.

Introducing the probes into the proper place in the flow relied to a great extent on smoke visualisation techniques (mentioned already in sections 3.1.1. and 3.2.2.). In addition the laser light sheet technique was used for a better understanding of the flow structure.

3.3.1. Pressure measurements

A basic tool for measurements of the fluctuating pressure were three miniature piezoresistive pressure transducers. Two of them (made by Entran) had an operating range of 15 PSI differential. The third (made by Kulite) had a range of 5 PSI differential. Both types were 2.41 mm in diameter and 9.53 mm (3/8") long (figure 3.7). The sensing element was protected by a casing with a number of small holes placed in the front. Four cables (2 for excitation, 2 for output signal) were connected to a bridge unit.

At the beginning of the investigations it was believed that the pressure fluctuations caused by the vortex breakdown could be detected by the transducers mounted in ports located on the wall of the vortex tube test section (a non-intrusive method), i.e. in the far field of the breakdown. Hence the diameter of the vortex tube

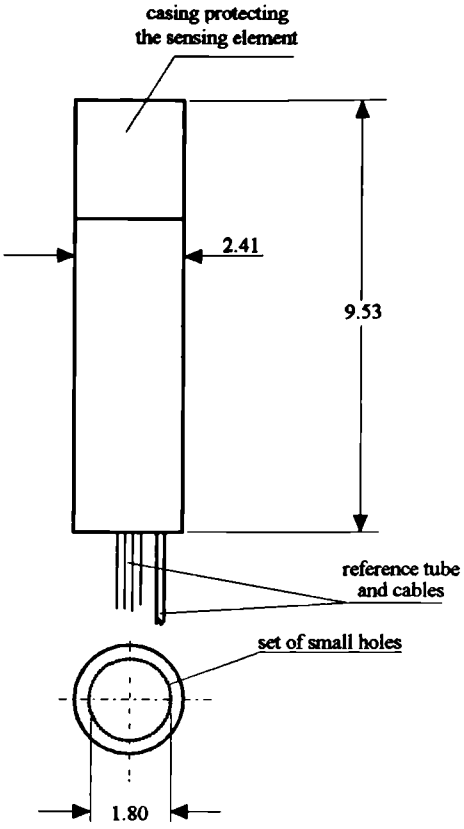

Figure 3.7. General dimensions of pressure transsducer.

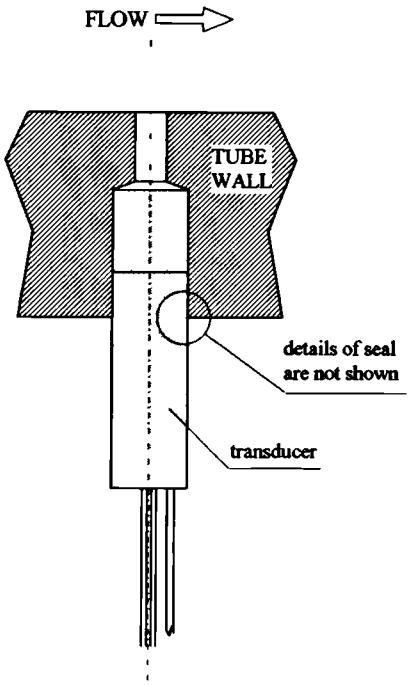

Figure 3.8. Flush mounted transducer.

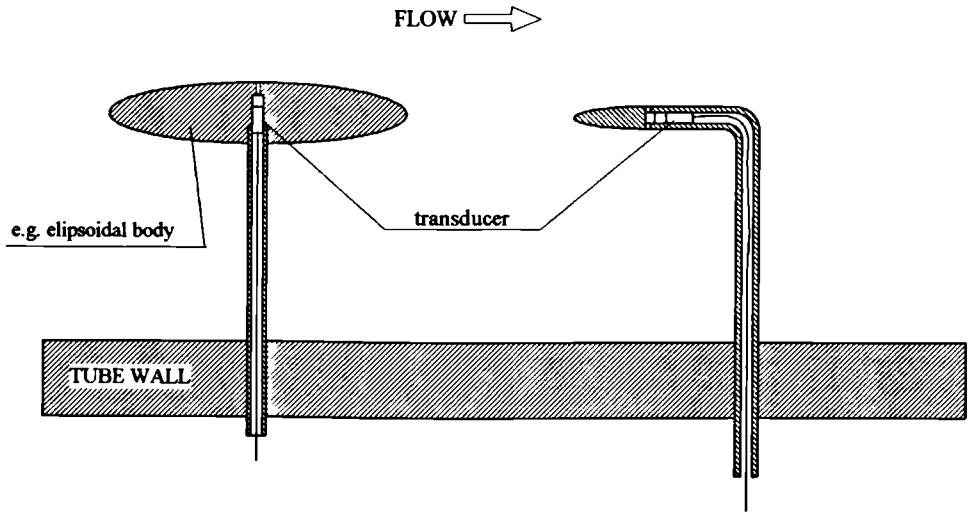

Figure 3.9.Two possible pressure probes incorporating transducers.

was increased in relation to Harvey's (1962) experiment - compare section 3.1. However, it soon became apparent (see *Signal and noise* in this section) that the fluctuations due to breakdown, which takes place around the tube's axis, do not propagate that far. Thus probes penetrating inside the vortex had to be designed.

Probe design

It is well known that the transducers will read the fluctuations in static pressure if mounted as, for example, in figure 3.8 (see Goldstein-1983). If the probe has to be introduced into the flow it should either take the form of a streamlined body or resemble a static tube (figure 3.9). The first solution was tested initially, but it significantly disturbed the flow (in the most severe cases the breakdown was deflected from its original position). The second solution is difficult to apply within the swirling flow because the probe's angle must be changed for each location during traversing, which itself is quite elaborate.

Hence, a more practical approach had to be taken for the probe design. The probe (figure 3.10) consisted of a stainless steel tube (20-30 cm long), through which the transducer was pushed first. Then the brass 'cap' was fixed to the transducer by means of silicon rubber, which served also as a seal. Finally the cap, with the transducer, was fixed to the steel tube by means of either a strip of PVC tape or a sleeve of soft rubber[1]. The orientation of the probe relative to the flow is given in figure 3.10 by an arrow in the left upper corner.

This probe design has the advantage of the least possible flow disturbance, and the probe readings are insensitive to the swirl. The apparent shortcoming was that the fluctuating pressure read was neither purely static nor dynamic (rather a kind of 'mixture'). This however was not so vital from the viewpoint of *frequency* of pressure fluctuations, which was one of the major concerns during the present investigations.

[1] The gap between the transducer and the 'cap' in figure 3.10 is very much exaggerated, in order to show the silicon seal.

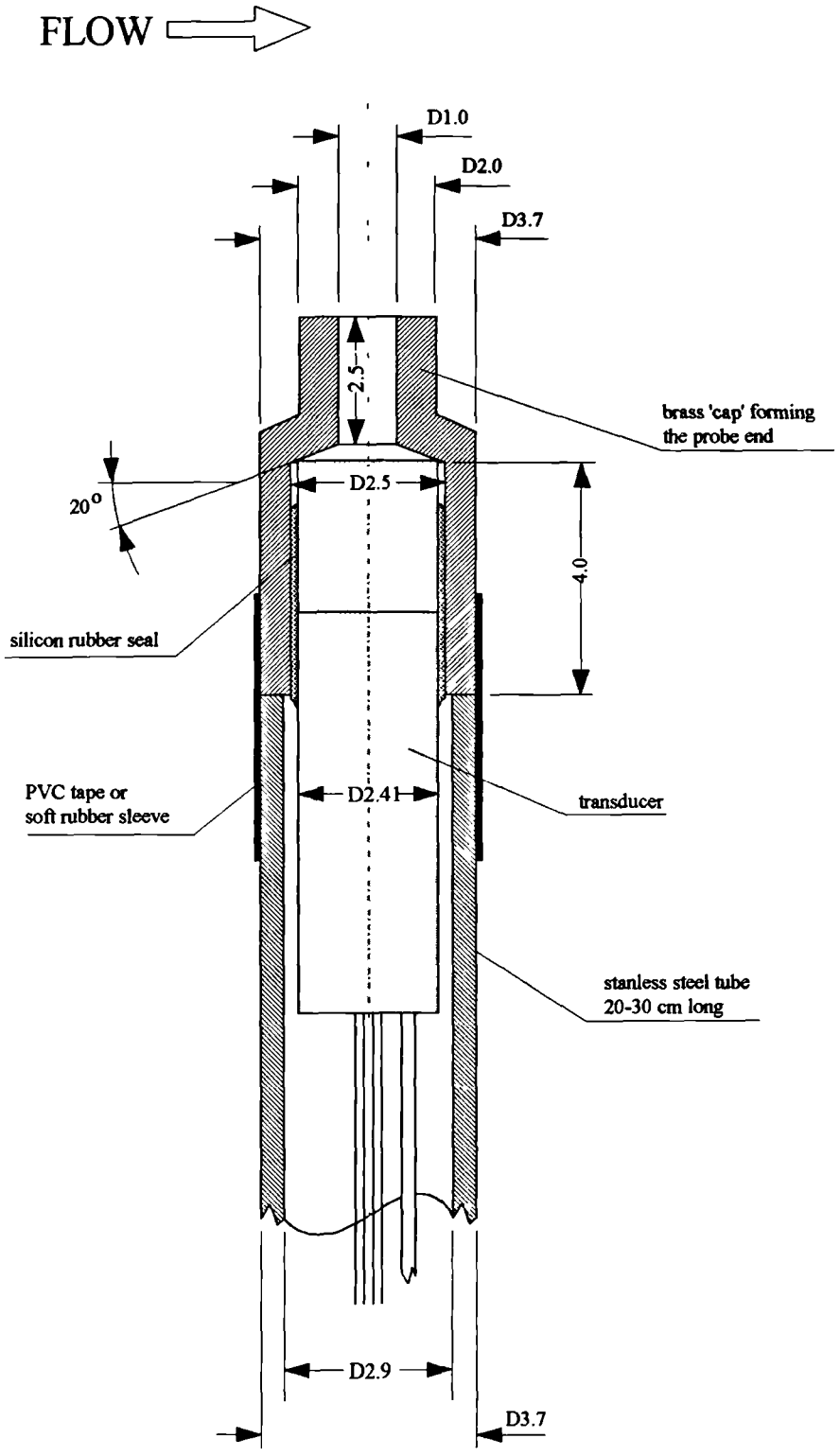

3.10. The design of pressure transducer probe for present research.

For the vortex tube measurements the reference tubes of the transducers were connected to thin plastic tubing, about 30 cm long, going through the probe. The loose end was exposed to ambient pressure. For the wind tunnel experiments it was found impractical to expose the reference tubes to the ambient pressure. Instead, since only the fluctuating component of pressure was measured, the loose ends of plastic tubing were 'jammed' with Araldite glue and pushed back inside the steel tube that forms the probe. Then the transducers operated effectively in an *absolute* and not a *differential* mode.

Signal conditioning and calibration procedures

The pressure transducers described were used together with an 8-channel signal conditioning system, shown schematically in figure 3.11. Both the signal conditioning system and pressure transducers were subject to extensive calibration procedures. Their description and sample results are given in Appendix A. The following conclusions were drawn:

- the frequency and phase characteristics of the bridge/amplifier units were 'flat'.
- the static characteristics of the transducers were linear.
- the dynamic calibration of the transducers indicated 'flat' frequency response (regardless of the way they were mounted - see Appendix A for details) in the range of interest, i.e. 0-1000 Hz.
- the phase shift between the output signals from the transducers was negligible.

Signal and noise

The ideal operating range of the transducers for this project would be 1 PSI or less, considering the speeds (or dynamic head) used in the experiments. Such transducers were not available, mainly for financial reasons. Using transducers of higher pressure range usually introduces higher noise to signal ratio. This might have had severe adverse effects, for example, on boundary layer measurements.

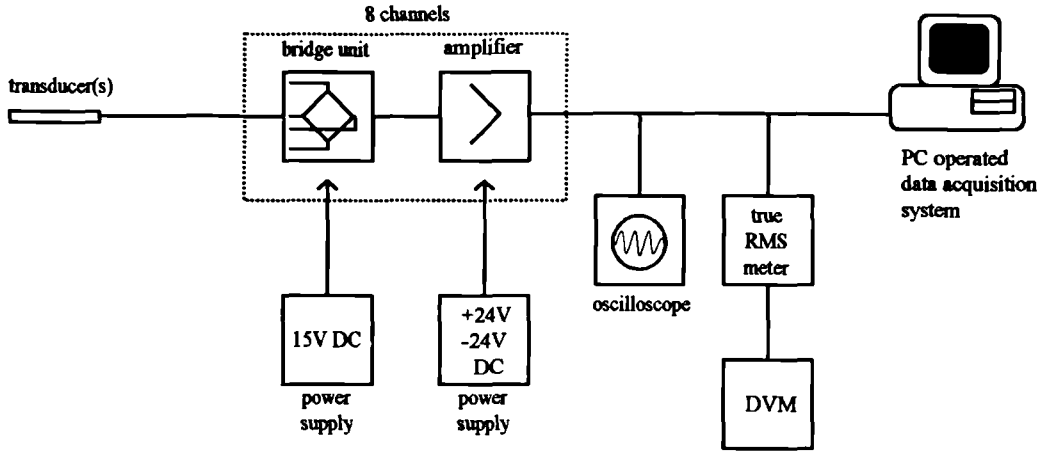

Figure 3.11.Signal conditioning system.

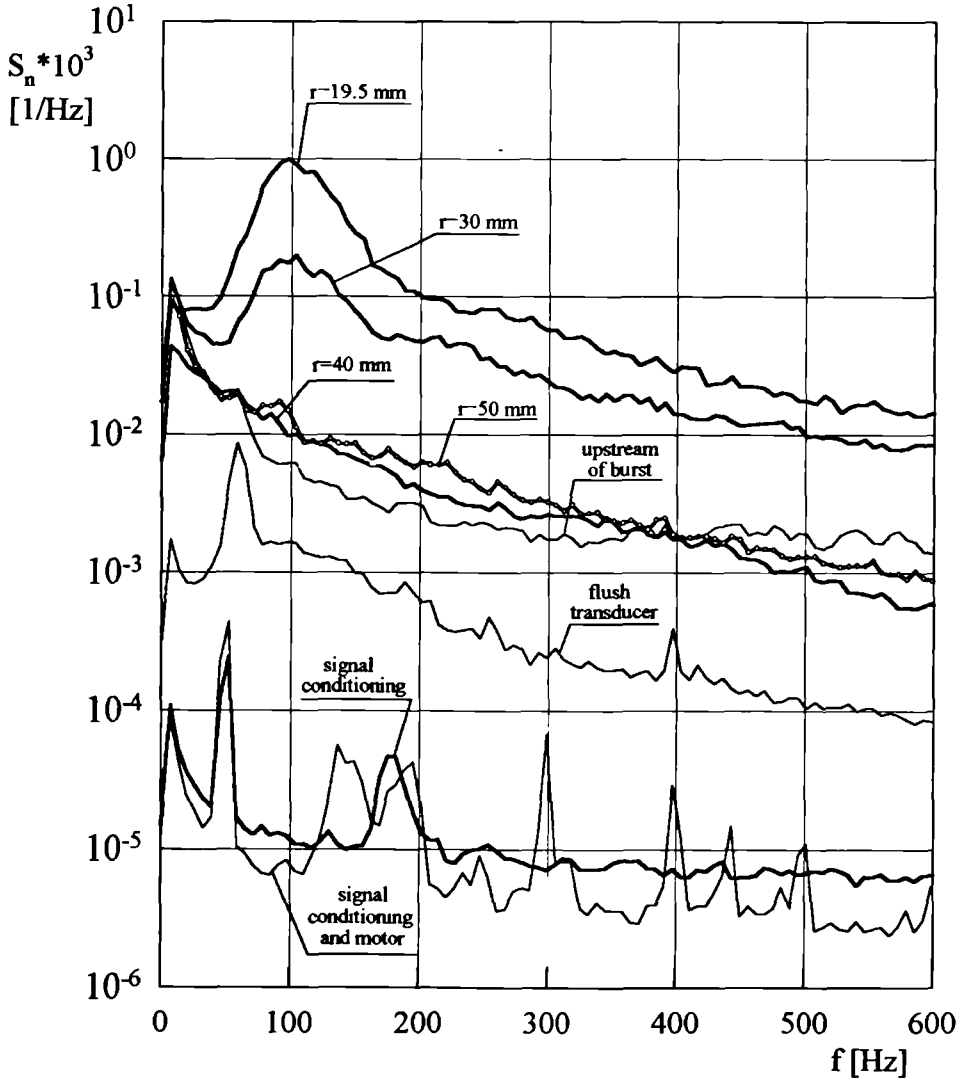

Figure 3.12.An example of noise and signal level analysis.

Directly after subsection "**Signal and noise**" *(which begins on page 123 and ends on page 125 - just before section 3.3.2) an additional subsection* "**Repeatability of measurements**" *follows. It contains an additional figure* 3.12A.

Repeatability of measurements

The repeatability of spectral mapping in the vortex tube depends on several factors. Careful calibration procedures (such as ones described in appendix A) are, of course, essential. However there are at least two additional sources of potentially poor repeatability.

One of them is the already mentioned scatter in the flow rate through the rig (± 2%). This may not have significant effects, for example, on determining the dominant frequency (which scales with velocity - and thus the error would also be of order of ± 2%). However, the scatter in the amplitude of pressure spectra, which may be regarded as proportional to the fourth power of velocity,could reach about 8%.

Another possible source of difficulties in achieving good repeatability are the changes in the mean position of the burst. The visual observations suggest that at relatively large flow rates (e.g. at full rig's capacity) the burst position oscillates about the mean position that is stable. The low speed experiments (such as the one described in section 4.1.4) show that the mean position of the burst tends to appear at different streamwise locations (but within say 10 to 15 mm) for time intervals of order of 10 seconds. This is believed to be induced by non-controllable factors (such as drafts in the laboratory or temporary instability in rotational speed of the fan). This may cause changes in both the dominant frequency of the spectra and the radial location of the sharpest spectrum.

Figure 3.12A is an example of good repeatability at high flow rates. Here two radial traverses were investigated in the time interval of several months. The conventions adopted in the graphs are explained later in Chapter 4. Both the dominant frequency and the characteristic radius, for which the highest excitation is present, remained practically unchanged. However the change in the spectral amplitude of about 10% is apparent. Another 'extreme' example is figure 4.40, in the next chapter, corresponding to a relatively low flow rate. Here the repeatability is poor, although the measurements are repeated on the same day. This is believed to be a consequence of the second of the effects described above.

Fortunately, the RMS level of pressure fluctuations due to breakdown is relatively high (in the order of 0.6 of the dynamic head). This gave a 'comfortable' noise to signal ratio, despite the high operating range of the transducers. Figure 3.12 shows one example of the spectra obtained in different situations and locations in the vortex tube, which are useful for noise and signal considerations. The upper six curves were obtained from measurements in the wake of the burst - namely for the medium choke, higher flow rate and x=80 mm (four thicker curves) - compare also figure 4.14 in the next chapter, and figure 4.1 for co-ordinate description. The curve 'r=19.5 mm' corresponds to the radial position of the probe at which the highest pressure fluctuations, with a peak at about 100 Hz, occur. The curve 'r=30 mm' still indicates the peak, however of lower magnitude. For 'r=40 mm' and 'r=50 mm' the peak is no longer visible and the level and the shape of spectra has a similar character to that upstream of the burst. The curve 'flush transducer' shows the spectrum obtained from the flush mounted transducer at x=200 mm. The peak for f=60 Hz was identified as a standing pressure wave due to the fan operation.

The curve 'signal conditioning' indicates the level of the noise coming from all the electronic devices used and the electromagnetic field present in the laboratory (with the motor switched off). Finally the curve 'signal conditioning and motor' corresponds to the no-flow conditions, but with the motor running (the two parts of the test section were not facing each other).

Similar analyses were made also for the wind tunnel test. They clearly indicated the transducers' functionality, despite their high operating range.

3.3.2. Velocity measurements

Velocity measurements played only a secondary role in the present investigation. Hence sophisticated methods giving detailed results, for example LDV techniques, were avoided. It is believed that 'conventional' methods, like two-dimensional mean-velocity measurements, using 3-tube pressure probe and thermal

November 1994

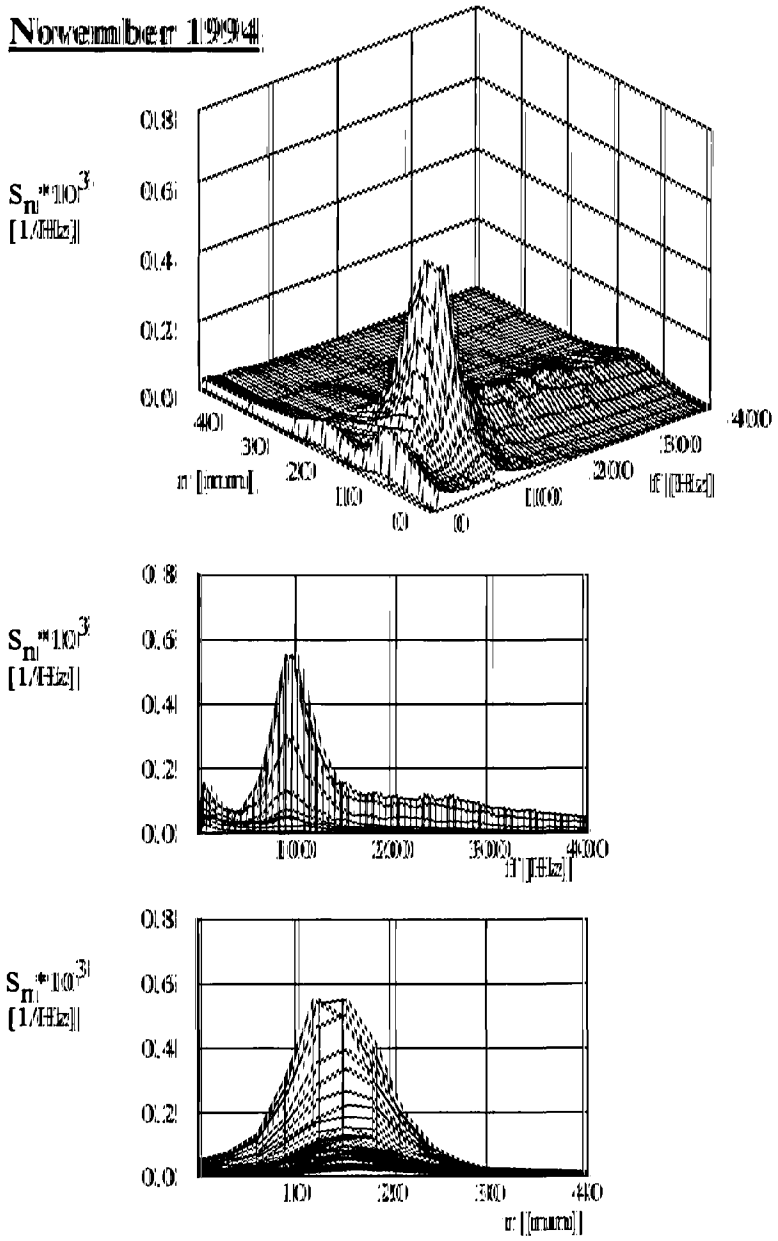

May 1995

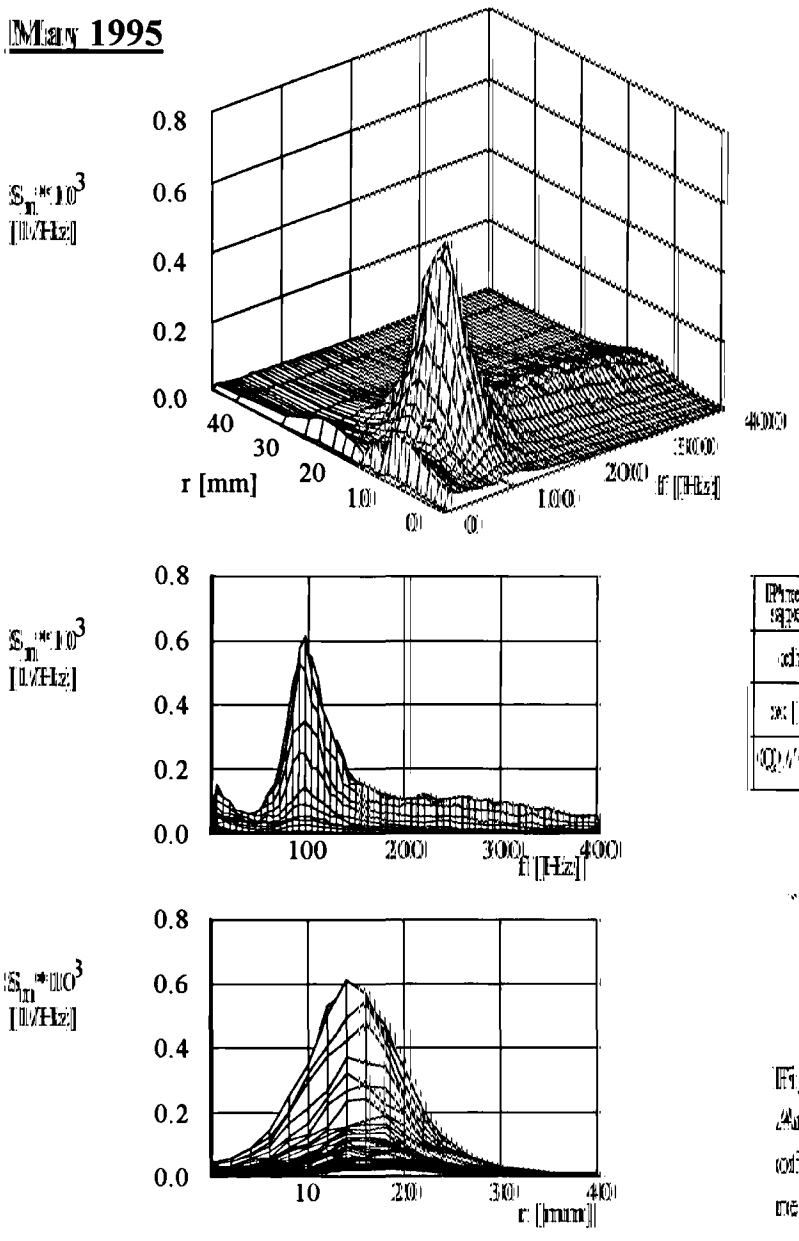

Press/Well spectra	P
diodes	L
x [mm]	1000
Q_i/Q_{max}	1.0

Figure 3.112.A. An example of measurements' repeatability tests

anemometry (hot-wire measurements), are sufficient to indicate the flow behaviour.

Initial measurements of the swirl and the axial velocity profiles in the vortex tube were conducted with the probe shown in figure 3.13. In general this kind of probe should have 5 ports (as described in Goldstein -1983), in order to measure the three components of the velocity. However, here the radial component of the velocity was assumed small compared to the swirl and axial velocities. Hence the 3-tube arrangement was used (Bryer and Pankhurst-1971). In principle, if the probe is aligned with the local direction of mean flow the pressure difference between the centre tube and each of the side tubes is the same. In addition this difference is related to the dynamic head, the relation being established by the calibration against an ordinary Pitot-static tube (see an example in Appendix A).

The probe was introduced into the flow through one of the probe ports described earlier. Its inclination at which the two pressures are balanced (and which also corresponds to the local helix angle) was established by an external protractor-pointer arrangement with the level gauge. Having obtained the velocity (vector length and its direction) the axial and the swirl velocities were calculated by simple decomposition. The method described has two drawbacks:

1) The measurements upstream of the breakdown cause the bubble to cling to the probe tip (a common feature of the probe-measurements of breakdown). The remedy was a slight reduction of swirl (0.5 to 1.0° in setting the guide vanes' angle). Hence it should be remembered that the swirl velocity profiles belong to the same *family*, but do not correspond *exactly* to the pre-breakdown conditions.
2) For the region downstream of the stagnation point (i.e. of reversed flow and the following region of vigorous turbulence, but with small mean values of the velocity) the probe becomes insensitive. Hence there are missing parts in the velocity profiles for small radii.

The objectives of the hot-wire measurements were twofold. The immediate one was a crude check as to whether the pressure spectra obtained have their equivalent (as far as the characteristic frequency and the general 'shape' are

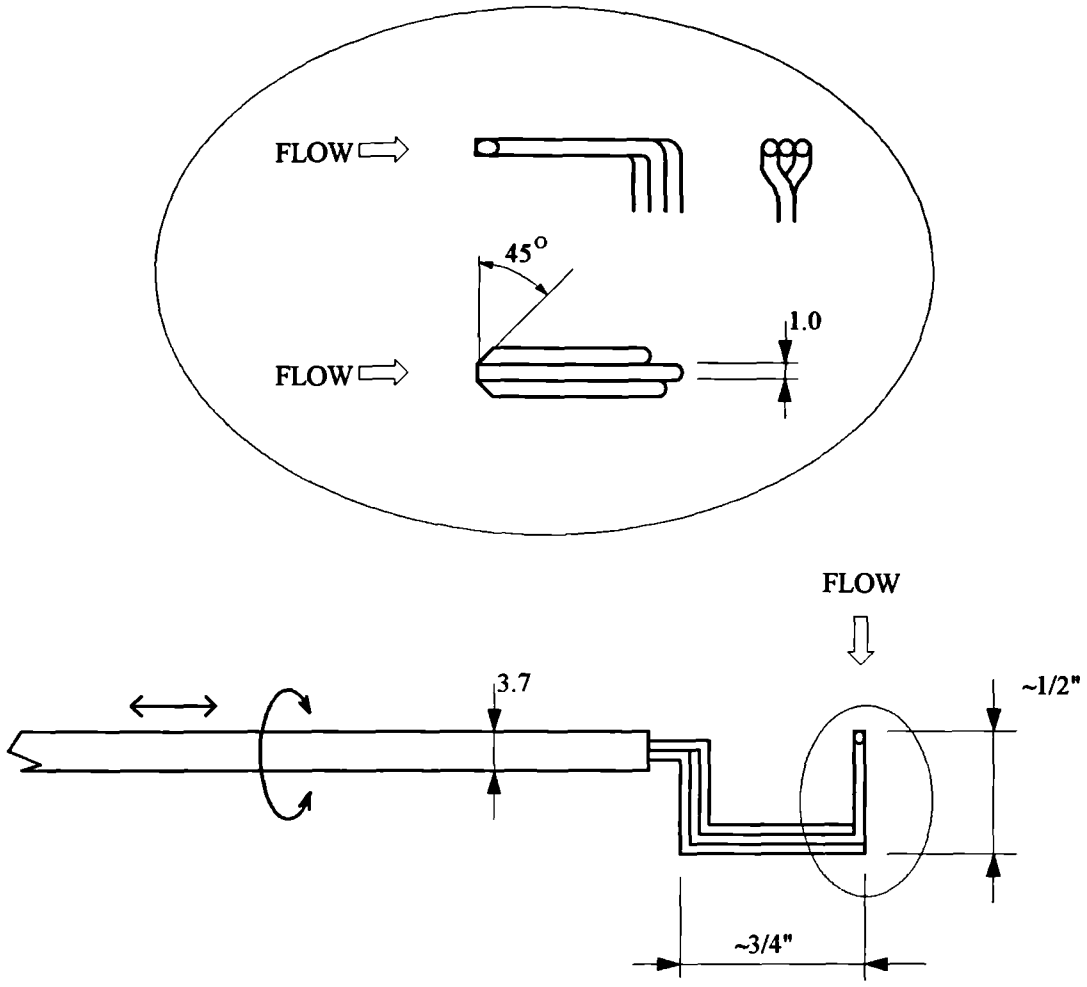

Figure 3.13.Three-tube pressure probe.

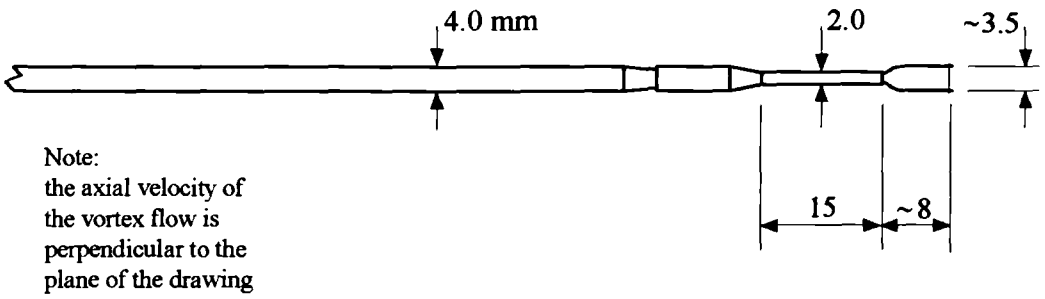

Figure 3.14.Hot-wire probe arrangement.

concerned) in the spectra of velocity fluctuations. The second one was to estimate the axial velocity profiles. This was crucial for the delta wing experiment, since the minimum in the axial velocity profile indicated the position of the vortex axis.

The hot-wire measurements were conducted by means of miniature *Dantec* single wire probes, fixed in a stainless steel tube of 4 mm external diameter (figure 3.14). The probes were introduced into the flow by means of the ports shown in figure 3.2 (vortex tube) or the arrangement from figure 3.6 (delta wing). A two-channel *PSI* thermal anemometer was used for signal conditioning (with both signal offset and amplification possible). The signal was digitised by the same A/D converter as for the transducer measurements.

The hot-wires were calibrated in the free stream flow against a Pitot-static tube which was connected either to an electrical multi-manometer (vortex tube) or a Betz manometer (wind tunnel). For the vortex tube the original intake was replaced by a short contraction (with ratio 9:1) attached directly to the shorter part of the test section with the longer part removed. This gave the nearly uniform axial flow required for calibration. The calibration data was approximated by King's law using a least square fit[2]. These non-linear characteristics were utilised later during the data processing (for both the mean and the fluctuating components of the velocity).

The following comments should be made on the accuracy of the hot-wire measurements:

1) The spectra of velocity fluctuations obtained with the single hot wire do not correspond to any particular fluctuating component of the velocity, but rather to the 'mixed' contributions from all of them. Despite this, the results were still valuable for comparing the pressure and velocity fluctuations.
2) The measurements just behind the burst, in the region of vigorous turbulence, are generally not valid (because of flow reversals, turbulence level higher than 20%, etc.). However they are still useful from the point of view of *frequency* and

[2] The maximum velocity obtained during calibration was about 14 m/s. Hence the calibration charts have to be extrapolated up to about 28 m/s (for the readings in the 'jet' of axial velocity)

location of the velocity fluctuations.

3) The mean axial velocity[3] upstream of the burst is reproduced well by the hot-wire measurements. This is supported by, and agrees well with the pressure probe measurements. Downstream of the burst, however, the mean axial velocity near the centre of the vortex, measured by the hot-wire, is higher than that measured by the pressure probe (which itself becomes insensitive). This apparent higher velocity is believed to be due to the high turbulence level. However the velocity profile still exhibited a minimum, which was associated with the vortex axis for the delta wing.

3.3.3. Data acquisition and processing

The analog signal from the 'Fylde' amplifier (for transducer measurements) or the PSI thermal anemometer (for hot-wire measurements) was digitised by means of a PC based 8-channel A/D converter (ACP1 made by Signalysys Ltd.). The full details of the A/D converter are given in the user's manual (Signalysys-1991). The maximum A/D input voltage was ± 5V. The signal conversion was performed with 16 bit resolution. The maximum sampling rate was 100 kHz per channel. The built-in DRAM could store up to 524000 samples per channel of continuous measurement. This corresponds to 78.6 seconds at a sampling rate of 6667 Hz. For spectral mapping, the lowest sampling frequency available was used (i.e. 6667 Hz)[4]. For correlations, sampling rates of 10, 25, 33 or 50 kHz were used (depending on the flow velocity). The usual length of the acquired data sets was 131,072 samples.

The data was processed using the standard Fast Fourier Transform (FFT) and correlation techniques as described by Press *et al.* (1992). The spectra were obtained

[3] The axial velocity was obtained from the hot-wire by assuming that the 'cosine law' holds (the helix angle is lower than 60°). Then the swirl velocity, which is parallel to the sensing element, is not contributing to the probe reading.

[4] From the viewpoint of the Nyquist critical frequency the sampling rate of 2 kHz would be sufficient. However this higher rate made no harm, apart from the data occupying larger disk space.

by the data windowing technique with overlapping segments. The method consisted of calculating the spectra of short fragments of a given data set (here, from 512 to 4096 samples; the data set usually of 131,072 samples) and their averaging. The window width was chosen according to the sampling rate and flow velocity in order to obtain detailed but smooth spectra (this had to involve a subjective judgement). The correlations were computed also by using the FFT as follows: the two data sets were transformed by FFT, one resulting transform was multiplied by the complex conjugate of the other, the result was transformed using the inverse FFT giving the required correlation function.

The software was tested not only by using dummy data sets (for which the results of the FFT or correlation were known) but also by conducting wind tunnel measurements in the wake of a circular cylinder, and within a boundary layer. These measurements are given in appendix B.

3.3.4. Light sheet techniques

To understand the flow physics, smoke traces were recorded either on VHS tape or as still photographs. For the vortex tube experiment a laser light sheet technique was used. A beam from a 4 W, continuous operation, green light laser was split by an arrangement of lenses to form a light sheet approximately 0.5-1.0 mm thick[5]. This sheet was then adjusted so that it illuminated the meridional 'cross-section' of the vortex breakdown. For wind tunnel tests the laser light sheet was replaced by a sheet produced by a restricted and concentrated beam from a slide projector. In addition the breakdown was filmed and photographed using conventional illumination (spotlights and/or flash light).

[5] To meet laser safety requirements the vortex tube was enclosed in a room built of wooden timbers and hardboard. One of the walls was adjacent to the air intake from the side of the test section. This did not seem to have any noticeable effect on the breakdown (this side of intake corresponds to the flow near the wall of the test section)

CHAPTER 4

RESULTS

Before the detailed results are presented , it is worthwhile making some brief general remarks on the conventions adopted. The frame of reference for the vortex tube experiment is sketched in figure 4.1. Here the streamwise co-ordinate x has an origin in the narrowest place of the choke (i.e. the nominal position of the burst's stagnation point). The radial position r is measured from the vortex axis. If the probe is going 'through' the vortex (i.e. passing the vortex axis) the corresponding radial co-ordinate is denoted as negative (although physically this has no meaning).

For the wing experiments the angle of attack is chosen so that the burst takes place in certain streamwise locations (say 0.25, 0.5 or 0.75 of the root chord). Thus the streamwise location of the probe is given as a fraction of the root chord (x/c). The location of the vortex axis (found from hot-wire measurements) is characterised by a spanwise co-ordinate (y/s) and a co-ordinate perpendicular to wing's surface (z/s). However the measurements obtained by traversing the probe across the vortex are related to the radial displacement from the vortex axis r.

For studies of buffet, that is the aerodynamic excitation provided by separated flows, it is recommended (Mabey-1989) that the spectra should be presented as a square root of a product of spectral density and frequency vs.

frequency[1] (AGARD notation), i.e. $(f S_n)^{0.5}$ vs. f. This, however, proved impractical in the current investigation for reasons shown most explicitly in figure 4.2. Here the spectra corresponding to three measurements (left column) were transformed into AGARD notation (right column). In the upper graph (a measurement in the wake of a circular cylinder - described in more detail in appendix B) the sharp peak in the spectrum is visible in both co-ordinates. Of course, strictly the AGARD notation - which is for continuous spectra - should not be applied to spectra with discrete frequencies. The middle and lower graphs (measurements within the vortex breakdown region[2]) show how such a transformation can 'spoil' the insight into the phenomenon (for example, if one was looking for the characteristic frequency). Figure 4.2b shows the well-pronounced excitation spectrum which preserves the spike after transformation to the AGARD notation. Figure 4.2c is an example of a weaker peak, whose identity is lost after the transformation. Thus the spectral density S_n was found more instructive for presenting the data. It is important to point out that the

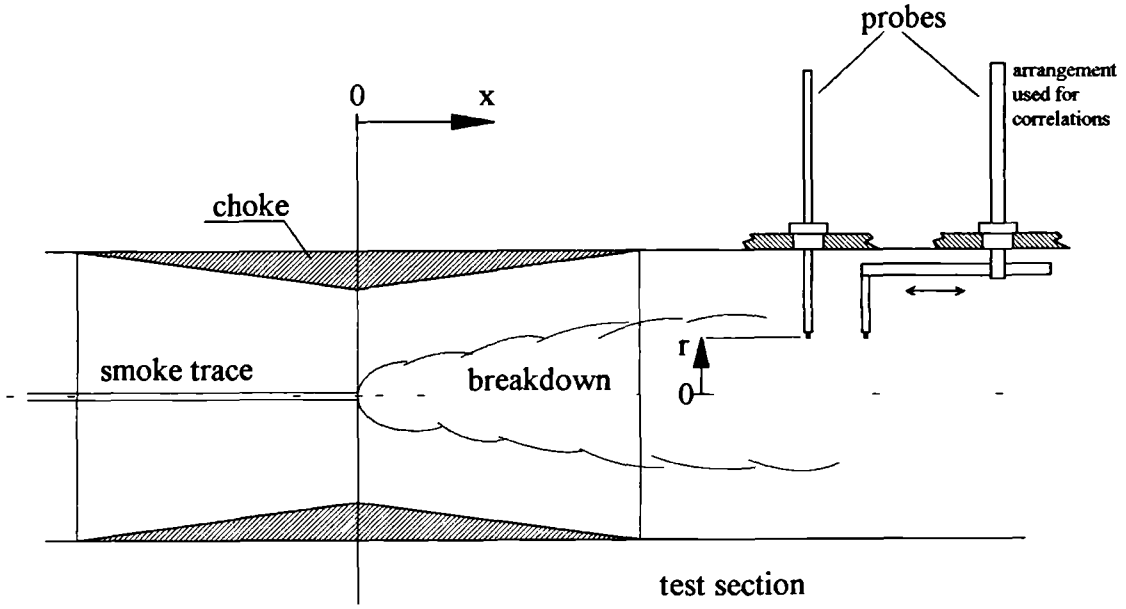

Figure 4.1.The frame of reference used for the vortex tube experiments.

[1] The frequency is often replaced by appropriate frequency parameter n=fL/U, where f, L and U are the frequency, reference length and velocity, respectively.

[2] The middle graph corresponds to a single "slice" from figure 4.14 (r=19.5 mm). Similarly the lower graph is a "slice" from figure 4.12 (r=11 mm).

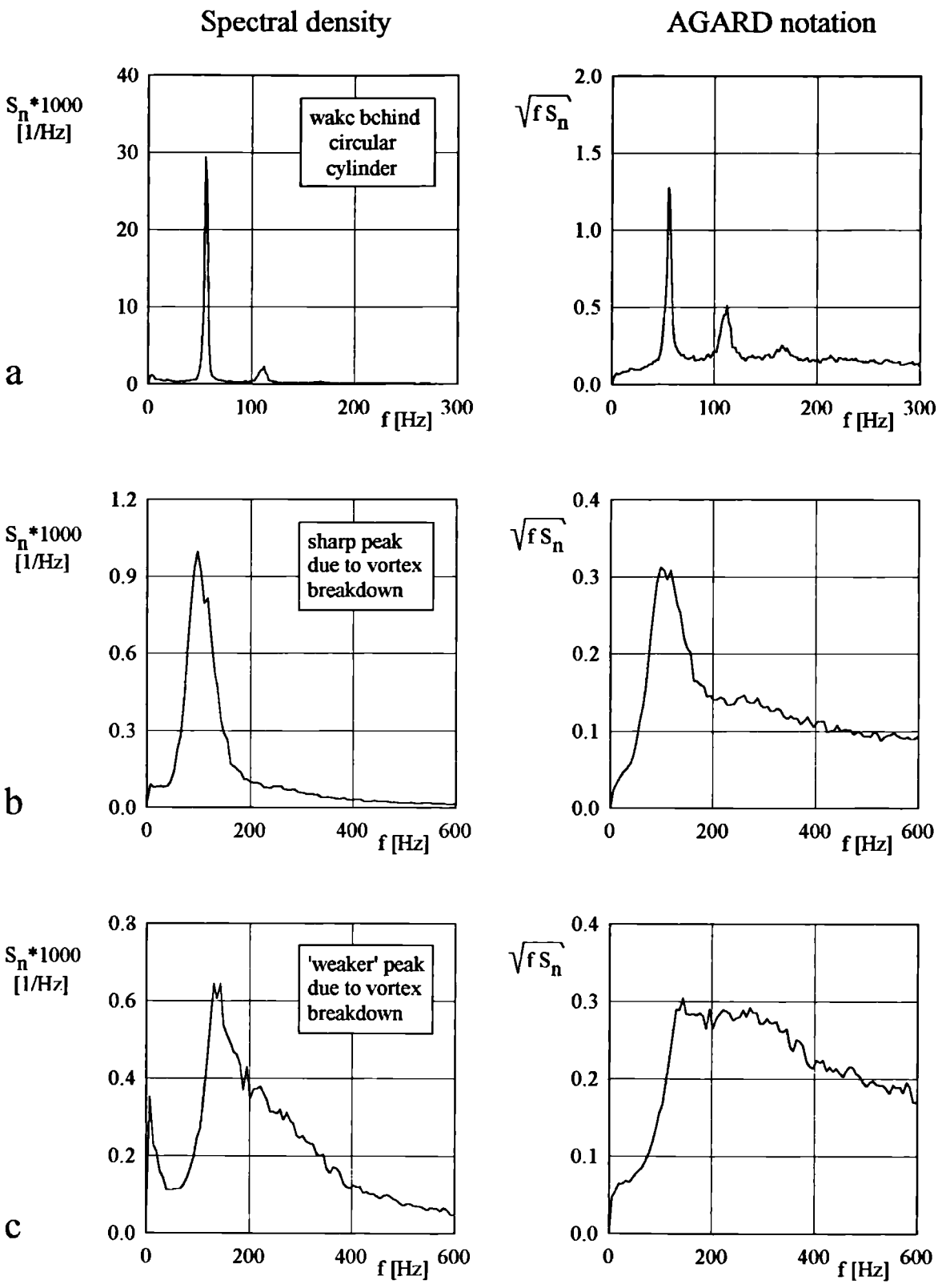

Figure 4.2.Comparison between spectral density and AGARD notation.

level of the latter two spectra in AGARD notation is about 0.3, representing a very high fluctuation level. Typically, at the reattachment point of the turbulent boundary layer the value of $(f S_n)^{0.5}$ is about 0.1 (Mabey-1989).

The major part of the research consisted of spectral mapping of the breakdown region (i.e. every point investigated is associated with a particular frequency spectrum - of either pressure or velocity). This leads to a vast amount of data, very often difficult to handle (altogether about 3000 spectra were obtained). Thus three dimensional "carpet" plots had to be used to show simultaneously the frequency spectra themselves, together with their spatial distribution (generally in radial direction) - see, for example, figures 4.8 through 4.19. In addition, to show the characteristic frequency and its spatial location more clearly, two projections of the "carpet" plot, on (f,S_n) and (r,S_n) planes, were given. Generally, the main text is comprised of as many spectra as is necessary to point out their basic features. Some other examples are also given in appendix C.

The spectra presented in this chapter are shown as functions of 'primitive' variables (i.e. frequency and radial distance from the vortex axis), for the following reasons:

- the reference length required for non-dimensionalisation is not straightforward (as, say, the diameter of a circular cylinder for vortex shedding) but changes from one streamwise location to another,

- the suggested reference length is appropriate for the spectra of "well-developed" fluctuations; so it is not sensible to apply it everywhere,

- it *is* interesting and instructive to trace how the spectra evolve from the viewpoint of frequency and core diameter *before* conclusions about the characteristic length scale are drawn.

The velocity effects on the characteristic frequencies are taken into account indirectly by selection of the co-ordinate's range. For example, in the vortex tube, where the ratio of two investigated flow rates is about 0.6, the frequency ranges are 0-360 Hz for the lower flow rate and 0-600 Hz for the higher. Thus the similarities in the spectra for a given arrangement - but of different speeds - can be made visible despite the lack of non-dimensionalisation. The amplitudes of the pressure spectra are made non-dimensional by dividing by the square of the dynamic pressure that corresponds to the free stream axial velocity in the narrowest cross-section of the chokes. For the velocity spectra the square of axial velocity was used. Thus the dimension of a spectral density is [1/Hz].

Each of the figures showing the spectra has a short legend on the right hand side (see, for example, figures 4.8 through 4.19) showing the physical quantity (P-pressure, V-velocity), kind of choke (L-long, M-medium, S-short), streamwise co-ordinate (x in millimetres), and the flow rate (Q/Q_{max} = 0.6 or 1.0). For the wind tunnel tests (see, for example, figures 4.46 through 4.54 and also figure 4.63) the legends show the quantity (also P or V), the kind of delta wing model (LM-large model, SM-small model), tunnel speed (U), angle of attack (α) , position of the burst as a fraction of the root cord (x_B/c), and the position of the cross-section investigated (x/c).

The results of space-time correlation (i.e. the correlation function vs. time lag present between the responses of two probes) are presented in such a manner that the maximum of the correlation function has a maximum for the negative time lag if the signal reaching the slave probe is *delayed* relative to the master probe. This, however, is only a matter of sign convention and if the results are properly interpreted it does not cause any particular problems. The best example is figure B.6 in appendix B, where the maxima in correlation functions shift to negative time lags as the slave probe moves further downstream from the master probe.

4.1. Vortex tube experiment

The results of a study of vortex breakdown inside the vortex tube are arranged in four subsections dealing with:the general properties of the vortices investigated (4.1.1), spectral mapping of fluctuating quantities (4.1.2), correlation analysis (4.1.3) and response of fluctuating flow field to small disturbances (4.1.4).

4.1.1. Size of the vortices

Figures 4.3 and 4.4 show the velocity profiles of vortices generated in the apparatus for the medium choke. Here the velocities were obtained by means of the 3-tube pressure probe. The axial velocities just before the burst (x=0 mm in figure 4.3) have typical jet-like profiles with an overshoot of about 1.7 - 1.9 times the free-stream velocity[3]. The two examples of the axial velocity profiles downstream of the burst (x=60 and 150 mm) exhibit wake-like profiles. The missing parts in the curves correspond to the probe becoming directionally insensitive (perhaps due to low velocities and vigorous turbulent mixing). Figure 4.4 shows the swirl velocity distributions for the corresponding situations[4]. Figure 4.5 shows the helix angle just before the burst for the two flow rates. Its maximum value is higher for the lower flow rate, which is a direct consequence of slightly increased circulation imparted to the flow. This was necessary to keep the burst inside the choke.

A comparison between axial velocity profiles obtained from the 3-tube probe and hot-wire measurements is shown in figure 4.6 (for the medium choke and higher flow rate). Manifestly, for both pre-burst and far-wake conditions the two techniques

[3] The free-stream velocity (W_0) corresponds to the flat parts of the profiles (and here was taken 16 and 9.5 m/s for two flow rates studied).
[4] As one can easily see, the maximum swirl velocity is 1.1 to 1.2 of axial velocity (in agreement with Squire's prediction).

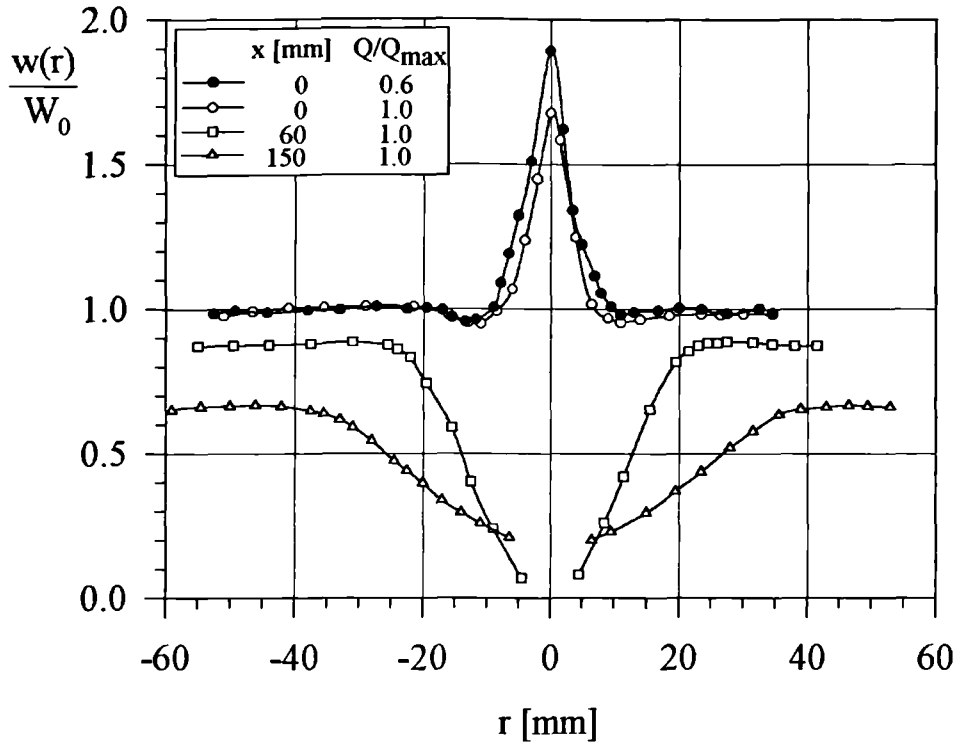

Figure 4.3. Typical axial velocity profiles generated in the vortex tube apparatus for the medium choke.

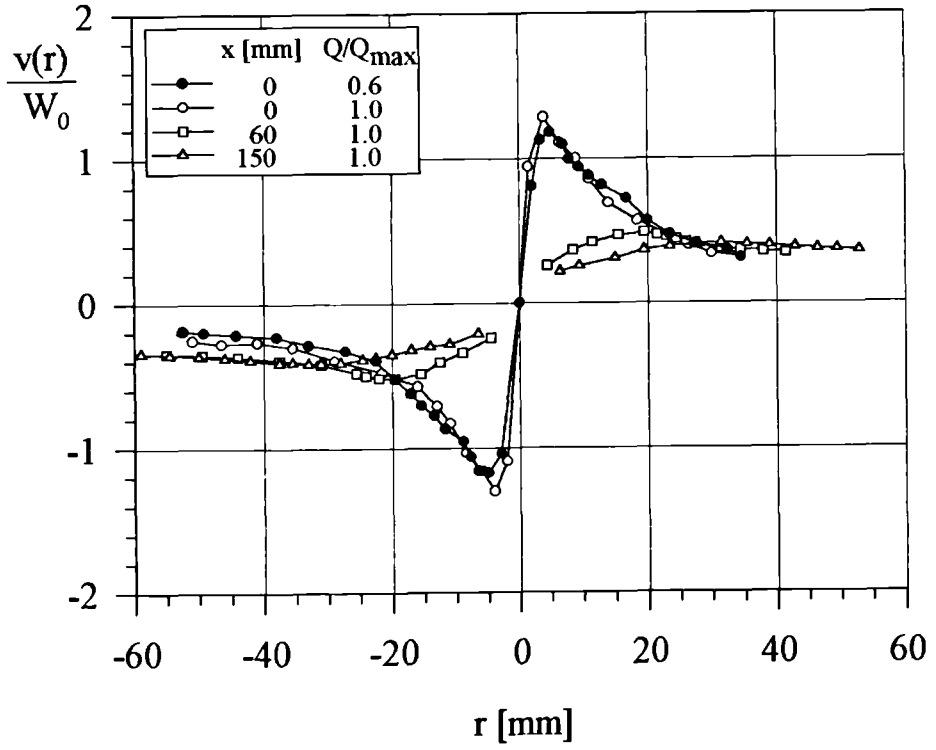

Figure 4.4. Typical swirl velocity profiles generated in the vortex tube apparatus for the medium choke.

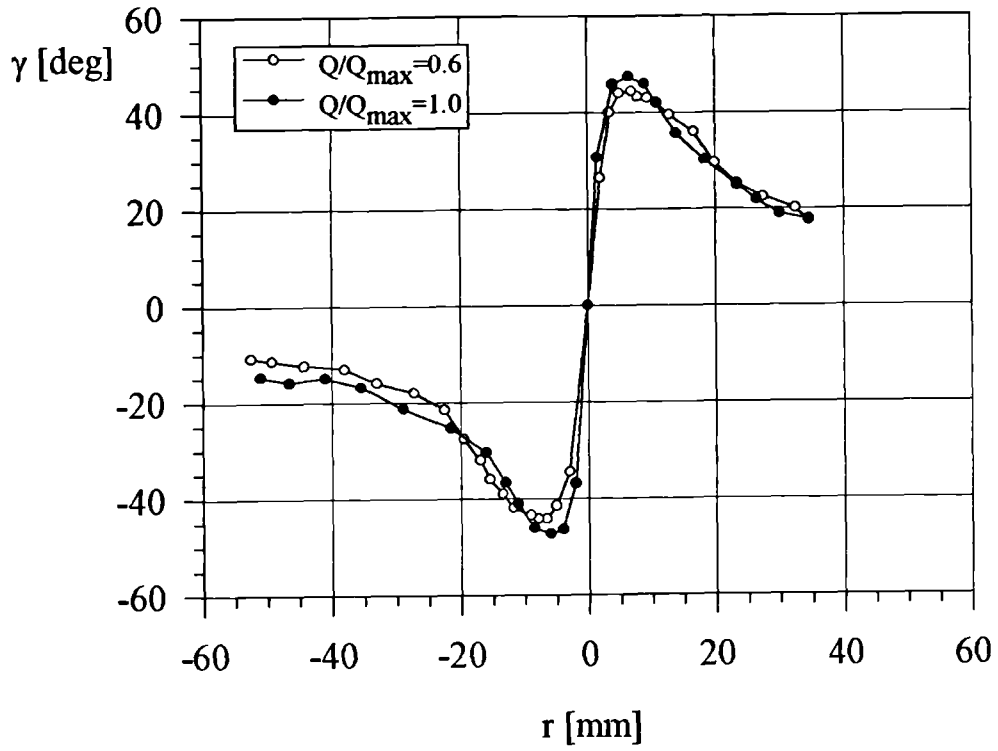

Figure 4.5.Helix angle just before the burst for two flow rates (medium choke).

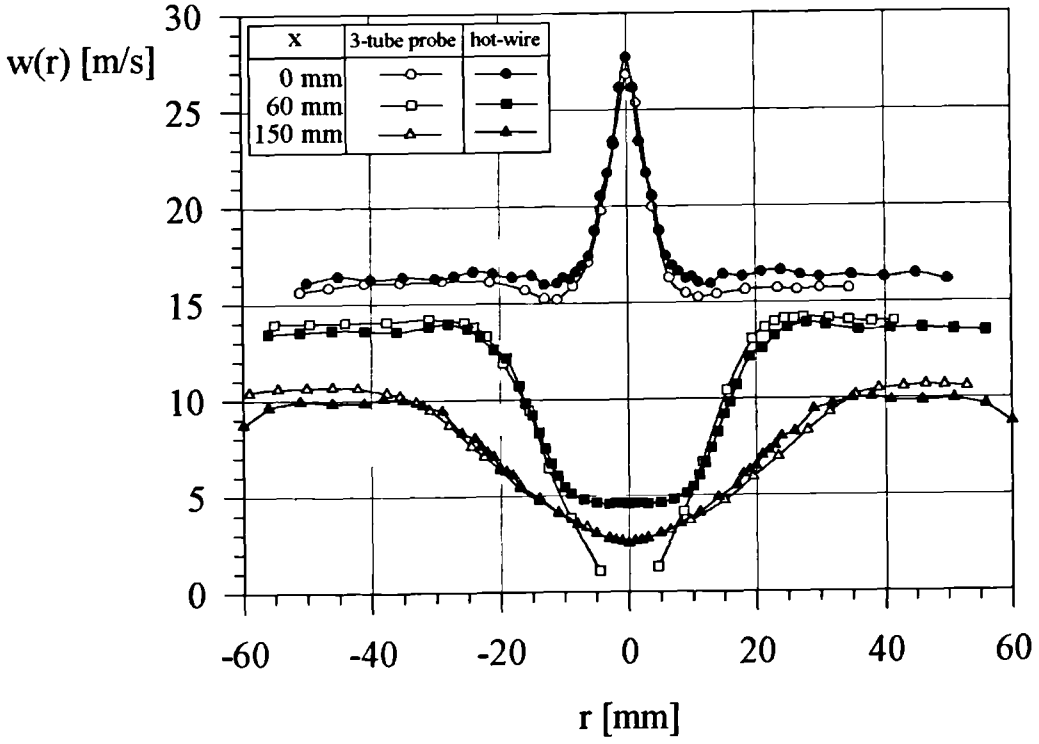

Figure 4.6.Comparison between measurements by 3-tube probe and hot-wire (medium choke).

give good agreement[5]. For the streamwise locations in the near-wake, serious discrepancies can be noticed close to the vortex axis. The main conclusion, however, is that the velocity profiles obtained from the hot-wire measurements (i.e. based on the assumption that the 'cosine law' holds) can be used to estimate both the free stream velocity and the size of the vortex core.

Figure 4.7 shows the axial velocity profiles prior to the burst and 80 mm downstream for three different choke shapes (for $Q/Q_{max}=1.0$). It is apparent that the vortex core grows more slowly for the longest choke than for medium and short chokes (for which the difference is less visible, but also present).

Generally, the vortices studied in the vortex tube experiment have core diameters of about 10 mm prior to the burst (for all chokes and both flow rates), whereas in the breakdown wake the core diameter can be changed, by applying chokes of different divergence angles, approximately by a factor of 2. The vortex dimensions for a given choke do not change significantly with the flow rate.

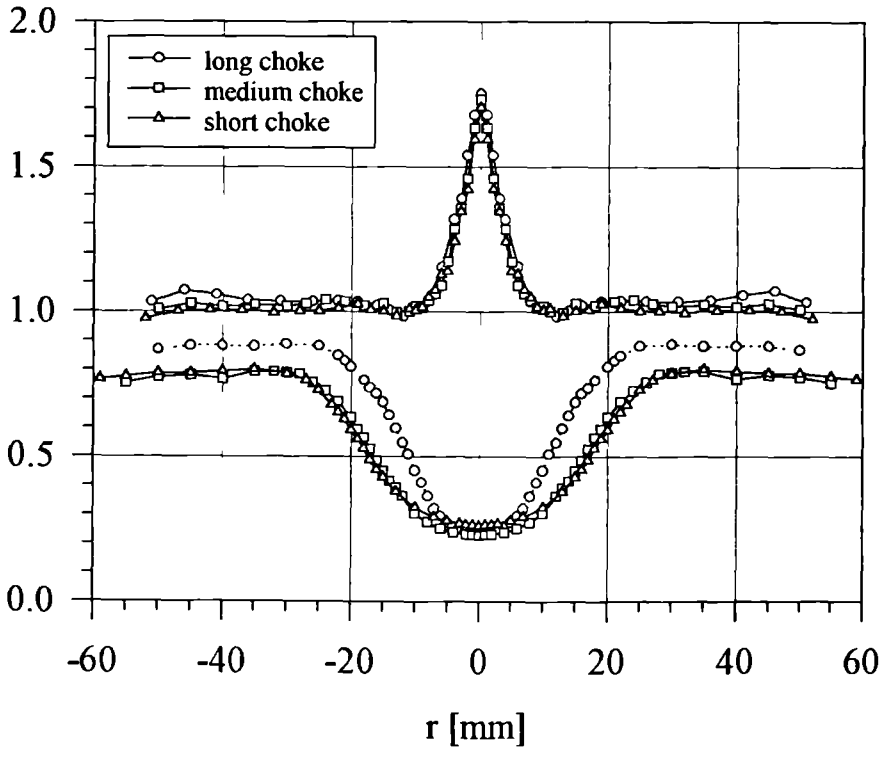

Figure 4.7. Vortex sizes prior to (x=0 mm) and after the burst (x=80 mm). Q/Q_{max}=1.0.

[5] The maximum differences between the velocities obtained from both methods are about 5%.

4.1.2. Spectral mapping of pressure and velocity fluctuations

The development of pressure spectra in the vortex breakdown region is shown briefly in figures 4.8 through 4.19. Each of the figures shows a set of pressure spectra for varying radial positions of the probe (carpet plots). The streamwise location changes from figure to figure and varies between $x=0$ and $x=650$ mm. The results presented are for the medium choke arrangement and for the higher flow rate. Some examples of the results for remaining experimental set-ups and flow rates are given in appendix C.

Figure 4.8 shows the pressure spectra for $x=0$ (i.e. the narrowest place of the choke and at the same time approximately the stagnation point of the burst). These conditions can be practically treated as pre-burst (the breakdown bubble was at worst attached to the probe for $r=0$, but never ahead). Here the dominant feature is a high level, low frequency, peak with the maximum for $r=5$ mm (i.e. corresponding roughly to the thickness of the vortex core before breakdown). This spectrum of the pronounced low frequency part corresponds supposedly to the instability of the streamwise position of the burst, as suggested, for example, on the measurements by Gursul (1995).

Figures 4.9 through 4.12 show the results for $x=10,17,30$ and 40 mm (see the legends for the streamwise location and other conditions), i.e. for an initial part of the bursting process, corresponding to the recirculation region. These and the following measurements can be thought of as 'piercing' the breakdown region with a probe to different depths (i.e. radial position). The shortest description of the spectra development is the appearance of a broad-band low-level 'hill' of high frequency, and its steady growth and shift to lower frequencies. The low frequency peak is at the same time loosing its strength. In figure 4.12 the sudden occurrence of a narrower peak (at about 130 Hz) can be observed for an increment in x of only 10 mm.

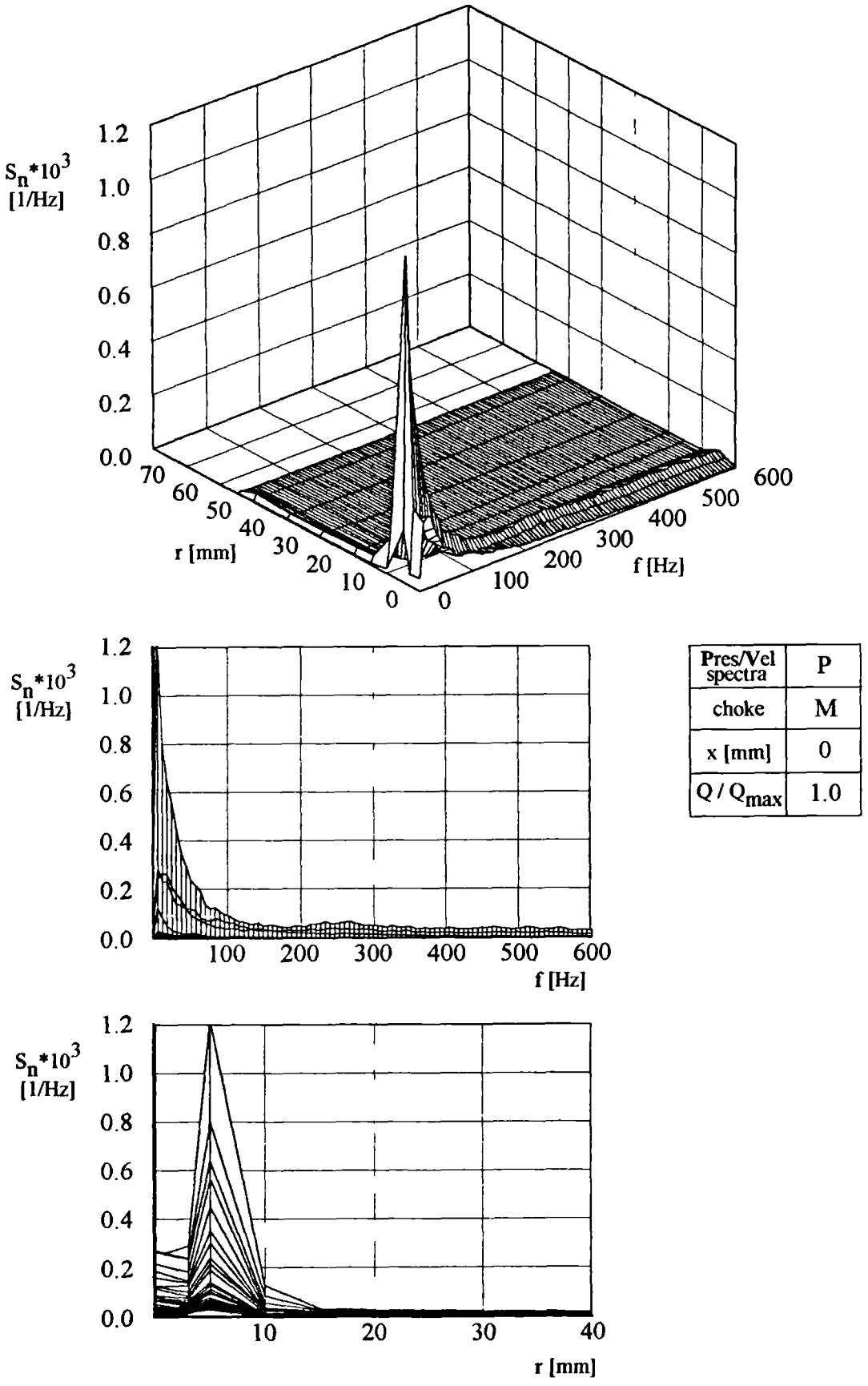

Figure 4.8.Pressure spectra (x=0 mm).

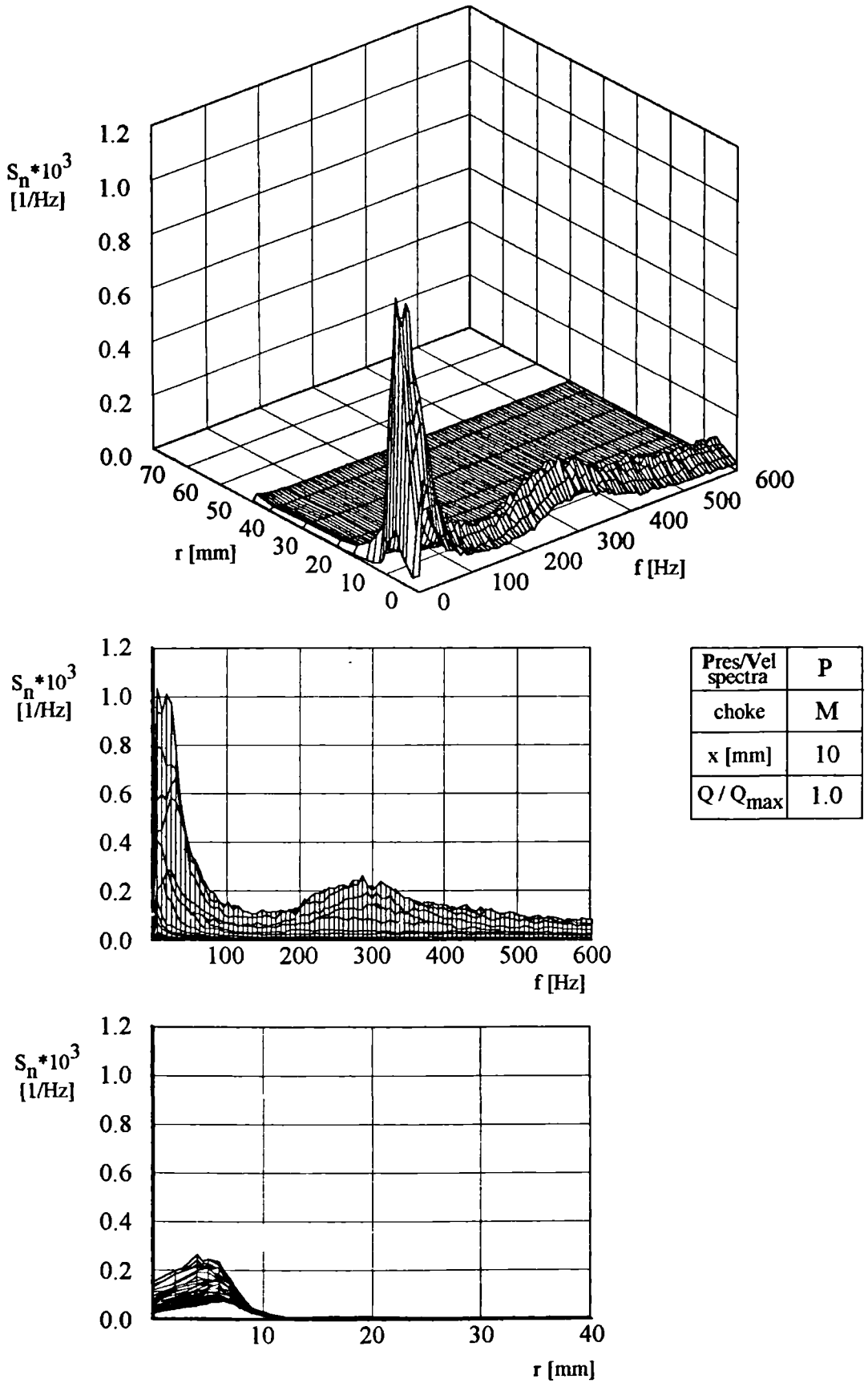

Figure 4.9.Pressure spectra (x=10 mm).

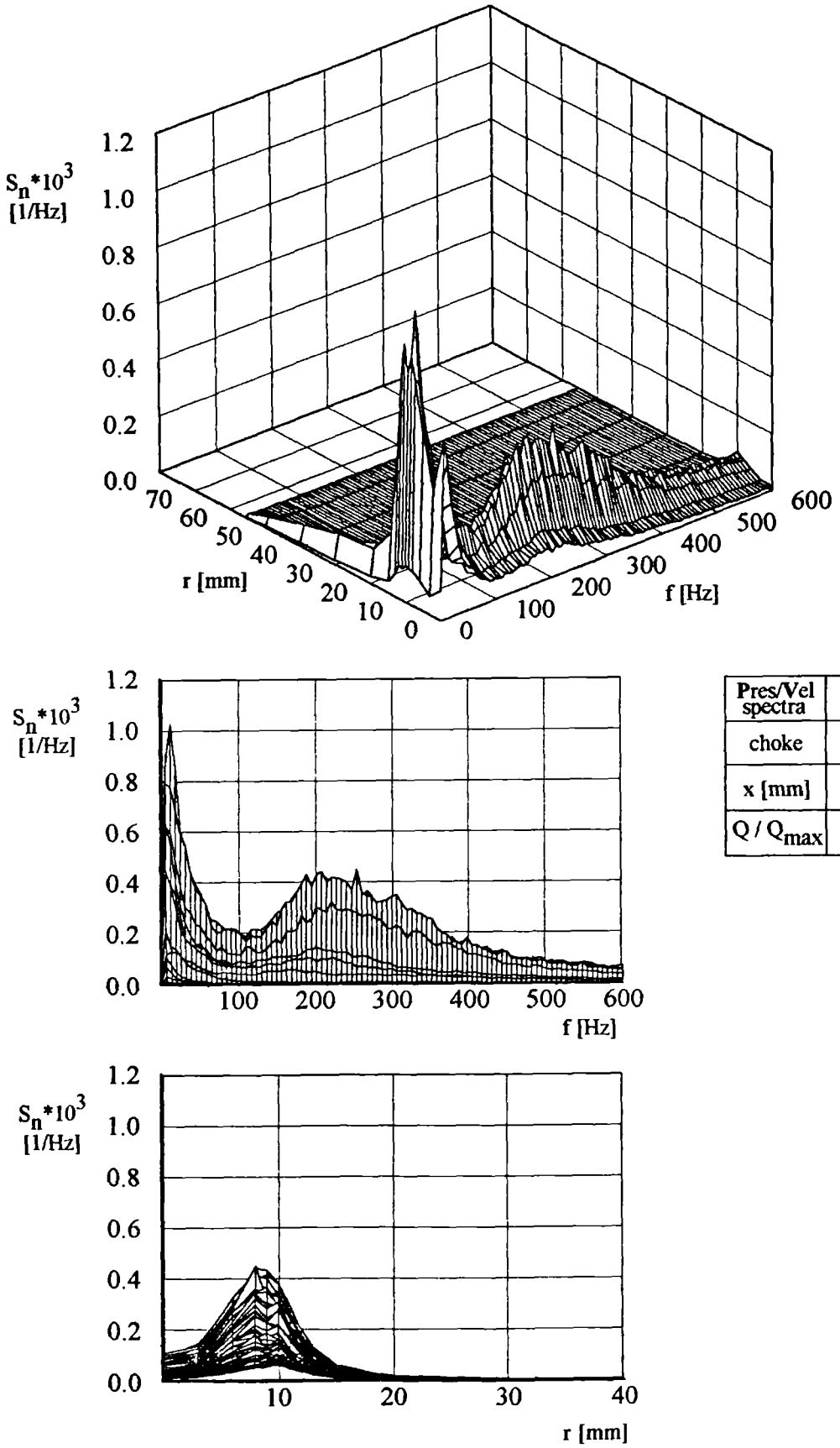

Figure 4.10.Pressure spectra (x=17 mm).

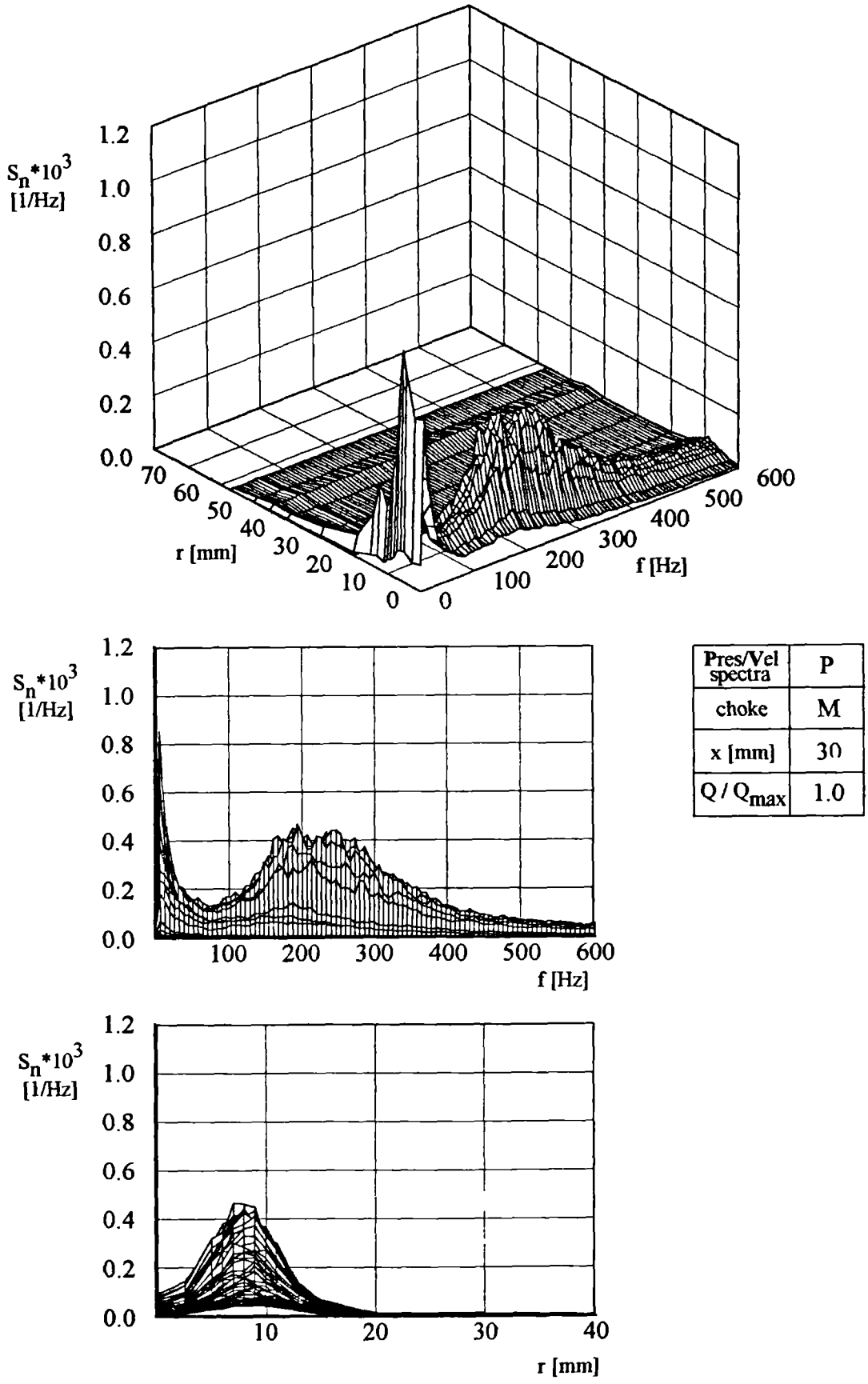

Pres/Vel spectra	P
choke	M
x [mm]	30
Q / Q_{max}	1.0

Figure 4.11.Pressure spectra (x=30 mm).

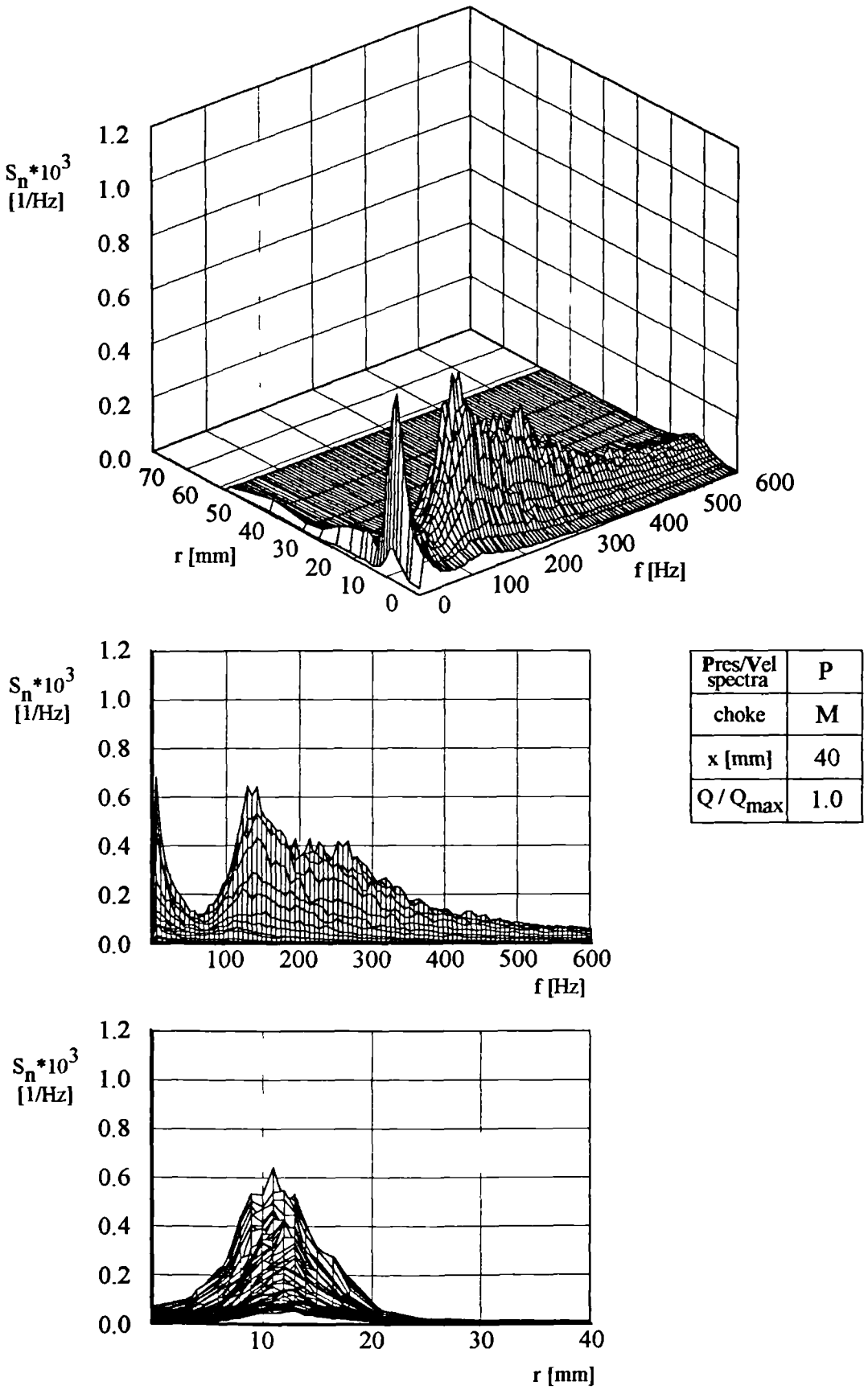

Figure 4.12.Pressure spectra (x=40 mm).

This narrow peak is more pronounced in figure 4.13 and finally becomes the dominating feature of the spectra (figure 4.14). Figure 4.14 (3-D view) shows most clearly the 'suddenness' of the quasi-periodic oscillations both in space and frequency. The well defined peak is maintained through figures 4.15, 4.16 and 4.17. However its strength is lost and the spatial location 'smeared' well downstream of the vortex burst and closer to the fan. Figures 4.18 and 4.19 show merely spectra due to a turbulent flow and noise due to the fan operation (the discrete frequency of about 60 Hz).

Every aspect of the pressure spectra described has its counterpart in the velocity spectra. Figures 4.20 through 4.26 show the spectra of velocity fluctuations which correspond to the pressure spectra in figures 4.9 through 4.15. The only noticeable difference between the velocity and pressure spectra is that the low frequency part of the latter is more persistent. Most importantly, however, the frequencies of the sharp peaks correspond to those of the pressure spectra. Their radial locations are also comparable.

Figure 4.27 (*a* through *l*) shows the RMS level of pressure fluctuations in the radial direction for the different streamwise locations (from $x=0$ to $x=650$) corresponding to the spectra in figures 4.8 through 4.19. The RMS value is normalised by the same dynamic pressure (q) as the pressure spectra. Graph *a* shows a maximum for $r=5$ mm of RMS level 0.4, but this is purely due to the low frequency part of the spectrum (compare figure 4.8), and not the fluctuations of higher frequencies considered here. Graphs *b*, *c*, *d* and *e* correspond to spectra in figures 4.9, 4.10, 4.11 and 4.12 of the low level and broad-band peaks. The RMS level is here about 0.6. The sharp spectra (figures 4.13 through 4.16) have their RMS levels shown in graphs *f* through *i*. The RMS level is gradually dropping from about 0.5 to 0.2. Graphs *j*, *k* and *l* reflect a decay and levelling-off (corresponding to the behaviour of the spectra from figures 4.17, 4.18 and 4.19). An important observation is that the highest values of RMS do not indicate the presence of the sharpest peaks in the spectra (these give lower RMS values).

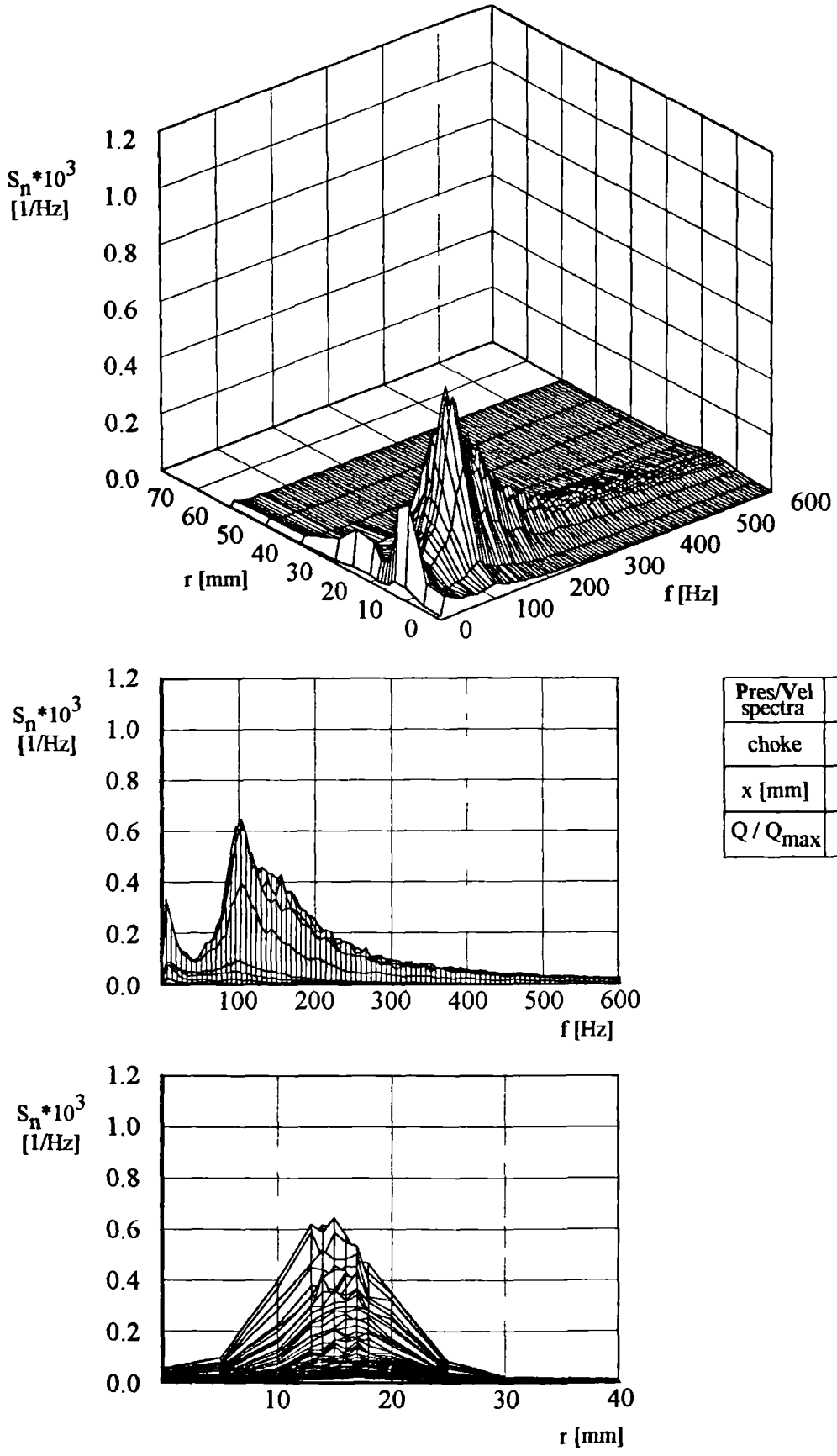

Pres/Vel spectra	P
choke	M
x [mm]	60
Q / Q_{max}	1.0

Figure 4.13.Pressure spectra (x=60 mm).

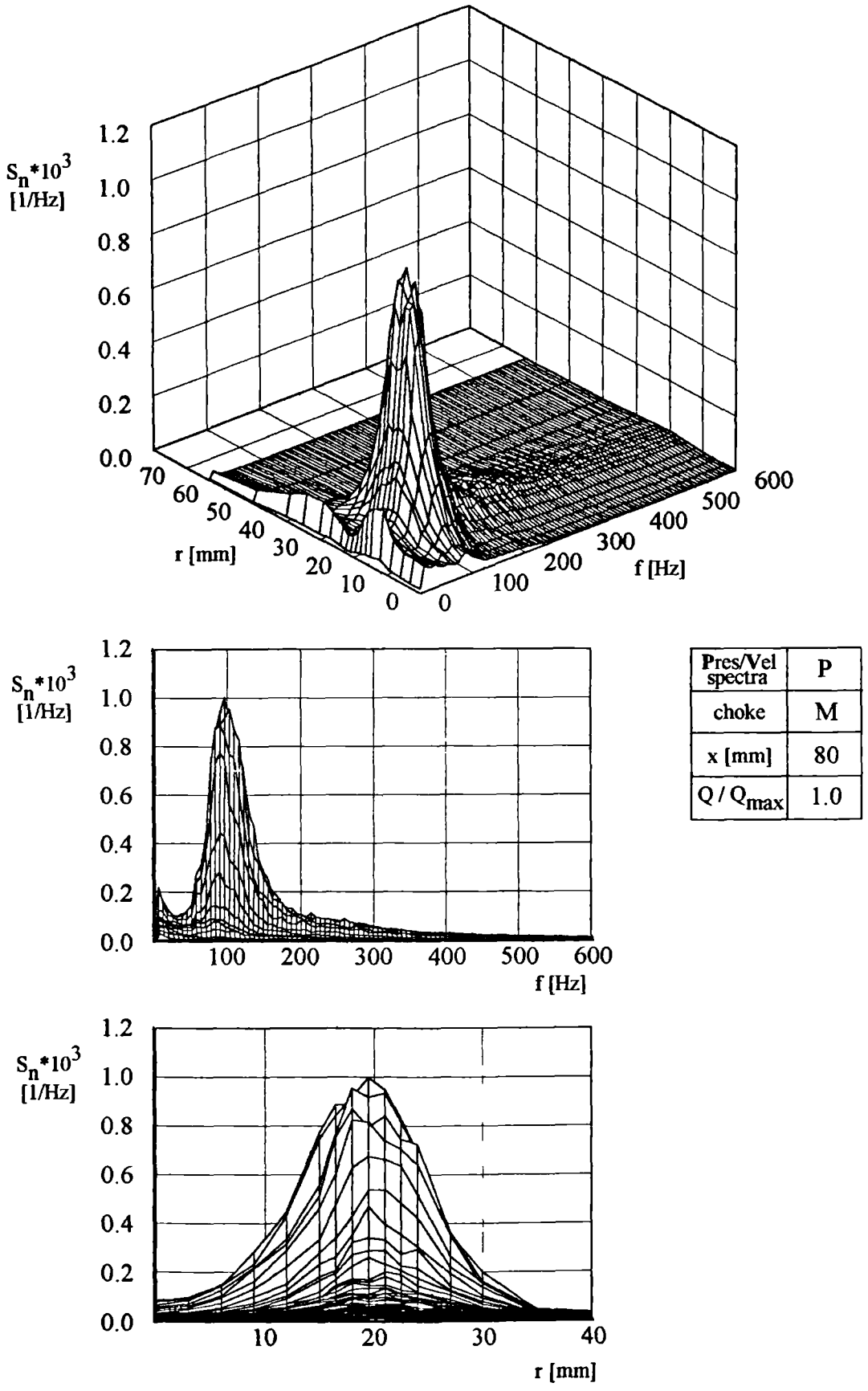

Figure 4.14.Pressure spectra (x=80 mm).

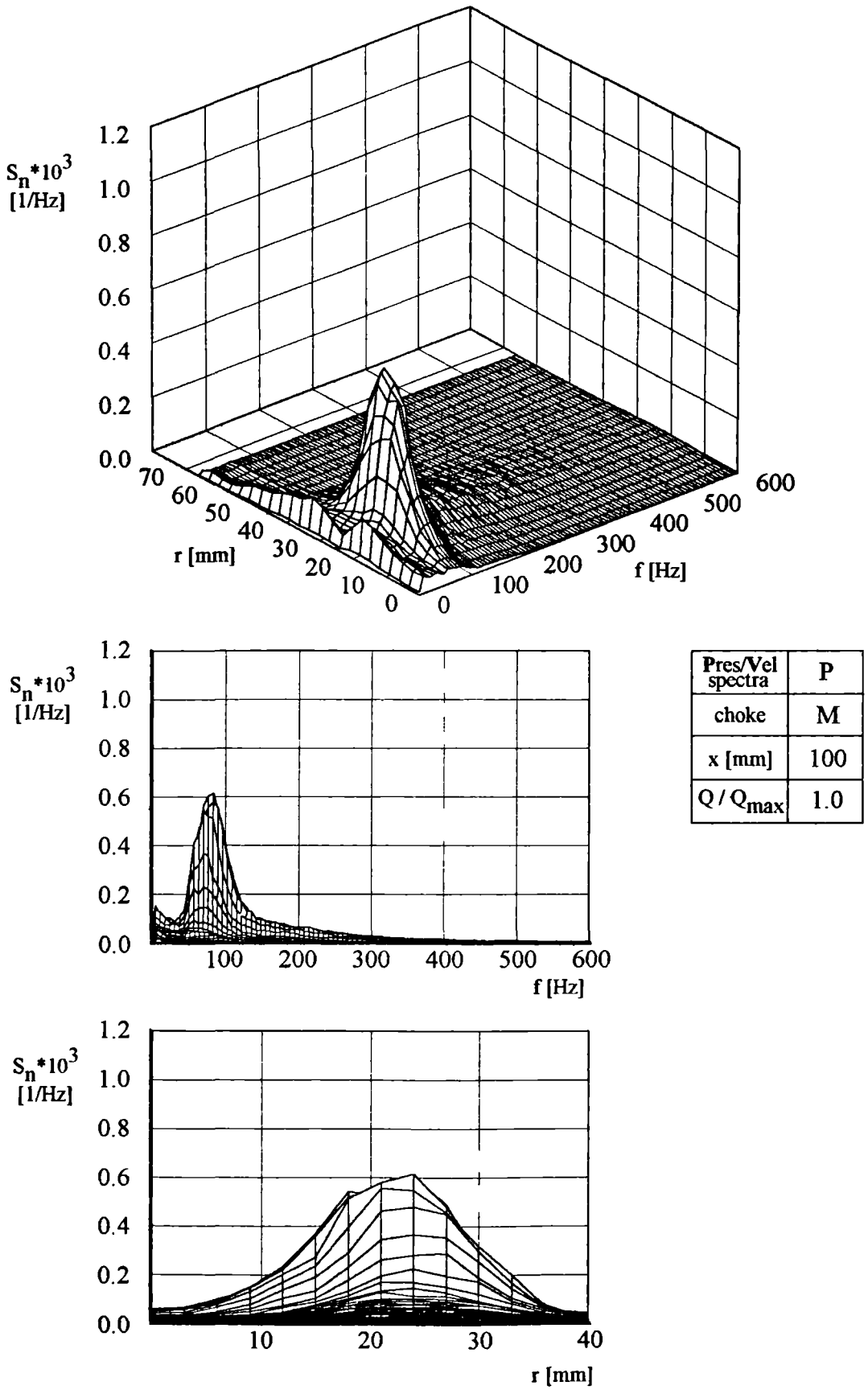

Figure 4.15.Pressure spectra (x=100 mm).

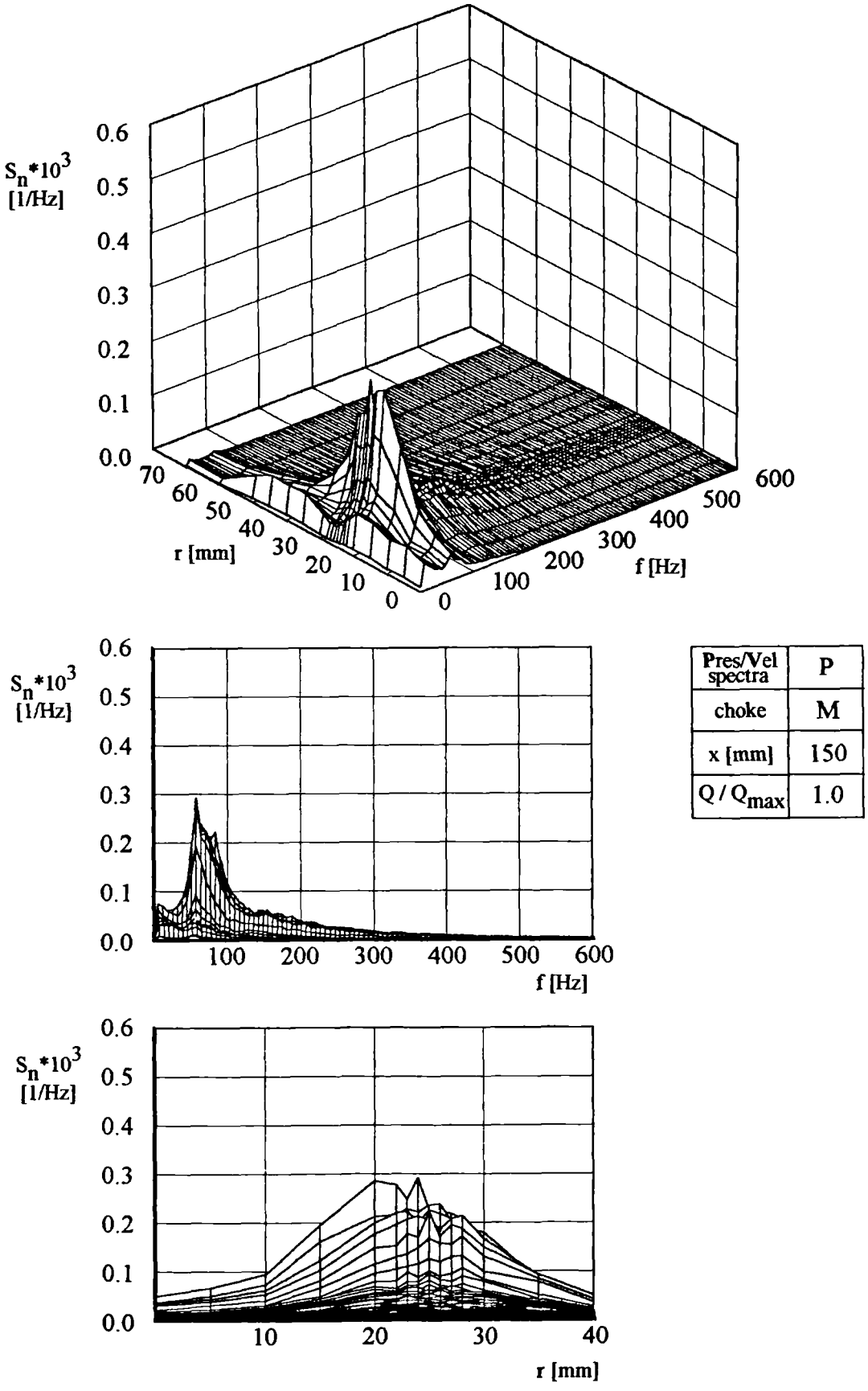

Figure 4.16.Pressure spectra (x=150 mm).

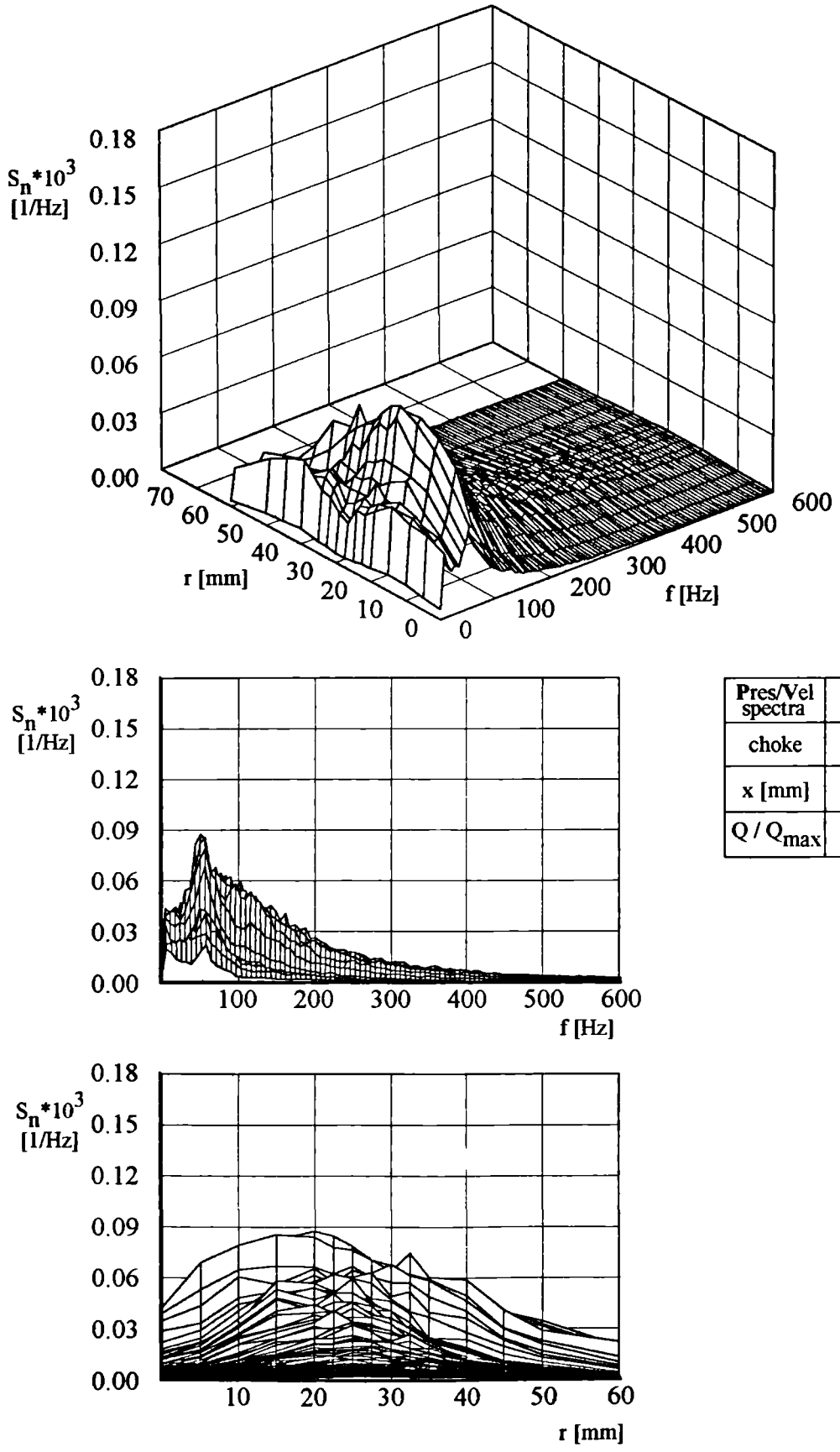

Figure 4.17.Pressure spectra (x=250 mm).

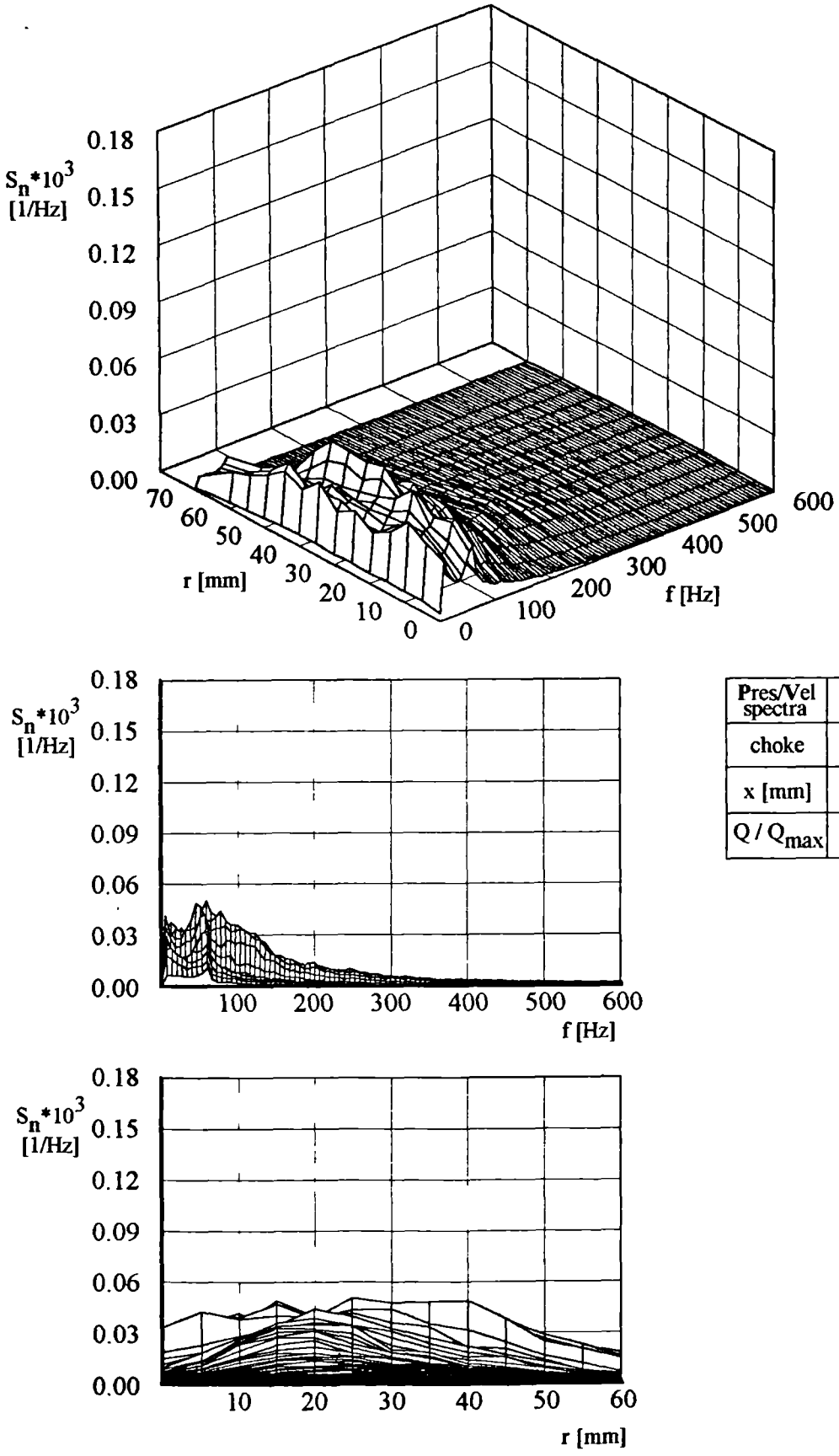

Pres/Vel spectra	P
choke	M
x [mm]	450
Q / Q_{max}	1.0

Figure 4.18.Pressure spectra (x=450 mm).

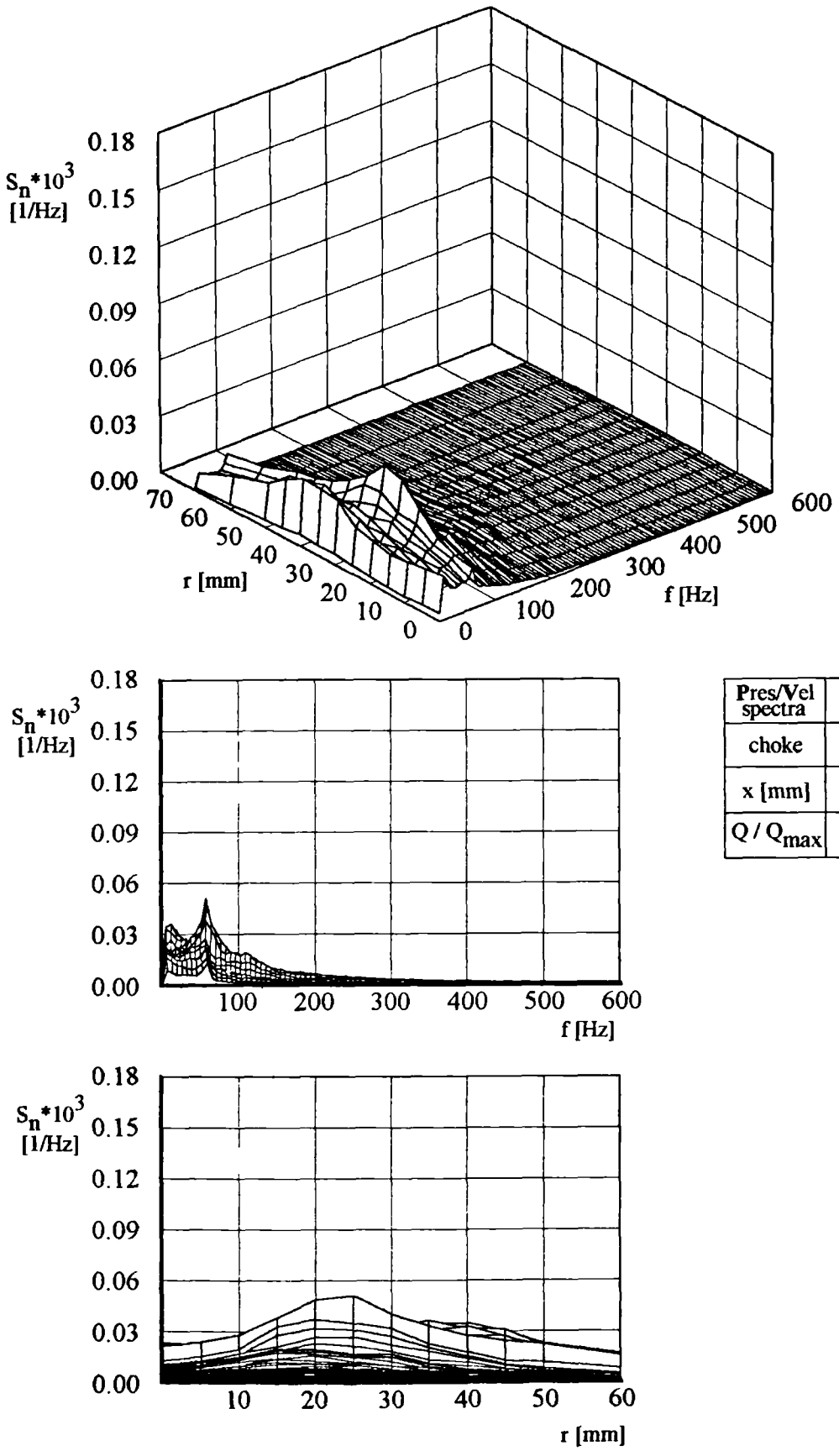

Figure 4.19.Pressure spectra (x=650 mm).

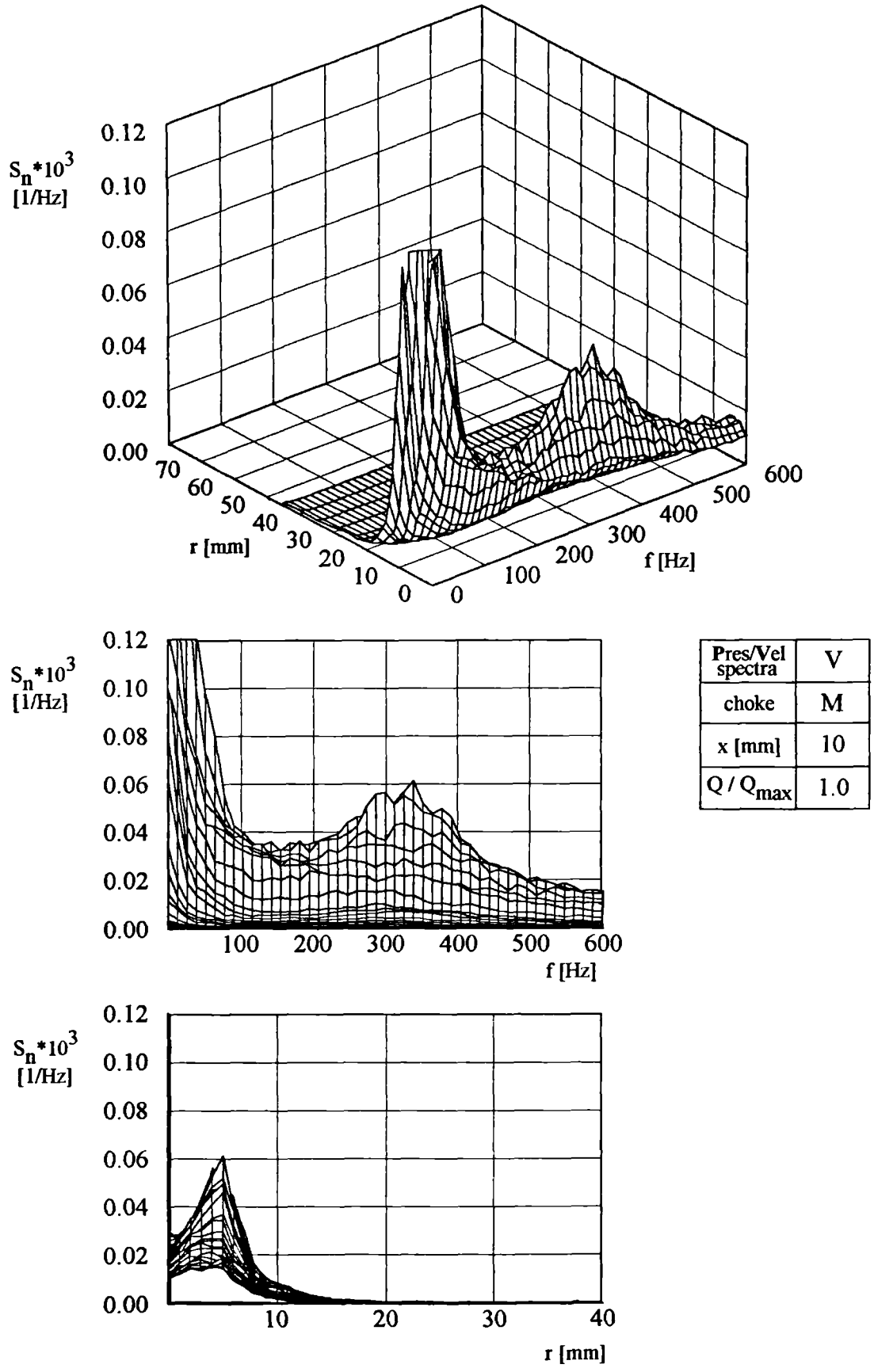

Figure 4.20. Velocity spectra (x=10 mm).

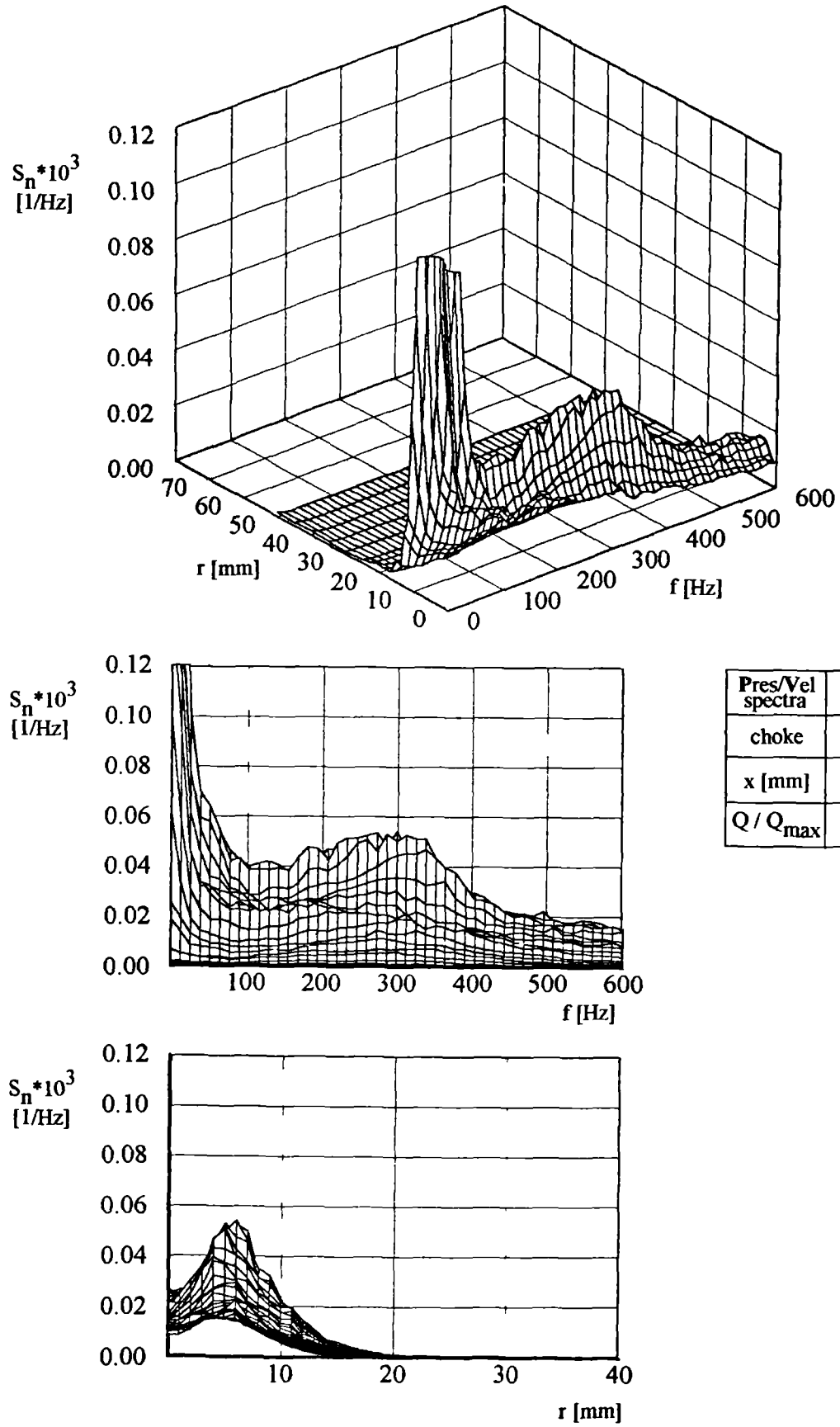

Figure 4.21. Velocity spectra (x=17 mm).

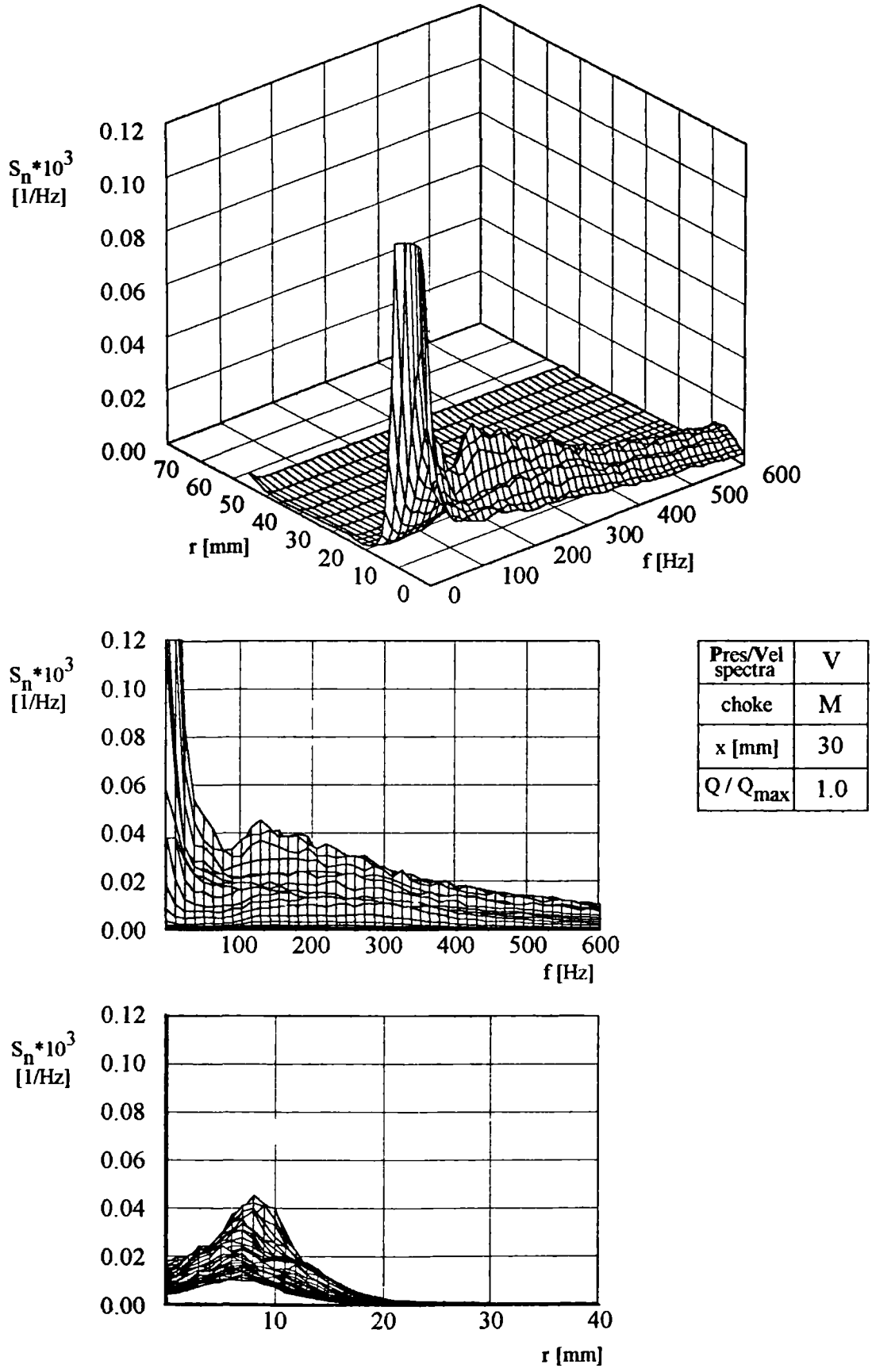

Figure 4.22. Velocity spectra (x=30 mm).

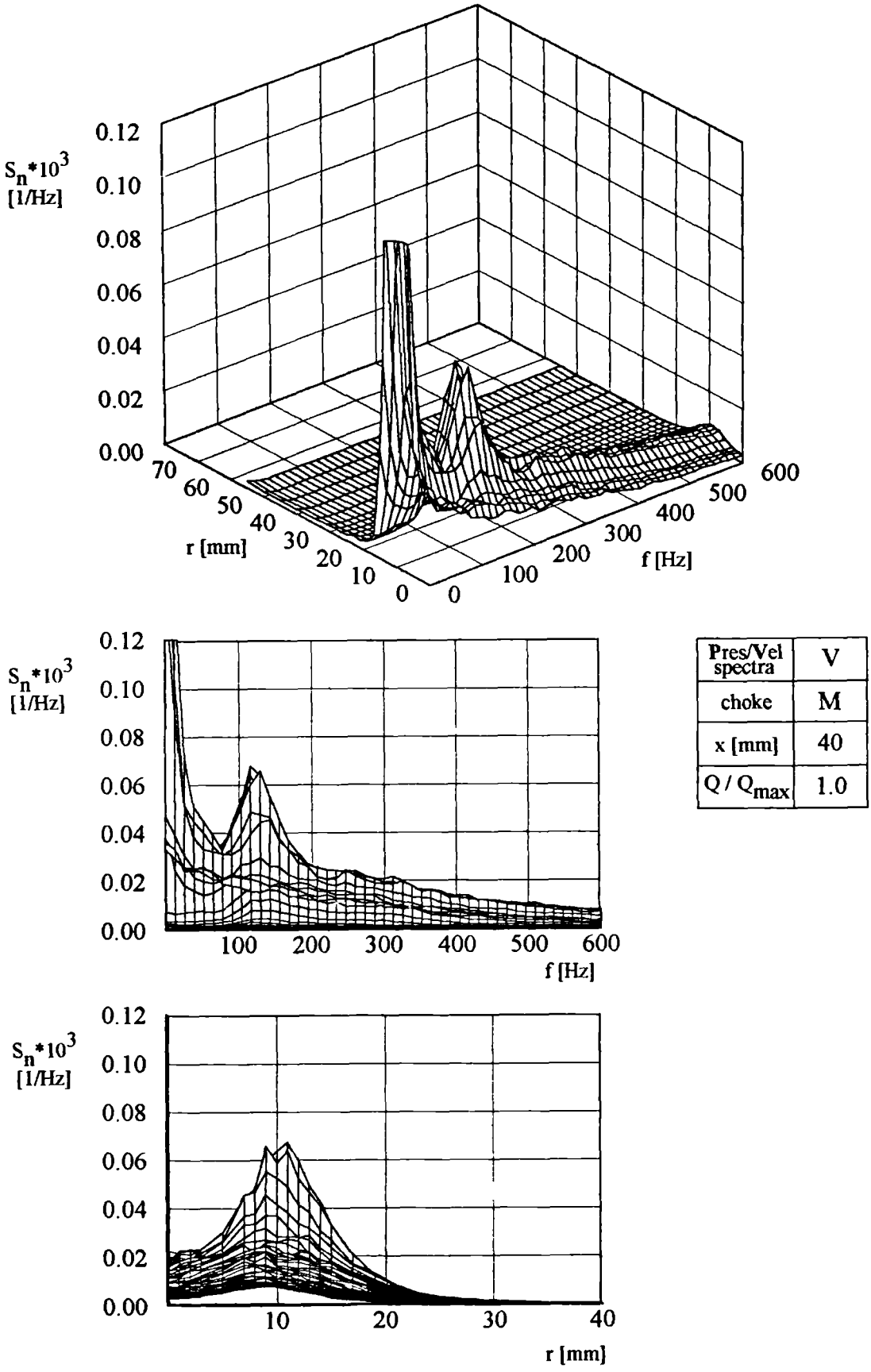

Figure 4.23. Velocity spectra (x=40 mm).

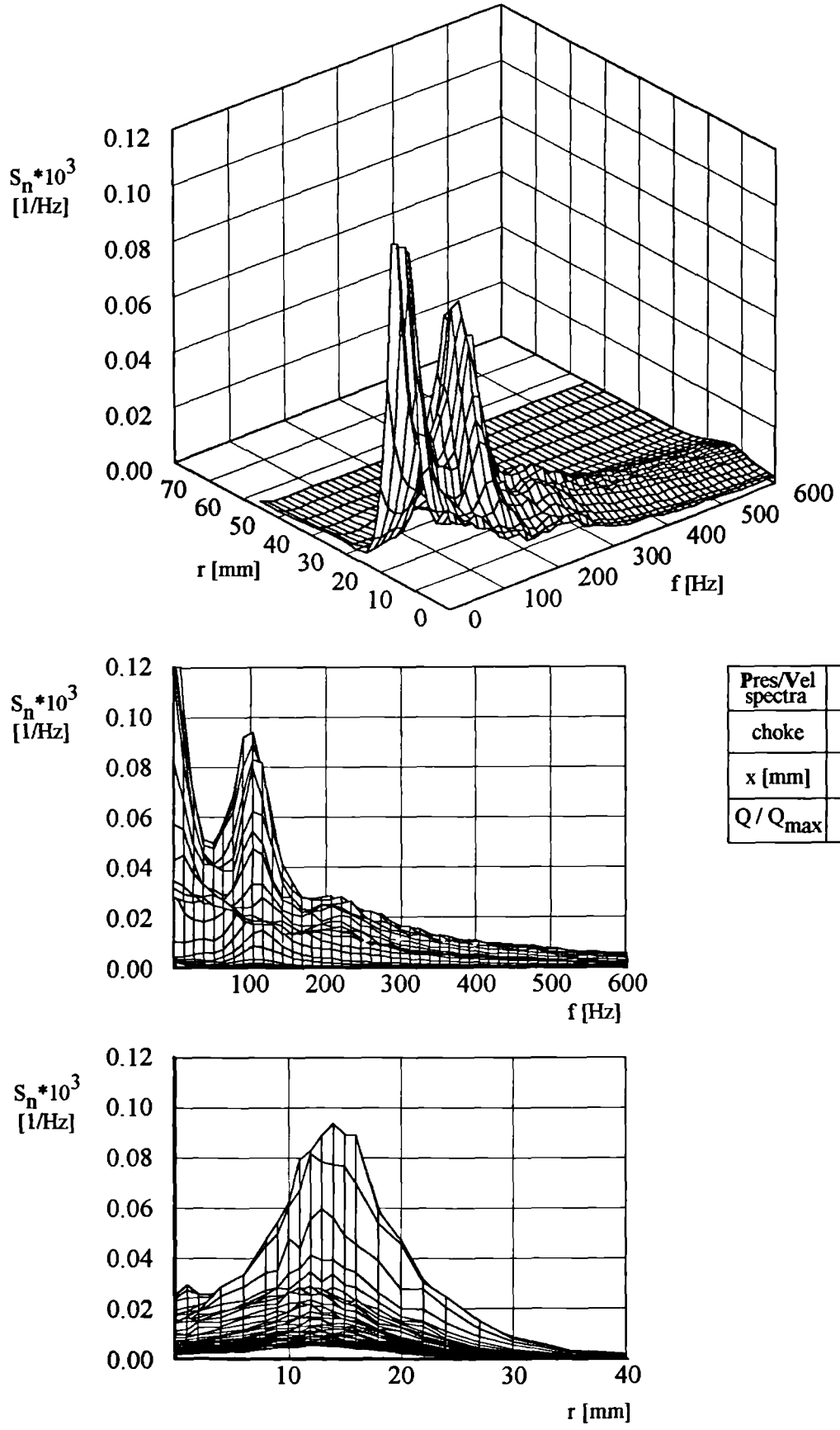

Figure 4.24. Velocity spectra (x=60 mm).

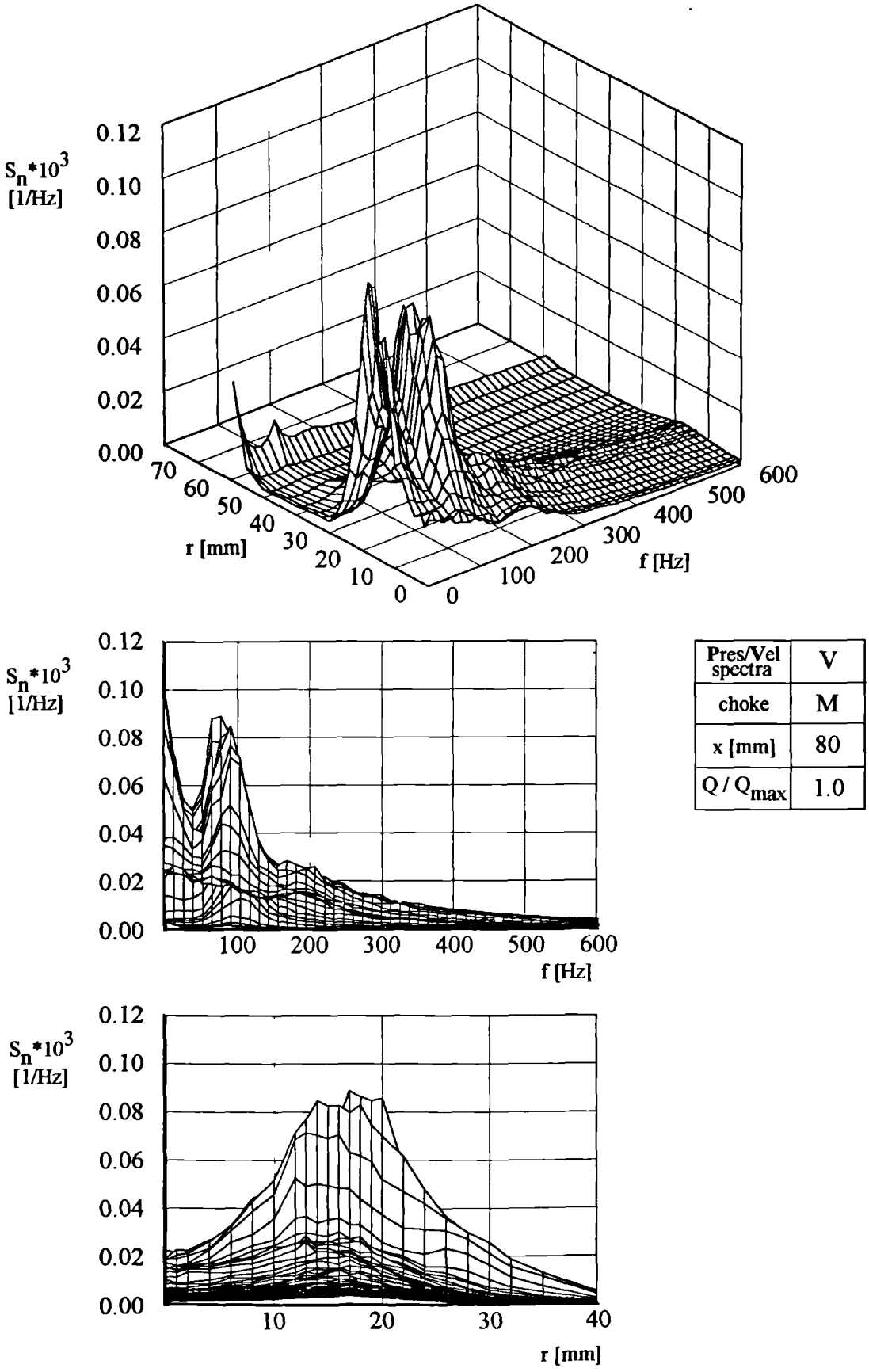

Figure 4.25. Velocity spectra (x=80 mm).

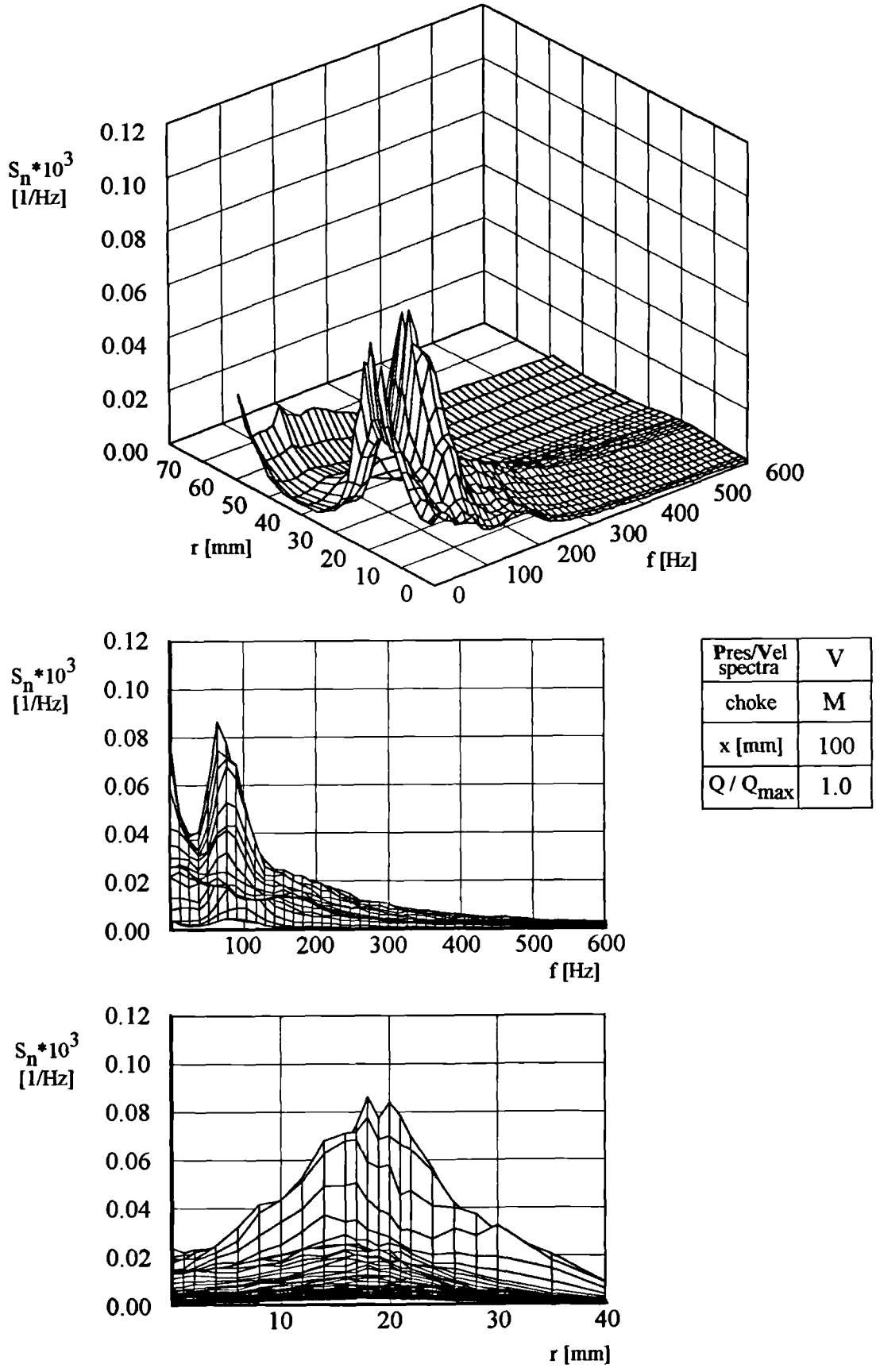

Figure 4.26. Velocity spectra (x=100 mm).

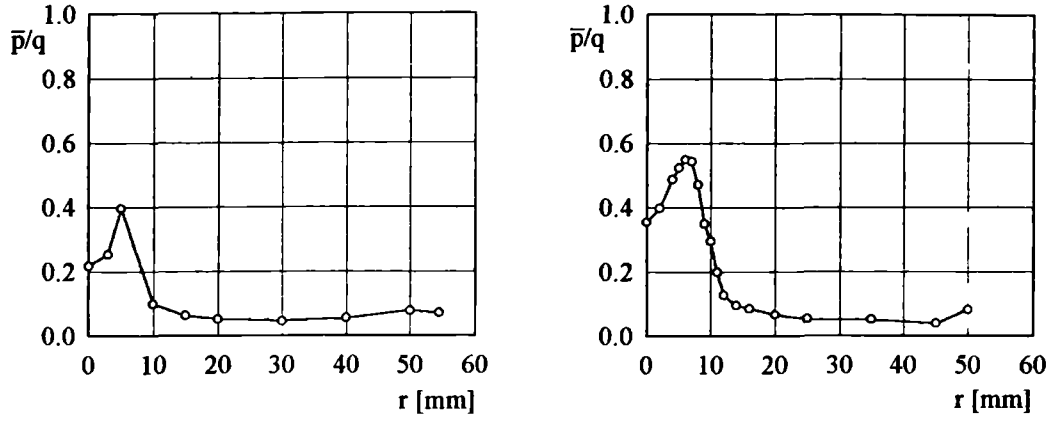

a x = 0 mm

b x = 10 mm

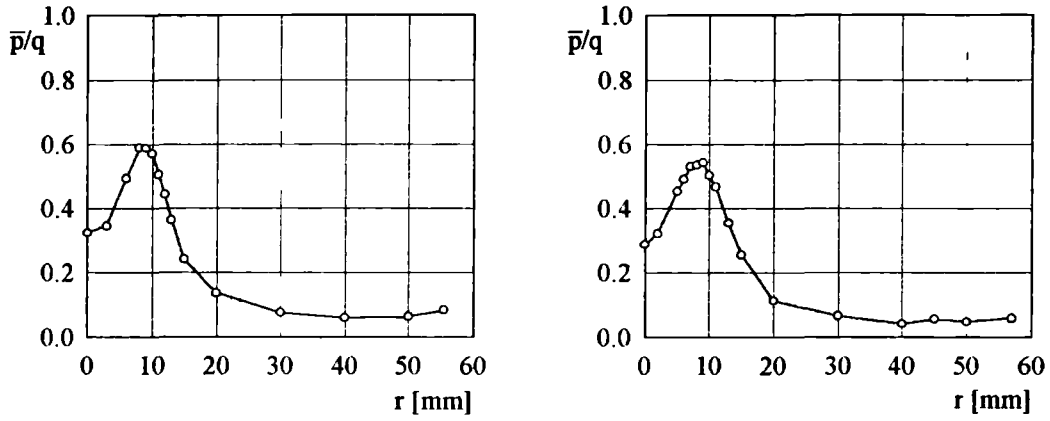

c x = 17 mm

d x = 30 mm

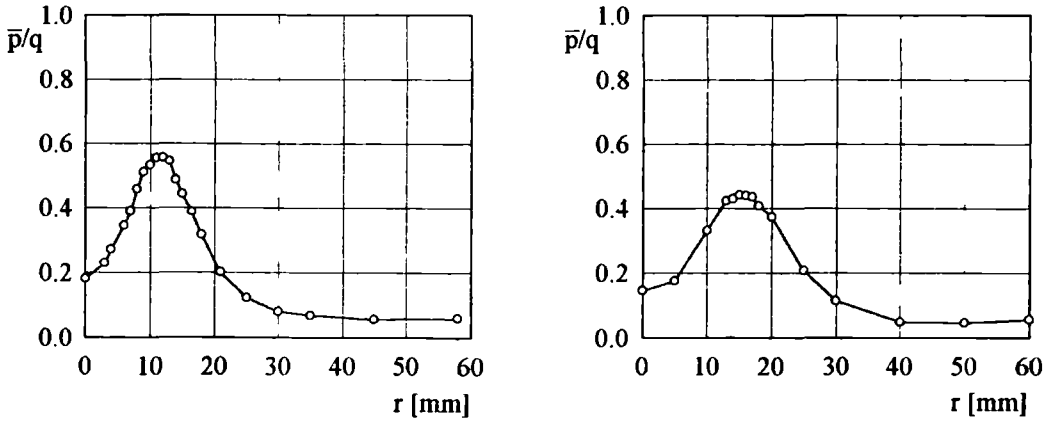

e x = 40 mm

f x = 60 mm

Figure 4.27.(*Continued on the next page*)

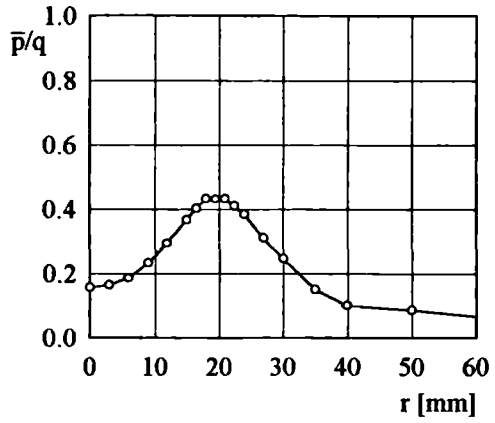

g x = 80 mm

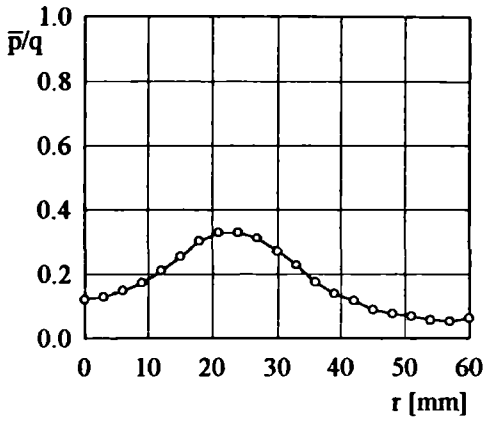

h x = 100 mm

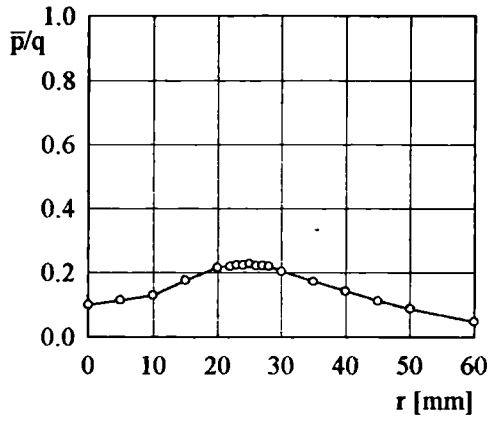

i x = 150 mm

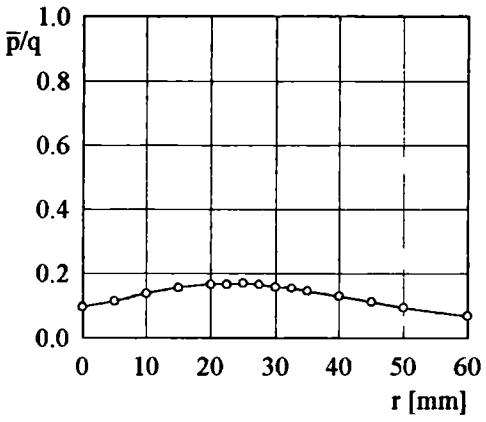

j x = 250 mm

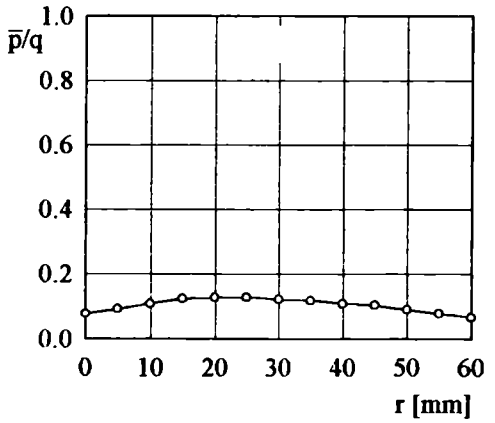

k x = 450 mm

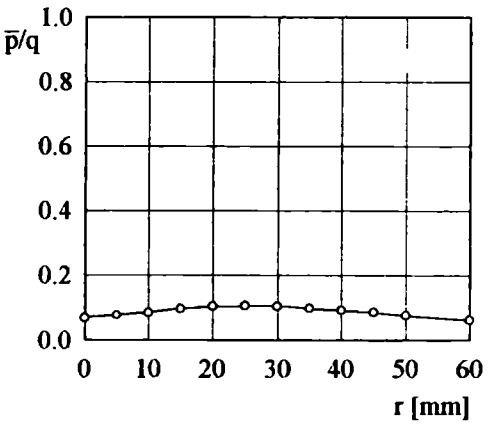

l x = 650 mm

Figure 4.27.RMS level of pressure fluctuations - radial distribution for different x.

The maximum values of RMS for all chokes, flow rates and streamwise locations investigated are shown in figure 4.28. Every point in a particular curve is taken as a maximum value from graphs similar to those in figure 4.27. The curves in figure 4.28 exhibit a rapid (nearly step-like) increase in the RMS level due to the burst (in all cases to about 0.6) and a gradual decrease to the value of 0.1. The sharp spectra, however, have corresponding values of RMS between 0.5 to 0.2.

From the pressure spectra (figures 4.8 through 4.19) and the RMS levels (as those in figure 4.27) it is possible to define a characteristic length associated with the pressure fluctuations as, for example,the diameter (twice the radius) at which the spectra reach their maxima or the RMS level is the highest. These are shown in the top chart of figure 4.29 as D_{rms} and D_{peak} as a function of streamwise co-ordinate (x). The diameter derived from the maximum RMS value is only slightly bigger than the one derived from the maximum of the spectra. Similarly the characteristic frequency from the spectra (whether it is the broad band or sharp spectrum) is shown in the middle chart. The proposed frequency parameter (a full discussion of this is given in chapter 5) is based on

- the diameters D_{rms} or D_{peak} ,
- the characteristic frequency corresponding to the peaks in the spectra (f),
- the 'free stream' axial velocity in the narrowest place of the chokes, i.e.

$$n_{rms} = f D_{rms} / W_o \tag{4.1}$$

or

$$n_{peak} = f D_{peak} / W_o \tag{4.2}$$

These frequency parameters are shown at the bottom chart of figure 4.29.

Figures 4.30 and 4.31 show the collected values of the frequency parameters given by equations (4.1) and (4.2) for all chokes and speeds. Judging by the scatter, it appears that the frequency and characteristic length are slightly better correlated by using D_{rms} , however both n_{rms} and n_{peak} are in close agreement[6] with each other.

[6] considering the quasi-periodic character of fluctuations, unlike for example those behind the circular cylinder with frequency parameter based on the cylinder diameter of 0.2 (approximately).

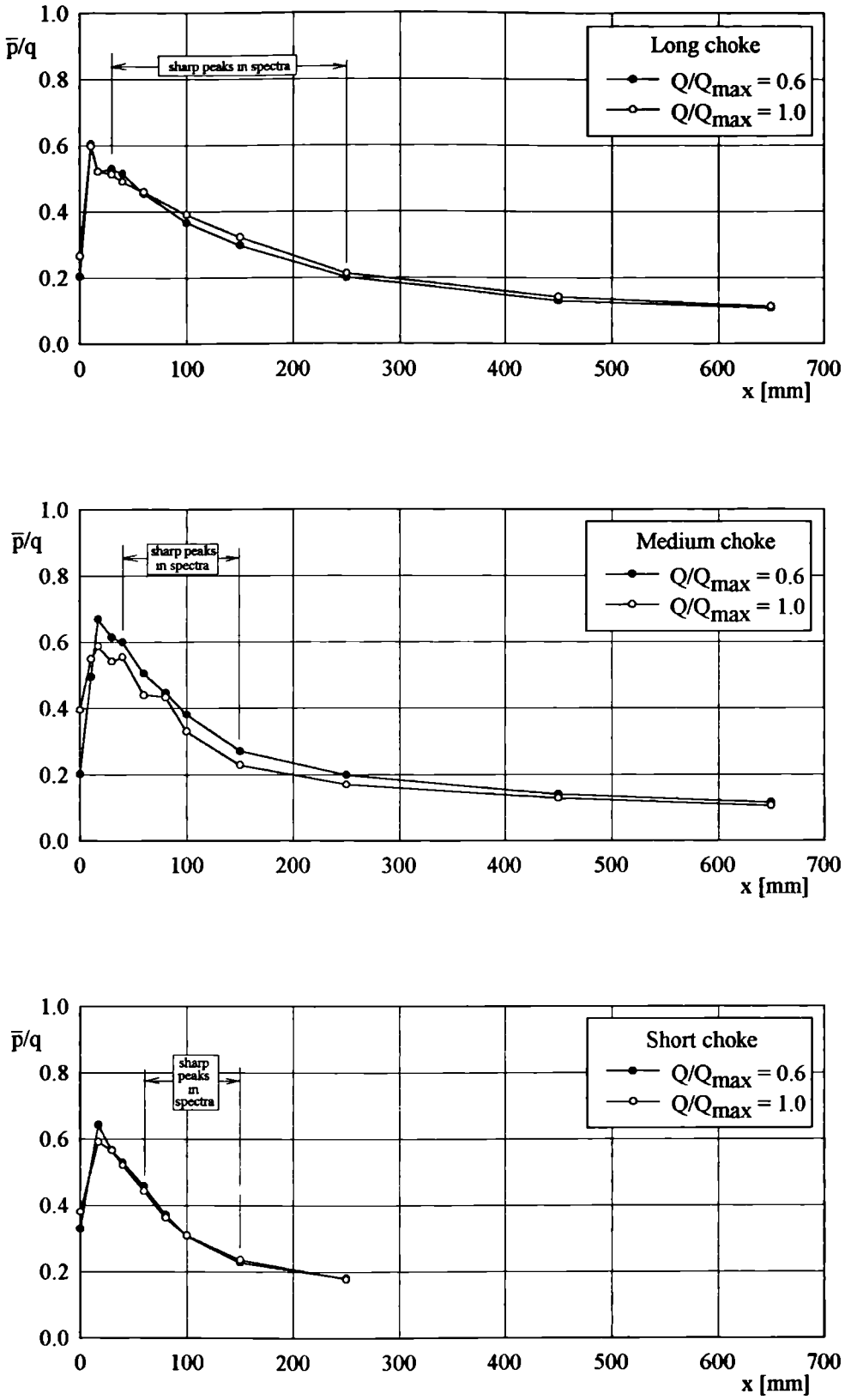

Figure 4.28.Maximum RMS level of pressure fluctuations in the streamwise direction.

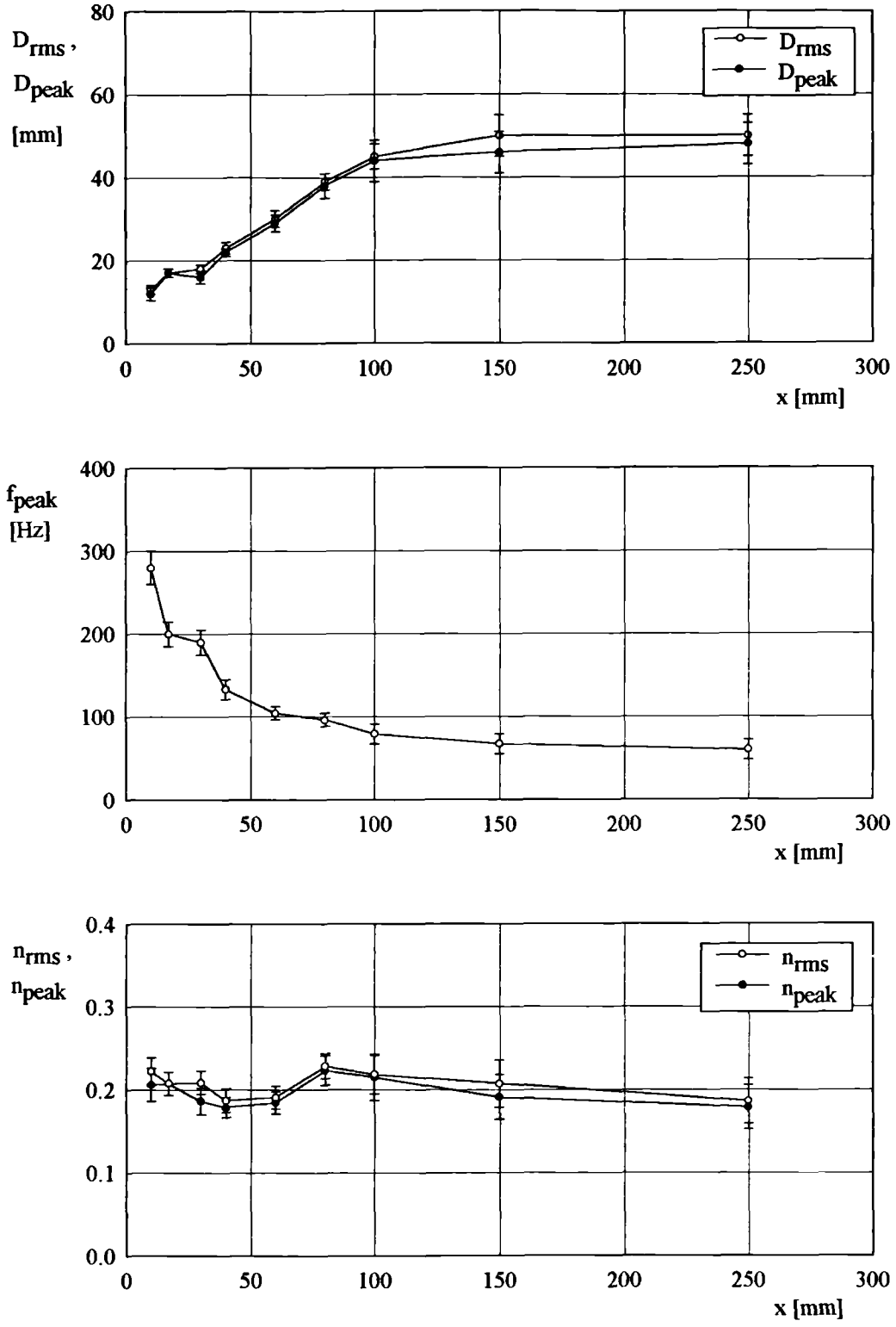

Figure 4.29.Characteristic length, frequency and derived frequency parameter for medium choke and Q/Q_{max}=1.0.

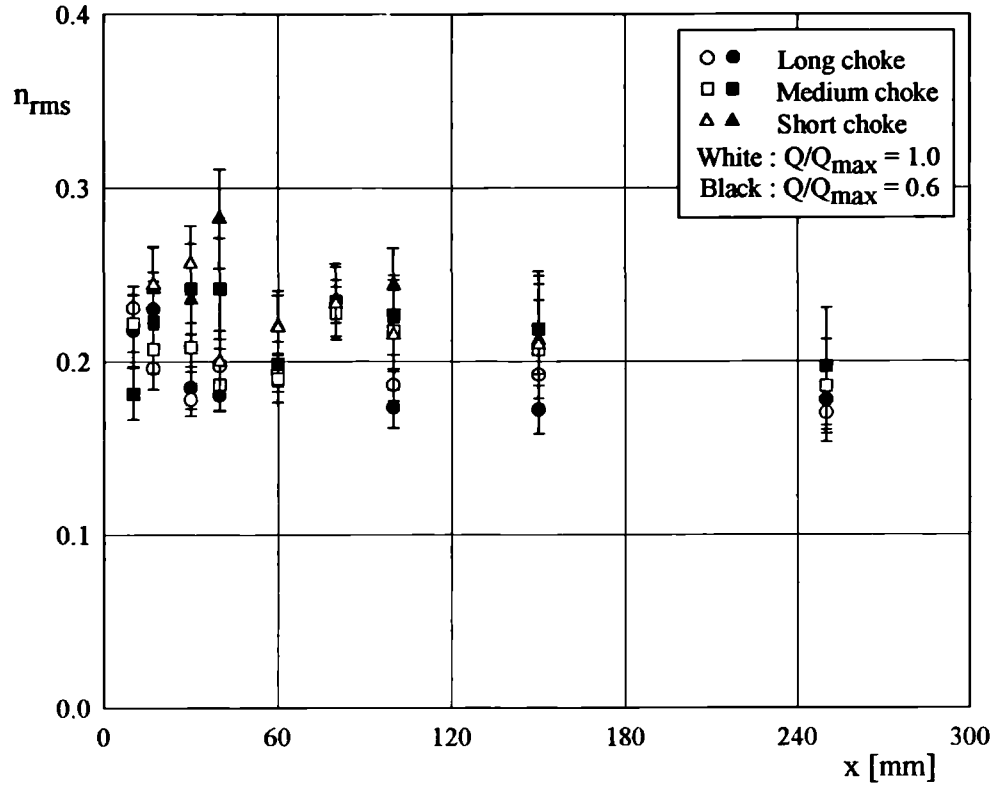

Figure 4.30.Frequency parameter based on the diameter of highest RMS level.

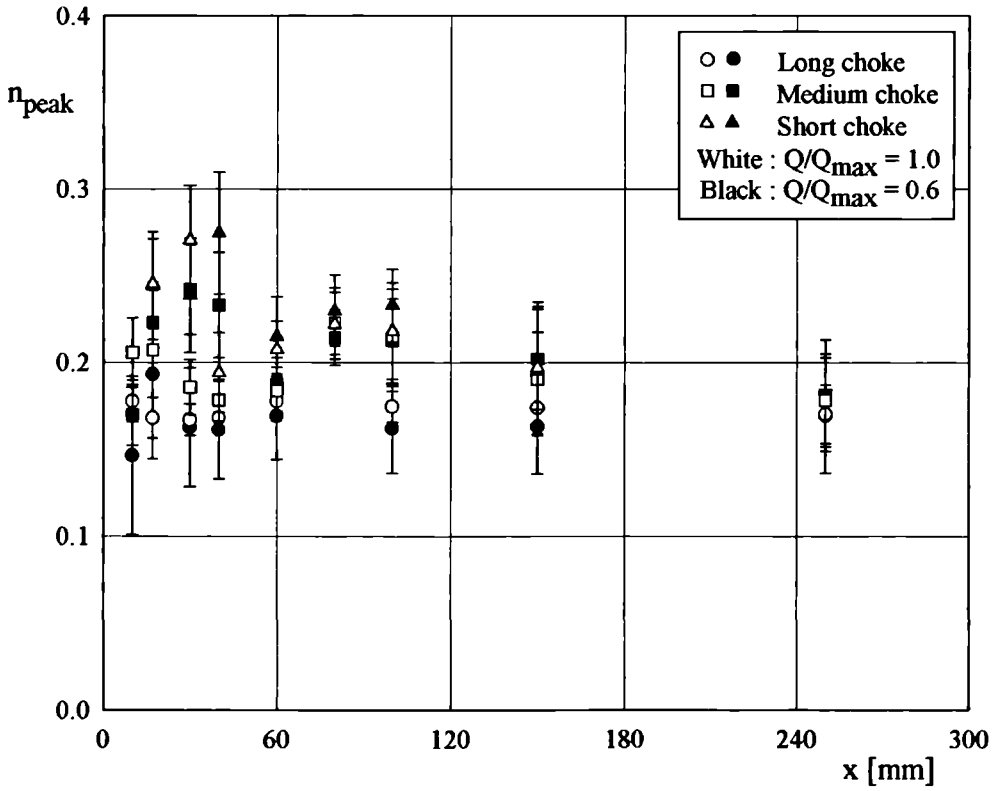

Figure 4.31.Frequency parameter based on the diameter of maxima in spectra.

The correlation is also better for the sharp peaks than the broad band ones (i.e. for x greater then, say, 60 mm). For the well-defined peaks both parameters assume values roughly between 0.17 and 0.23.

An interesting question from the viewpoint of the possible source of the quasi-periodic oscillations is the location of their appearance in relation to the axial velocity profile. Figure 4.32 shows a typical example of a velocity profile (thick line with black circles) together with the RMS level of pressure fluctuations (empty squares) and velocity fluctuations (empty triangles). The large hexagon and rhombus show the location of the maxima of the pressure and velocity spectra[7]. The results suggest that all the quantities characteristic for the quasi-periodic features of the flow have their maxima fairly close to the point of inflection in the velocity profile. This might serve as an estimate of the characteristic length parameter obtained directly from the velocity profiles, in the absence of other results (such as pressure and velocity spectra or their RMS 'profiles').

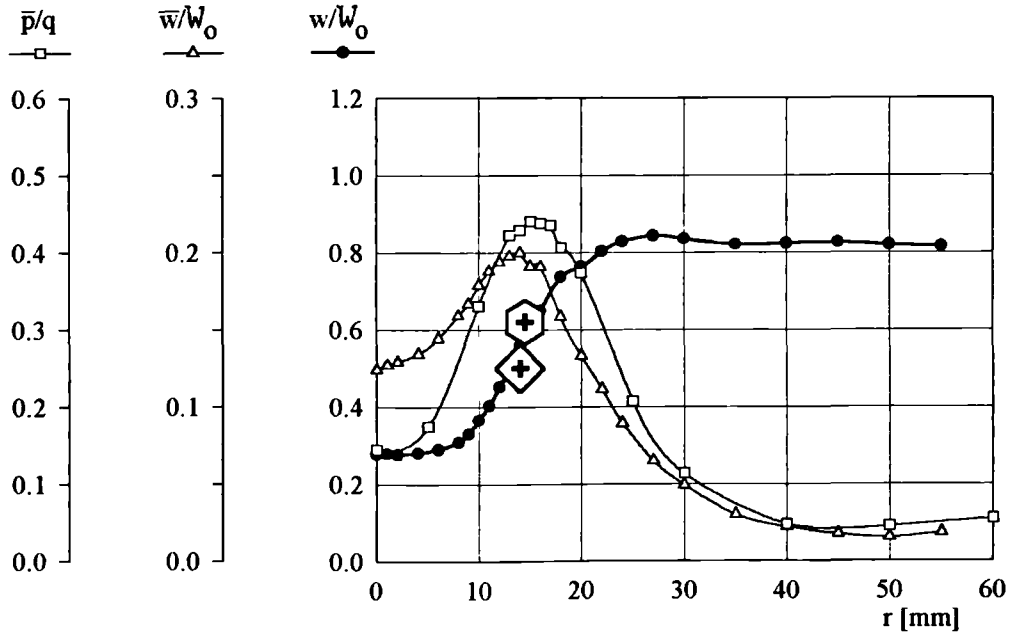

Figure 4.32. Velocity profile (medium choke, x=60 mm, Q/Q_{max}=1.0) with RMS level of fluctuations and locations of maxima in spectra.

[7] Their vertical location in the figure has no meaning. They were placed close to the velocity distribution for better presentation.

4.1.3. Correlations of pressure fluctuations

Figure 4.33 shows schematically the actual orientation of the flow inside the test section. The streamlines, according to the velocity measurements, form spirals of the opposite sense to that of a right-handed screw (see the small drawing at the bottom of figure 4.33). The probes are introduced in two perpendicular meridional planes, which are called for simplicity 'vertical' and 'horizontal' - compare also figure 3.2 (for ports' orientation) and 4.1. (for the actual traversing arrangement for moving the 'slave' probe).

It is worth repeating that the character of the flow inside the choke is remarkably different (and more complicated in certain aspects) from the flow past a delta wing. Here there is no real 'free stream' (or reference) velocity for the flow. Instead, the flow inside the choke's diffuser is decelerated from cross-section to cross-section due to diverging boundaries. Hence the 'free stream' velocity (say, taken as the axial velocity outside the vortex core) is not constant (compare figure 4.3, where w/W_0 outside the vortex core changes from about 1.0 to 0.65). This in turn must affect the propagation speed of disturbances, which will be expected to decrease in a similar manner to the 'free stream'.

Figure 4.34 compares the *mean* axial velocity in the tube (calculated from the flow rate through the rig) with the axial velocity in the flow surrounding the vortex, i.e. *outer flow*, both as a functions of streamwise co-ordinate x. The data are shown for the long choke and the maximum flow rate (for which correlation measurements have been made); the figure is given as a reference for the propagation speeds obtained later in this section.

Ideally, in the situation described, the propagation speed should be assessed by using a pair of probes (say with a constant distance from each other) both displaced in the streamwise direction. This however was impractical in the vortex tube experiment due to difficulties in rearranging and aligning the probes inside the test section. Hence only the slave probe was moved. The apparent shortcoming of

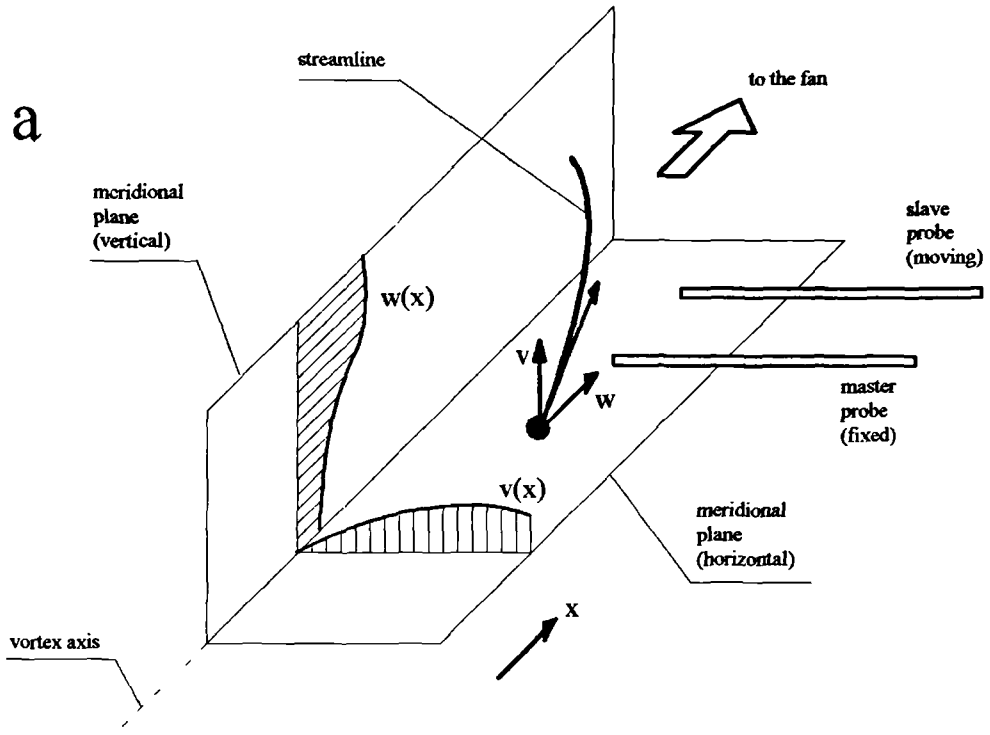

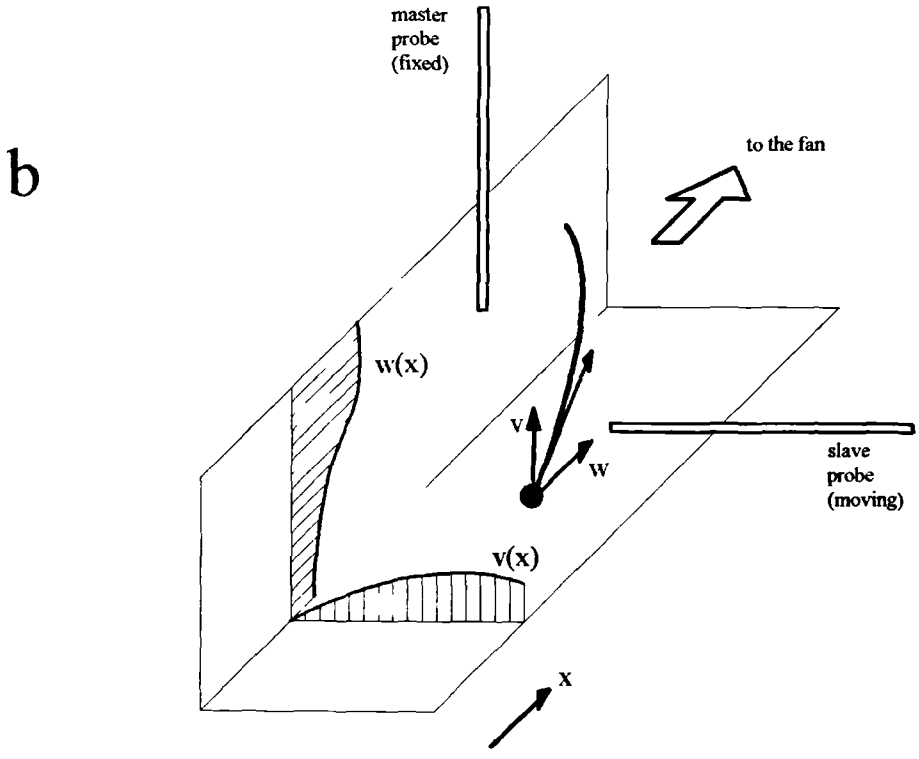

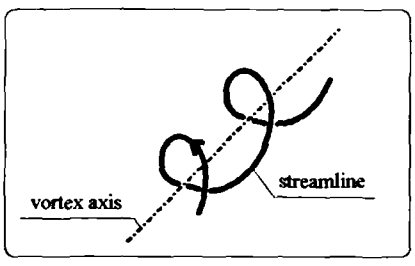

Figure 4.33.Different probe arrangements for correlations.

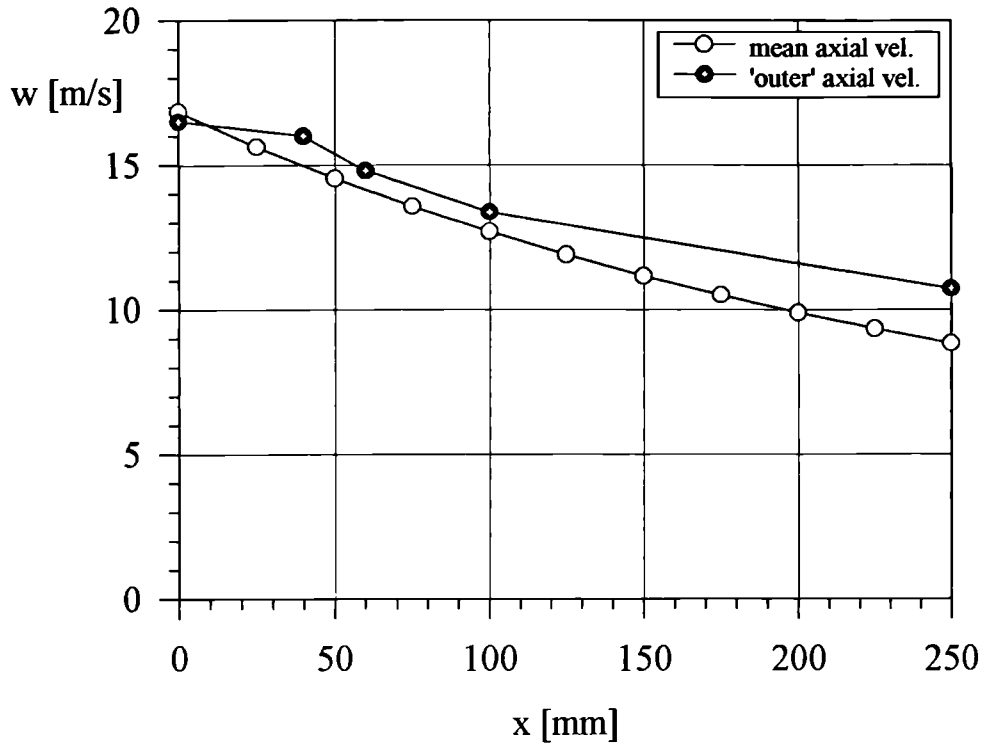

Figure 4.34.The mean and 'outer' axial velocities in the long choke at the maximum flow rate.

the method is that,as the frequency of the quasi-periodic fluctuations decreases from cross-section to cross-section, the interpretation of the propagation speed may be somewhat difficult (correlation should involve signals of similar frequency)[8]. Therefore, it is suggested that the propagation speed (say at $x=60$ mm) is inferred as a derivative of the function $x=x(t)$ (t is the time lag), within the distance where the frequency does not change too much; and not by the slope of the straight line obtained by regression of all data points.

The correlation measurements were made using the long choke (where the frequency of quasi-periodic fluctuations changes most slowly). Two probe configurations were used:

[8] The technique of conditional sampling has been also used, but it proved inefficient. The main difficulty was the quasi-periodic character of the signal . Thus it was impossible to fix any reasonable 'trigger'. This method would be ideal for tracking the isolated disturbances (which can be distinguished from the 'background').

- the one shown in figure 4.33a, where the probes are introduced in the same plane. Here the master probe is fixed at $x=60$ mm and the radial position at which the highest peak in frequency spectra is recorded. The slave is traversed in both the streamwise and radial direction (again keeping the radial co-ordinate such that the highest peaks in the spectra appear). The actual co-ordinates are given with the results. This measurement was to establish the longitudinal propagation speed of the pressure disturbances.
- the one in figure 4.33b, where the probes are in two perpendicular planes. The master probe is fixed in the vertical plane at $x=60$ mm. The slave probe is traversed in the streamwise direction in the horizontal plane. This configuration was introduced in order to check the character of the disturbances (spiral or ring vortices). For ring vortices, the time lag between the master and the slave probes placed in the same cross-section should be zero (or near enough). This is not true for spiral vortices. Furthermore, for the spiral disturbance it is possible to establish its helix angle by finding the streamwise slave probe position for which the time lag vanishes.

Figure 4.35 (a series of graphs *a* through *i*) shows the time correlation (denoted as *R*) for the first arrangement of probes (see figure 4.33a) with the distance between the probes increasing. The first graph shows the autocorrelation of the signal obtained from the master probe. Remarkably, the quasi-periodic character of the signal, indicated by the power spectra, is confirmed by the 'wavy' character of the autocorrelation function, with several 'periods' easily seen in the graph. In addition the dominant frequency of the spectrum is well reflected in the 'period' of the autocorrelation. For probes fairly close to each other (say up to 30 mm, i.e. graphs *b* through *e*) the correlation function maintains a 'periodic' character with a sharp peak. The magnitude of the peak is relatively high (0.50 to 0.25). For greater distances between the probes (40 to 70 mm, i.e. graphs *f* through *i*) the

a

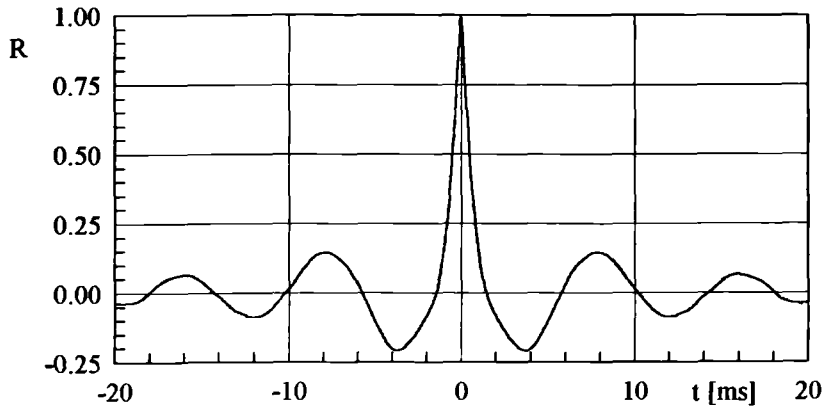

b

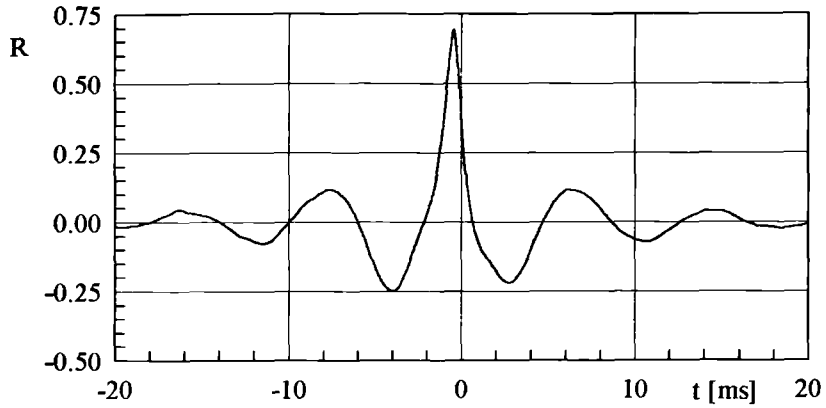

c

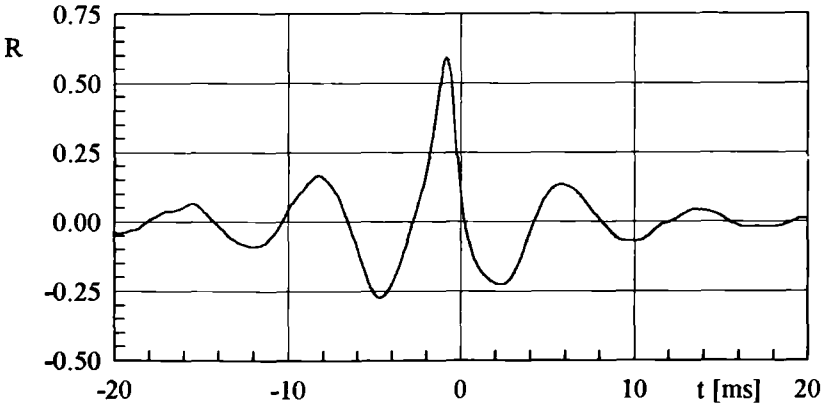

Master probe in horizontal plane at x = 60 mm and r = 11.0 mm
Slave probe in horizontal plane:

a) x = 60 mm (autocorrelation), r = 11.0 mm
b) x = 66 mm (+06 mm in relation to master), r = 11.5 mm
c) x = 70 mm (+10 mm in relation to master), r = 12.0 mm

Figure 4.35.(*Continued on the next page*).

d

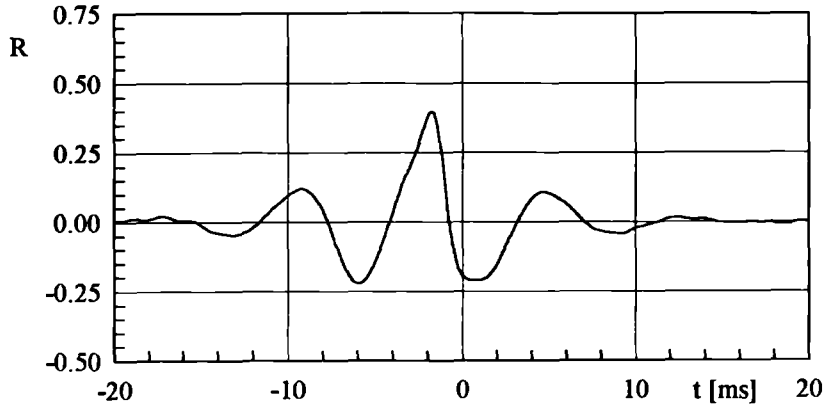

e

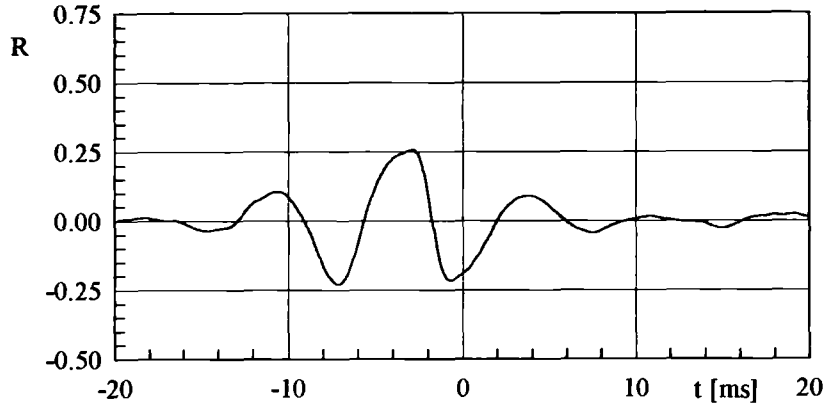

f

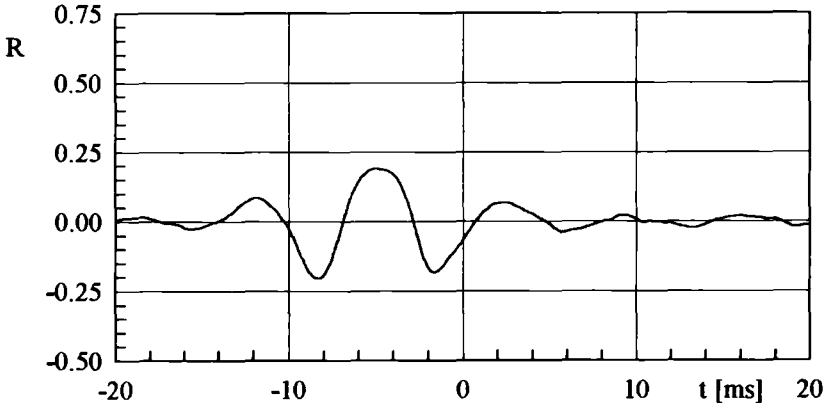

Master probe in horizontal plane at x = 60 mm and r = 11.0 mm
Slave probe in horizontal plane:

d) x = 80 mm (+20 mm in relation to master), r = 13.0 mm
e) x = 90 mm (+30 mm in relation to master), r = 14.0 mm
f) x =100 mm (+40 mm in relation to master), r = 15.0 mm

Figure 4.35.(*Continued on the next page*).

g

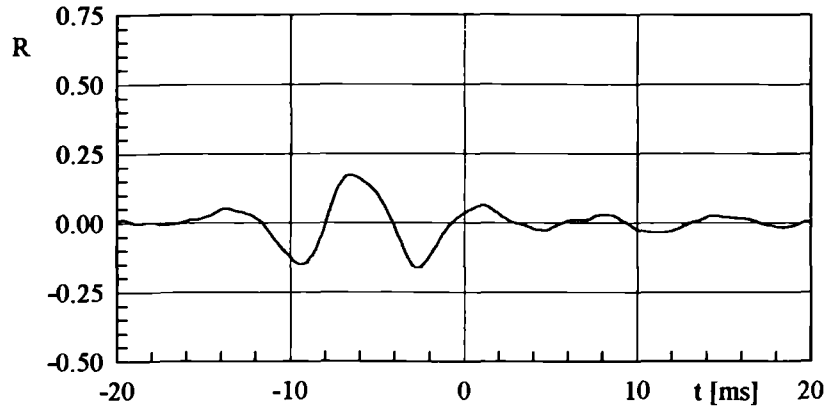

h

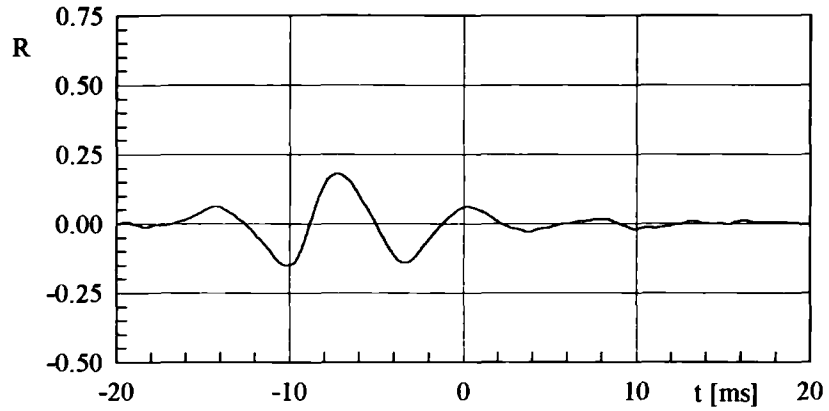

i

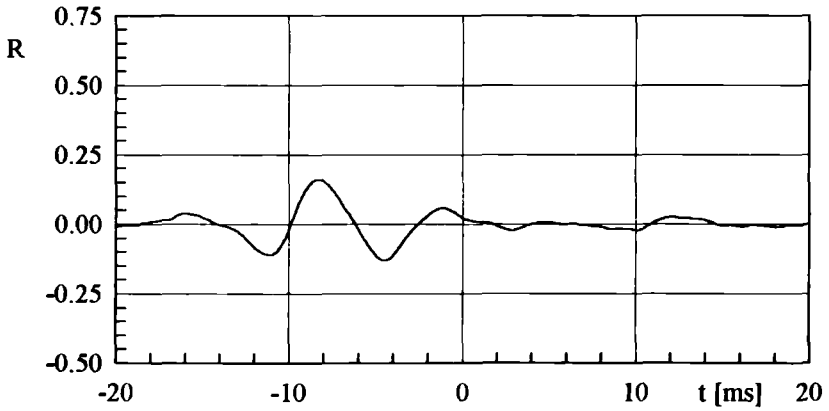

Master probe in horizontal plane at x = 60 mm and r = 11.0 mm
Slave probe in horizontal plane:

g) x =110 mm (+50 mm in relation to master), r = 15.5 mm
h) x =120 mm (+60 mm in relation to master), r = 16.0 mm
i) x =130 mm (+70 mm in relation to master), r = 16.0 mm

Figure 4.35.Time correlation for the probe arrangement from figure 4.33a.

clear character of the correlation function is lost (although it is still possible to recognise the maximum and some periodic features). The maximum of the function falls to about 0.15. It is worth noting that the shedding frequency of the probe in the experiment discussed is approximately 500 Hz and is much higher than the dominant frequencies in both the spectra and correlation functions (about 130 Hz). Thus the probe's shedding frequency is unlikely to produce the results in figure 4.35.

Figure 4.36. shows the time lag (found from the maxima of correlation function) vs. the distance between the probes. The ordinate and the abscissa have been swapped for easier interpretation (distance vs. time and velocity as the

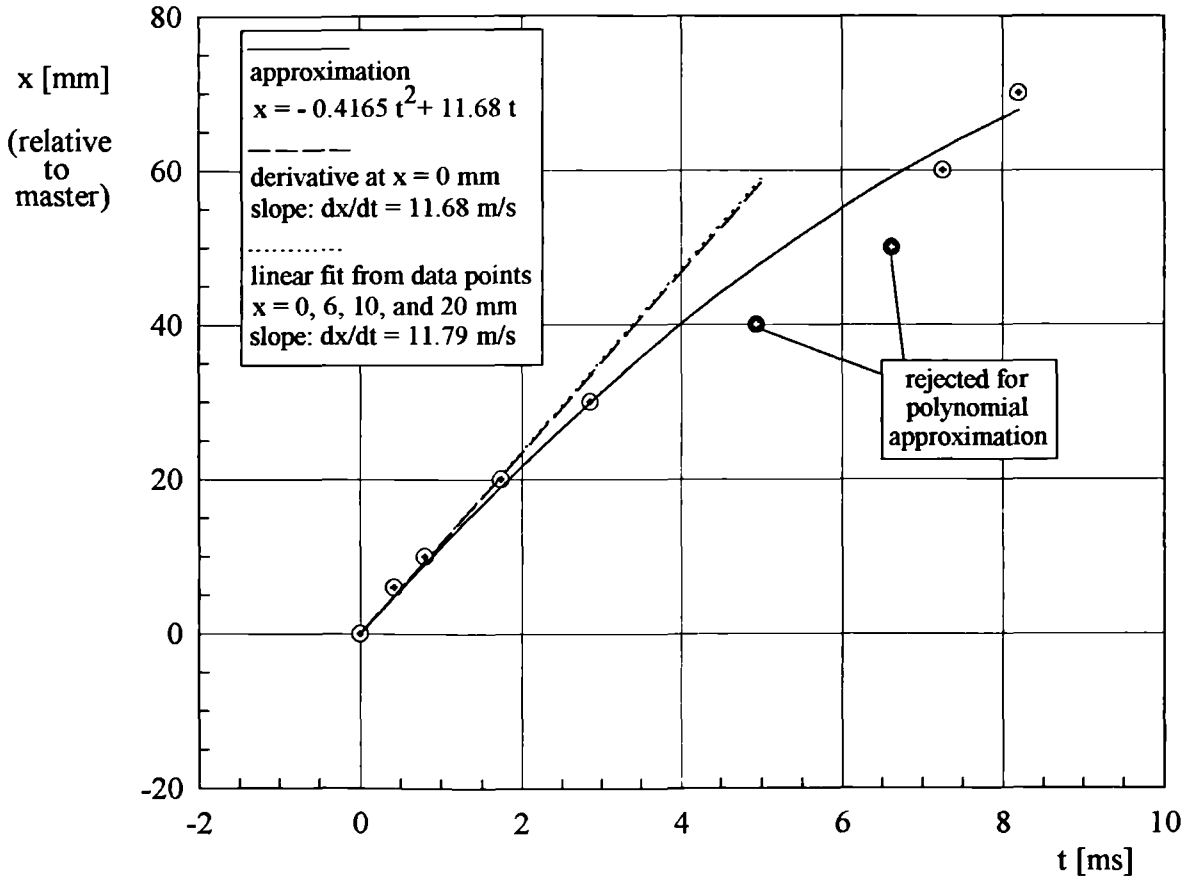

Master probe in horizontal plane at x = 60 mm and r = 11.0 mm
Slave probe in horizontal plane at (x,r) - in [mm] as follows:
(66, 11.5) , (70, 12.0) , (80, 13.0) , (90, 14.0),
(100, 15.0) , (110, 15.5) , (120, 16.0) , (130, 16.0)

Figure 4.36.Time lag vs. distance for probe arrangement from figure 4.33a.

derivative). The two points marked black were somewhat arbitrarily excluded from the analysis. It was anticipated that their scatter may be related to the slave probe being in the wake of the master, since this distance corresponds roughly to the helix angle of the streamline. The data points were approximated by a polynomial of type $x=at^2 + bt$ (a=-0.4165mm/(ms)^2, b=11.68mm/(ms), compare figure 4.36). It was chosen as the simplest expression which takes into account any possible deceleration[9]. The lack of a free term in the polynomial indicates that if the probes were at zero distance (not possible in reality) the time lag would have been zero. The propagation speed of pressure disturbance at x=60 mm, taken as the derivative of the polynomial expression, is 11.68 m/s [10], whereas as the linear fit of the first four data points, it is 11.79 m/s. The 'free stream' velocity (i.e. the local velocity outside the core) for cross-section x=60 mm is about 14.8 m/s. This gives a ratio of longitudinal propagation speed to 'free stream' axial velocity of approximately 0.8

A set of graphs in figure 4.37 shows the changes in the time correlation function for the arrangement shown in figure 4.33b as the slave probe is traversed in the horizontal plane. The slave position changes from x=45 mm, i.e. effectively 15 mm upstream of the master probe, to x=120 mm, i.e. 60 mm downstream. Figure 4.38 shows the time lag between the probes' response vs. the streamwise distance between probes. From the charts *a* through *d* (figure 4.37) it can be seen that the pressure disturbance reaches the slave probe earlier than the master probe (positive time lag, as described at the beginning of the chapter). The time lag is becoming negative in graphs *e* through *i*. The data points were approximated with the polynomial expression $x=at^2+bt+c$ (a=-0.3771mm/(ms)^2, b=10.38mm/(ms), c=11.55mm). The longitudinal propagation speed of pressure disturbances, obtained

[9] The reason for this procedure is more explicit for the second probe arrangement.

[10] The accuracy of two decimal places is of course meaningless from the experimental viewpoint. Here it is given as an exact result of a mathematical operations (numerical approximation of experimental data). This remark holds for many other quantities presented in this chapter, which were obtained by similar methods.

a

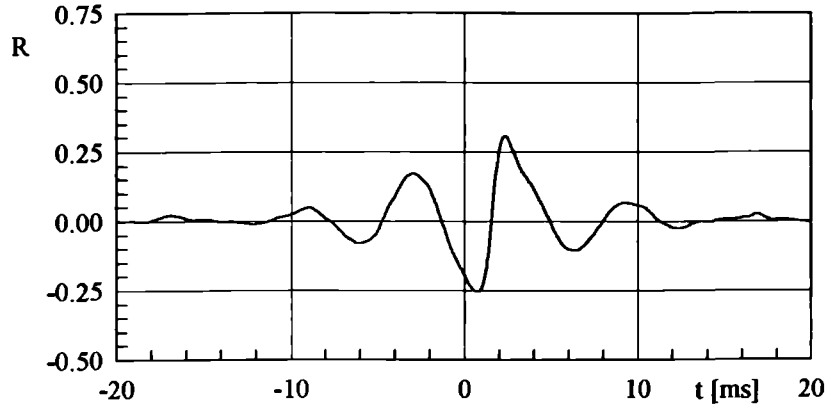

b

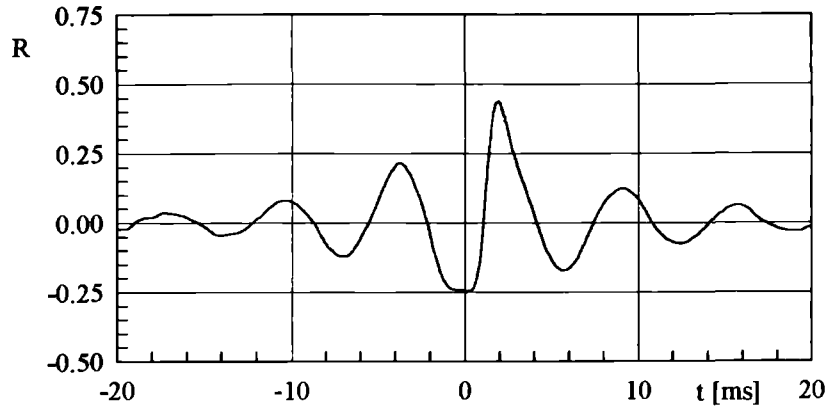

c

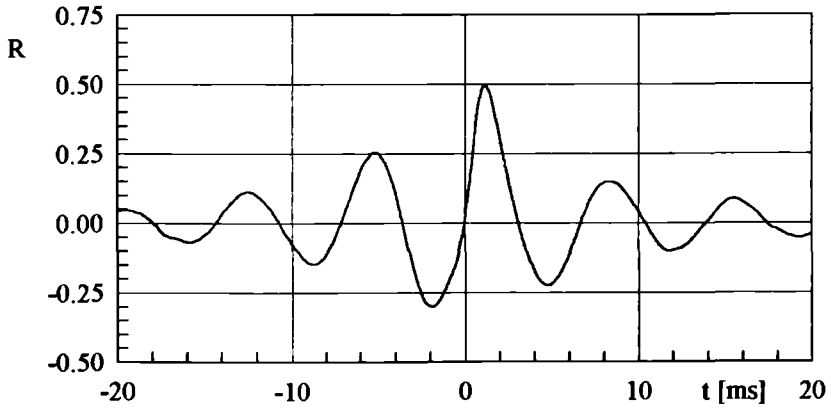

Master probe in vertical plane at x = 60 mm and r = 11.0 mm
Slave probe in horizontal plane:

a) x = 45 mm (-15 mm in relation to master), r = 9.0 mm
b) x = 50 mm (-10 mm in relation to master), r = 10.0 mm
c) x = 60 mm (the same cross-section as master), r = 11.0 mm

Figure 4.37.*(continued on the next page)*.

d

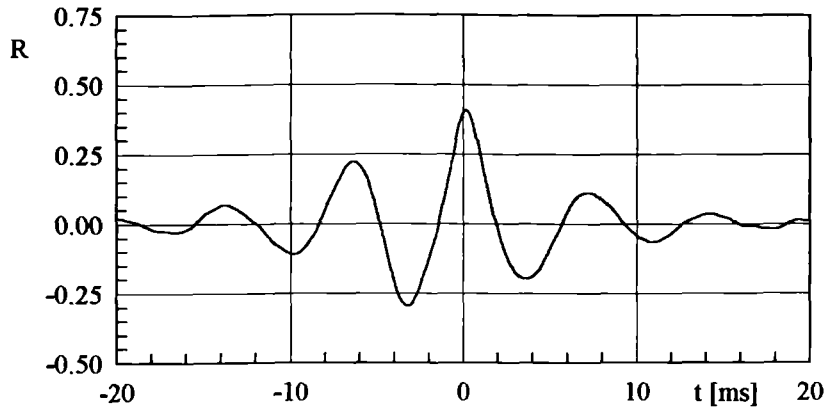

e

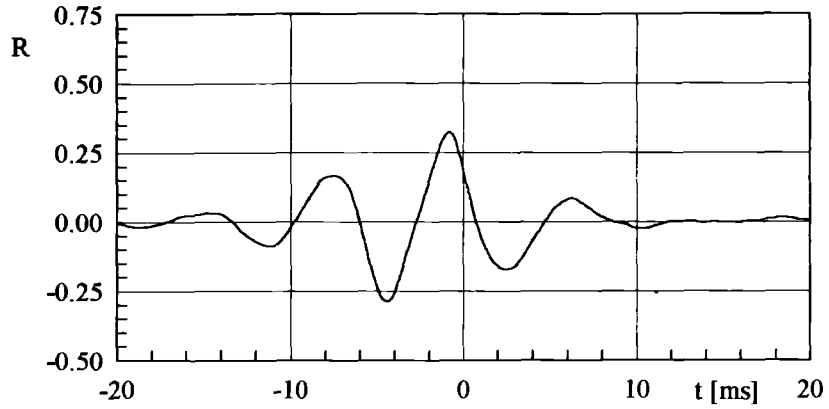

f

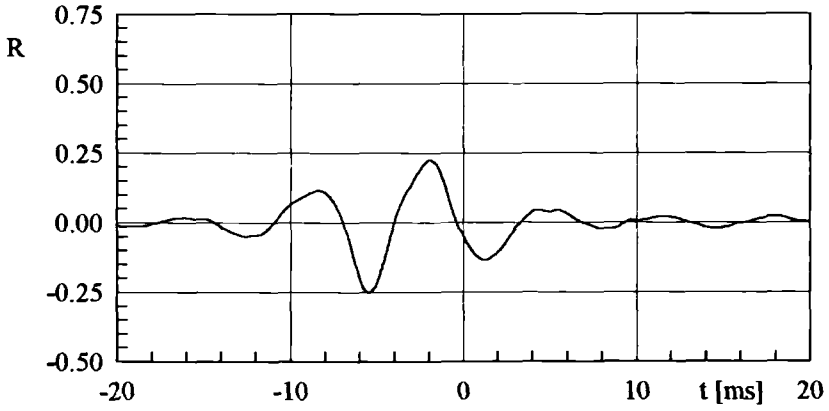

Master probe in vertical plane at x = 60 mm and r = 11.0 mm
Slave probe in horizontal plane:

d) x = 70 mm (+10 mm in relation to master), r = 12.0 mm
e) x = 80 mm (+20 mm in relation to master), r = 13.0 mm
f) x = 90 mm (+30 mm in relation to master), r = 14.0 mm

Figure 4.37.(*Continued on the next page*).

g

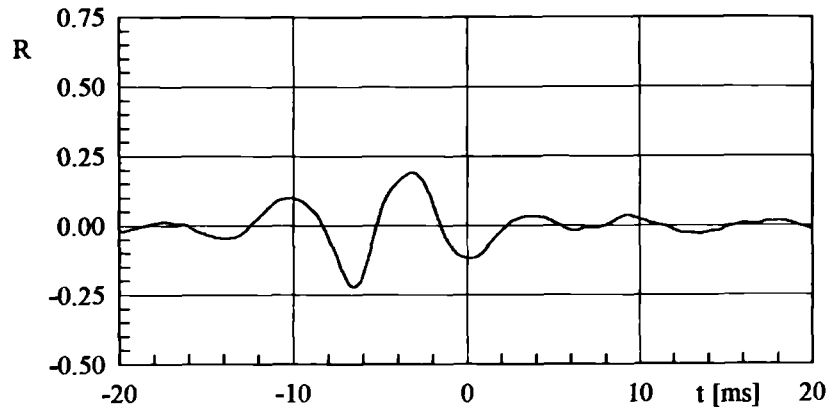

h

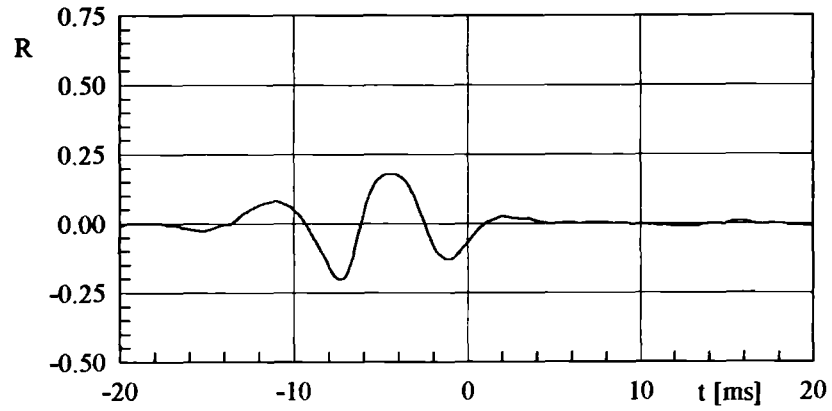

i

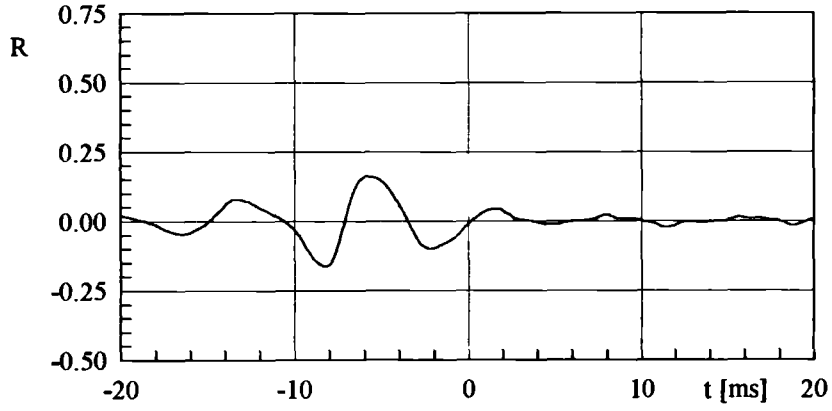

Master probe in vertical plane at x = 60 mm and r = 11.0 mm
Slave probe in horizontal plane:

g) x = 100 mm (+40 mm in relation to master), r = 15.0 mm
h) x = 110 mm (+50 mm in relation to master), r = 15.5 mm
i) x = 120 mm (+60 mm in relation to master), r = 16.0 mm

Figure 4.37.Time correlation for the probe arrangement from figure 4.33b.

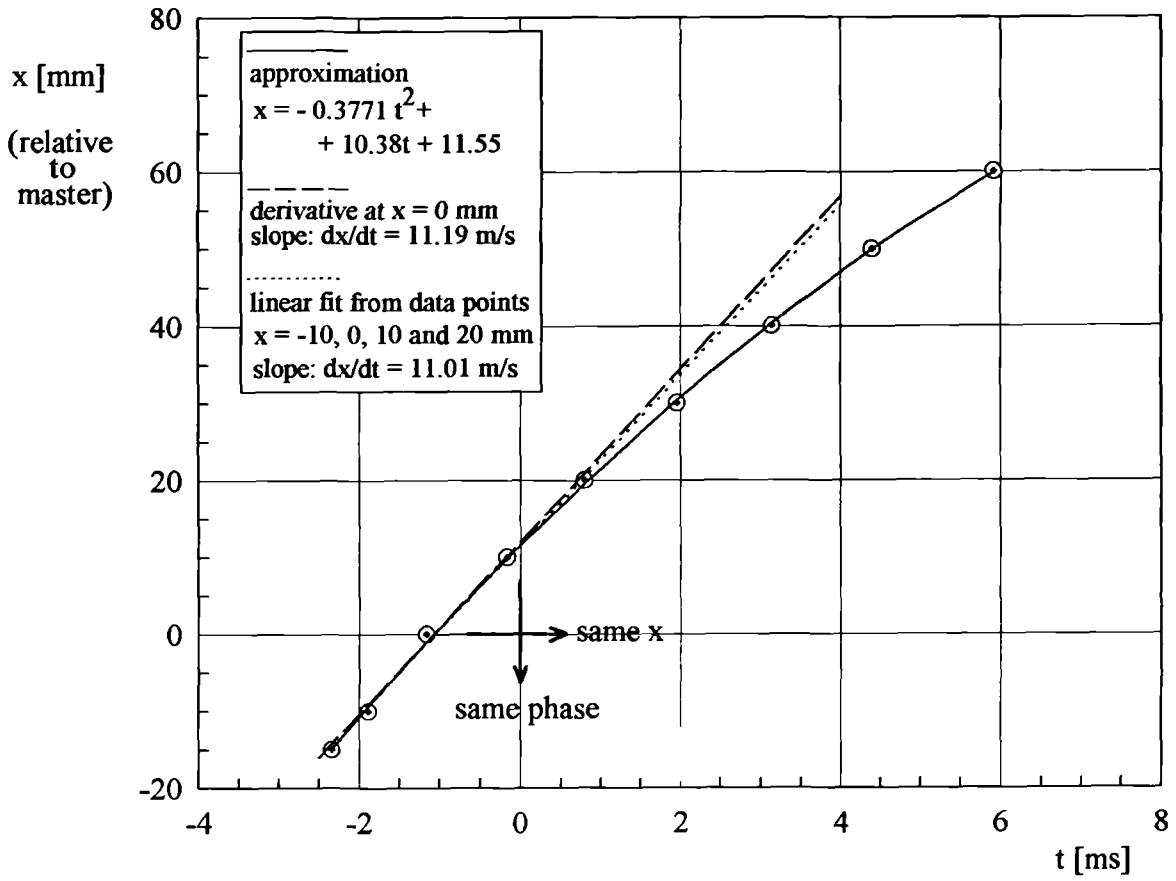

Master probe in vertical plane at x = 60 mm and r = 11.0 mm

Slave probe in horizontal plane at (x,r) - in [mm] as follows:

(45, 09.5) , (50, 10.0) , (60, 11.0) , (70, 12.0),
(80, 13.0) , (90, 14.0) , (100, 15.0) , (110, 15.5),
(120, 16.0)

Figure 4.38.Time lag vs. distance for probe arrangement from figure 4.33b.

as a derivative of the polynomial expression, is 11.19 m/s, whereas from the linear fit of the first four points it is 11.01 m/s (which is close to the results from the previous configuration). From graph 4.38 the position of the slave probe, at which the signals are *in phase* is x=11.55 mm downstream of the master[11]. This suggests the important conclusion that the disturbance is of a spiral kind, and not ring-like. From figures 4.37c and 4.38 it can be inferred that the apparent speed of propagation of pressure disturbances in the azimuthal direction (obtained from the azimuthal

[11] See footnote 10 on page 176.

distance and time delay) is 16.1 m/s. Here the ratio of azimuthal propagation speed to 'free stream' axial velocity is about 1.1.

It should be emphasised that the magnitude of both the longitudinal and the azimuthal propagation speeds may result from the convection and simultaneous rotation of the anticipated spiral structure (if this tentative hypothesis is correct). The relatively simple tests described do not allow more specific inferences to be drawn. The ratio of azimuthal and longitudinal distances between the probes for the situation in which the signals are in phase gives the helix angle of the spiral structure as $\gamma=\arctan(17.28/11.55) \approx 56^{\circ}$ [12]. In addition the sense of the spiral would have to be *opposite* to the sense of streamlines (which were obtained from the velocity measurements) to justify the appearance of zero time lag - see figure 4.39.

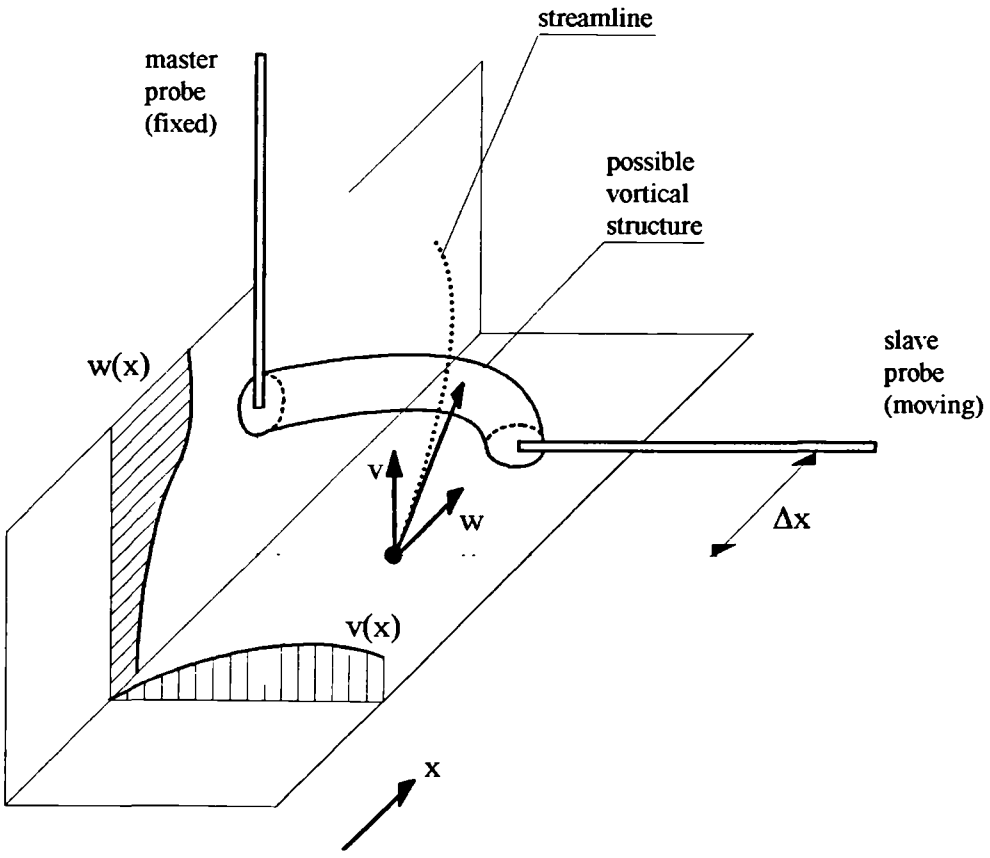

Figure 4.39.Orientation of the possible spiral structure.

[12] The argument of arctan is the quarter of the circumference of a circle of 11 mm radius divided by the longitudinal (streamwise) distance between the probes.

4.1.4. Vortex breakdown response to small perturbations

As shown in section 4.1.2 the pressure field associated with the vortex breakdown exhibits distinct quasi-periodic features. They can be easily seen in the pressure (and velocity) spectra as pronounced peaks, appearing some distance downstream of the burst. This led to an idea that the breakdown may perhaps be treated as a mechanical system exhibiting some resonance properties. If so, perturbations imposed upstream of the breakdown might influence the burst.

In order to investigate the response of the quasi-periodic flow field to small periodic perturbations, the vortex tube was equipped with a mechanism which oscillated one of the guide vanes in the air intake. The amplitudes of blade oscillation were approximately 1°, 2° and 3° for the frequency ranges of 0-150 Hz, 0-137 Hz and 0-125 Hz, respectively (the higher the amplitude, the lower the frequency range - because of the characteristics of the electromagnetic transducer used).

The measurements were conducted in the long choke at the streamwise location $x=60$ mm and radial co-ordinate $r=12$ mm (highest RMS level). The flow speed was reduced so that the 'free stream' axial velocity in the narrowest place of the choke was 6 m/s. This was done in order to cover all characteristic frequencies emerging in the flow field by the possible frequency range of the blade excitation.

Figure 4.40 shows pressure spectra obtained for three different runs without the blade oscillations. This gives a rough idea of the scatter of the results, both in the amplitude and the characteristic frequency of pressure fluctuations. It is worth mentioning that generally at lower speeds the spectra are less 'repeatable' as far as amplitude is concerned. This is caused by an increased unsteadiness at low Reynolds numbers (possibly due to an increased sensitivity to drafts in the laboratory) and also less reliable fan control. This problem was not experienced at higher speeds during the usual spectral mapping.

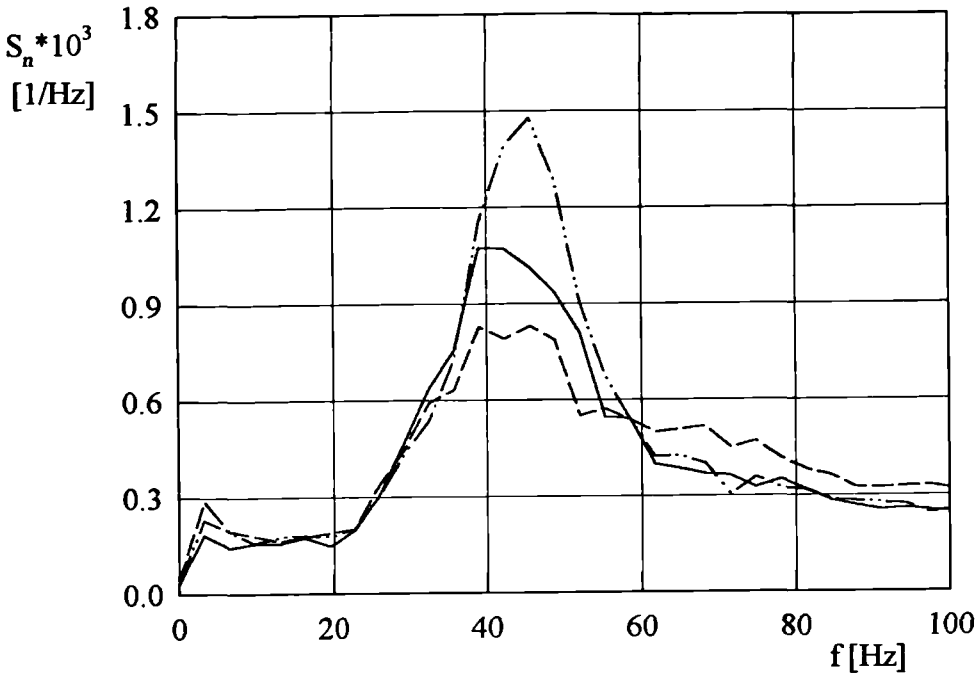

Figure 4.40.Pressure spectra from three different measurements for still blade.

Figure 4.41 shows the pressure spectra for the probe location given above for an amplitude of blade swing of 1° and changing frequency of blade oscillation. Figures 4.42 and 4.43 show the analogous results for blade swing 2° and 3°, respectively.

The tests show that (within the error of measurement) the vortex breakdown is not sensitive to small periodic perturbation. Any 'mechanical' resonance was not revealed in the experimental conditions considered. The exception are graphs *j* and *k* in figure 4.43, for which one can observe an increase in the amplitude of the spectra and a slight shift of the peaks to lower frequencies, especially for the blade oscillating at 112 Hz. These results, however, were obtained when the experimental conditions were far from being small perturbations. In fact the 3° amplitude and high frequency introduced strong unsteadiness, moving the burst ahead of the narrowest place in the choke. Here the dye filament oscillated within 10 mm about the centre of the tube.

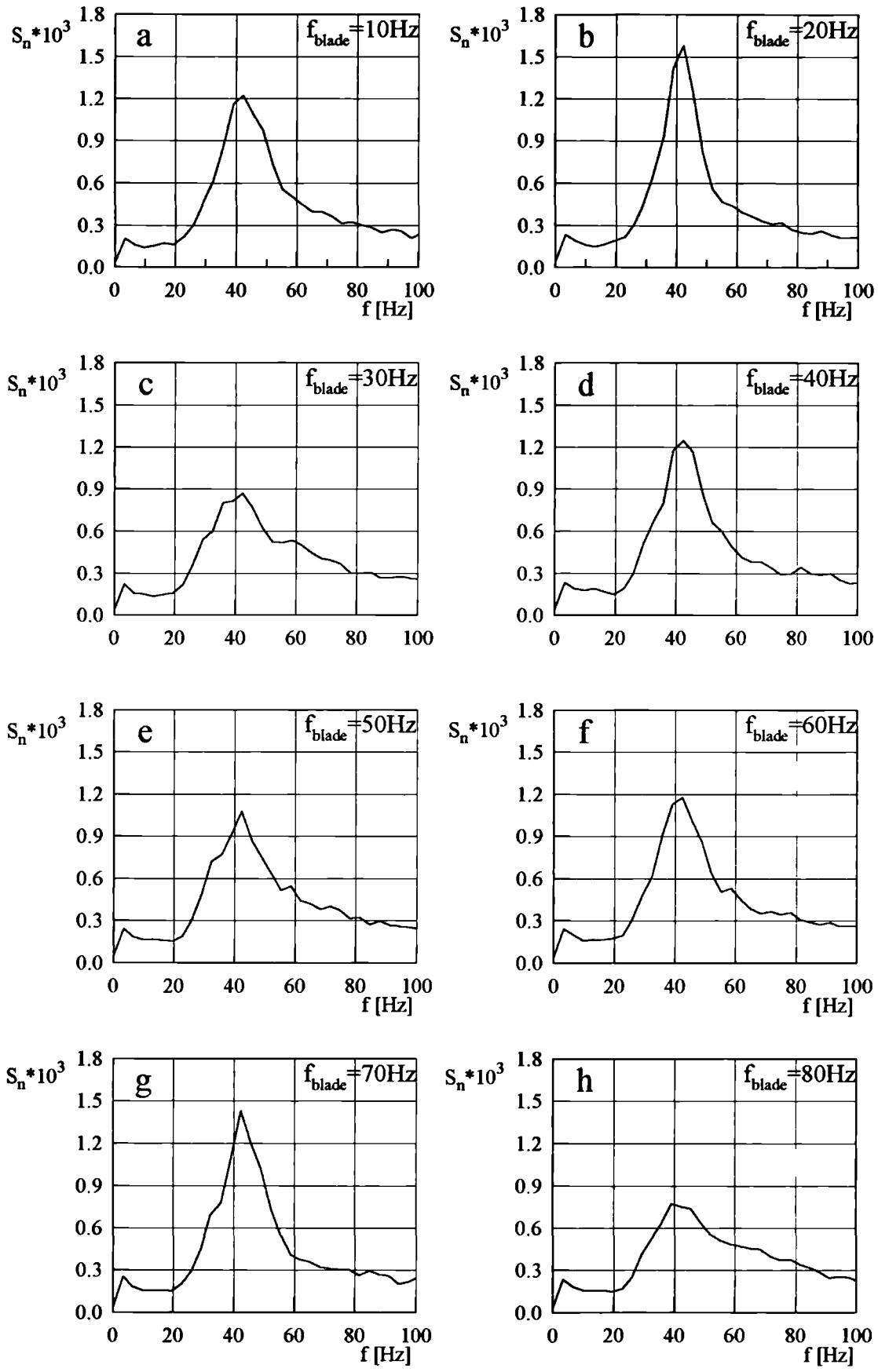

Figure 4.41.(*Continued on the next page).*

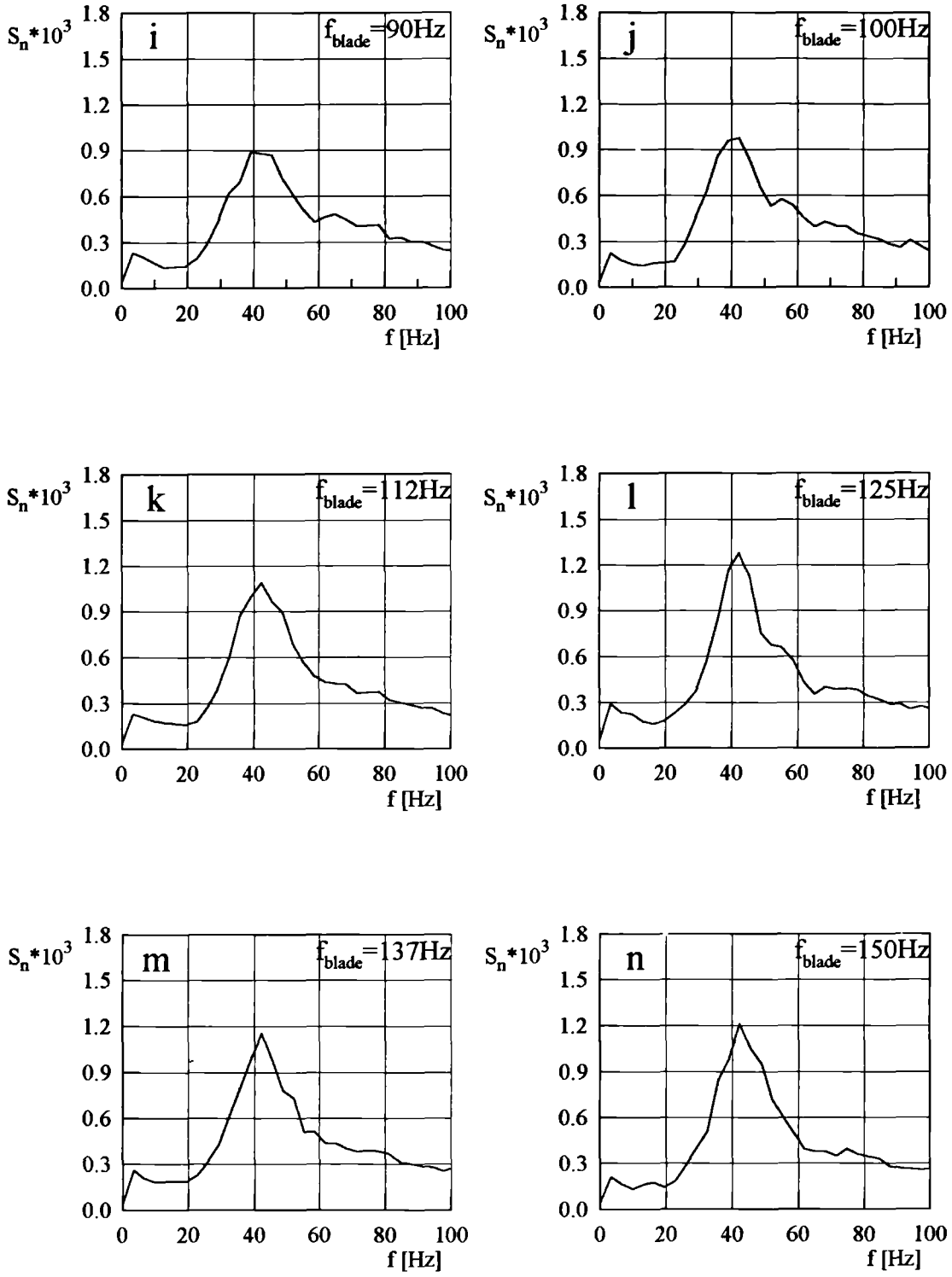

Figure 4.41.Pressure spectra for the blade swing ± 1°.

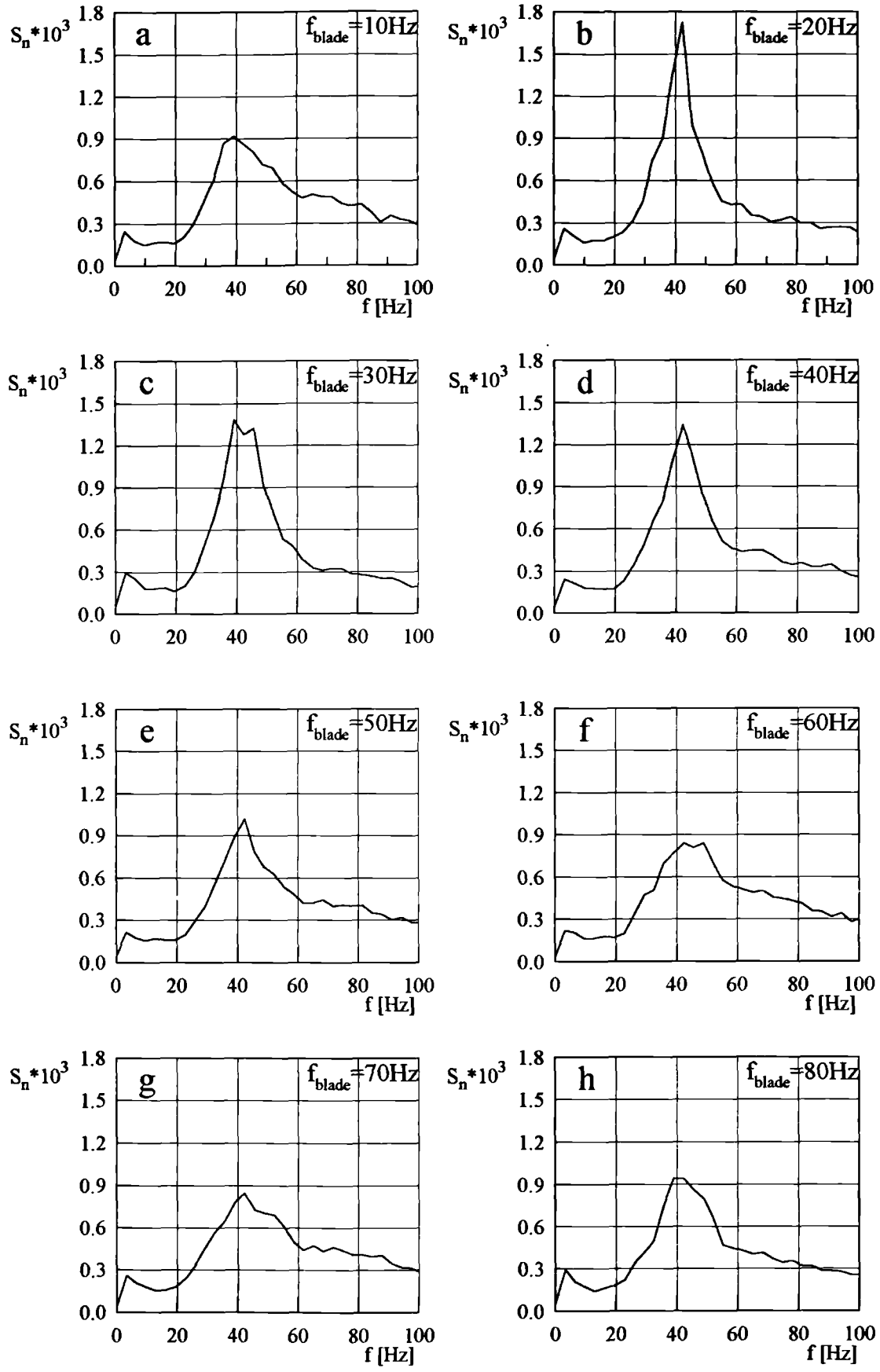

Figure 4.42.(*Continued on the next page).*

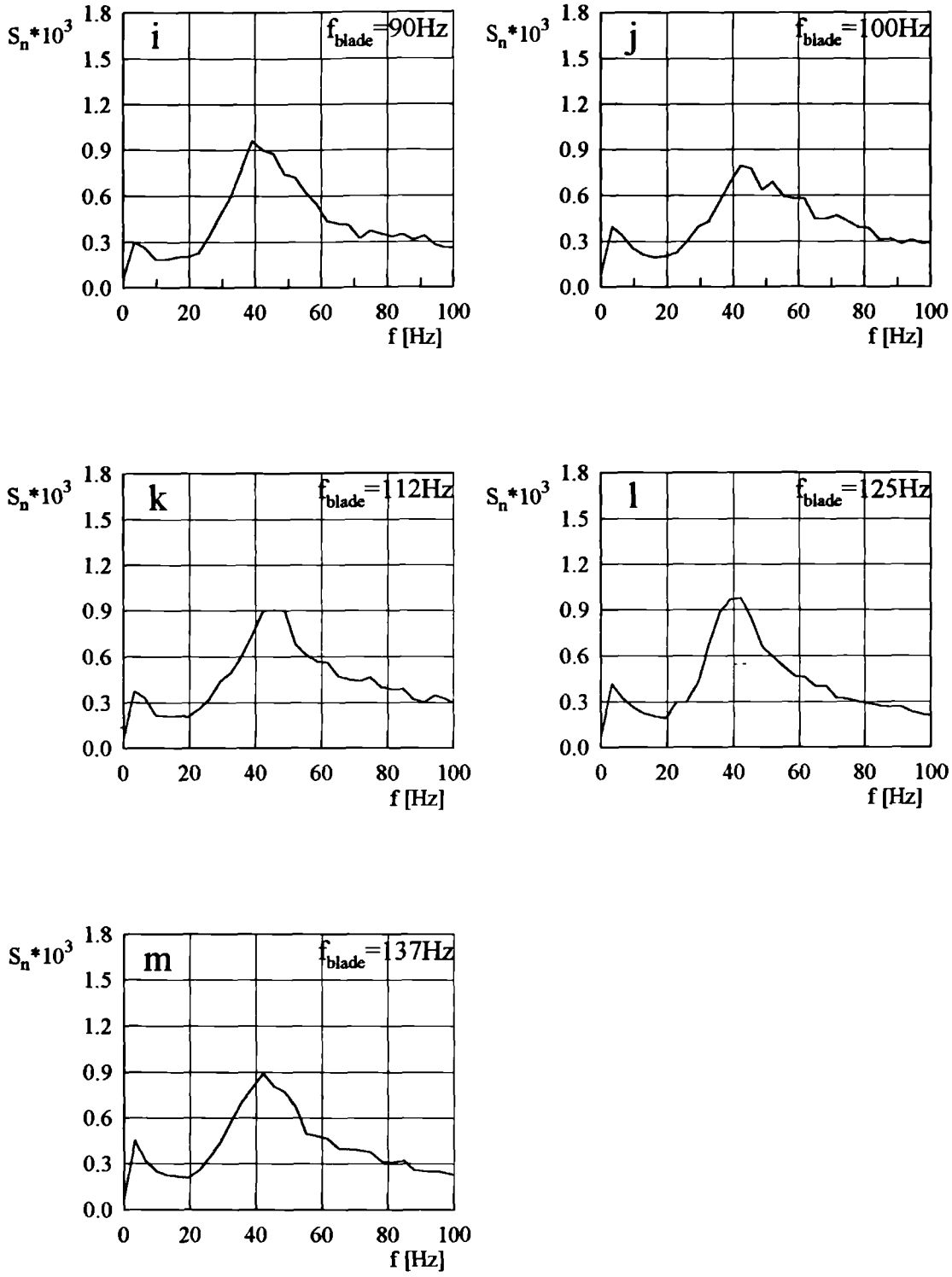

Figure 4.42. Pressure spectra for the blade swing ± 2°

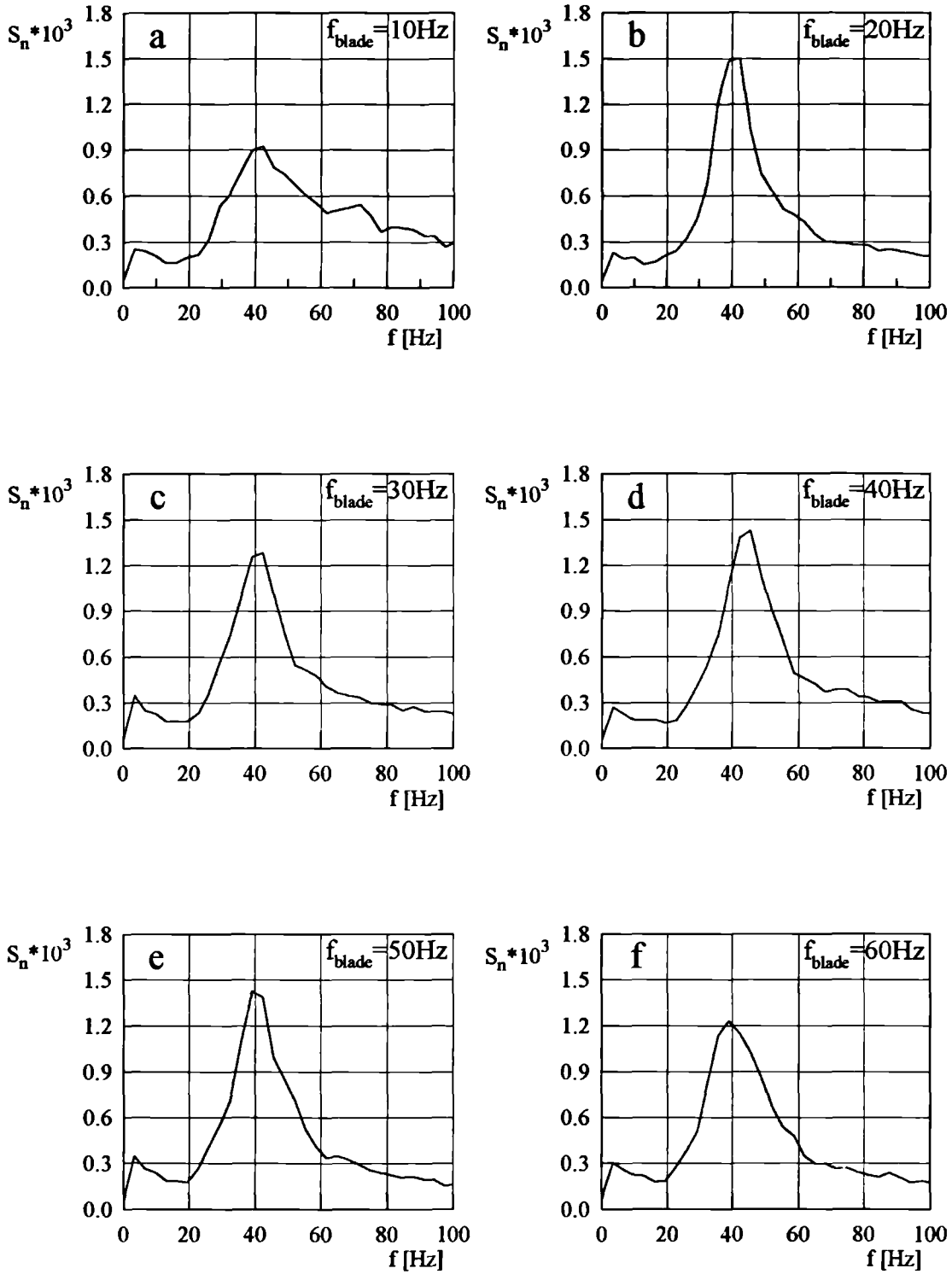

Figure 4.43.*(Continued on the next page).*

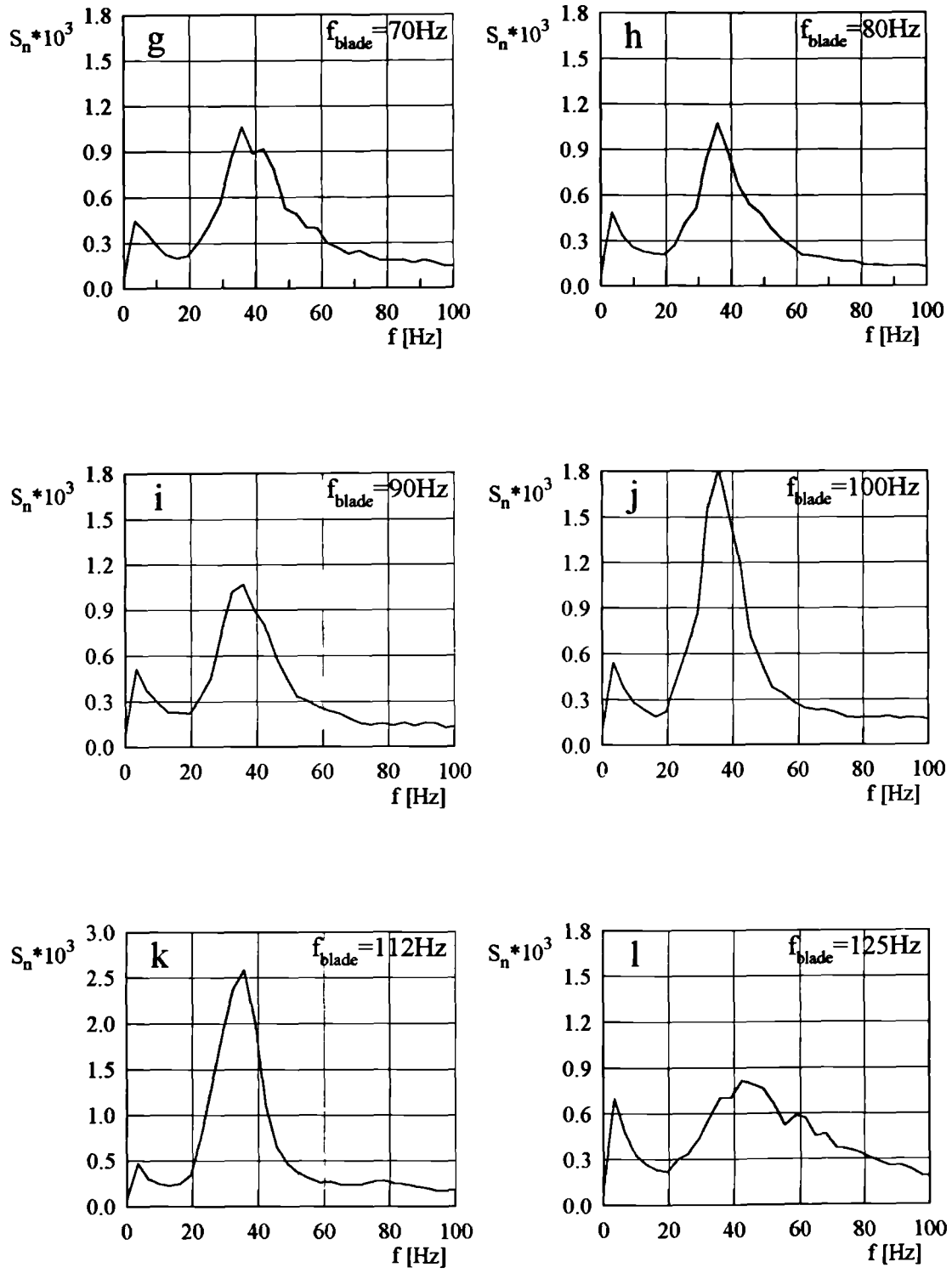

Figure 4.43. Pressure spectra for the blade swing ± 3°

4.2. Wind tunnel tests on delta wing models

The delta wing experiments were conducted for the 65° sweep models described in chapter 3. Table 4.1 gives some details of the tunnel speed (with corresponding Reynolds number based on the root chord), angles of attack, resulting

	Tunnel speed [m/s] *(Re #)*	Angle of attack [deg.]	Approximate burst location (in x/c)	Locations tested (in x/c)
Small model (SM)	6 *(Re=0.13×10⁶)*	21 23 29	0.75 0.50 0.25	1.00 0.85 1.00 0.64 0.85 1.00
	10 *(Re=0.22×10⁶)*	21 23 29	0.75 0.50 0.25	1.00 0.85 1.00 0.64 0.85 1.00
	29 *(Re=0.63×10⁶)*	23	0.50	0.80 1.00
Large model (LM)	6 *(Re=0.26×10⁶)*	24	0.50	0.80
	10 *(Re=0.45×10⁶)*	24	0.50	0.80
	12.5 *(Re=0.56×10⁶)*	24	0.50	0.80
	29 *(Re=1.29×10⁶)*	22 24 29	0.75 0.50 0.25	1.00 0.65 0.80 1.00 0.50 0.75 1.00 1.20

Table 4.1. Configurations tested during wind tunnel experiments.

burst locations, and streamwise locations of the cross-sections tested. Naturally, the burst location (x/c) is established from flow visualisation and, strictly speaking, is only an approximate value, however for simplicity the symbol '=' will be used throughout the text.

4.2.1. Velocity profiles

Figure 4.44 shows the axial velocity radial profiles of obtained from the hot-wire measurements on the smaller model at a tunnel speed of 10 m/s. The angle of attack was 23°, with a resulting burst position at a chordwise location of x/c=0.5. The upper graph (*a*) shows the jet-like profile of an unburst vortex (at x/c=0.35). The two graphs beneath (*b* and *c*) show the wake like profiles obtained downstream of the burst (x/c=0.85 and 1.0).

Figure 4.45 gives axial velocity profiles downstream of the burst[13] for the larger model and a tunnel speed of 29 m/s. The range of the radial co-ordinate r is doubled, so that one can see geometrical similarity (with a factor of 2) between the vortices on both models. The left ends of the curves correspond to the wing surface reached by the probe (figure 4.44) or the most distant point due to its limited length (figure 4.45). The minima in the velocity profiles were associated with the vortex axis. The profiles are not symmetric in relation to vortex axis. The axial velocity of the more outboard side of the vortex is lower (less than the free stream), whereas it is higher on the inboard side (more than the free stream). These differences are reduced moving downstream.

[13] The axial velocity profile prior to the burst was not measured because of the large tunnel speed required for probe calibration - over 70 m/s for an overshoot of the axial velocity of 2.5 times the free stream velocity. This was not achievable at the blockage ratio due to the wing's incidence. In addition the sensitivity of the probes used (thus accuracy of measurements) would be questionable.

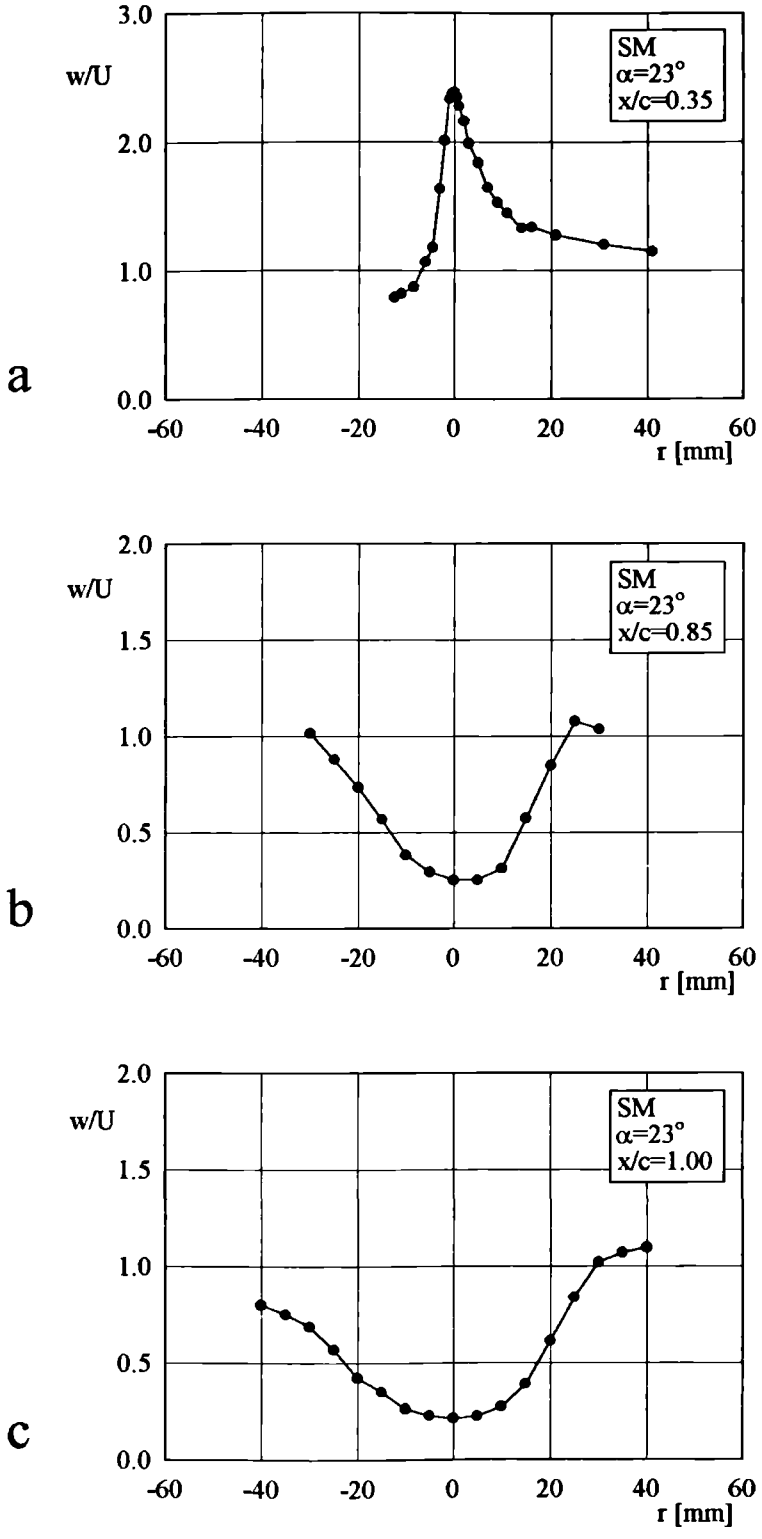

Burst position $x_B/c=0.50$

Figure 4.44.Axial velocity profiles (U=10 m/s, $\alpha=23^{o}$, small model).

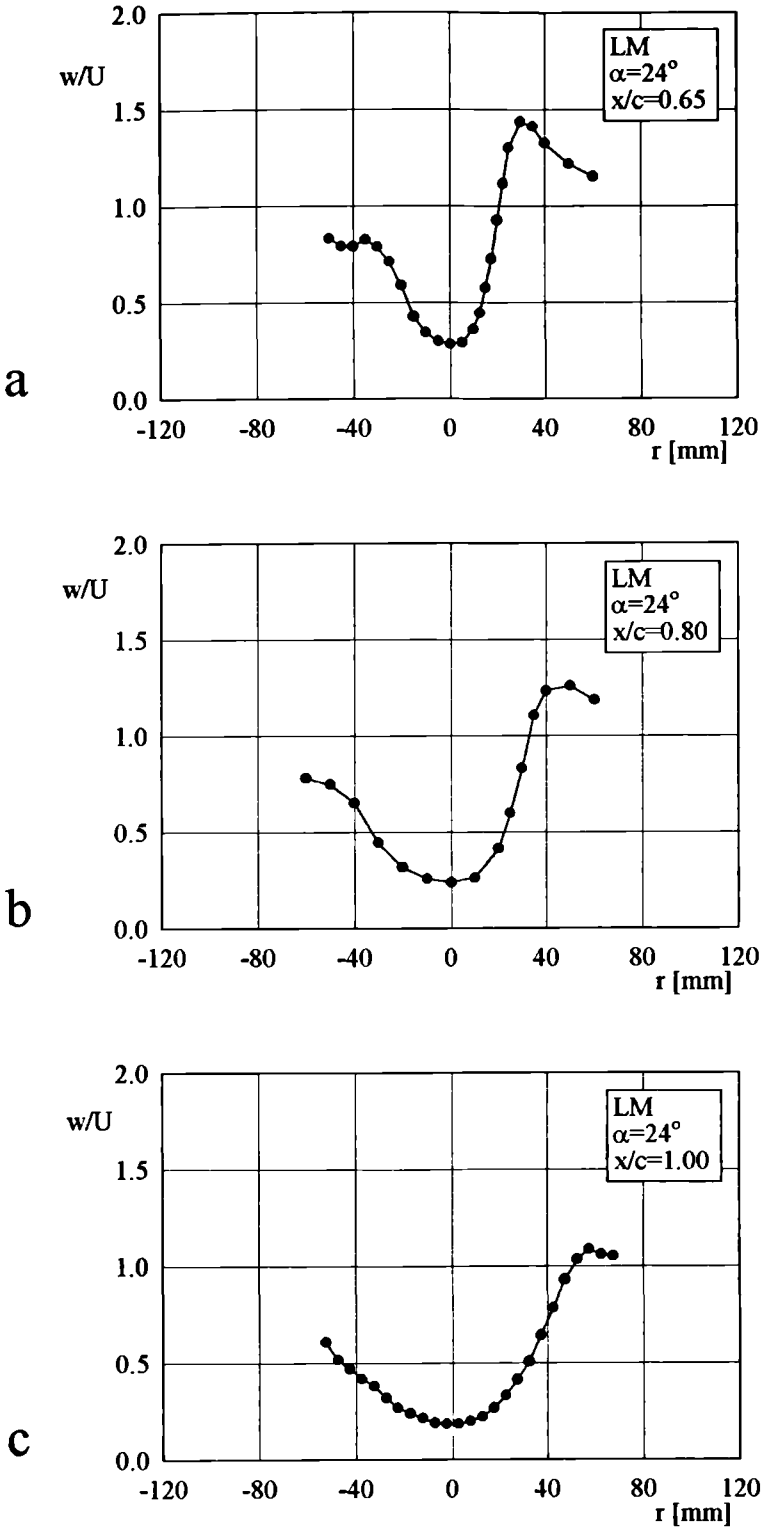

Figure 4.45.Axial velocity profiles (U=29 m/s, α=24°, large model).

4.2.2. Spectral mapping of pressure and velocity fluctuations.

It is worthwhile recalling that in the delta wing experiments, burst location control is much more difficult than inside the choke of the vortex tube. Introducing a probe into the flow affects the burst to a greater extent (its location is more sensitive to the probe's presence). In addition there is no other way of controlling the circulation than a change in the angle of attack. This in turn changes the position of the vortex relative to the wing and the measurements for different streamwise locations become incomparable. Therefore a full picture of the spectra development, including the early stages of the 'broad-band' peaks, is not available. Instead only the results of measurements at a *reasonable* distance behind the burst point are given (i.e. where the probe presence was believed not to affect the measurements).

The arrangement for probe traversing on the delta wing was described briefly in section 3.2.3 It was adopted to enable the same methodology of measurements and presentation methods as those used for the vortex tube experiment. Although the results are somewhat less clear, mainly due to the more complicated flow structure, direct comparisons can be made with the vortex tube experiments.

An example of the development of pressure fluctuation spectra is given for the larger model at an angle of incidence 29° and a tunnel speed 29 m/s. For this configuration the burst takes place at x/c=0.25. Figures 4.46 through 4.49 show the spectra obtained for non-dimensional streamwise co-ordinates of 0.5, 0.75, 1.0 and 1.2 (downstream of the trailing edge). They are presented in the same manner as figures 4.8 through 4.19. Only the inboard side of the vortex is considered (as being less affected by the presence of the probe).

The pressure spectra for x/c=0.5, 0.75 and 1.0 have distinctive peaks (about 200, 90 and 80 Hz, respectively). For x/c=1.2 (figure 4.49) the discrete frequency is lost, perhaps due to the complicated structure of the vortical flow merging with the flow from underneath the wing. It looks as if the frequency due to the breakdown is falling further to about 70 Hz. However a new component of the spectrum (at

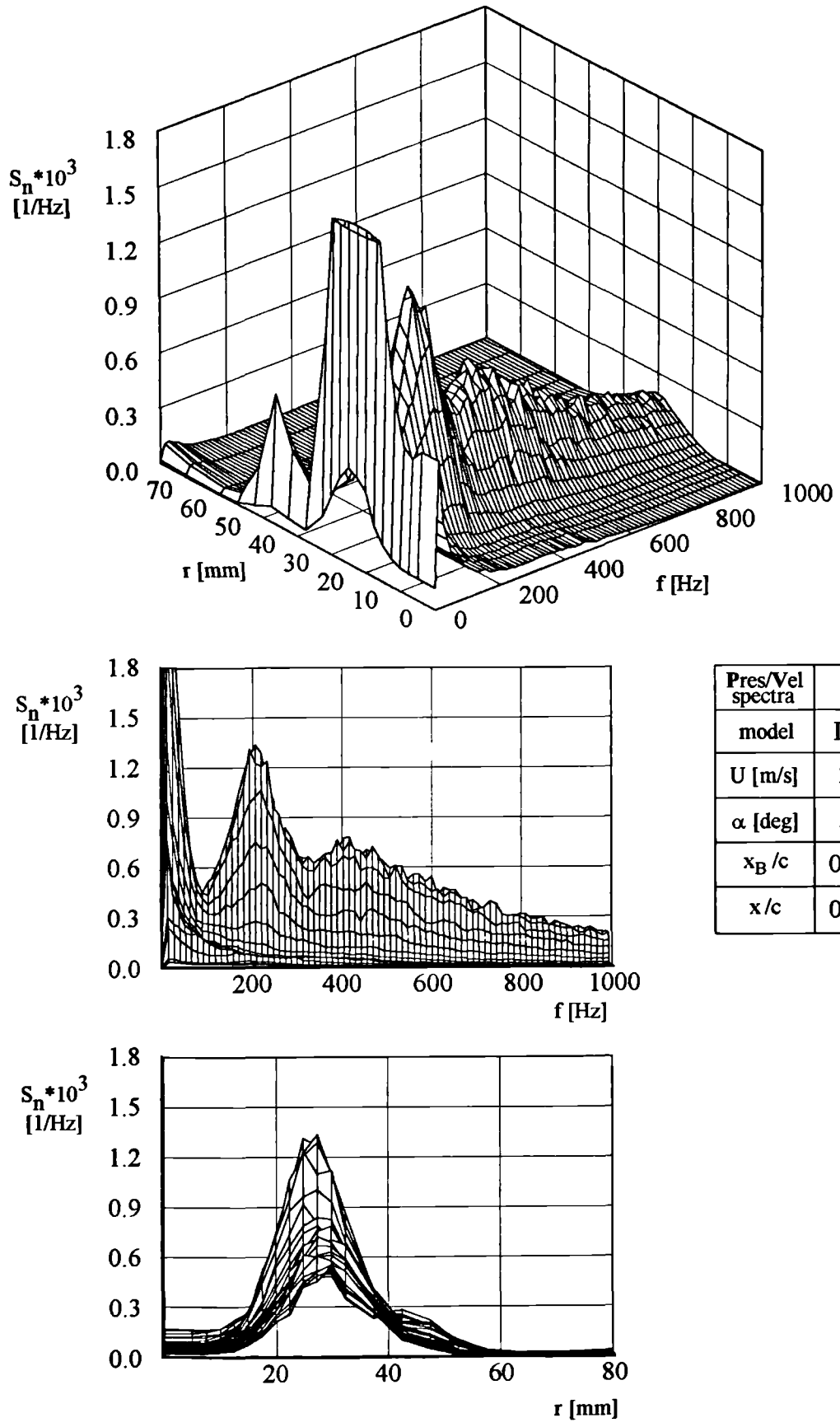

Pres/Vel spectra	P
model	LM
U [m/s]	29
α [deg]	29
x_B /c	0.25
x /c	0.50

Figure 4.46.Pressure spectra (x/c=0.50).

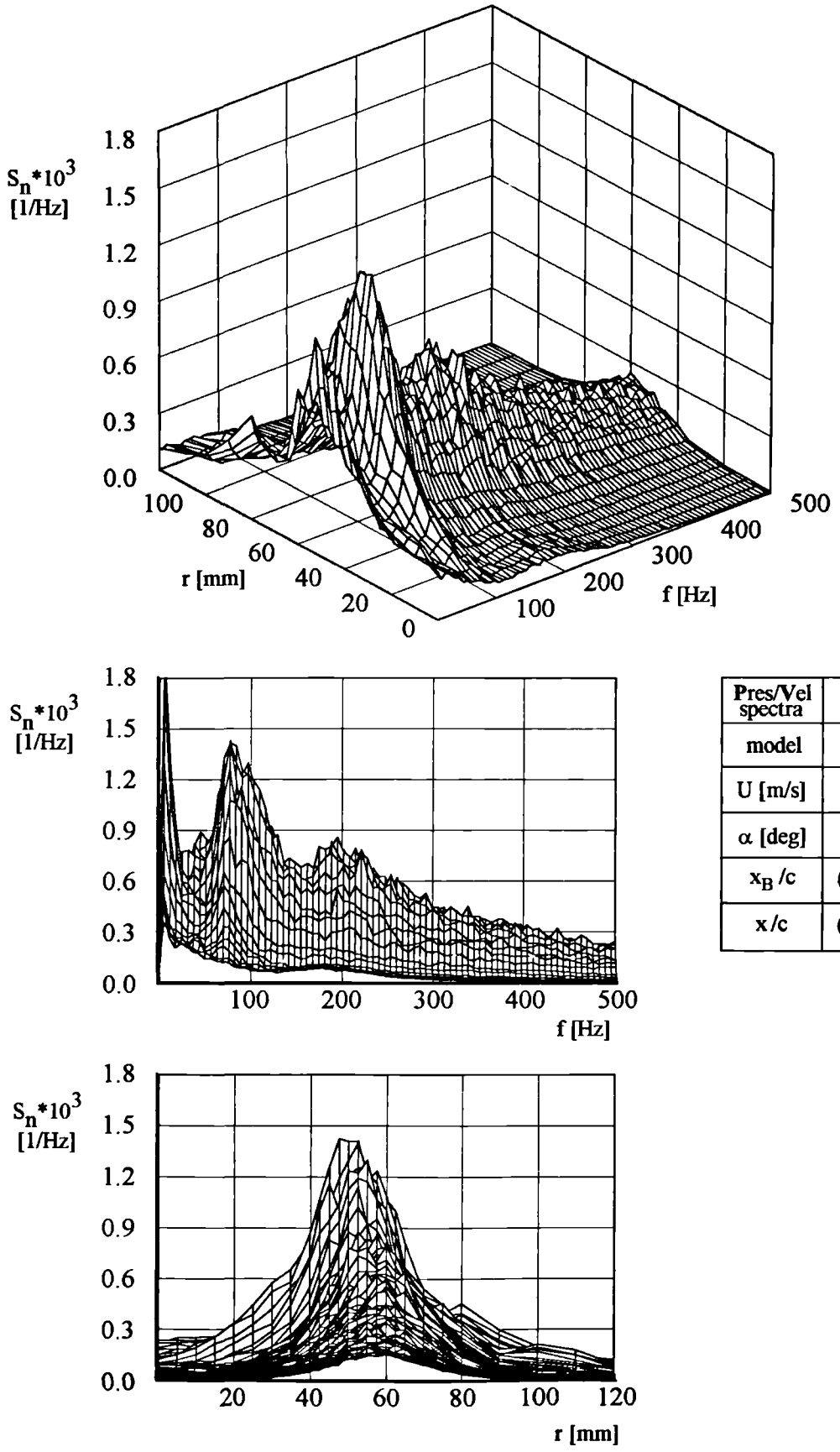

Pres/Vel spectra	P
model	LM
U [m/s]	29
α [deg]	29
x_B /c	0.25
x/c	0.75

Figure 4.47.Pressure spectra (x/c=0.75).

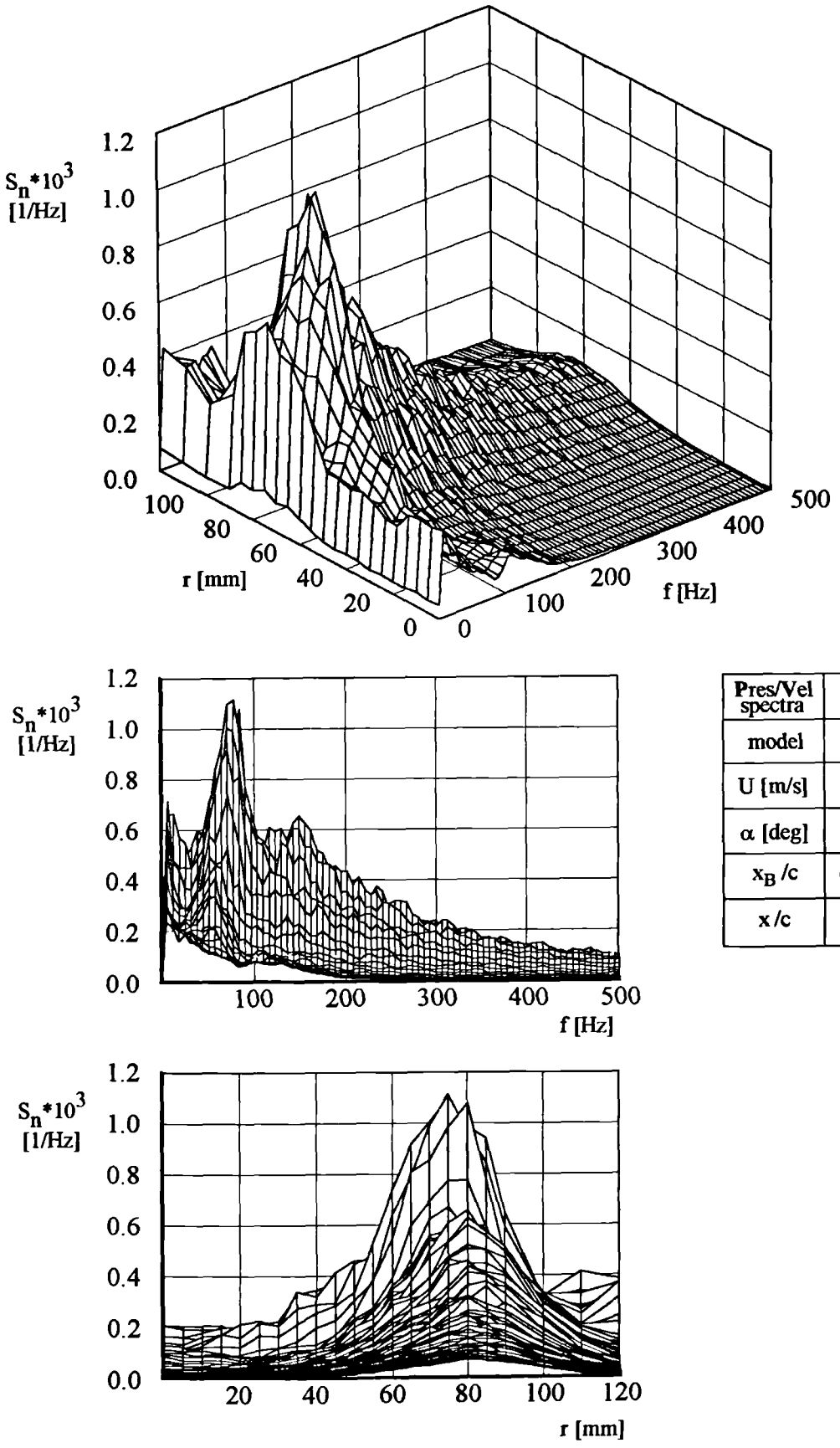

Pres/Vel spectra	P
model	LM
U [m/s]	29
α [deg]	29
x_B /c	0.25
x /c	1.00

Figure 4.48.Pressure spectra ($x/c=1.00$).

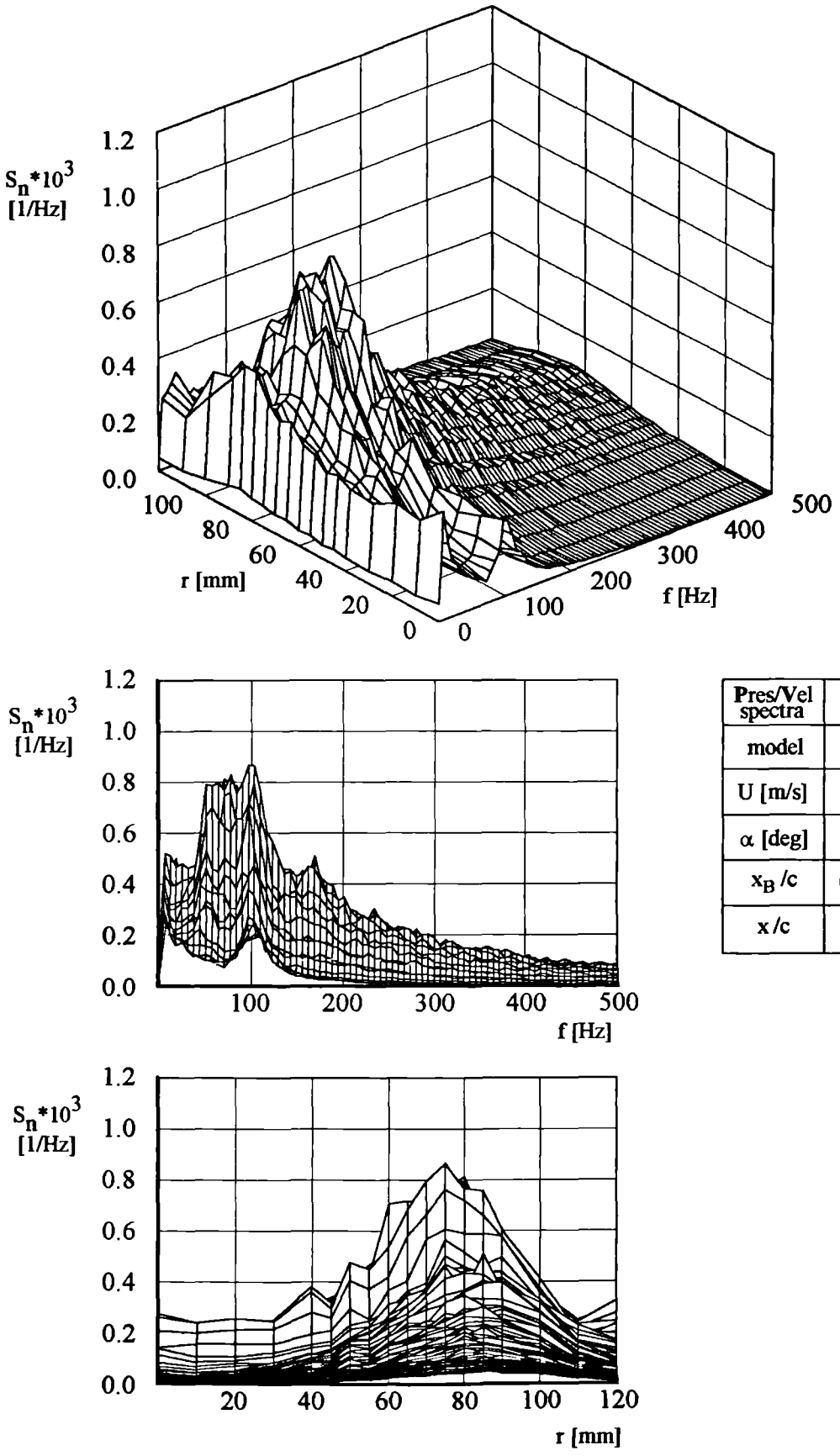

Pres/Vel spectra	P
model	LM
U [m/s]	29
α [deg]	29
x_B /c	0.25
x /c	1.20

Figure 4.49.Pressure spectra (x/c=1.20).

about 100 Hz) begins to dominate. Thus the picture is unclear. The radial position of the peaks is growing in the chordwise direction from about r=25 mm to r=75 mm. Remarkably the amplitude of the spectra (normalised by the square of dynamic pressure in the free stream flow) is close to that obtained in the vortex tube.

The velocity spectra given in figures 4.50 through 4.53 agree fully with the pressure spectra in terms of the dominant frequency and also the radial location of peaks. The last of these figures (i.e. figure 4.53 for x/c=1.2) is again unclear, both in terms of frequency and the radial co-ordinate. Figure 4.54 shows an attempt to 'regain' the information about the breakdown-related features by showing the 'slices' for narrow frequency band and restricted radial co-ordinate.

Figures 4.55, 4.56 and 4.57 show the RMS levels of pressure and velocity fluctuations together with the velocity profiles (similar to figure 4.32). The large hexagon and rhombus mark the radial co-ordinates for which the peaks in the pressure and velocity spectra occur. Here, as for the vortex tube, the maxima in the RMS levels and the maxima in spectra are located closely to the points of inflection in the velocity profiles. The maximum RMS levels in the figures drop from about 1.2 to 0.65 and are generally higher than in the vortex tube. However direct comparison between the spectra (for example figures 4.14 and 4.48) indicates that the increased RMS level comes from the entire contents of the spectrum, rather than from the energy of the quasi-periodic fluctuations. The amplitudes of the quasi-periodic fluctuations are comparable, as noted earlier. The reasons for this different behaviour of spectra for the wing experiments may be sought both in the probe misalignment (the air may 'blow' directly into the probe's port) and also in the character of the flow. The vortical flow is formed from a shear layer separating on the leading edge and not by means of the carefully designed guide vanes.

Some attempts at measurements including burst and pre-burst conditions were made for 10 m/s. This required a manual adjustment of the probe and the angle of attack (say within 0.5°) with smoke visualisation present during the measurement, to assure the correct burst position (despite the presence of the probe). This method

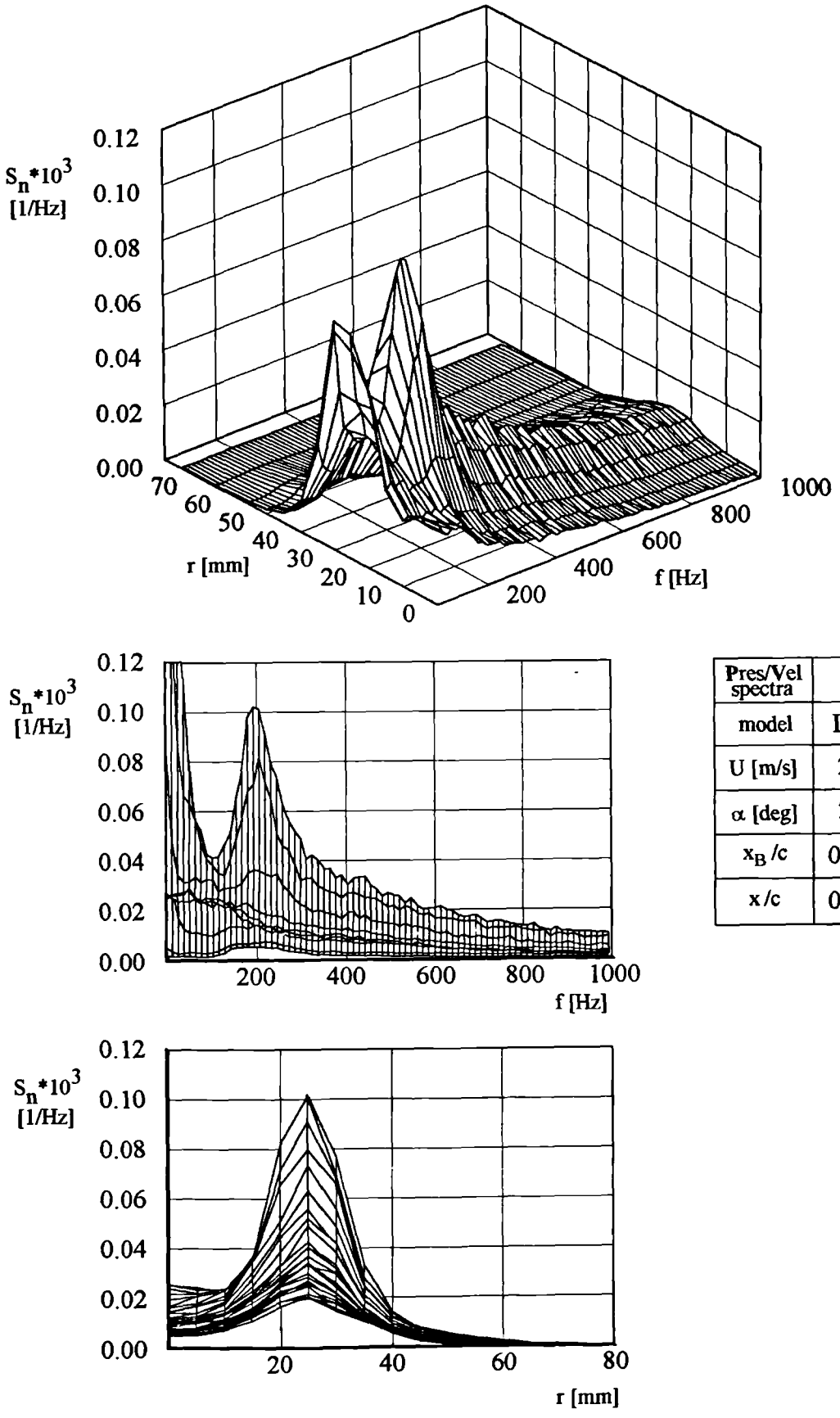

Pres/Vel spectra	V
model	LM
U [m/s]	29
α [deg]	29
x_B /c	0.25
x /c	0.50

Figure 4.50. Velocity spectra (x/c=0.50).

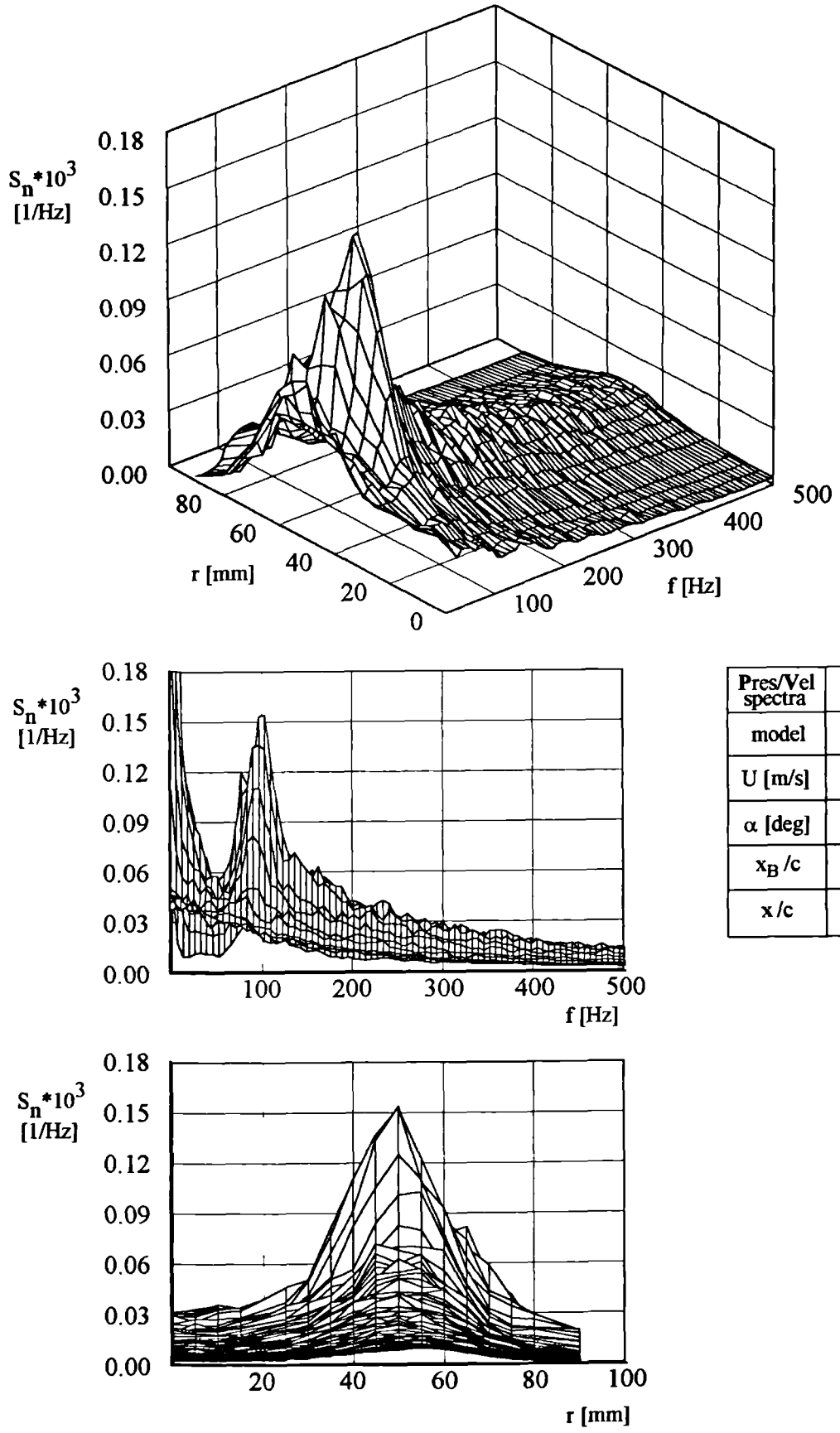

Pres/Vel spectra	V
model	LM
U [m/s]	29
α [deg]	29
x_B /c	0.25
x /c	0.75

Figure 4.51. Velocity spectra (x/c=0.75).

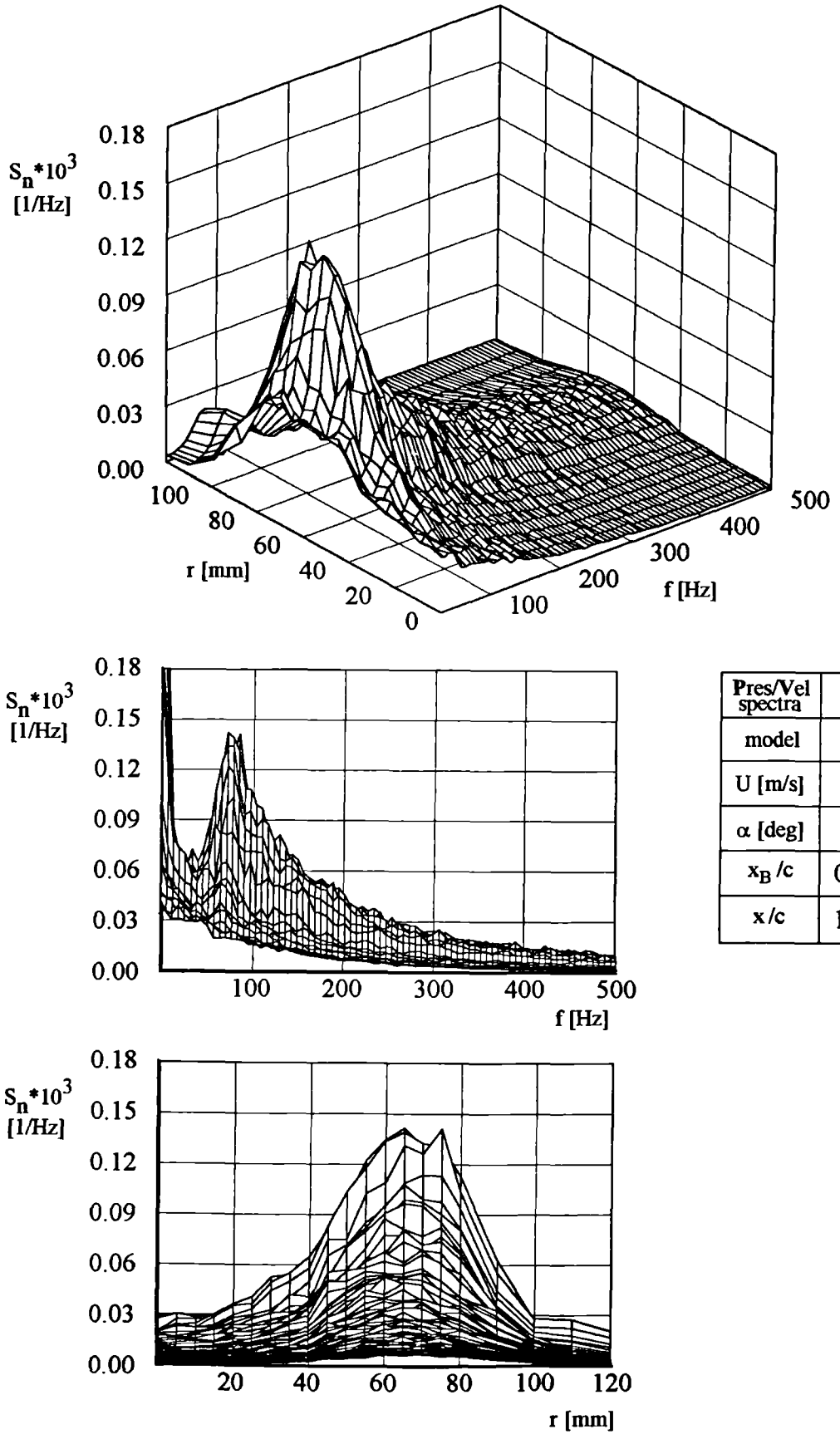

Pres/Vel spectra	V
model	LM
U [m/s]	29
α [deg]	29
x_B/c	0.25
x/c	1.00

Figure 4.52. Velocity spectra (x/c=1.00).

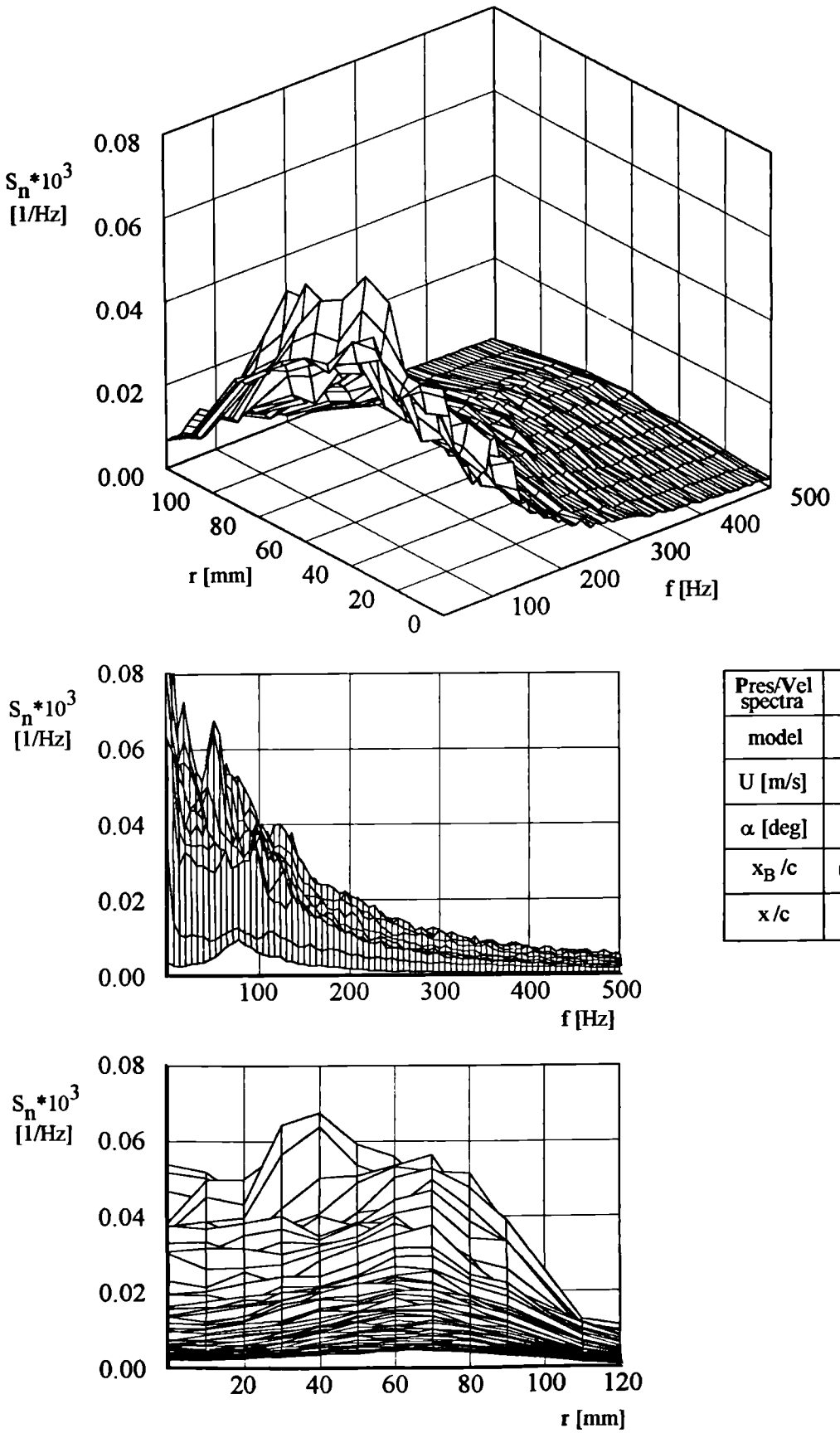

Pres/Vel spectra	V
model	LM
U [m/s]	29
α [deg]	29
x_B /c	0.25
x /c	1.20

Figure 4.53. Velocity spectra (x/c=1.20).

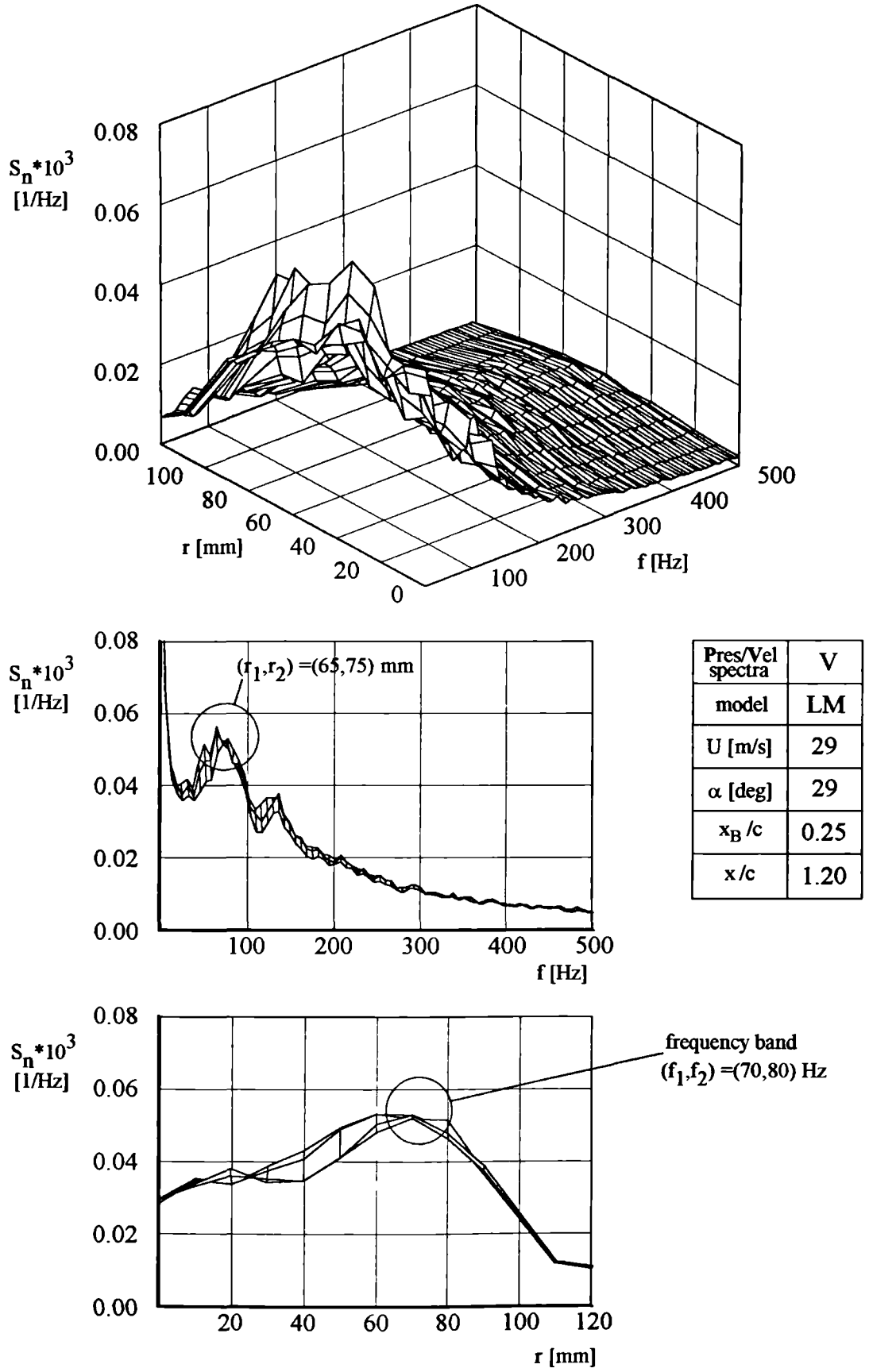

Pres/Vel spectra	V
model	LM
U [m/s]	29
α [deg]	29
x_B /c	0.25
x/c	1.20

Figure 4.54. Velocity spectra (x/c=1.20) - selected bands.

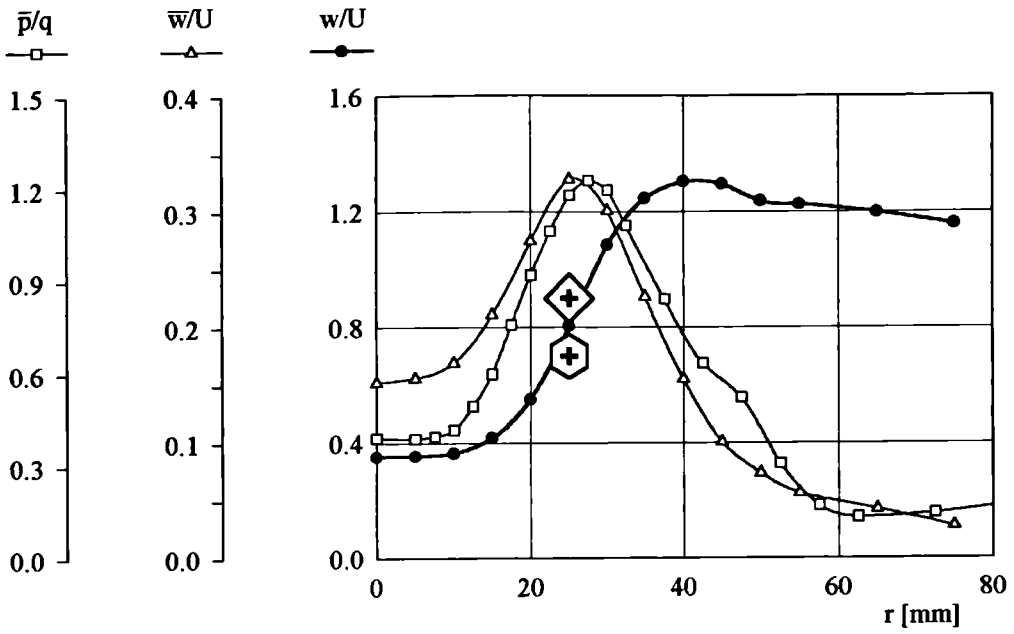

Figure 4.55.Axial velocity profile at x/c=0.50 (U=29 m/s, α=29^{o}, large model), with RMS level of fluctuations and locations of maxima in spectra.

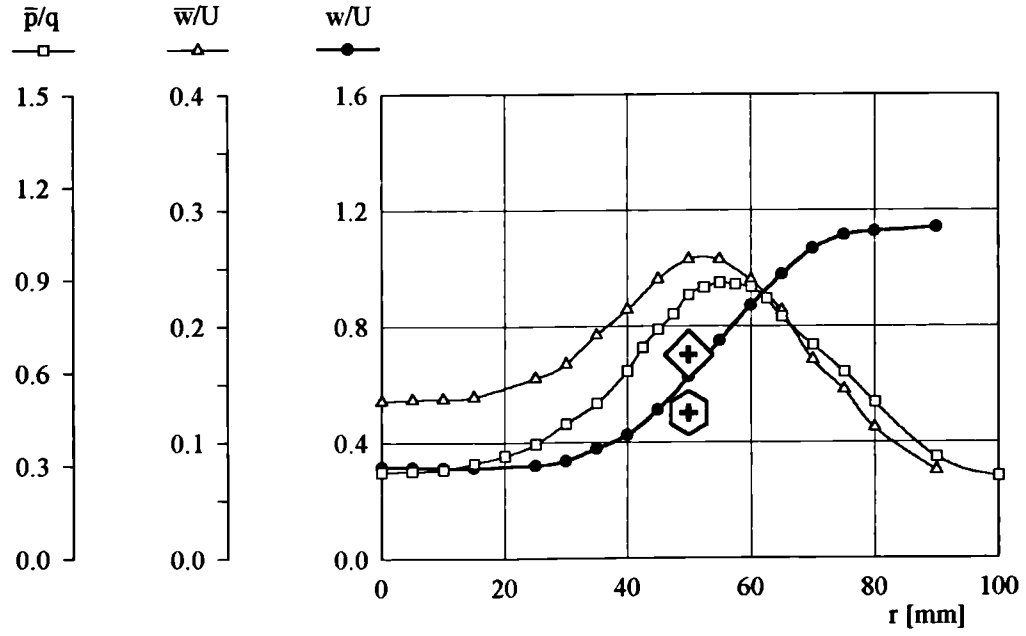

Figure 4.56.Axial velocity profile at x/c=0.75 (U=29 m/s, α=29^{o}, large model), with RMS level of fluctuations and locations of maxima in spectra.

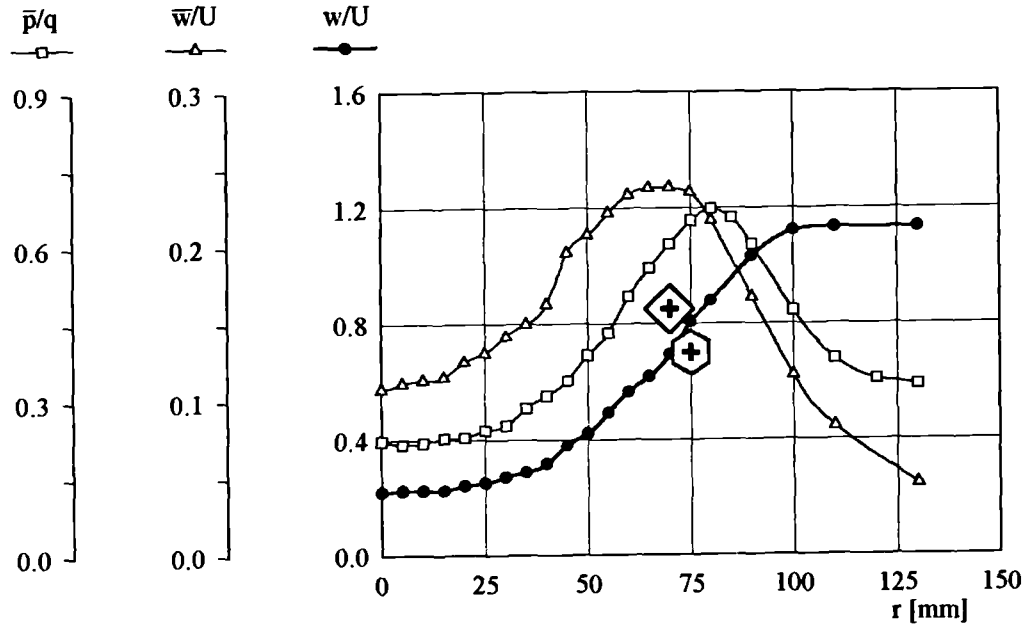

Figure 4.57.Axial velocity profile at x/c=1.00 (U=29 m/s, α=29°, large model), with RMS level of fluctuations and locations of maxima in spectra.

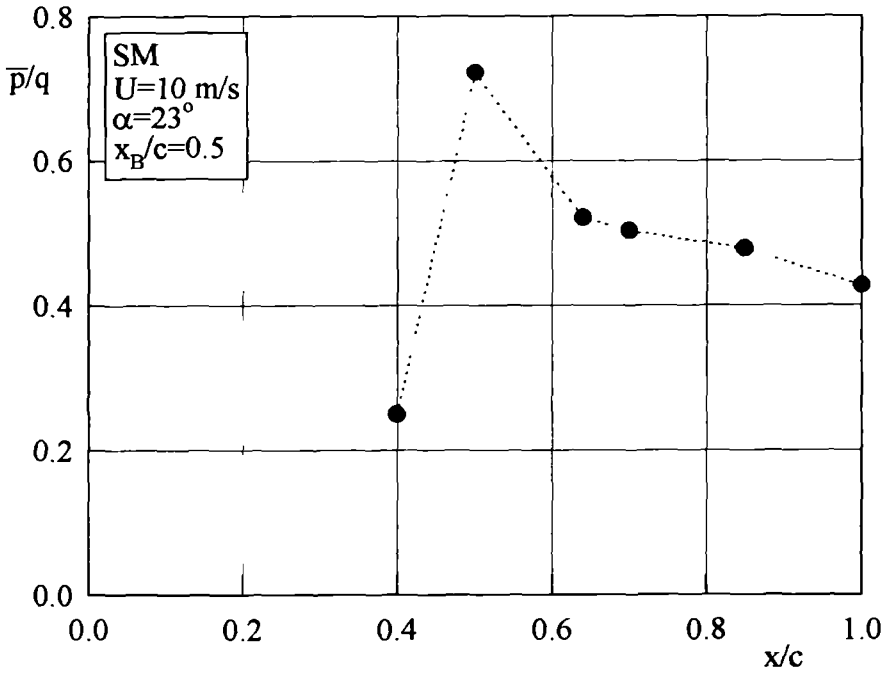

Figure 4.58. Streamwise distribution of maxima in RMS level of pressure fluctuations (U=10 m/s, α=23°, small model).

permitted the recording of a few sets of data corresponding to the highest RMS level indicated by the RMS meter. Figure 4.58 (similar in character to figure 4.28 for the vortex tube) shows the streamwise distribution of the maxima in the RMS level of the

pressure fluctuations for the smaller model at 23° angle of attack and a tunnel speed of 10 m/s. Figure 4.59 shows the corresponding streamwise development of pressure spectra. Here, as for the vortex tube, the spectrum obtained while the probe was 'touching' the surface of the burst 'bubble' has a broad-band character (graph *b*, for $x/c=0.5$). For the following cross-sections the spectra are getting sharper with well pronounced peaks. Finally for $x/c=1.0$ the clear shape of the spectrum is lost.

The spectral mapping of the pressure fluctuations led to the frequency parameters which are defined in a similar manner to the vortex tube experiments. Here the reference velocity in the narrowest place of the choke is replaced by the free stream velocity (tunnel speed):

$$n_{rms} = f D_{rms} / U \tag{4.3}$$

or

$$n_{peak} = f D_{peak} / U \tag{4.4}$$

Figures 4.60 and 4.61 show the frequency parameters based on the diameter of highest RMS level and peaks in the spectra, respectively. These parameters are shown as functions of the Reynolds number based on the root chord. The data points enclosed in circles correspond to a single Reynolds number; they are deliberately scattered to avoid merging. Inside the circles the data for the lowest incidence is placed to the left, moderate in the middle and the highest to the right. The open and filled symbols mark the experiments on the smaller and larger model, respectively. Importantly the data from both models overlap (a lower speed and the larger model give results similar to a higher speed and smaller model). Both frequency parameters are increasing slightly with Reynolds number, although the variation is small. The frequency parameter n_{rms} varies between 0.28 and 0.39 and has the mean value of 0.333 with the standard deviation of 0.029. The frequency parameter n_{peak} varies between 0.28 and 0.36 with the mean value of 0.316 and a standard deviation of 0.027.

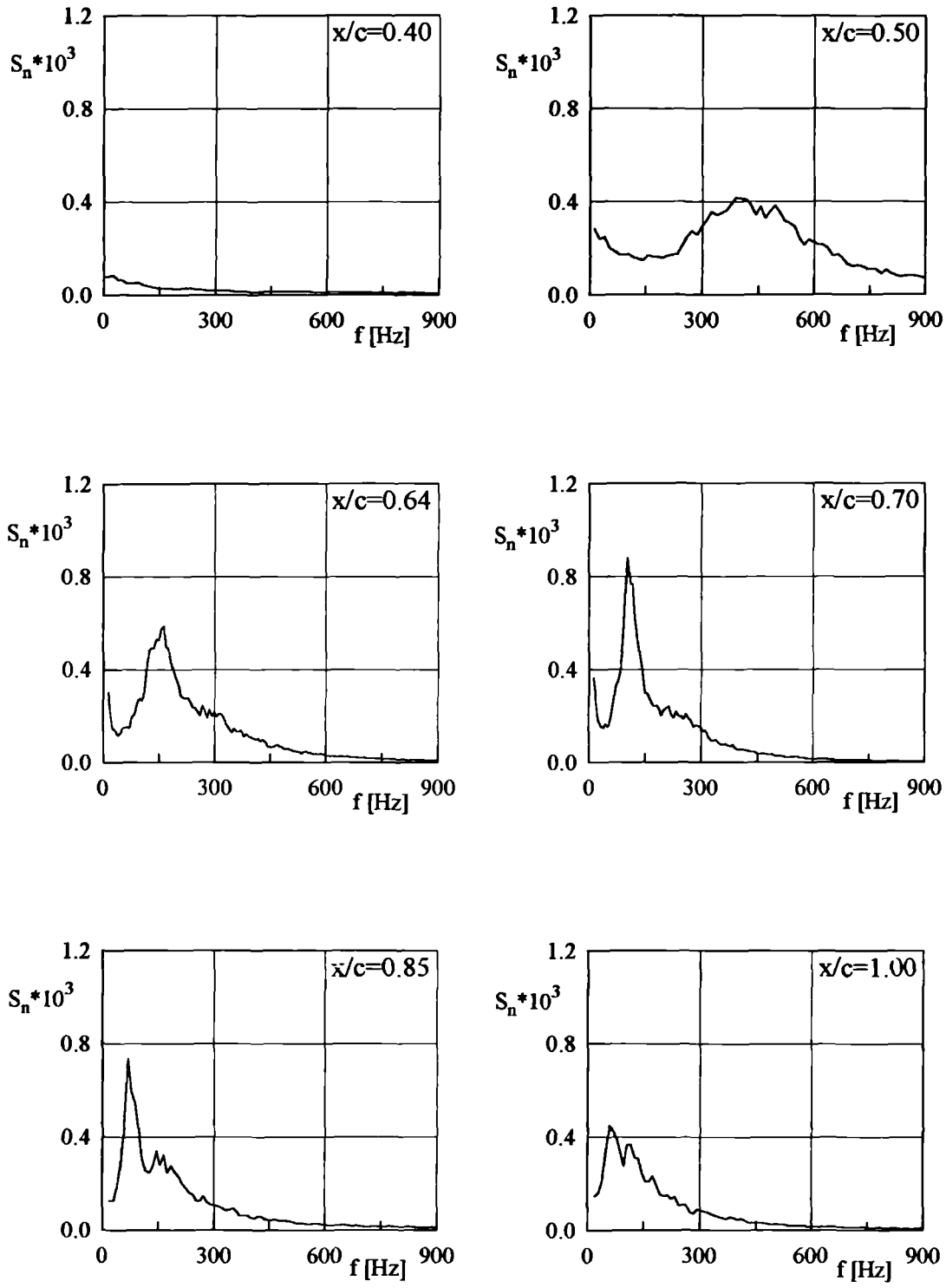

P	SM	U=10 m/s	α=23°	x_B/c=0.50

Figure 4.59. Streamwise development of the sharpest spectra (U=10 m/s, α=23°, small model).

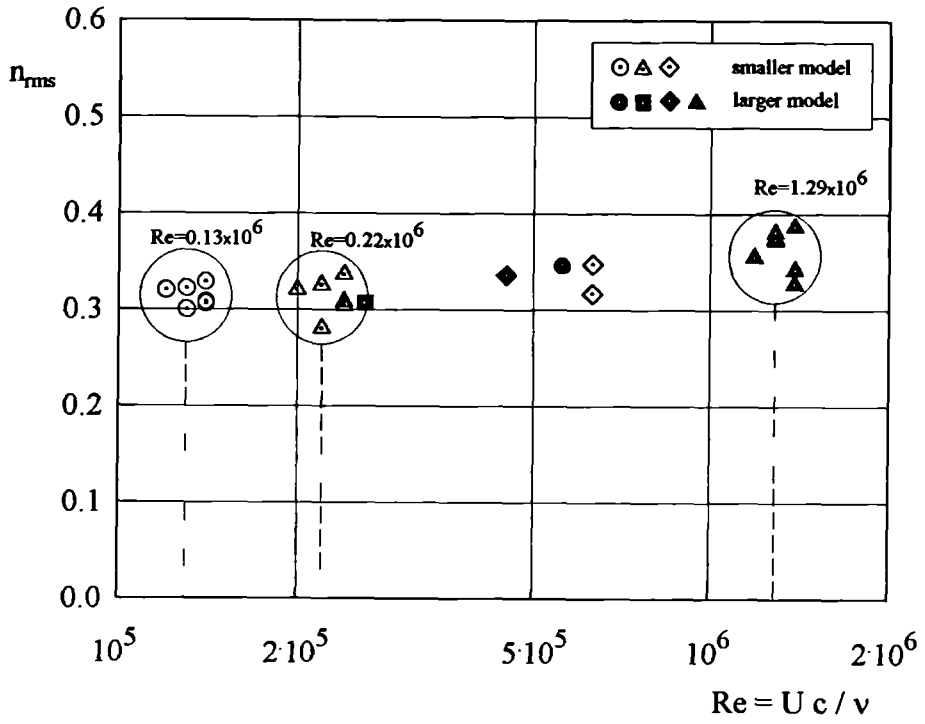

Figure 4.60.Frequency parameter based on the diameter of highest RMS level.

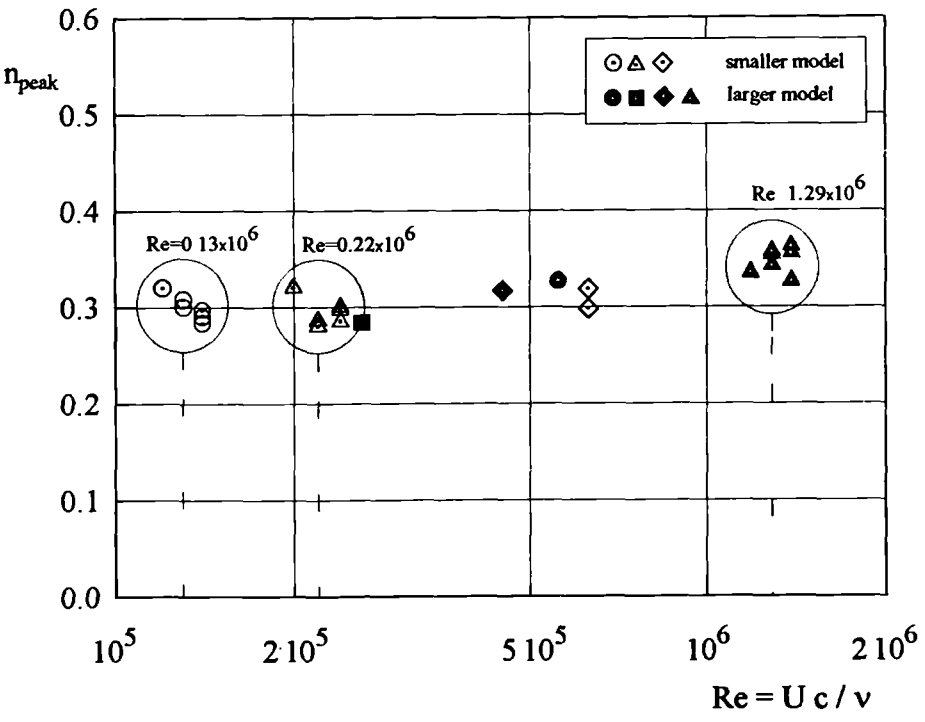

Figure 4.61.Frequency parameter based on the diameter of maxima in the spectra.

The values of peak frequencies for all configurations and wind tunnel speeds tested were substituted into the expression for a frequency parameter proposed by Mabey (1995), and given by equation 2.56. Interestingly, the value of the frequency parameter obtained from the present measurements is $n=0.43 \pm 0.06$, instead of the suggested 0.25 ± 0.02. Perhaps, more systematic measurements would be required to establish a precise value of n.

An important issue from the viewpoint of this investigation was the relation between the pressure fluctuations caused by the vortex breakdown (and indicated by the probe introduced into the flow) and the excitation present on the wing's surface. This was tested by using both the probe (located such that the peaks in the pressure spectra were sharpest) and the flush mounted transducer, introduced directly beneath the vortex axis (figure 4.62). Naturally, both devices were located at the same chordwise co-ordinate (same cross-section of the vortex core). The direct comparison between spectra from the probe and the flush transducer allows inferences to be drawn about the source of the excitation on the wing's surface.

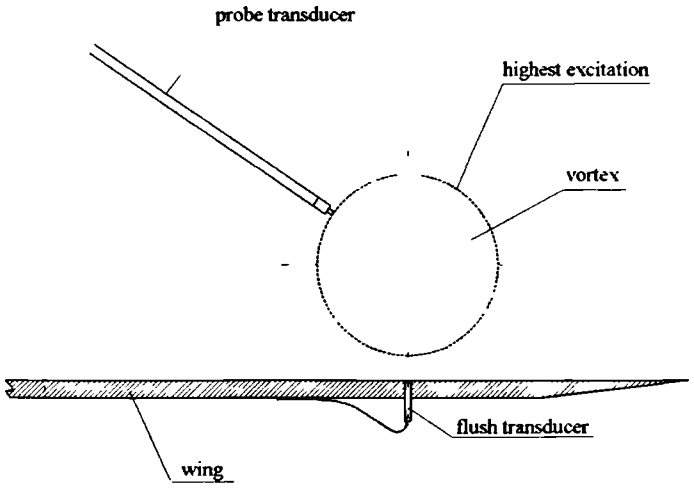

Figure 4.62. Transducer arrangement for comparing vortex core and wing surface pressure fluctuations.

Figures 4.63, 4.64 and 4.65 summarise the measurements for three angles of attack: 22°, 24° and 29° for the larger model at 29 m/s. At the incidence of 22° the burst takes place at x/c=0.75. The pressure spectra were measured (figure 4.63) at the trailing edge (x/c=1.0). Here the peak at about 150 Hz is repeated in both spectra. However the spectrum for the flush transducer has a pronounced peak at lower frequencies (about 40 Hz). Hence measurements including only the wing's surface pressure could lead to false conclusions about the breakdown characteristic frequency. For the incidence of 24° the burst occurs at x/c=0.50. For this configuration two chordwise locations were tested: x/c=0.65 and 0.80 (figure 4.64). For the first location the only common feature of both spectra is the high level and low frequency component (which is not associated directly with the quasi-periodic oscillations). For the second location the spectra have much more in common. The peak due to the vortex breakdown (at about 160 Hz) is present in both of them. However, for the flush transducer the low frequency component is still of the same magnitude as the peak due to bursting. At the incidence of 29° the burst takes place at x/c=0.25. For this situation three chordwise locations were investigated: x/c=0.50, 0.75 and 1.00 (figure 4.65). Here at x/c=0.50 the two spectra have peaks for slightly different frequencies (the reason for this is not known). At x/c=0.75 and 1.00 the spectra from the probe and the flush transducers correspond to each other (the characteristic peak is of the same frequency: about 90 and 80 Hz respectively).

Figure 4.66 shows the ratio of maximum spectral density, obtained from the probe measurements, to the maximum of spectral density, obtained from the flush transducer, for three angles of attack. The amplitudes of peaks related to the breakdown were divided by each other and denoted by $S_{n\,probe}/S_{n,flush}$. From the figure it is apparent that the excitation on the wing's surface increases with incidence. The qualitative explanation for this is given in figure 4.67. For the higher incidence the axis of the vortex is higher relative to the wing's surface, but at the same time the size of the vortex (taken as, say, the diameter of highest excitation D_{rms} or D_{peak}) is

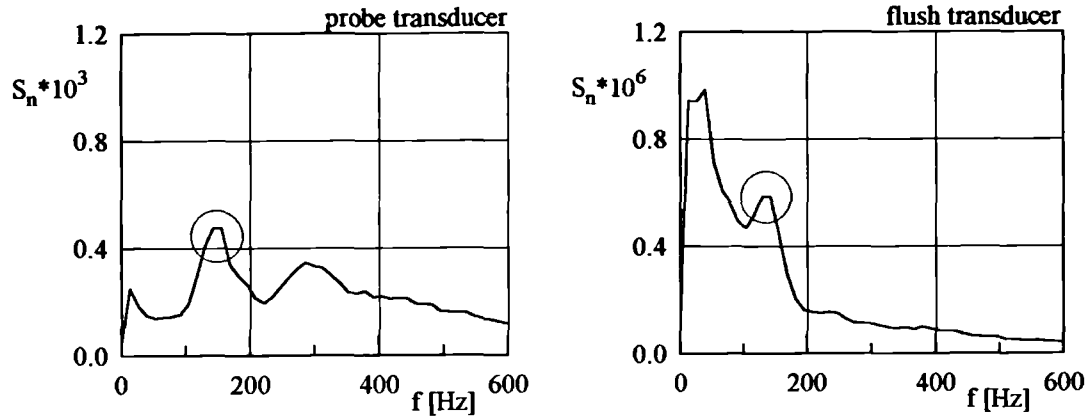

P	LM	U=29 m/s	α=22°	x_B/c=0.75	x/c=1.00

Figure 4.63.Comparison between vortex core and surface pressure fluctuations (α=22°).

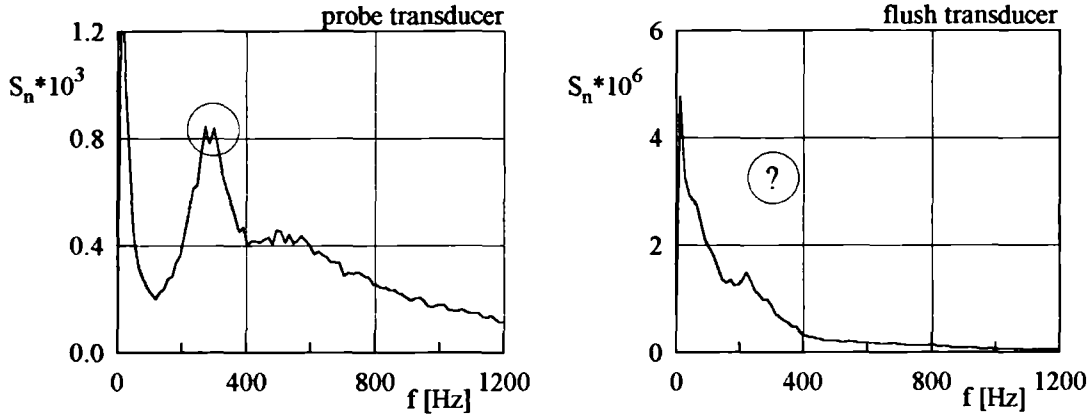

a

P	LM	U=29 m/s	α=24°	x_B/c=0.50	x/c=0.65

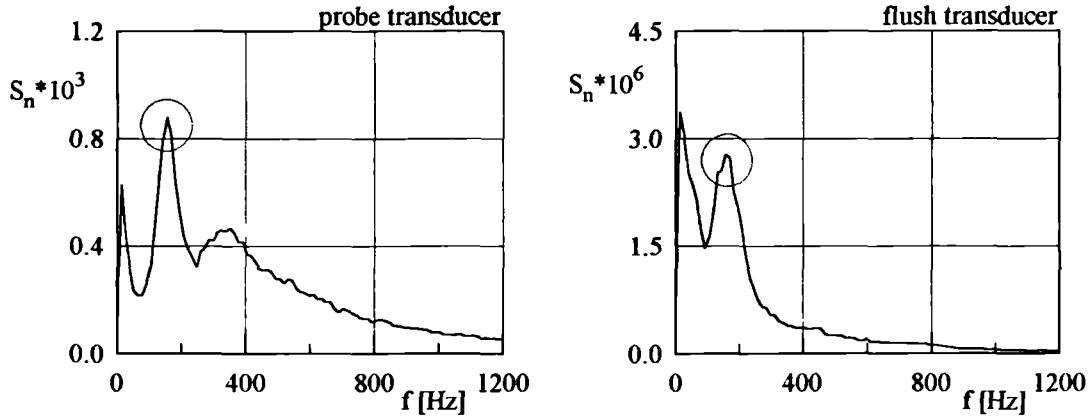

b

P	LM	U=29 m/s	α=24°	x_B/c=0.50	x/c=0.80

Figure 4.64.Comparison between vortex core and surface pressure fluctuations (α=24°).

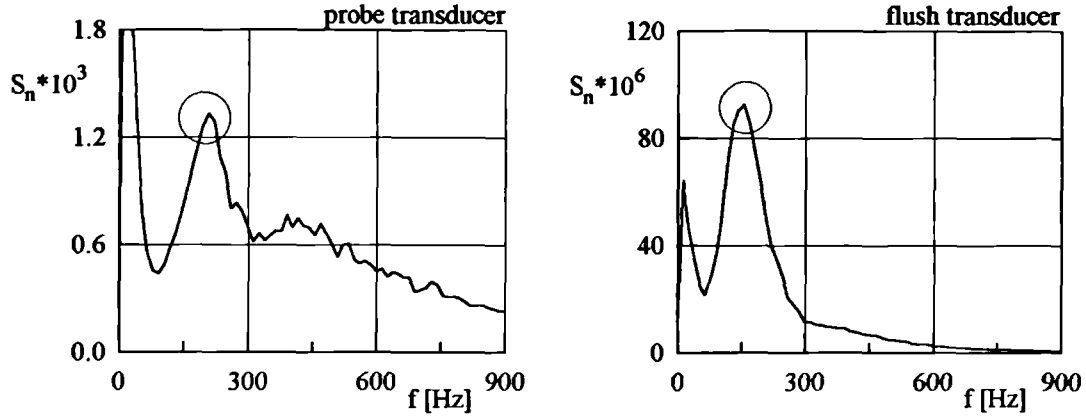

a

P	LM	U=29 m/s	α=29°	x_B/c=0.25	x/c=0.50

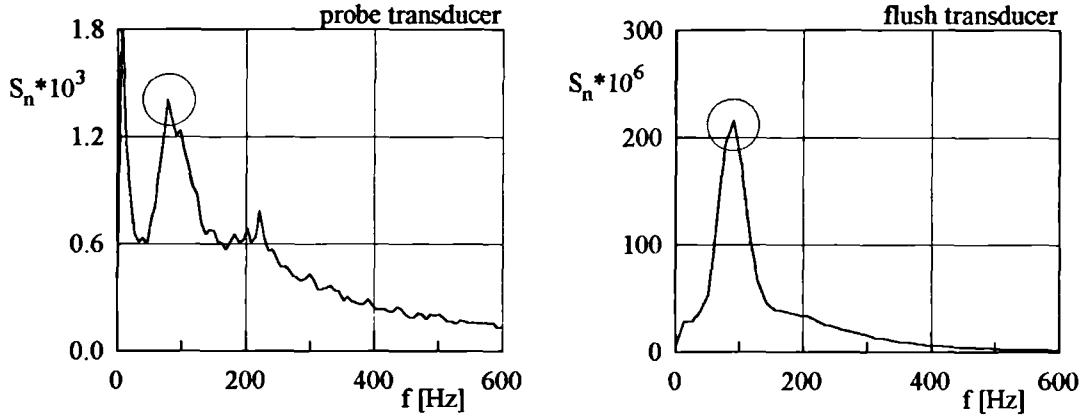

b

P	LM	U=29 m/s	α=29°	x_B/c=0.25	x/c=0.75

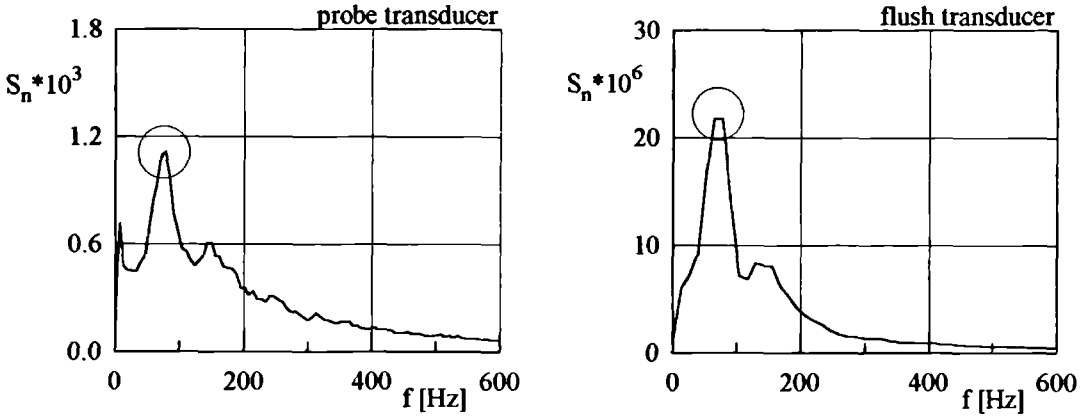

c

P	LM	U=29 m/s	α=29°	x_B/c=0.25	x/c=1.00

Figure 4.65.Comparison between vortex core and surface pressure fluctuations ($\alpha=29^{O}$).

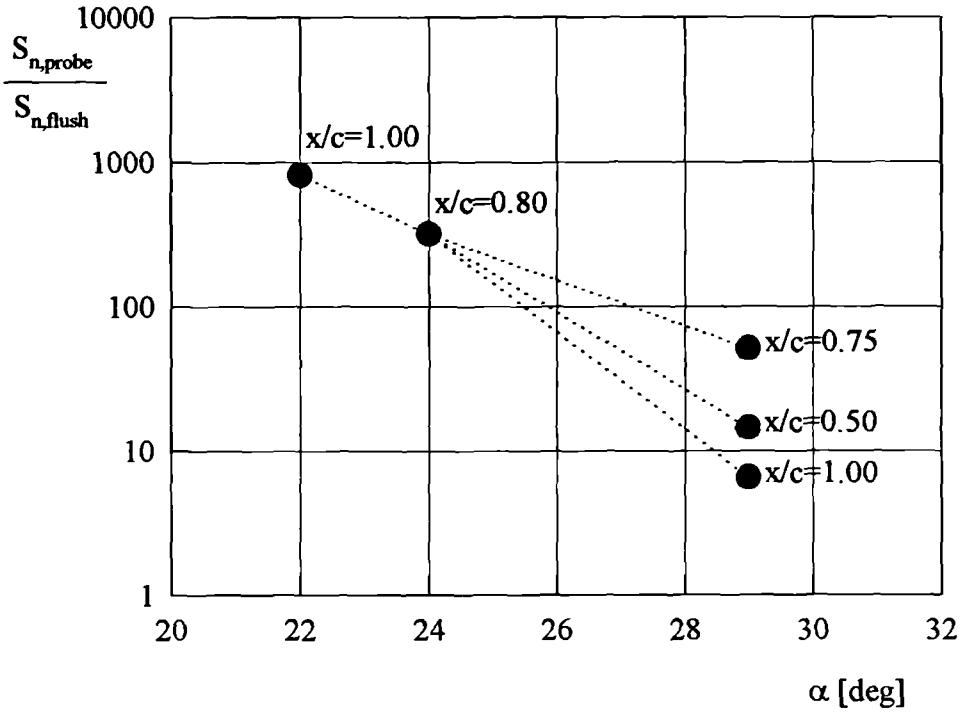

Figure 4.66.Ratio of signal level in the vortex core to signal level on the wing's surface.

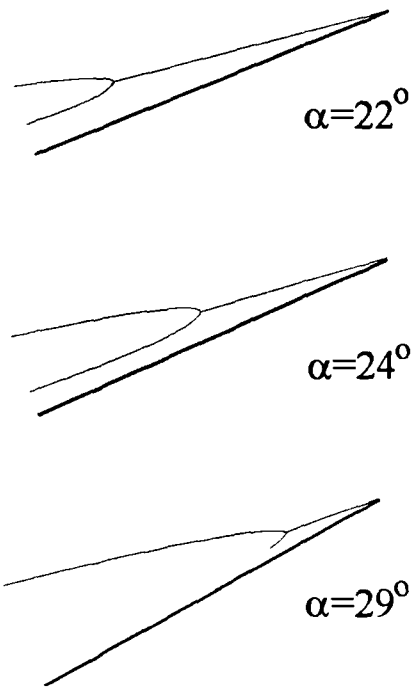

Figure 4.67.A qualitative explanation of results shown in figure 4.66.

greater. Hence, effectively, the coherent structures responsible for the excitation are closer to the wing's surface. This leads to a somewhat paradoxical conclusion that the burst which is far ahead of the trailing edge for high angles of incidence (namely at x/c=0.25 in this particular situation) manifests its presence more strongly on the wing's surface near the trailing edge than the burst at x/c=0.75 (for α=22°). Figure 4.67 suggests also that the reason for the great differences between spectra from probe and flush transducers (figures 4.63 and 4.64a) is the relatively large distance from the source of fluctuations to the wing's surface. Another important conclusion is that measurements using flush transducers are not reliable in every situation and can be misleading sometimes (e.g. figures 4.63, 4.64a). For example, inspection of the right hand graph in figure 4.63 (without being aware of the left one) might lead to incorrect conclusions about the characteristic frequency due to the burst.

4.2.3. Correlations of pressure fluctuations

The correlation techniques applied in the wing experiments can be divided generally into two groups:

1) correlations within one vortex similar in character to those in the vortex tube (the starboard vortex was chosen since it was closer to the tunnel door).
2) correlations between the starboard and the port side vortices, to check possible interaction between them. This also included the experiment with vortex shedding at a large angle of incidence.

Within the first group three probe arrangements were used (see figure 4.68):

- streamwise correlations, using probe transducers inserted in two chordwise locations, on the vortex radii with the highest peaks in the excitation spectra. The pair of transducers is traversed along the vortex (with the chordwise distance between them approximately constant),

- streamwise correlations, using flush mounted transducers located directly beneath the vortex axis (found from the minimum of the axial velocity profile). The pair of transducers is traversed along the vortex.
- 'mixed' correlations; transducers placed at the same chordwise co-ordinate (one enclosed in the probe, another flush mounted) - this measurement gives an estimate of the transverse propagation speed of pressure disturbances. For the estimation of the helix angle of the spiral disturbance the probe mounted transducer was fixed, whereas the flush transducer was traversed along the vortex axis.

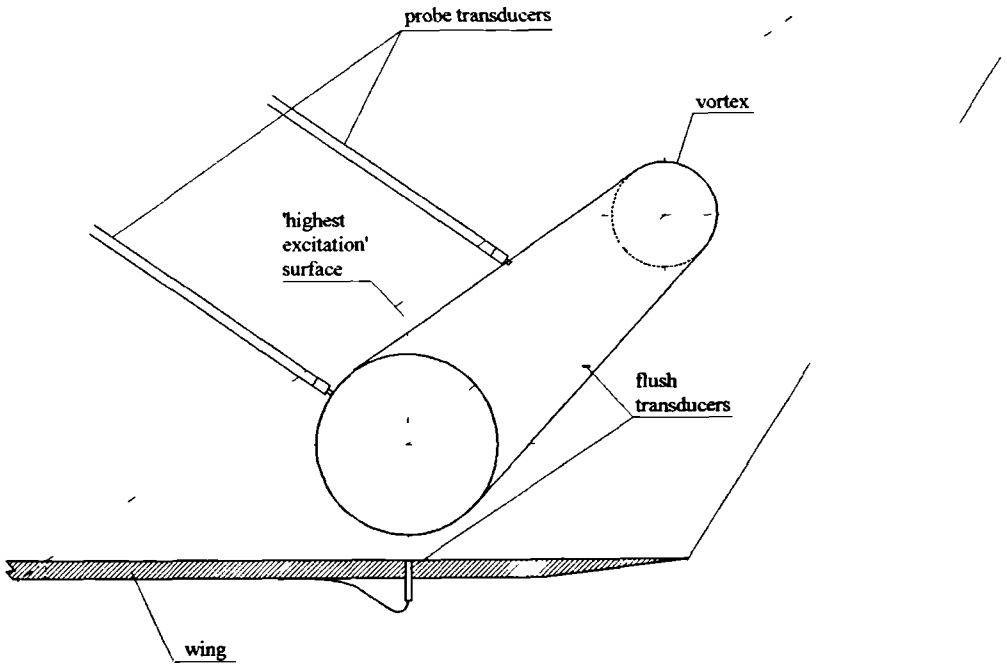

Figure 4.68.Probe arrangement for correlations within one vortex.

The correlation measurements were conducted on the larger model at an angle of incidence of 29°. The highest incidence investigated was chosen because of the unclear picture of breakdown induced excitation on the wing's surface for the low angles of attack (compare the preceding section). Otherwise the comparison between the results from the probe and the flush mounted transducers might be uncertain.

Page 217, line 9 from the top

After the sentence:

"The time lag obtained from the maxima of each correlation function presented against the streamwise distance is given in figure 4.70."

the following statement is added:

"In this figure, both the streamwise distance and the time lag are presented in a 'cumulative' manner, thus the range of the time lag is broader than it would appear from the graphs in figure 4.69 (the same remarks apply later to figure 4.72)."

After the above statement the sentence:

"The linear fit of the data points leads to the propagation speed of pressure disturbances of 27.2 m/s (the slope of the line)."

follows and the text is unchanged otherwise.

Figure 4.69 shows the correlation between the pressure fluctuations read by two probe mounted transducers. The probes are at a constant distance of $0.125c$ except for the last measurement, see captions for details) and are traversed downstream along the vortex (e.g. master at $x/c=0.5$, slave at 0.625; then master at $x/c=0.625$, slave at 0.75 etc.). Each graph has two curves which correspond to different sampling rates. Data sets for each sampling rate consist of 262,144 samples. Hence for the lower rate a longer time interval is covered (this is reflected in 'smoother' correlation functions). The time lag obtained from the maxima of each correlation function presented against the streamwise distance is given in figure 4.70. The linear fit of the data points leads to the propagation speed of pressure disturbances of 27.2 m/s (the slope of the line). This gives a ratio of the longitudinal propagation speed to the free stream velocity of about 0.94.

Figure 4.71 (graphs *a* through *h*) shows the correlation functions obtained from measurements with flush transducers. Here the streamwise co-ordinate s is measured as a distance along the curve passing through the transducers' (x,y) co-ordinates. This co-ordinate is believed to measure the distance *along the vortex* better than the chordwise distance. The time delay (t) against s (figure 4.72) leads to the propagation speed of 28.9 m/s. This gives a ratio of the longitudinal propagation speed to the free stream velocity of nearly 1.0 and is in excellent agreement with the probe measurements.

Figure 4.73 shows the correlation functions between signals from the probe and flush transducers located in the same plane (see figure 4.62). Graphs *a*, *b* and *c* correspond to the three planes investigated ($x/c=0.5$, 0.75 and 1.0). From the distance over the arc from the probe to the flush transducer and the time delay one can calculate the transverse propagation speed of the pressure disturbances. This is presented in figure 4.74 for three chordwise locations and both sampling rates. The propagation speed changes from about 20 to 27 m/s (or 0.69 to 0.93 of free stream velocity).

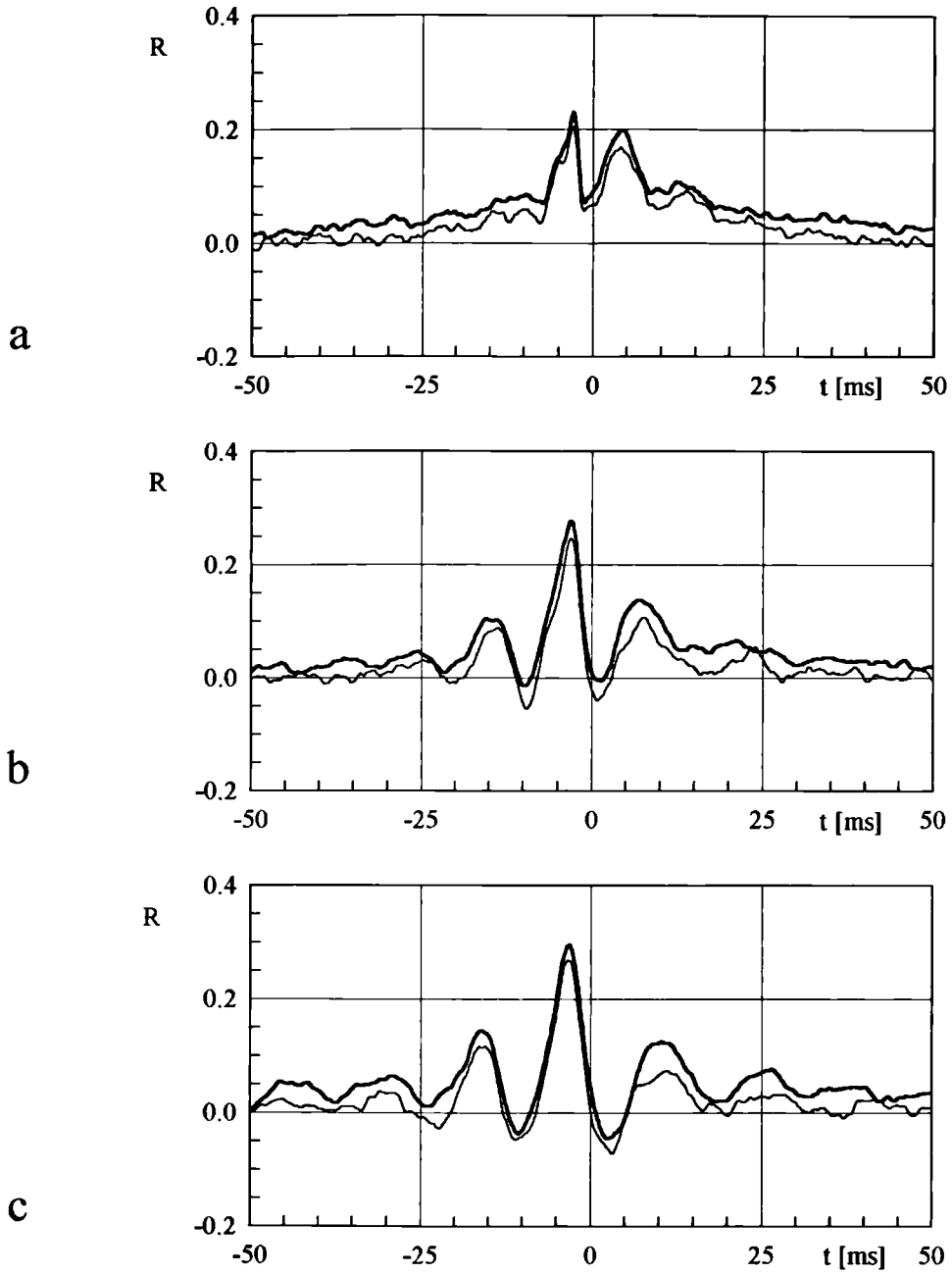

a) master probe at x/c=0.5 ; slave probe at x/c=0.625
b) master probe at x/c=0.625; slave probe at x/c=0.75
c) master probe at x/c=0.75 ; slave probe at x/c=0.875

P	LM	U=29 m/s	α=29°	x_B/c=0.25

sampling rate:
——— 6.667 kHz
——— 33.0 kHz

Figure 4.69.(*Continued on the next page*).

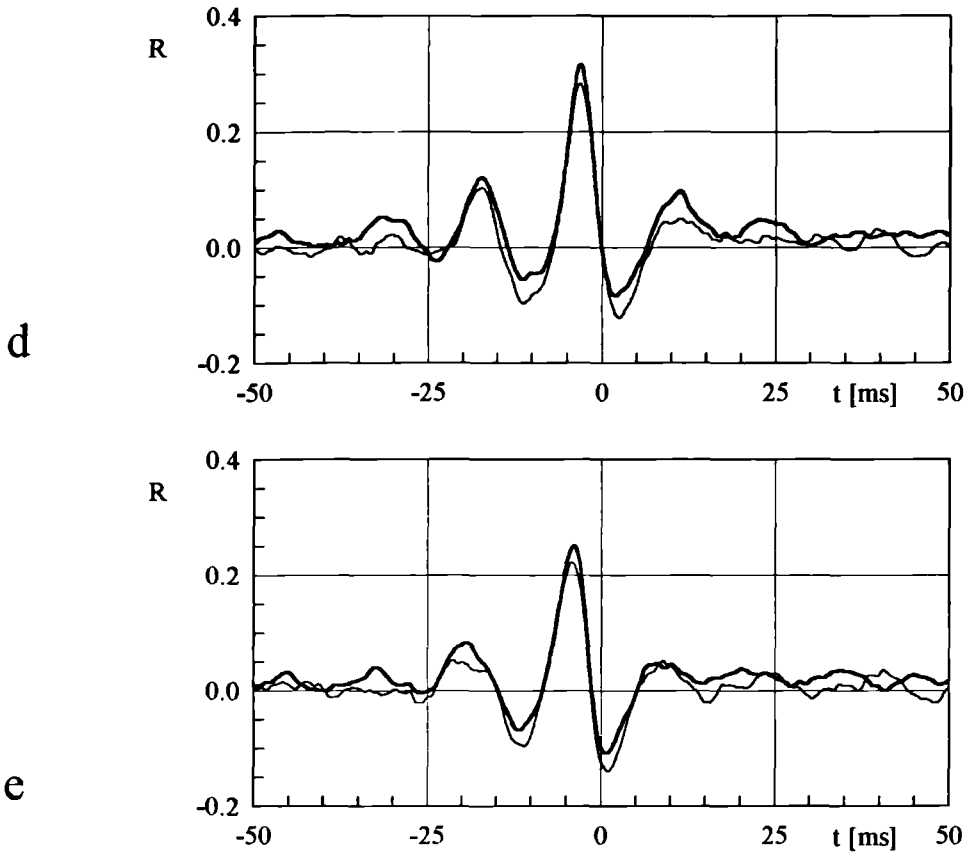

d) master probe at x/c=0.875; slave probe at x/c=1.0
e) master probe at x/c=1.0 ; slave probe at x/c=1.2

P	LM	U=29 m/s	α=29°	x_B/c=0.25

sampling rate:
——— 6.667 kHz
——— 33.0 kHz

Figure 4.69.Correlations within one vortex measured along the vortex core. See captions for details.

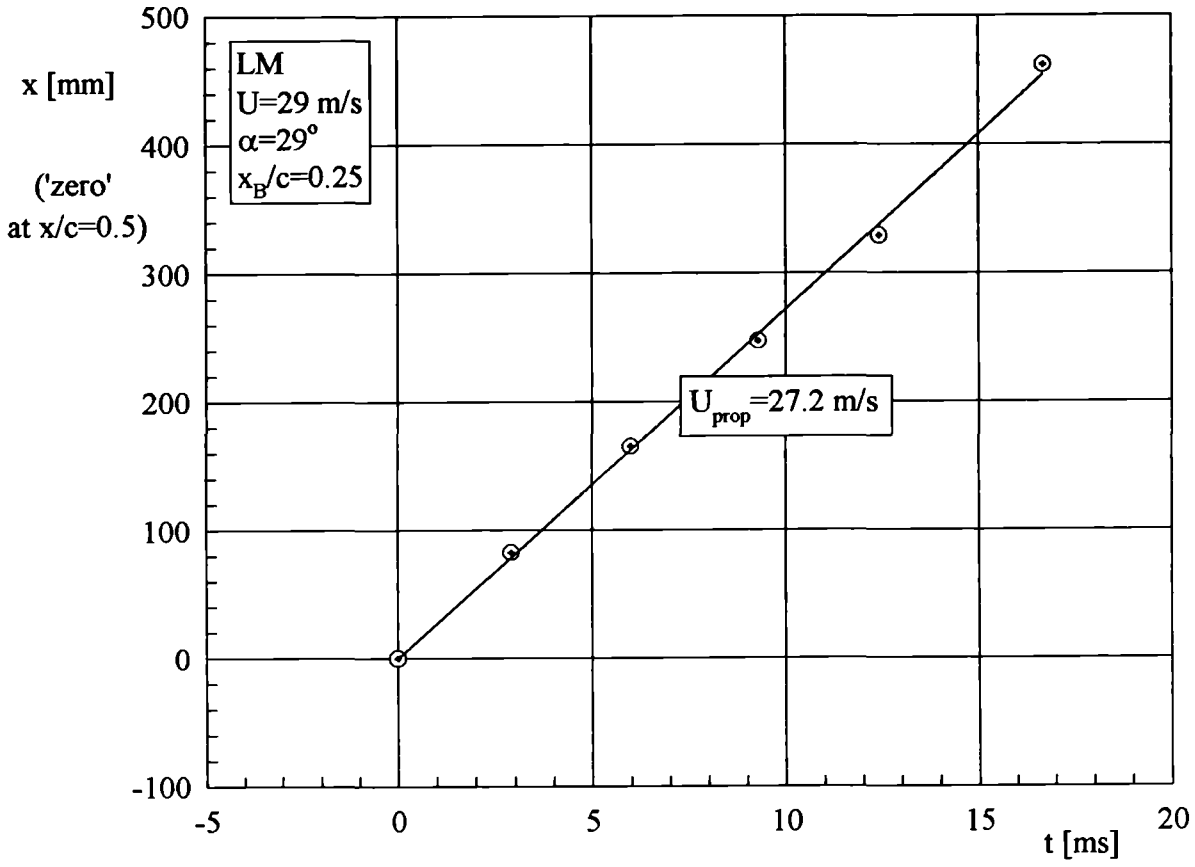

Figure 4.70.Time lag vs. distance obtained from the results in figure 4.69.

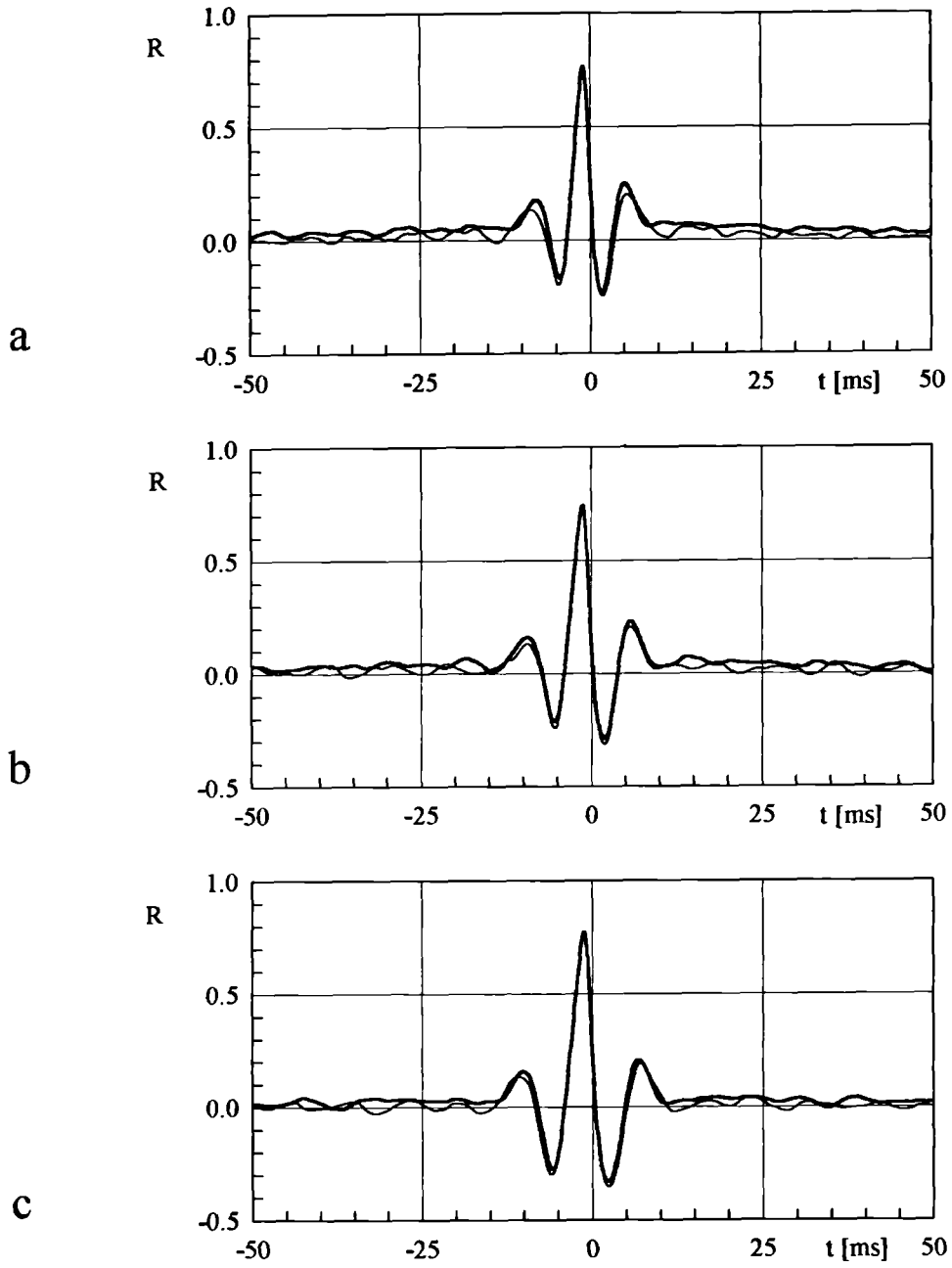

a) master at x/c=0.504, y/s=0.320; slave at x/c=0.549, y/s=0.348
b) master at x/c=0.549, y/s=0.348; slave at x/c=0.602, y/s=0.383
c) master at x/c=0.602, y/s=0.383; slave at x/c=0.650, y/s=0.412

sampling rate:
——— 6.667 kHz
——— 33.0 kHz

P	LM	U=29 m/s	α=29°	x_B/c=0.25

Figure 4.71.(*Continued on the next page*).

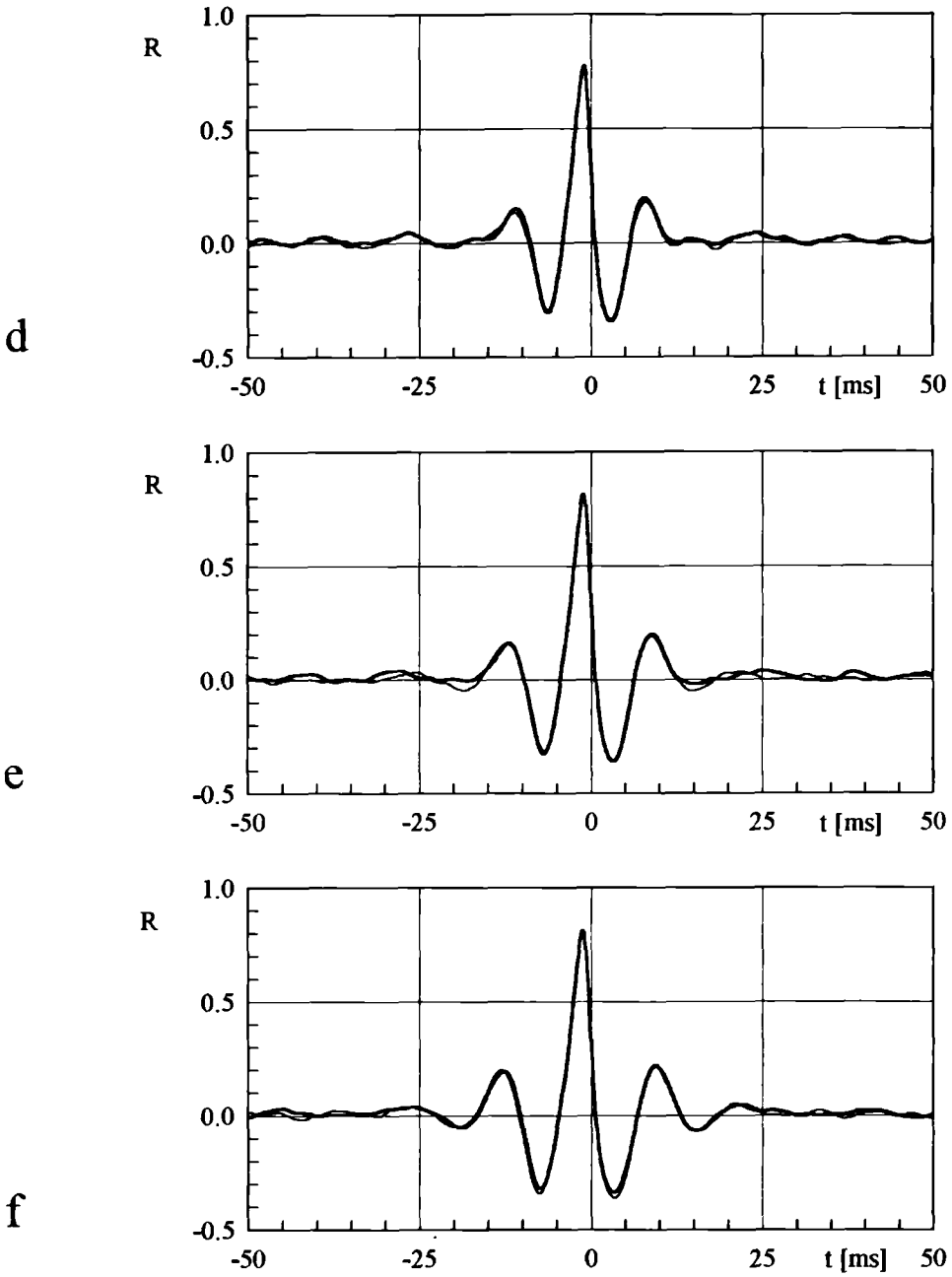

d) master at x/c=0.650, y/s=0.412; slave at x/c=0.701, y/s=0.208
e) master at x/c=0.701, y/s=0.208; slave at x/c=0.748, y/s=0.478
f) master at x/c=0.748, y/s=0.478; slave at x/c=0.800, y/s=0.505

sampling rate:
——— 6.667 kHz
——— 33.0 kHz

P	LM	U=29 m/s	α=29°	x_B/c=0.25

Figure 4.71.(*Continued on the next page*).

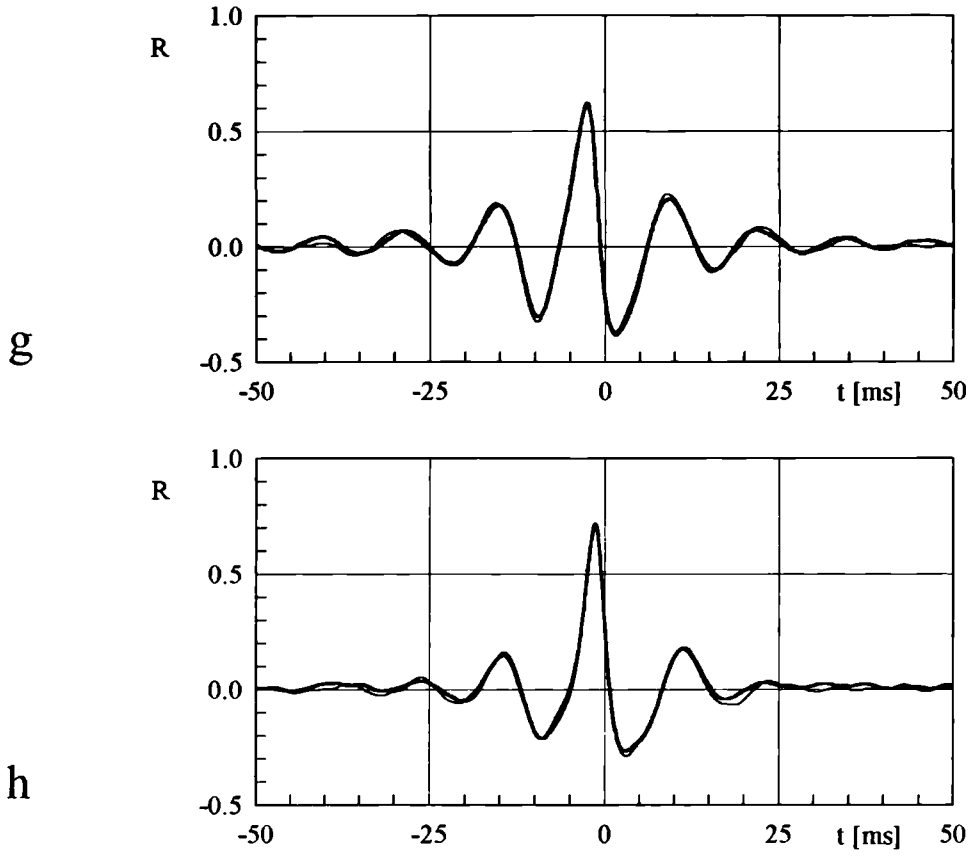

g) master at x/c=0.800, y/s=0.505; slave at x/c=0.901, y/s=0.545
h) master at x/c=0.901, y/s=0.545; slave at x/c=0.979, y/s=0.585

sampling rate:
——— 6.667 kHz
——— 33.0 kHz

P	LM	U=29 m/s	α=29°	x_B/c=0.25

Figure 4.71.Correlations within one vortex measured along the vortex on the wing's surface. See captions for details.

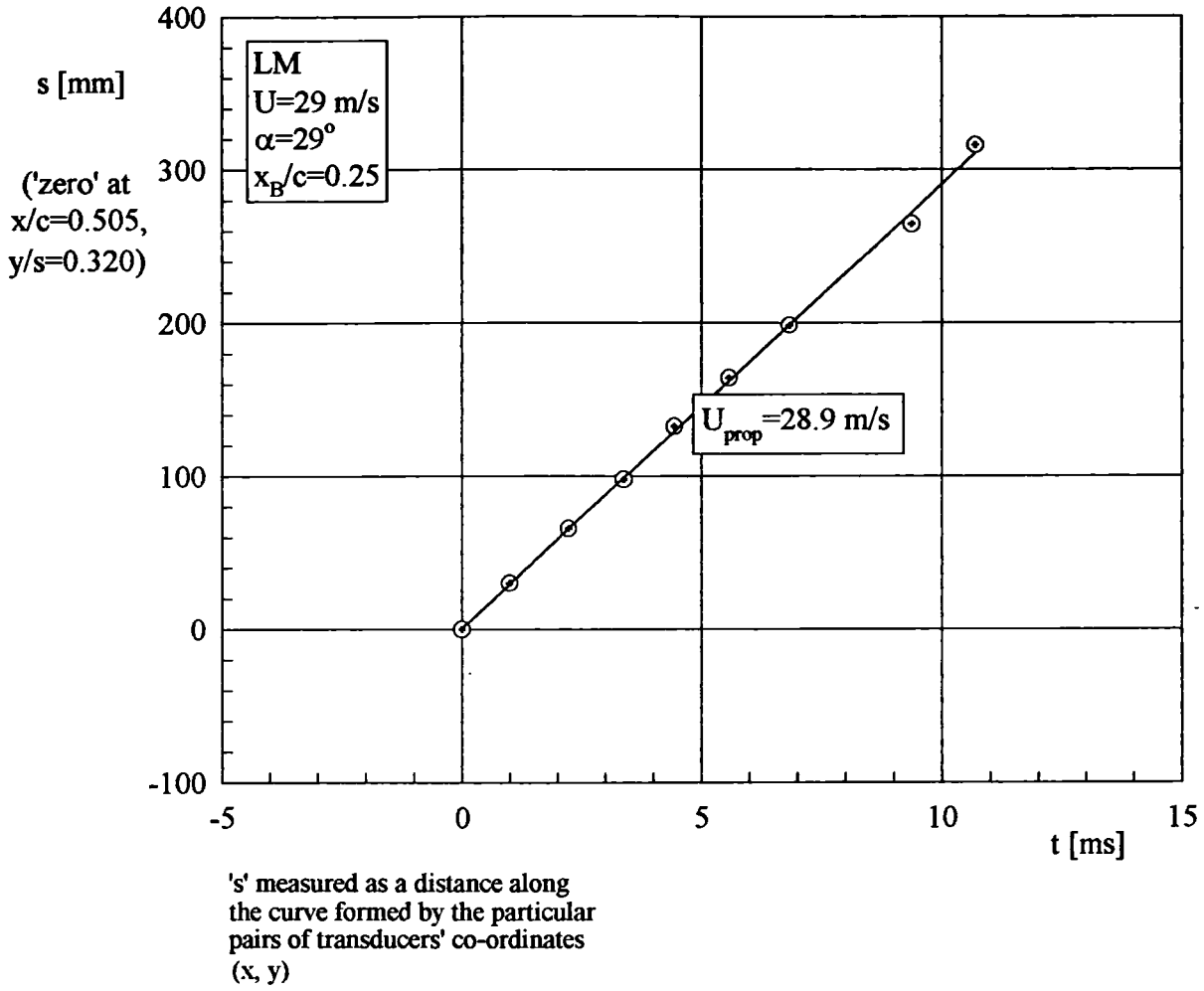

Figure 4.72. Time lag vs. distance obtained from the results in figure 4.71.

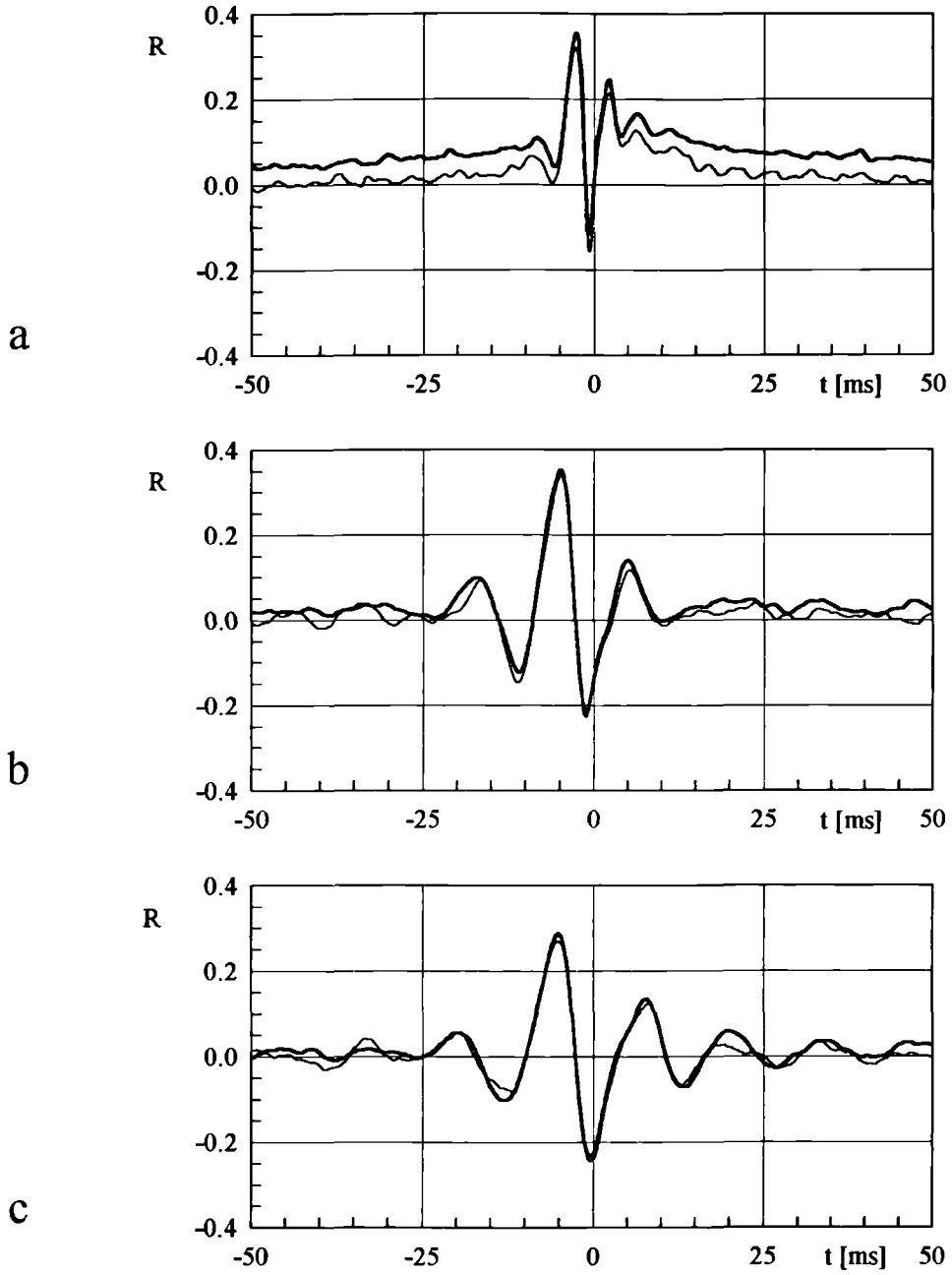

a) master probe at x/c=0.5 ; slave (flush) at x/c=0.504, y/s=0.320
b) master probe at x/c=0.75 ; slave (flush) at x/c=0.748, y/s=0.478
c) master probe at x/c=1.0 ; slave (flush) at x/c=0.979, y/s=0.585

P	LM	U=29 m/s	α=29°	x_B/c=0.25

sampling rate:
——— 6.667 kHz
——— 33.0 kHz

Figure 4.73. Transverse correlations within one vortex (between probe and flush transducers) at three streamwise locations. See captions for details.

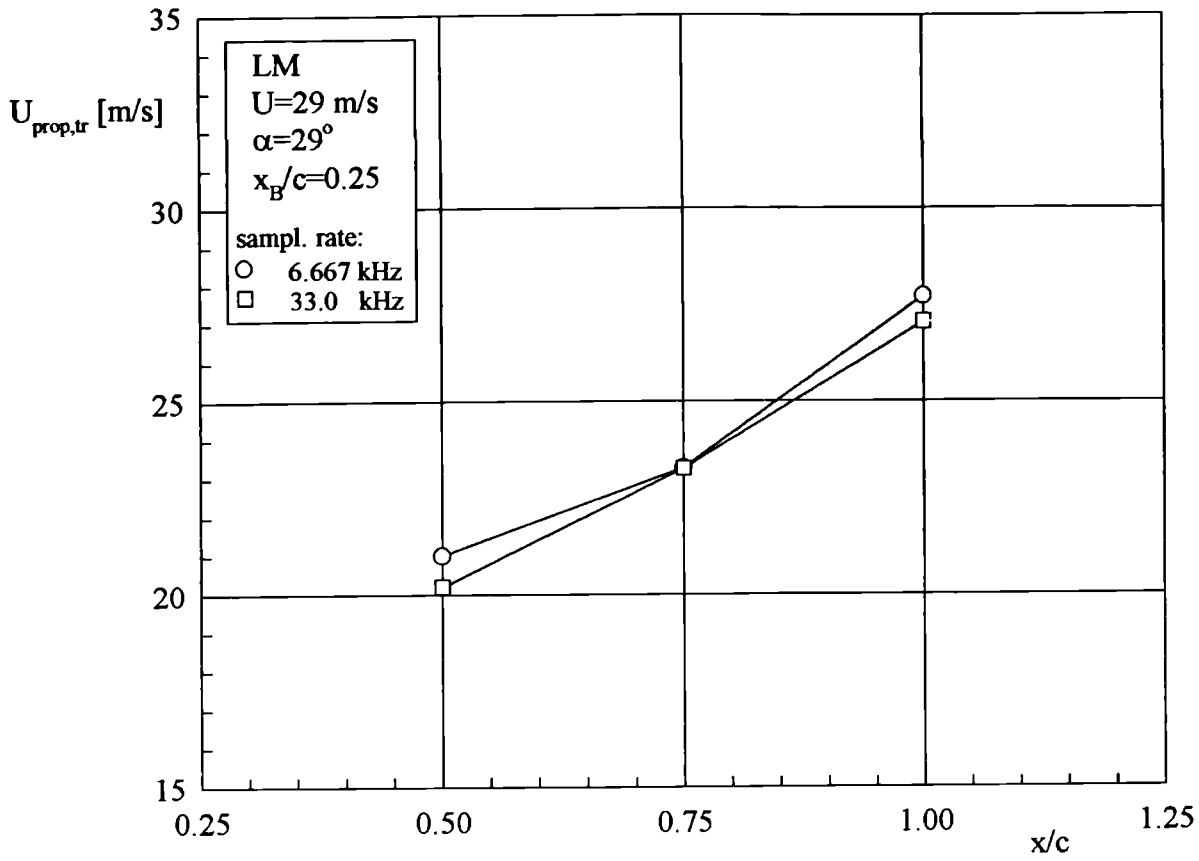

Figure 4.74.Transverse propagation speed of pressure disturbances vs. x/c. (From results in figure 4.73 and vortex-wing geometry).

Figure 4.75 shows the correlation function between signals from the probe transducer (fixed at x/c=0.75) and the flush transducer in two locations (x/c=0.549 and 0.602). The time lag for graphs *a* and *b* (from maxima of the functions) is of different sign. Therefore the location of the flush transducer for which the signals *are in phase* is somewhere between x/c=0.549 and 0.602. From linear interpolation (with respect to time lag and x/c) this position turns out to be about x/c=0.59. This leads to the important conclusion that the disturbance is of a spiral type. In addition the spiral's sense can be identified as opposite to the sense of streamlines. These two features are exactly the same as for the vortex tube experiment. The simplified considerations of the vortex geometry give the helix angle of this disturbance of about 45°.

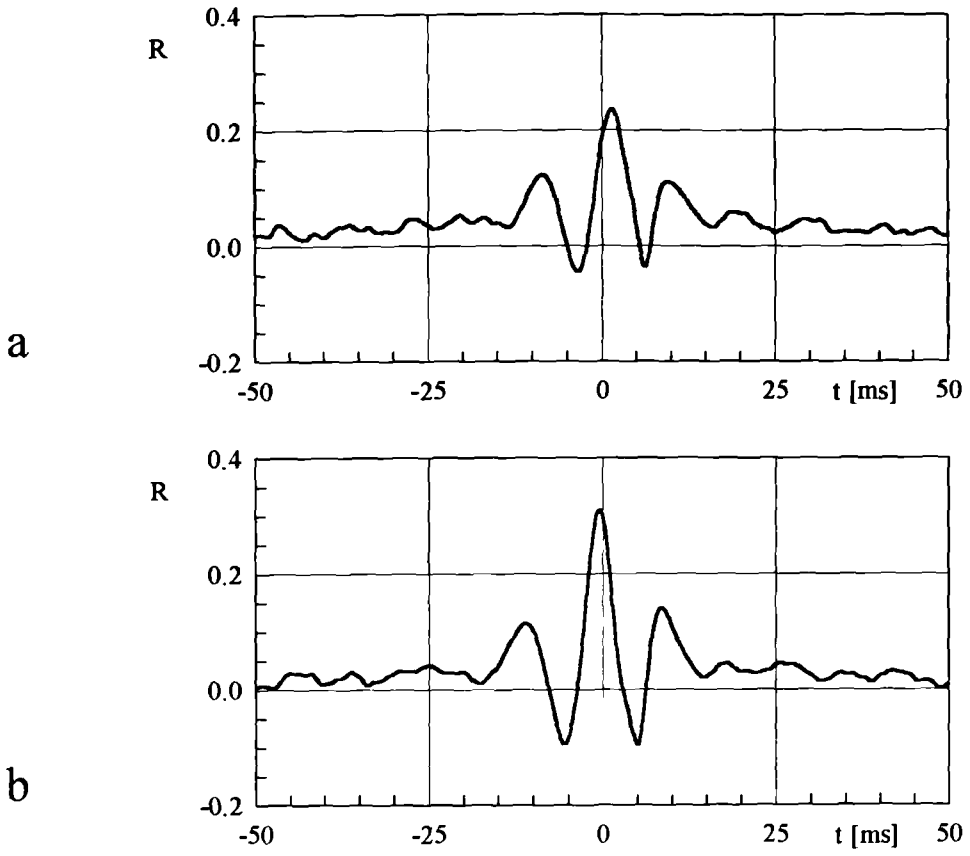

a) master probe at x/c=0.75 ; slave (flush) at x/c=0.549, y/s=0.348
b) master probe at x/c=0.75 ; slave (flush) at x/c=0.602, y/s=0.383

Δt=0 for slave at x/c≅0.59 from the vortex geometry: -spiral helix angle ~45° -spiral's sense opposite to streamlines

P	LM	U=29 m/s	α=29°	x_B/c=0.25

Figure 4.75. Correlations between fixed probe transducer and flush transducer in two streamwise locations (giving time lag of opposite sign). See captions for details.

Experiments of the second class, i.e. the correlations between two vortices, were conducted using the probe transducers placed symmetrically over both sides of the wing (in the places of highest excitation). Figures 4.76, 4.77 and 4.78 show the spectra of pressure fluctuations obtained from starboard and port side probes and the correlation function between them. The figures are given for an incidence of 29° and three chordwise locations (0.5, 0.75 and 1.0). The results for two lower values of α are similar and therefore omitted here. It is observed that for all three configurations the corresponding spectra from both sides of the wing are close to each other (both in frequency and amplitude).

Somewhat surprisingly, none of the correlation functions demonstrate a 'periodic' behaviour, which could be related to the characteristic frequencies present in the breakdown wake. In fact, only low level 'noise' can be seen. This indicates the independence of the fluctuations originating from the two burst regions. Interestingly, the correlation function from figure 4.76 has a large scale 'hollow' [14]. Its scale (of the order of 200 ms) may be related to the low frequency component present in the spectra (1/200 ms = 5 Hz). This low frequency component is usually associated with the oscillation of the mean burst position. The orientation of the 'large scale' correlation (a 'hollow', and not a 'hump') suggests in turn that mean positions of bursts are oscillating in an antiphase. This suggests an important conclusion - that the burst regions interact with each other (supposedly by imposing a pressure gradient), however the quasi-periodic fluctuations are produced independently.

For $\alpha=29^\circ$ the burst takes place at $x/c=0.25$. In this configuration the two burst regions on each side of the wing are physically close to each other. Hence their relatively strong interaction at $x/c=0.5$ (still close to the bursts) could be logically explained. For the locations further downstream the low frequency component of the fluctuations is becoming less pronounced (compare the appropriate spectra). Similarly the results for $\alpha=22^\circ$ and 24° (not shown here) do not indicate any 'large scale' correlations (this would be even less expected due to larger distances between bursts).

[14] Such character of the correlation was present *exclusively* for this configuration.

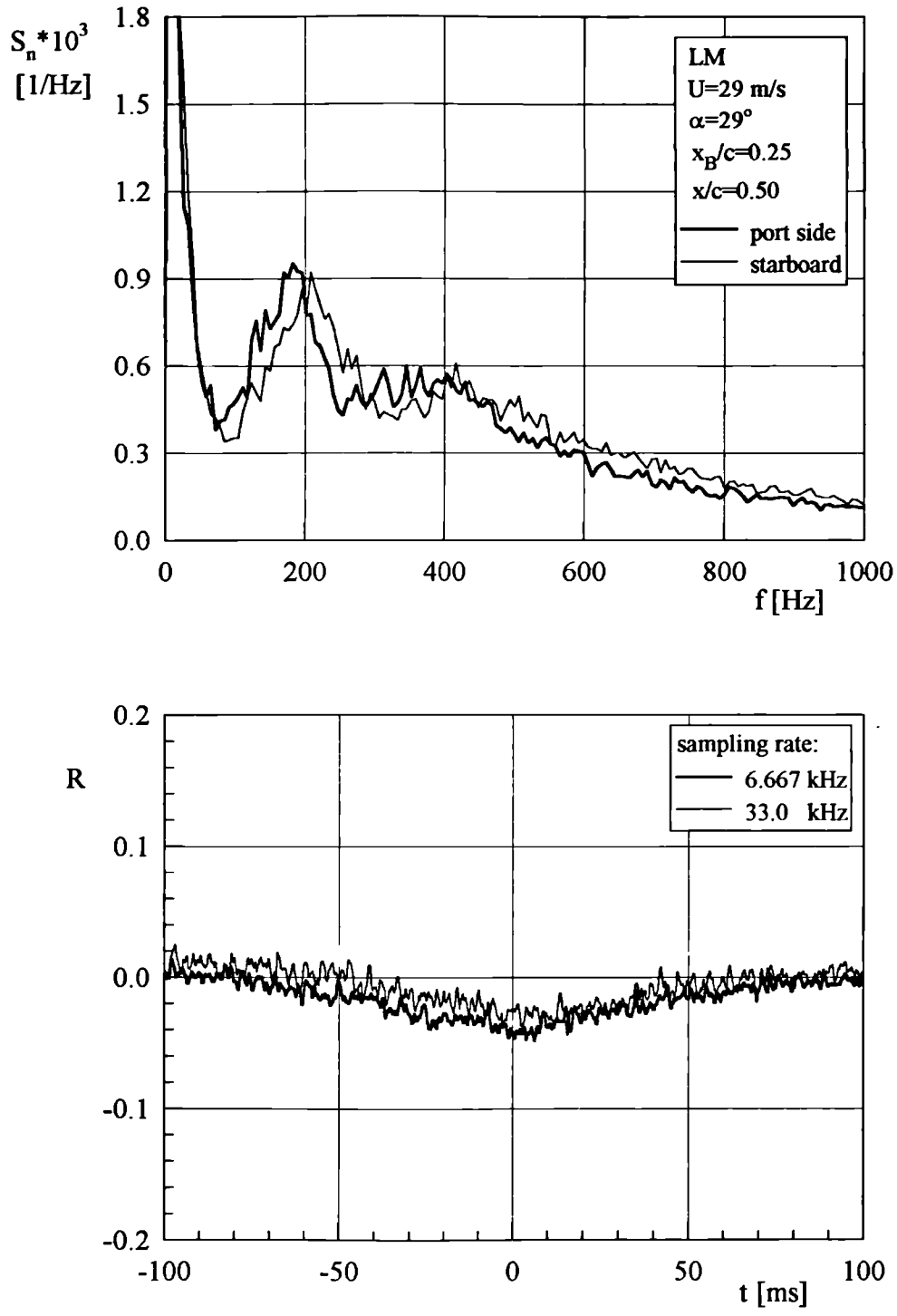

Figure 4.76. Spectra of pressure fluctuations from starboard and port side vortices together with their correlation function. (x/c=0.50).

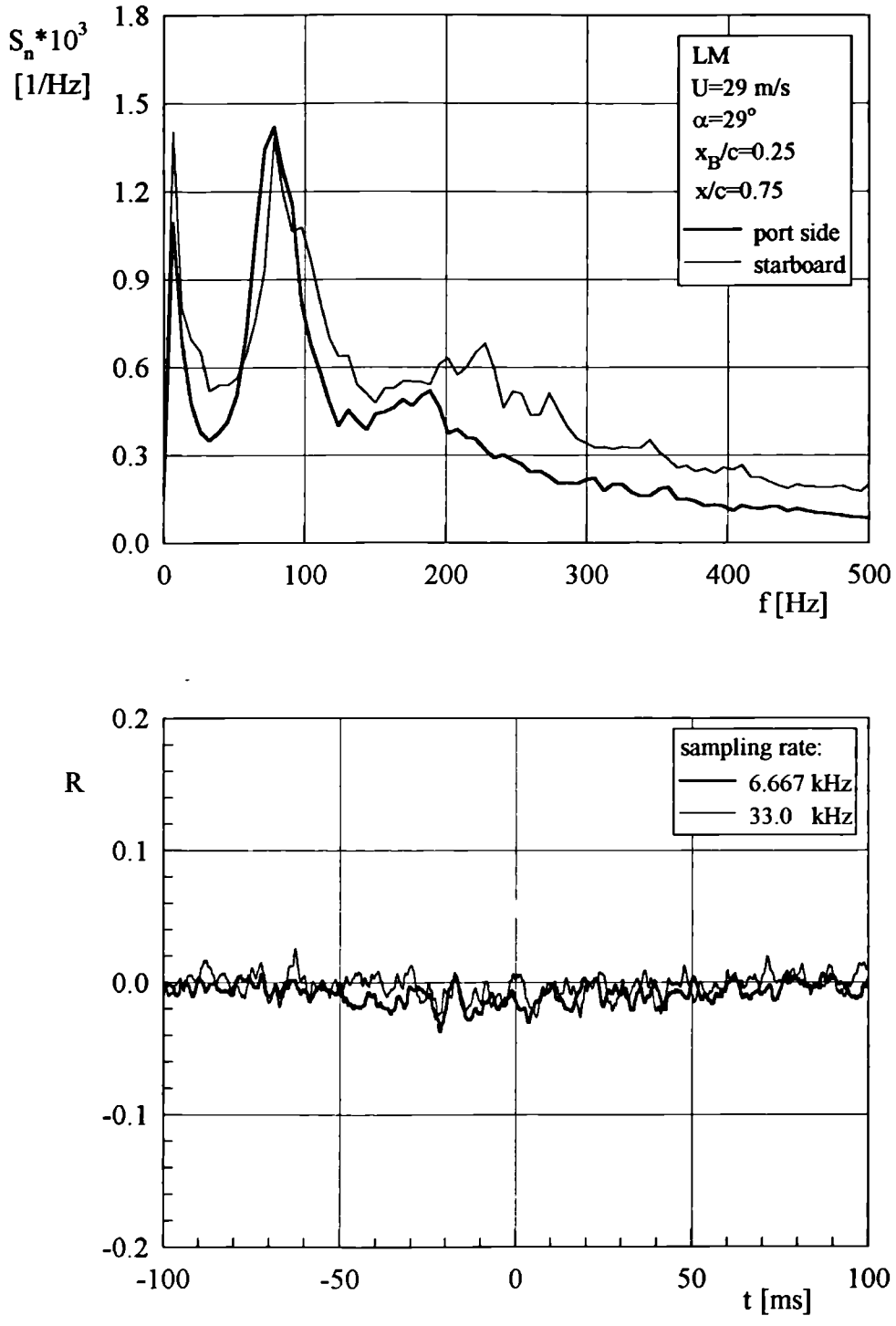

Figure 4.77. Spectra of pressure fluctuations from starboard and port side vortices together with their correlation function. (x/c=0.75).

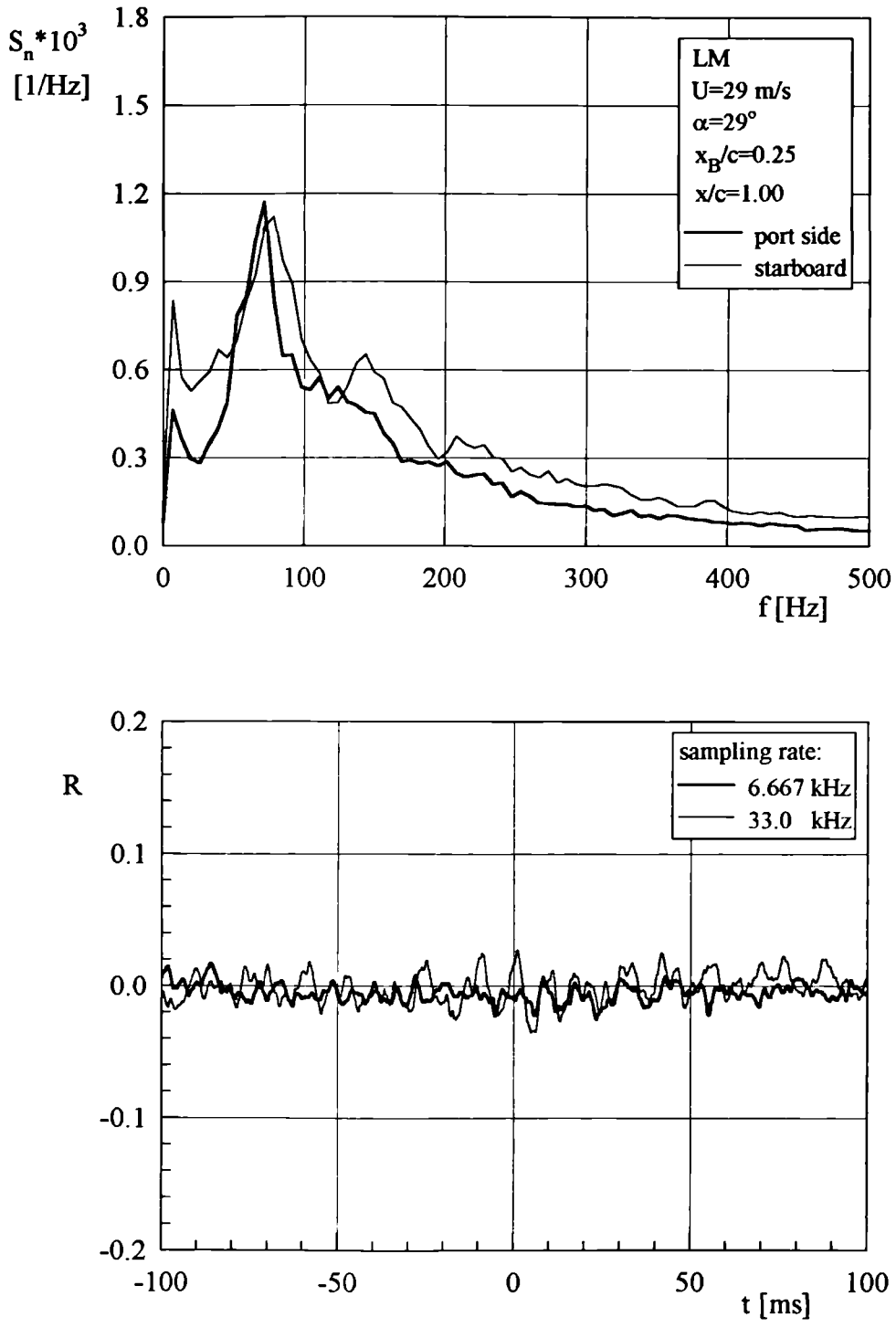

Figure 4.78. Spectra of pressure fluctuations from starboard and port side vortices together with their correlation function. (x/c=1.00).

Figure 4.79 shows the rear view of the probe arrangement for the measurement of the pressure fluctuations caused by *bluff body vortex shedding* behind the delta wing at high incidence. Here the smaller model was set at an incidence of 51° (for which the vortex burst is no longer present, but replaced by vortex shedding). The probes (150 mm over the wing's surface) were placed in the spanwise locations corresponding to the highest excitation. Figure 4.80 shows the spectra of pressure fluctuations on both sides of the wing. Pronounced peaks (at about 52 Hz are present in both spectra). The correlation level is low (this is typical for highly three-dimensional flows). However the correlation function (for both sampling rates) has a 'periodic' character. The length of the 'period' is in excellent agreement with the frequency of the peaks in the spectra. A maximum in correlation function at about $t=0$ suggests a symmetric shedding of the vortices.

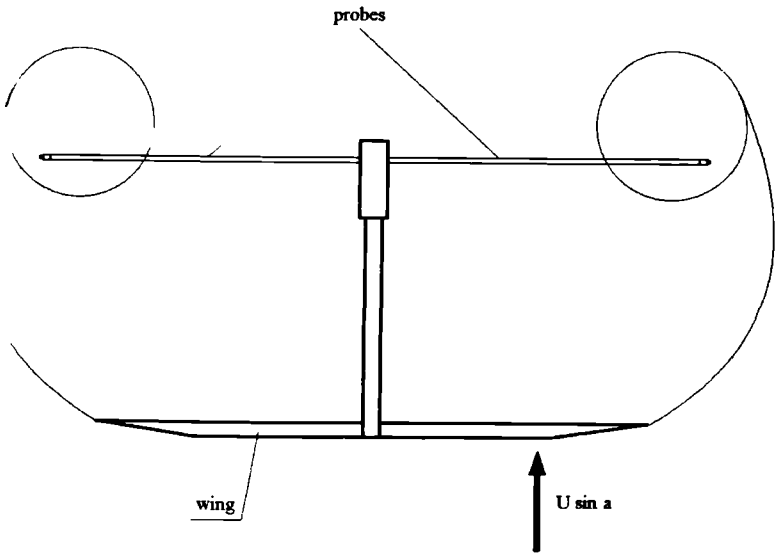

Figure 4.79.Rear view of probe arrangement for bluff body vortex shedding experiment.

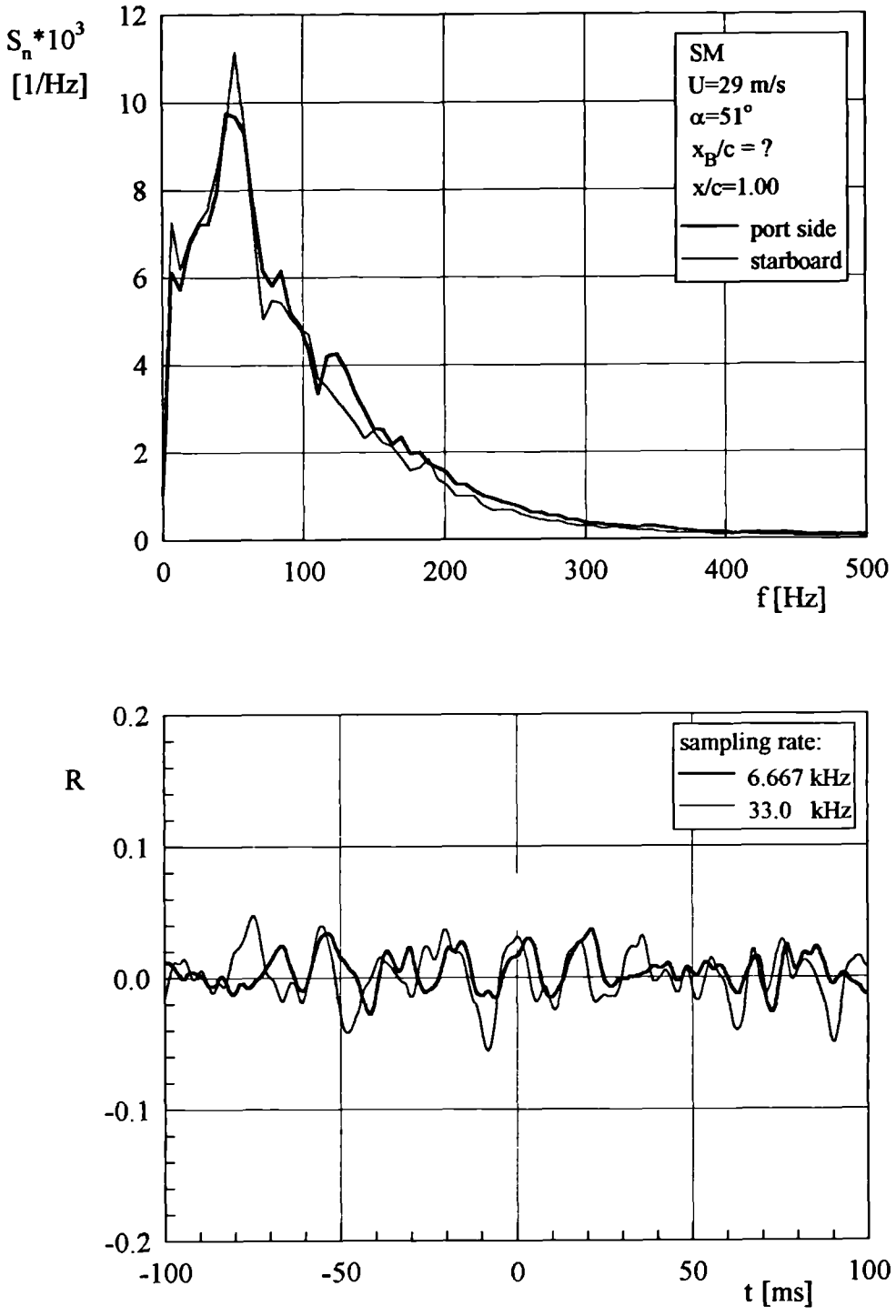

Figure 4.80. Spectra of pressure fluctuations from starboard and port side due to bluff body shedding together with their correlation function. (x/c=1.00).

4.2.4. Influence of the turbulence level on vortex breakdown

The influence of free stream turbulence level on the pressure fluctuations caused by vortex breakdown was investigated on the larger model at an incidence of 24° and a chordwise location x/c=0.8. The free stream velocity was 12.5 m/s for all tests[15]. The measurements were conducted for low turbulence flow and then with three turbulence grids (called here fine, medium and coarse) giving free stream turbulence levels of 0.16, 0.48, 3.6 and 7.2% , respectively . The spectra of the free stream turbulence, obtained from hot-wire measurements, are given in figure 4.81. The spectral density is normalised by the square of the free stream velocity (hence units 1/Hz).

Figures 4.82 through 4.85 show the spectra of pressure fluctuations. The captions indicate the turbulence levels. For the first three conditions (smooth flow, fine and medium mesh) the character of the spectra remains unchanged. For the last one (coarse grid) the identity of the peak due to breakdown (60-70 Hz) is lost. The maximum becomes 'broader' and is shifted to lower frequencies. Here the visual observations do not allow identification of the exact location and character of the breakdown.

It is worth noting that the usual magnitude of the *velocity fluctuations* due to breakdown (see figures 4.50 through 4.52) is of order of 0.1×10^{3} Hz^{-1} (normalised by the square of the free stream velocity). From figure 4.81 the level of the free stream turbulence for the coarse grid is also close to 0.1×10^{3} Hz^{-1}. Thus the actual structure of the breakdown flow field is destroyed by the large fluctuations present in the free stream (external) flow, which are of comparable magnitude as those related to the breakdown (as can be judged from the spectra). This explains the sudden change of the spectral character in figure 4.85 (in relation to the first three configurations).

[15] This was the maximum 'safe' speed for highest blockage ratio (coarse turbulence grid).

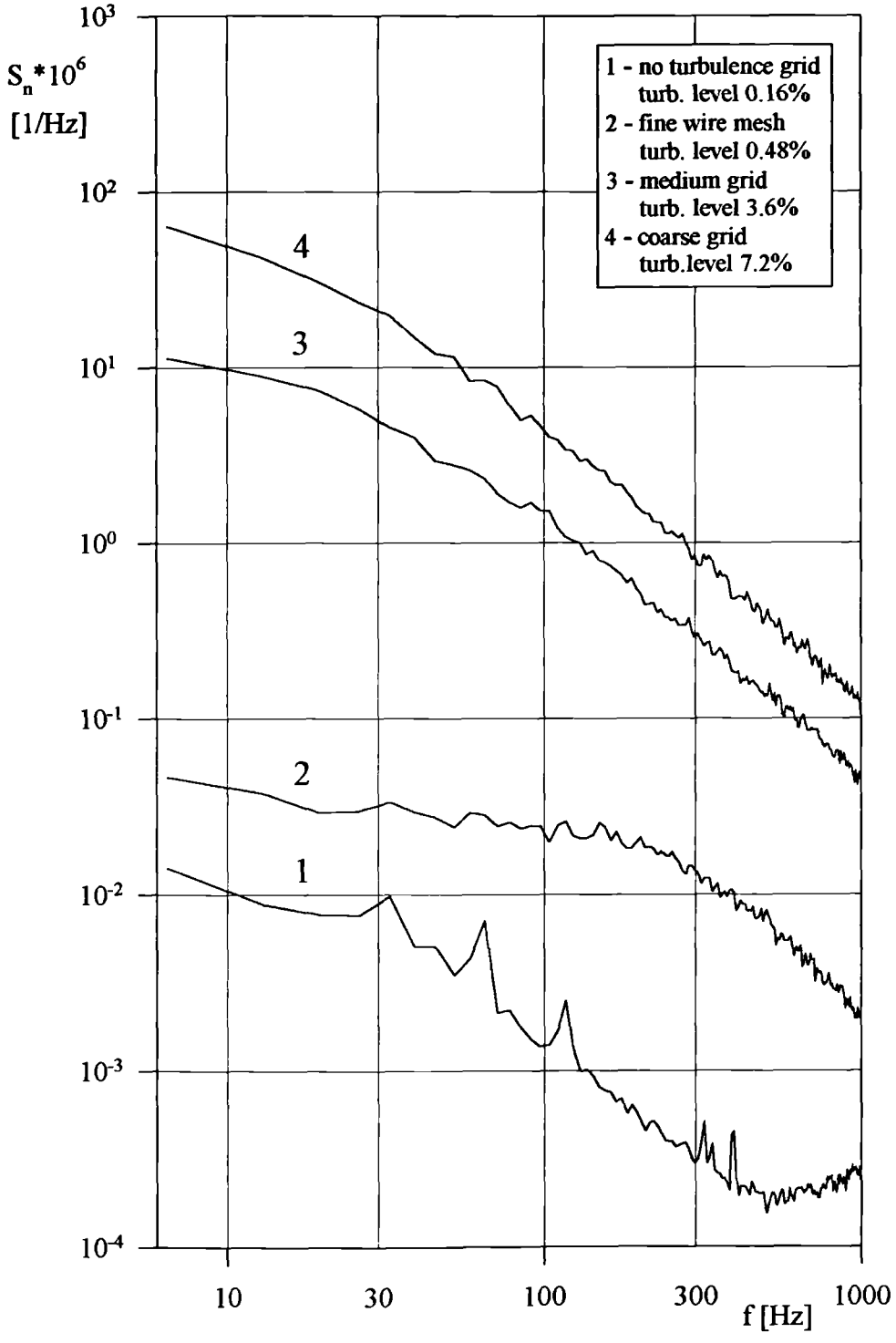

Figure 4.81.Spectra of velocity fluctuations in free stream flow for no turbulence grid (1) and three different turbulence grids (2,3,4).

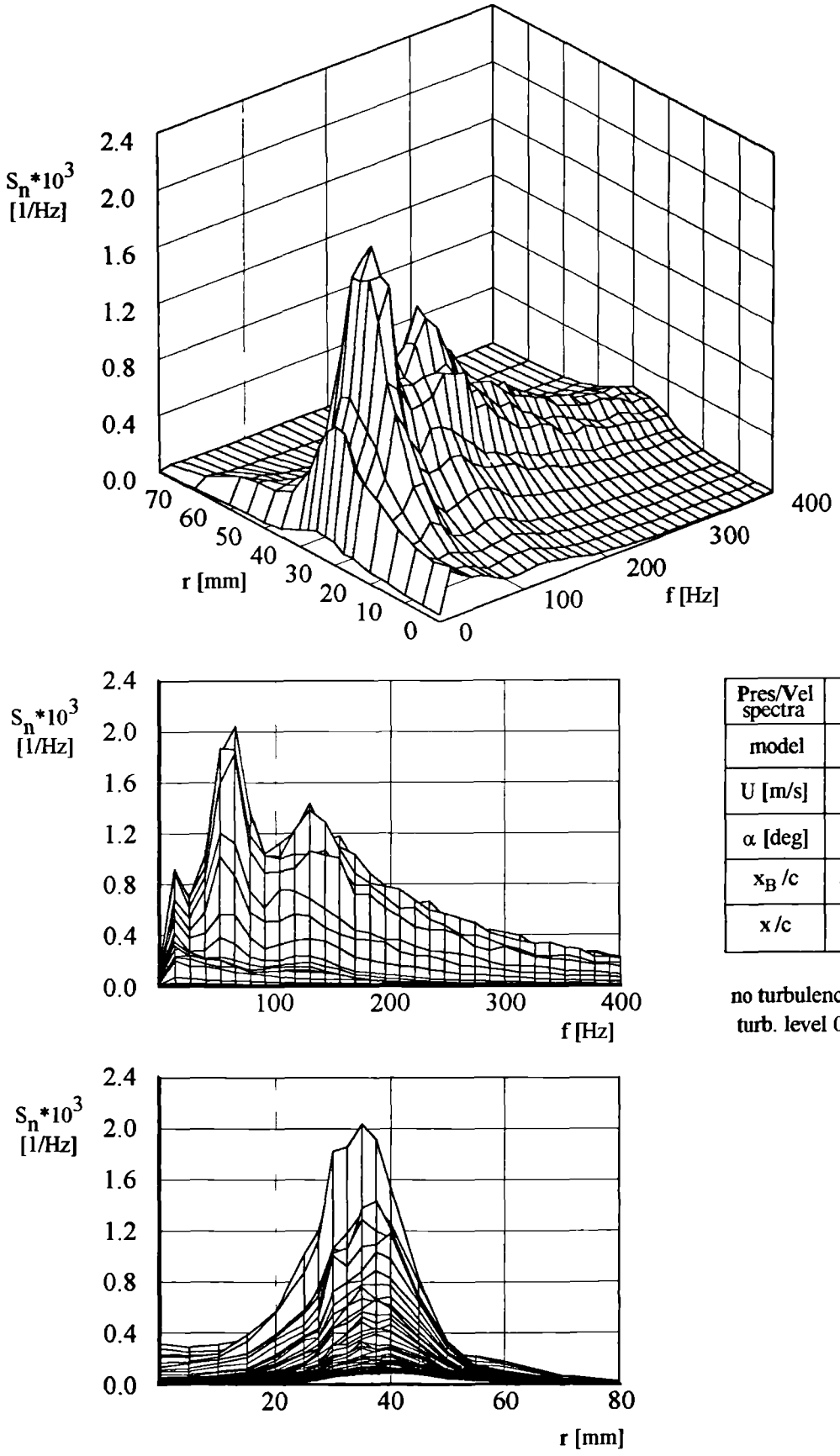

Pres/Vel spectra	P
model	LM
U [m/s]	12.5
α [deg]	24
x_B /c	0.50
x /c	0.80

no turbulence grid
turb. level 0.16%

Figure 4.82.Pressure spectra with no grid (turbulence level 0.16%).

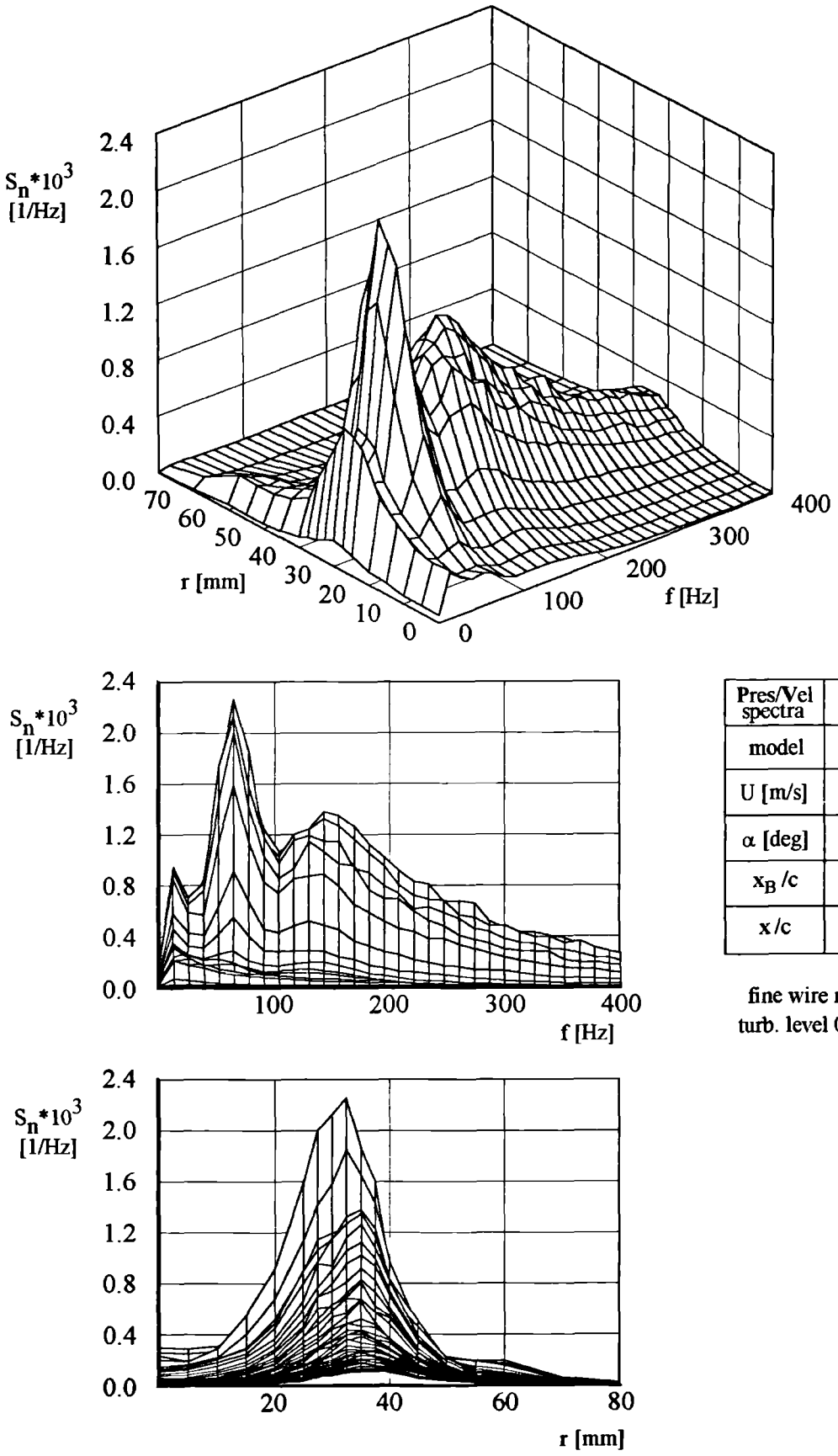

Pres/Vel spectra	P
model	LM
U [m/s]	12.5
α [deg]	24
x_B /c	0.50
x/c	0.80

fine wire mesh
turb. level 0.48%

Figure 4.83.Pressure spectra with fine wire mesh (turbulence level 0.48%).

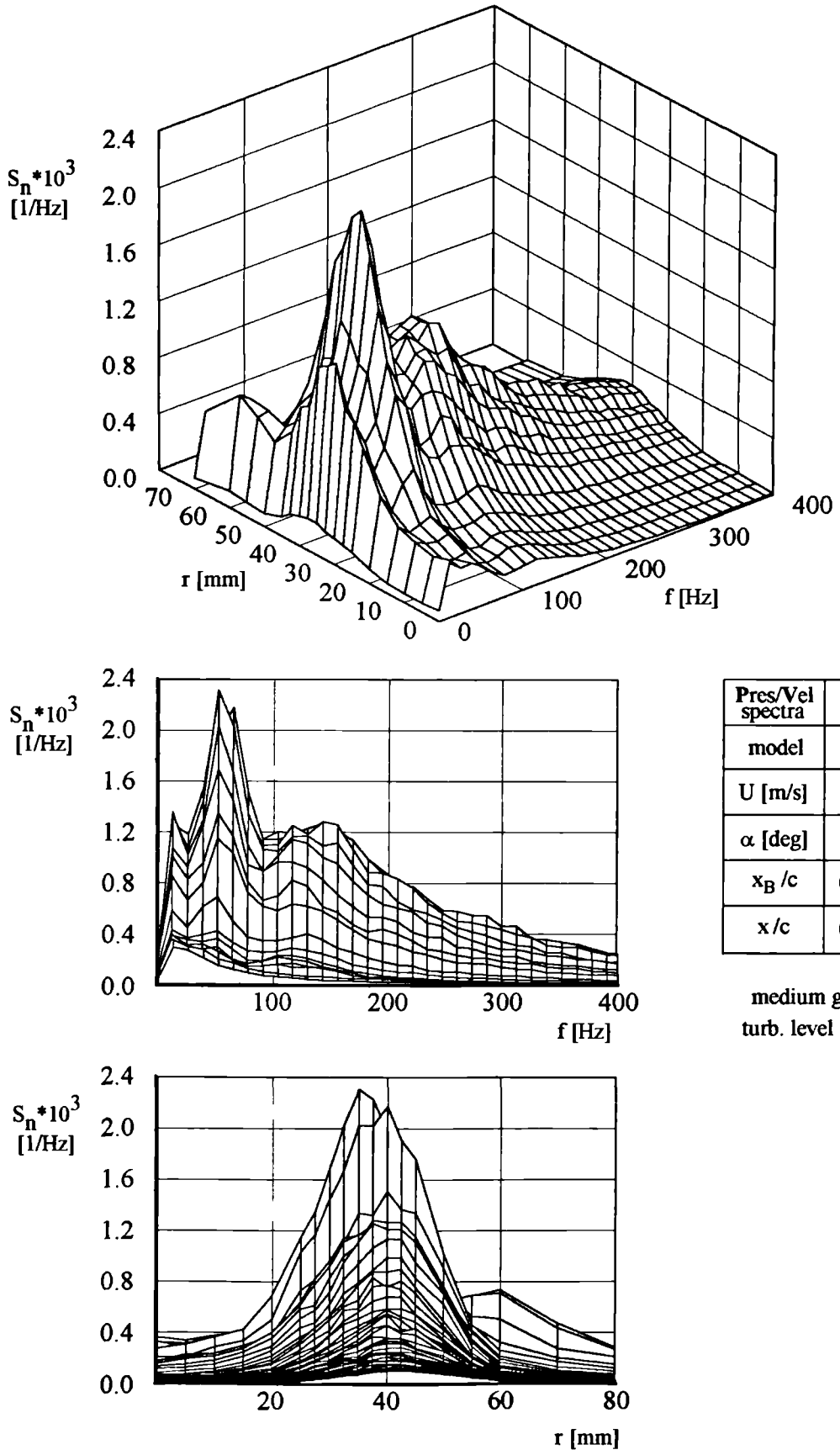

Pres/Vel spectra	P
model	LM
U [m/s]	12.5
α [deg]	24
x_B /c	0.50
x/c	0.80

medium grid
turb. level 3.6%

Figure 4.84.Pressure spectra with medium grid (turbulence level 3.6%).

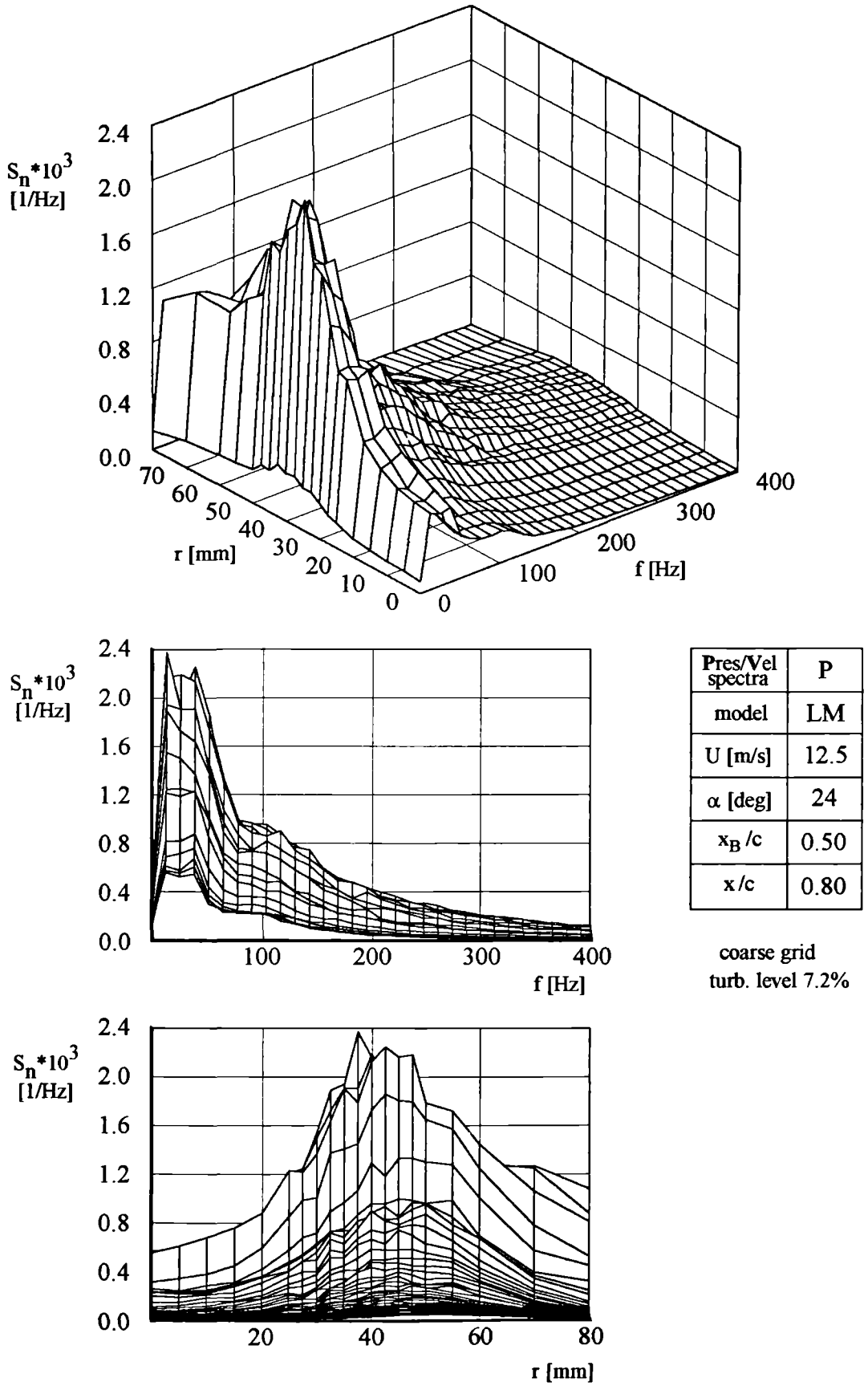

Figure 4.85.Pressure spectra with coarse grid (turbulence level 7.2%).

CHAPTER 5

DISCUSSION

Most of the results, given in chapter 4, have already been the subject of preliminary comments and discussions. The objectives of this chapter are twofold. Firstly, the breakdown phenomena taking place in two widely different experimental configurations are compared with each other in order to find their common features. Secondly, several aspects of the breakdown phenomenon which deserve particular attention from the viewpoint of understanding the nature of quasi-periodic pressure fluctuations, are discussed further. No attempt, however, is made to support or refute any of the numerous existing theories of vortex breakdown, nor to develop any new ones based on the results presented. This was not within the scope of the current investigation.

5.1. General comparison of vortex breakdown in the two experiments

Despite the apparent differences in the flow configurations, due to two widely different experimental set-ups (i.e. the vortex tube and on the delta wing) the results obtained are in many respects similar and fully comparable.

First of all, in terms of the mean flow, the profiles of the axial velocity

(shown in figures 4.3 and 4.6 for the vortex tube, and in figures 4.44 and 4.45 for the delta wing) indicate that both experiments were dealing with vortices of similar dimensional scale and character (i.e. a jet-like profile prior to the burst and a wide wake-like profile downstream).

Secondly, spectral mapping of the pressure fluctuations due to the vortex bursting gave results which are directly comparable with each other. The difficulties experienced with probe interference for the delta wing experiment did not permit as detailed a picture being obtained as for the vortex tube experiment. Nevertheless, inspection of figures 4.13 through 4.17 for the vortex tube and 4.46 through 4.49 for the delta wing, shows clearly that the pressure fluctuations in both cases *are* quasi-periodic (sharp peaks in narrow frequency bands), and can be detected only within a limited radial range (relative to the vortex axis). Similar features are exhibited by the spectral mapping of the velocity fluctuations (see, for example, figures 4.24, 4.25 and 4.26 for the vortex tube and 4.50, 4.51 and 4.52 for the delta wing). In addition, both pressure and velocity fluctuations are most pronounced for the radial location corresponding approximately to the point of inflection in the velocity profiles (figure 4.32 for the vortex tube and 4.55, 4.56 and 4.57 for the delta wing).

Thirdly, judging from the correlations obtained, the form of the disturbance causing the pressure fluctuations is similar; it is plausible to assume that it is of spiral form. This is discussed further, amongst other topics, in the following sections.

5.2. Form of the vortex breakdown

The examples of different forms of vortex breakdown were given in section 2.4.1 of the literature review. It should be noted, however, that most of them were revealed at relatively low Reynolds number. For example various forms of breakdown in th early work of Sarpkaya (1970,1971) and Faler and Leibovich (1977) were documented for Reynolds numbers only up to about 10^4 (based on the test

section diameter[1]), in carefully selected and controlled experimental conditions, where the flow is basically laminar. The 'maps' of vortex breakdown forms were shown in figures 2.34 and 2.35.

Little is known about the nature of the vortex breakdown in the vortex tube at high Reynolds numbers, and in particular, about disturbances emerging in the breakdown wake. Only recently Sarpkaya (1995) described a so-called 'conical' or 'turbulent' breakdown (figure 2.33d) for a range of Reynolds numbers (based on tube diameter) of between 5×10^4 and 22.5×10^4. However, his observations do not give an insight into the flow character downstream of the burst, apart from noting the region of turbulence. The present measurements in the vortex tube were conducted for $Re \approx 13\times10^4$, which falls within the range of Sarpkaya's (1995) conical burst and his visual observations are confirmed fully. However, the quasi-periodic behaviour of the flow field in the breakdown wake indicates the presence of coherent structures (i.e. the flow is *organised* to a certain extent, rather than just turbulent in a disorderly manner).

The coherent structures in the breakdown wake are captured in figure 5.1 which shows the meridional cross-section of the flow in the vortex tube, obtained by means of laser-sheet technique. The most noticeable feature is the appearance of a pattern of staggered vortical structures (called here for brevity 'eddies') originating from the initial burst, which are identified as the cross-section of a spiral structure. Of course, it is difficult to judge from this or similar photographs whether the cross-section shown represents a 'cut' through a spiral structure or a set of tilted vortex rings. The main argument for rejecting the possibility of 'ring like' structures[2] are the experiments by Brücker and Althaus (1995), who used the PTV techniques with volume scanning. They showed that the axisymmetric bubble-type breakdown changes into spiral mode after a certain value of *Re* is reached (see figure 2.38). This value in terms of maximum choke speed and choke diameter happens to be 1600. The

[1] A Reynolds number based on the vortex core diameter which is probably a more meaningful length would be approximately one order of magnitude lower.
[2] although such structures have been observed in condensation trails.

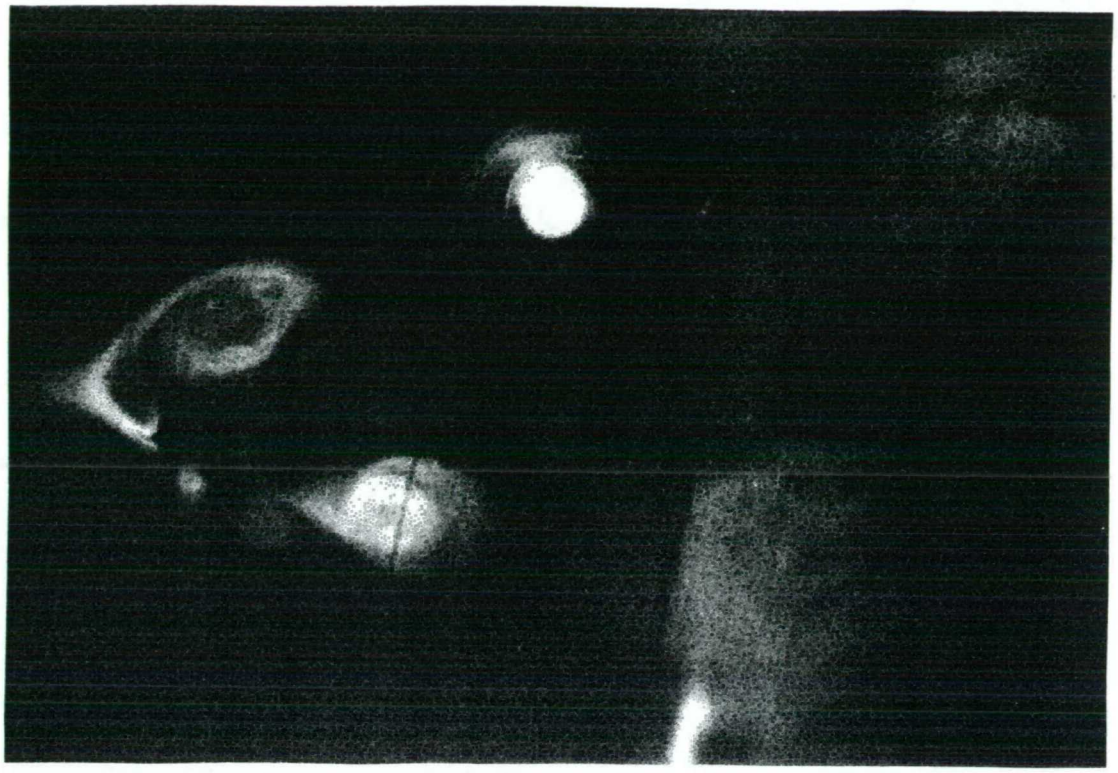

Figure 5.1.Light sheet visualisation of vortex breakdown in the vortex tube (short choke). Approximate flow velocity in the choke 2 m/s.

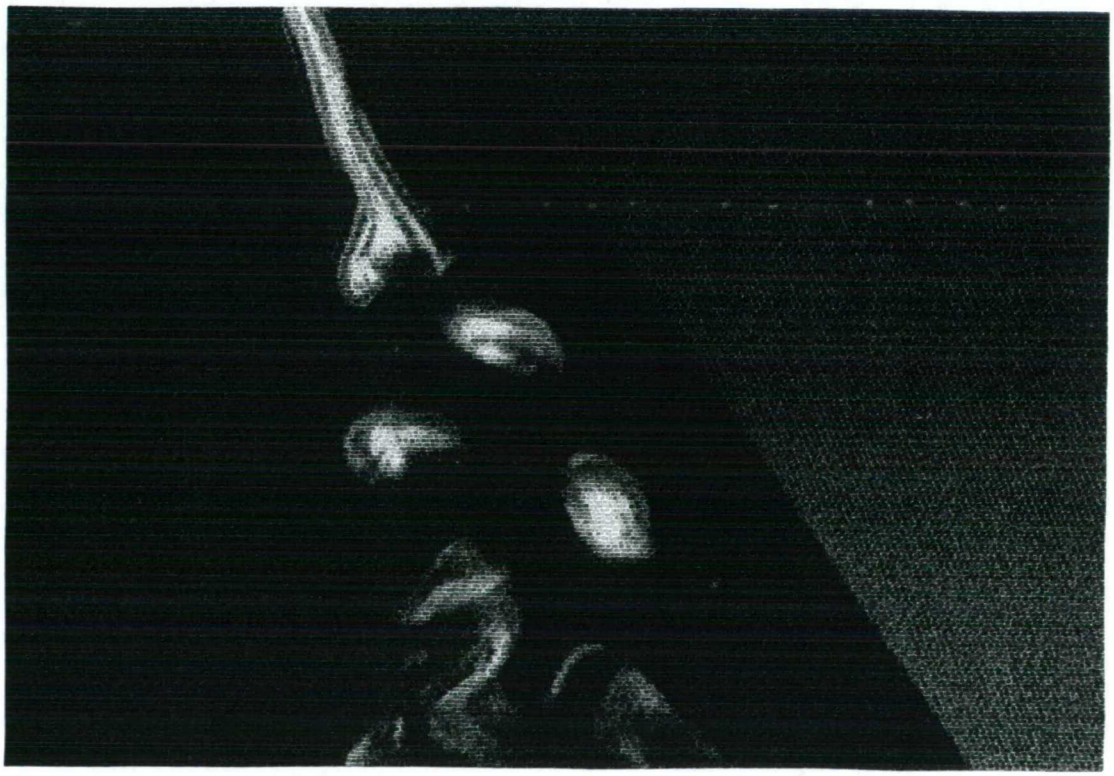

Figure 5.2.Light sheet visualisation of vortex breakdown on the delta wing (small model). Approximate tunnel speed 0.3 m/s, $\alpha=23^{O}$, $x_B/c=0.50$.

corresponding *Re* in figure 5.1 is one order of magnitude greater (i.e. $Re = 1.5\times10^4$), whereas the present measurements were conducted for $Re \approx 13\times10^4$. Thus the assumption that 'ring-like' disturbances are present during the current investigation, appears to be baseless[3].

It is also worth noting that the phenomena investigated take place in a turbulent state of the flow. Turbulence, due to its character, is a source of three-dimensional (or non-axisymmetrical) perturbations. These perturbations are thought to induce instability in the vortex breakdown. Thus the spiral structures in the turbulent flow regime would be a logical consequence of this instability. Another indication of the spiral character of the coherent structures is included (however not explicitly stated) in the observations by Sarpkaya (1995). The so-called 'conical' form of breakdown (figure 2.33d) develops from the 'bubble' form (shown in figure 2.33c) in such a manner that the spiral tail is growing, while the bubble's size is decreasing. At the same time both structures are merging. This can be explained by the wave theory of Leibovich (1985) as the 'leakage' of energy from axisymmetric fluctuations (bubble form) to non-axisymmetric ones (spiral form), which eventually take control over the phenomenon.

The form of breakdown in the vortex tube could have been investigated by using techniques similar to those applied by Brücker and Althaus (1995). However this would represent a serious research programme and was never considered to be a part of the current investigations. The ambiguity concerning the form of the structures emerging from the breakdown, which was realised after the results were obtained, could have been resolved by simultaneously using three probes introduced in different meridional planes. This would distinguish between possible ring or spiral structures. Alternatively, an oblique, continuous wave, laser sheet might have been introduced so that it would cross the plane of a ring structure (giving a 'circular'

[3] If the structures were vortex rings, there would be no reason, why they should be tilted in the same manner and at similar angle relative to the vortex axis (as would appear from figure 5.1). As the choke diverges, the swirl component changes and vortex rings would have to rotate with different rates, so that the pattern would have to be less orderly.

image). However, this method is much less practical and more elaborate than using three probes, since the correct inclination of the sheet would have to be found somewhat 'by chance'.

Figure 5.2. shows a similar flow pattern to the one in figure 5.1, but obtained from the delta wing experiment. Here, at a tunnel speed of 0.3 m/s, it was possible to identify the structure as a spiral (in a normal light beam). Hence there is no ambiguity about the 'origin' of the staggered pattern revealed by the light sheet technique. It is worth mentioning that generally it is accepted that the breakdown over delta wings assumes a spiral form (Gursul-1994, Hubner and Komerath-1995).

In the light of the above facts, it is concluded that in both experiments the actual form of breakdown is a spiral one. This is supported also by the correlation measurements commented on briefly in chapter 4 and discussed in more detail later in this chapter.

5.3. Source of pressure fluctuations - interpretative hypothesis

An important issue from the viewpoint of the physics underlying the occurrence of quasi-periodic pressure and velocity fluctuations is to establish their source. There are at least three possibilities:

- pressure fluctuations that are sound waves.
- pressure fluctuations that correspond to waves which propagate on vortex flows (which are known to be so-called 'wave guides').
- pressure fluctuations that are caused by vortical structures (eddies) convected by the flow.

The first possibility can be rejected since sound waves propagate at the speed of sound. This would have to produce a nearly zero time lag during the correlation measurements (the test section length is 1.5 m). Although there is probably not enough evidence to refute the second possibility definitely, in the author's opinion, both the motion pictures and still photographs (such as these in figures 5.1. and 5.2)

clearly indicate the presence of well-defined vortical structures (similar in character to vortices shed behind bluff bodies) rather than waves.

It is worth adding that the experiments combining the laser sheet visualisation with the measurements of the pressure fluctuations indicated that the sharpest peaks in the spectra correspond roughly to the radial location of the centres of the vortical structures ('eddies'). Furthermore, the motion pictures show that the material particles rotate around the spiral filament in agreement with the axial velocity profile, which has a higher velocity outside the vortex core and a lower one inside.

The above findings, together with the location of the highest excitation level in relation to the radial profiles of axial velocity (see figures 4.32, 4.55, 4.56 and 4.57), are the basis for an interpretative hypothesis concerning the possible sources of the quasi-periodic fluctuations. This is suggested in figure 5.3. It shows the redrawn flow pattern from figure 5.1 with the axial velocity profile and the surface of the highest excitation level added. It is anticipated that the spiral structure (or 'eddies' in terms of longitudinal cross-section) is directly responsible for the appearance of quasi-periodic fluctuations of pressure and velocity.

The 'scenario' presented in figure 5.3 can explain most of the features of the vortex breakdown and in particular:

- The broad band spectra present at the early stages of the breakdown can be interpreted as either an indication of transition within the laminar vortex core or a manifestation of some transient features related to the coils of the spiral which are not 'separated' fully from the initial burst, and thus do not yet have a well defined size. A possible example are the structures of smaller dimensions (seen in the lower half of figure 5.1), emerging just after the initial burst. The sudden appearance of sharp peaks within a short streamwise distance (Δx = 10 mm between figures 4.11 and 4.12) may be interpreted as the end of the process of spiral formation.
- The definite size and spatial distance between the 'eddies' justify the quasi-periodic character of the fluctuations. The well-defined radial position of the

'eddies' determines the local character of the fluctuations (within a limited radial range).

- It can be anticipated that the most severe changes in the flow field (e.g. periodic increase and decrease in velocity, and thus in pressure) take place at the radial co-ordinate corresponding to the location of the centres of the eddies. This must be related to the high level quasi-periodic fluctuations.

It should be added that the azimuthal component of velocity present in the breakdown wake must cause the spiral's rotation (for simplicity, say, as a rigid body revolving about the tube's centreline, although this concept may not be applicable in the region of turbulent flow). This rotation, however, does not change the anticipated mechanisms of pressure fluctuations (i.e. the 'eddies' from the photographs in figures 5.1 and 5.2 still exist, and it is their apparent streamwise convection speed which is affected[4]).

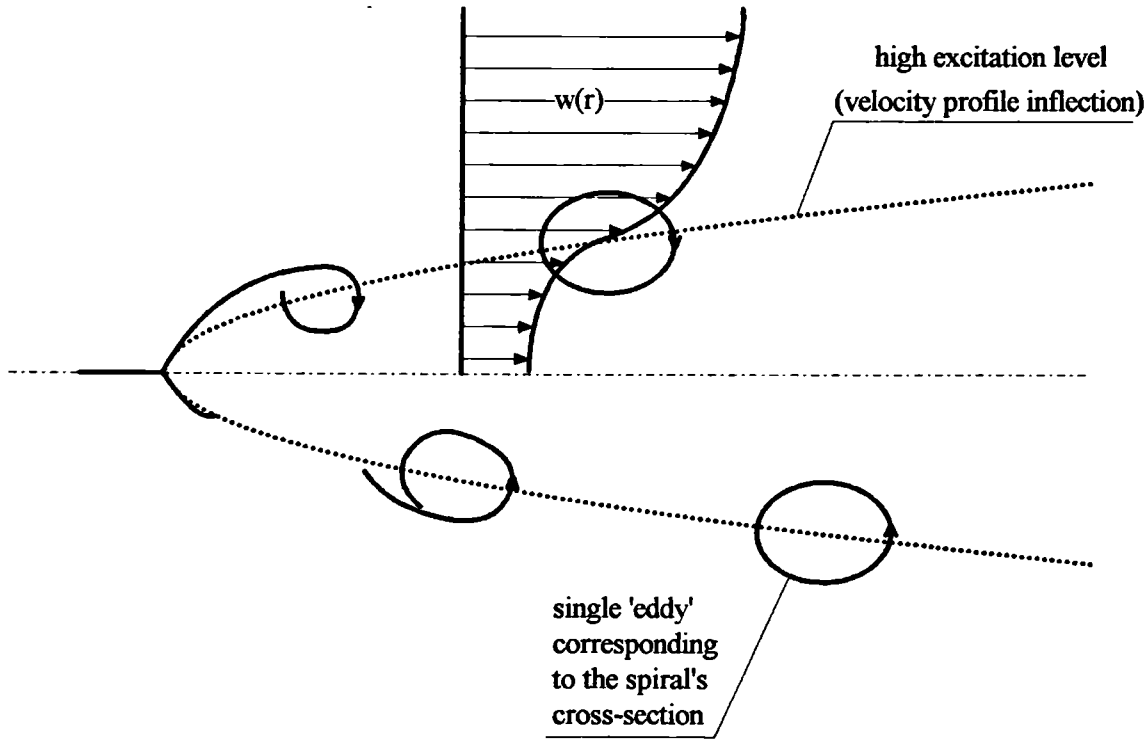

Figure 5.3. Interpretative hypothesis concerning the source of the quasi-periodic pressure and velocity fluctuations.

[4] A somewhat similar effect may be obtained by rotating a wire spring about the axis. The spring's coils appear to 'flow' along the axis although the position of the spring remains constant. In the case of the spiral filament a displacement of the spring along its axis should be added to make this analogy complete.

Another interesting question is the sense (or direction of winding) of the spiral structure when compared to the sense of streamlines. There is a general consensus in the existing literature that the spiral structure rotates in the direction indicated by the streamlines, however the sense of the filament forming the spiral (or in other words the winding of spiral's coils) is opposite to that of streamlines (e.g. Lambourne and Bryer-1962, Brücker-1993). Similar conclusions can be deduced from the present correlation measurements with master and slave probes located in two meridional planes perpendicular to each other - as already explained in section 4.1.3. Figure 5.4 shows the vortex and probes' arrangement (compare also with figure 4.33b). The slave probe was traversed in the streamwise direction both upstream and downstream of the master. The figure shows a particular probe arrangement[5] when master and

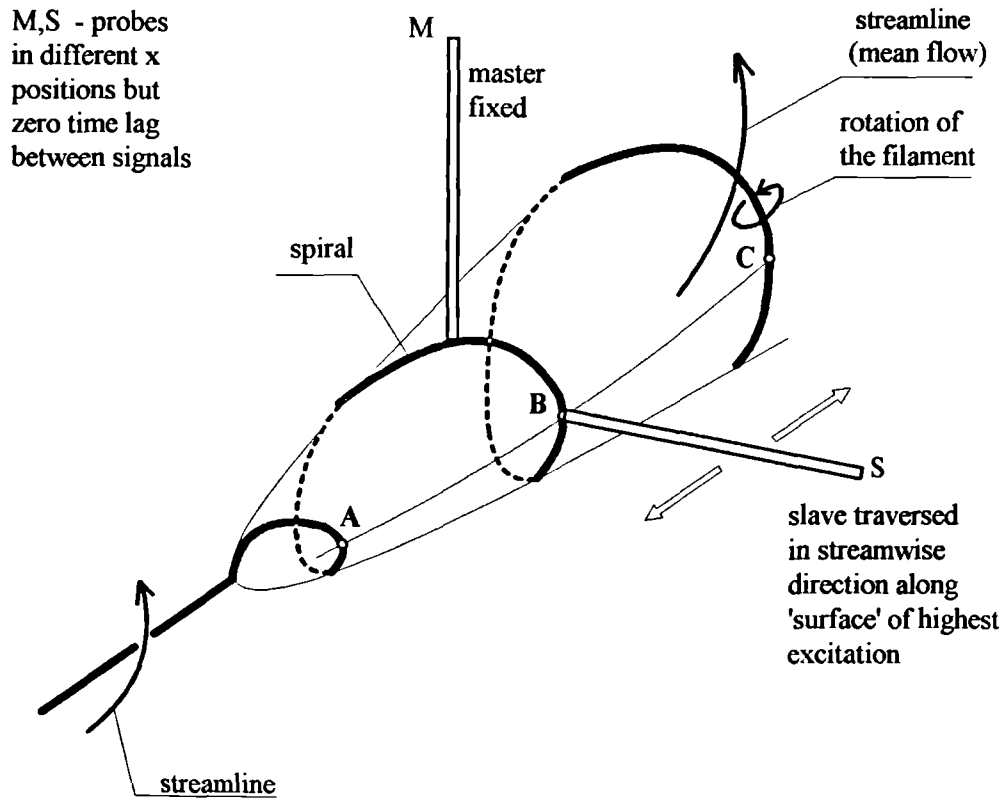

Figure 5.4.Spiral structure emerging from the burst (correlation measurements).

[5] Δx between master and slave was 11.55 mm as indicated, for example, in figure 4.37.

slave probes read the pressure 'pulse' with 'zero' time lag (i.e. *in the same phase*). Therefore, the deduced direction of the spiral's winding is opposite to the direction of the streamlines' winding.

Similar results were obtained from the wing experiment. Here the master probe was introduced at a certain streamwise position within the vortex, as explained in section 4.2.3, whereas the slave was a transducer mounted flush beneath the vortex axis at various streamwise locations (compare also figure 4.75).

It should be noted that generally the correlation between the master and slave separated by more than one spiral's turn (e.g. point C in figure 5.4) was never as good as between master and slave at B - compare graphs 'd' and 'h' in figure 4.37. This may have been caused by the characteristic frequency of fluctuations changing rapidly within a short distance along the vortex. On the other hand, the strong vortical structures may decay significantly within one spiral's turn (note the smeared character of the 'eddies' close to the right edge of the figure 5.1 compared to the 'eddies' emerging immediately from the initial burst). This may be caused simply by viscous dissipation, however the possibility of some breakdown phenomena within the spiral filament itself (i.e. on a smaller scale that the primary burst) cannot be ruled out.

It can be argued that there is another possible spiral arrangement leading to 'zero' time lag between master and slave, as shown in figure 5.5. In figure 5.4 the master and slave are separated by only one quarter of turn of the spiral, whereas in figure 5.5 they are separated by three quarters of the spiral which is 'tighter' and of opposite sense. The latter situation is ruled out, because the correlation between the master and the slave at location A' should be *better* than for the slave at location B'. The traversing of the slave in the upstream direction went much beyond point A' and such a *better* correlation was not found. Therefore, the only plausible assumption about the spiral orientation is the one from figure 5.4, where the direction of the spiral's winding is opposite to the direction of the streamlines' winding.

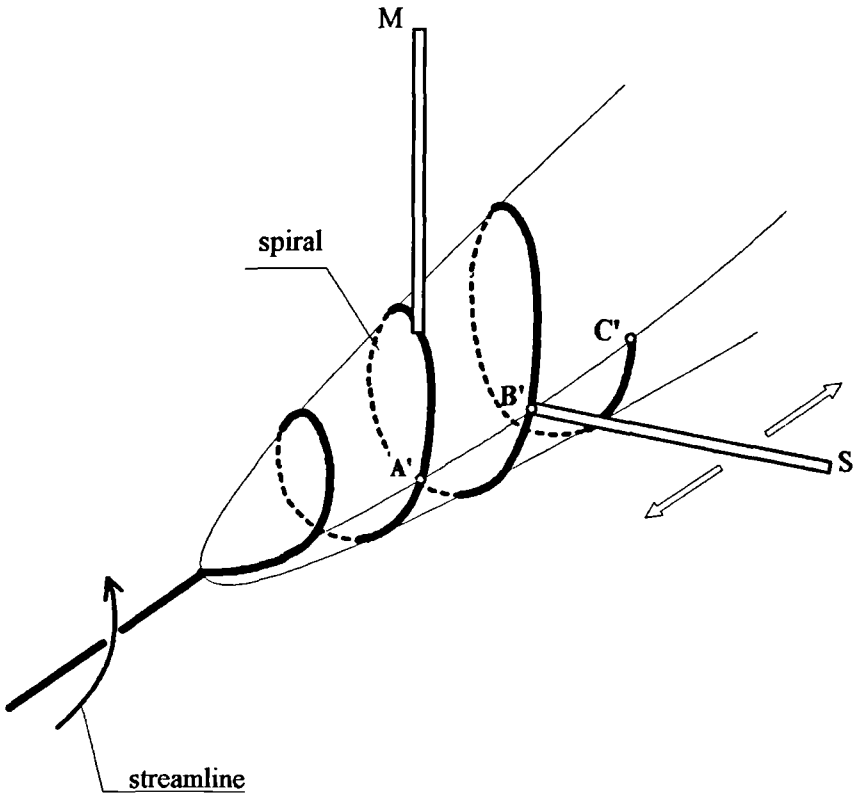

Figure 5.5.A possible spiral's orientation producing similar results as the one from figure 5.4.

5.4. Frequency parameter

The frequency parameters proposed in sections 4.1.2 and 4.2.2 for both vortex arrangements (equations 4.1 through 4.4) require further comments. Generally speaking, they are based on the core diameter defined as the diameter of highest excitation level (either in terms of RMS or actual maximum in spectral density) and a somewhat arbitrarily chosen reference velocity. Two questions, related to each other, should be addressed. First, what is the reason for apparently different values of the frequency parameter for the vortex tube (say, between 0.17 and 0.23) and the delta wing (say, between 0.3 and 0.4)? Second, what are the other possible length scales and reference velocities, which might be considered as the basis for alternative frequency parameters?

The discrepancy raised by the first question can be explained by considering the reference velocities used in the expressions for the frequency parameters. For the vortex tube the axial 'free stream' velocity in the narrowest place of the choke was taken as the reference. For the wind tunnel tests the tunnel speed seemed the most straightforward. It can be argued, however, that neither of these velocities is the one which 'controls' the phenomenon. In the vortex tube the 'free stream' velocity changes in the streamwise direction by about a factor of two (so, the choice of the highest *is* somewhat arbitrary). Clearly, a lower reference velocity would produce a higher frequency parameter. Yet, for the delta wing the actual velocity which 'controls' the bursting phenomena may be up to 50% higher than the tunnel speed (see the maxima in the axial velocity profiles in figure 4.45). If, just for argument, the reference velocity for the vortex tube was 30% lower and for the delta wing 30% higher than the ones used, the frequency parameters in both situations would be quite close (say, within the range of 0.25 to 0.30). Therefore, the possible differences (if any) should not be judged by the value of the frequency parameters introduced in chapter 4, but rather by the general features exhibited by vortices in both experiments (outlined briefly in section 5.1). These indicate that, despite the widely different arrangements, the actual phenomena *are* the same.

The second question, concerning other possible reference lengths and velocities, is much more difficult to answer on the basis of the present research. For example, in the vortex tube experiment, the reference velocity can be defined in many different ways; three possible examples are given below:

- the 'free stream' velocity, which is a single value (taken from the narrowest part of the choke) or which changes in the streamwise direction (say, the local 'free stream' velocity, i.e. outside the core).
- the propagation speed of the pressure disturbances (axial or tangential or their sum)
- the axial velocity at the point of velocity profile inflection.

Clearly, the data collected does not allow an investigation of all possibilities. Some of the results are only fragmentary (as for example the propagation speeds), hence there was no chance to investigate corresponding frequency parameters.

There is also a wide choice of the length parameters. Usually, for experiments with confined vortices, the reference length is taken as some characteristic length of the apparatus (most often it happens to be the diameter of the test section). This approach, however, is erroneous. The scale of the phenomena is controlled by the various features of the flow, which in turn do not necessarily depend upon the dimensions of the rig.

For the delta wing experiments the reference length is usually taken as some characteristic wing dimension (say, the root chord or the wing span). Mabey (1995) introduced the reference length which is effectively a product of the wing's semi-span and sine of the angle of incidence. These approaches are generally acceptable, because the length scale of the breakdown *does* depend on the size of the wing. However, from the viewpoint of the basic research (i.e. the physics of the breakdown flow field) a length related more directly to the phenomenon itself would be desirable.

Another length parameter used in breakdown studies is the diameter of the vortex core upstream of the burst (taken, for example, as the diameter of the axial velocity jet or the diameter related to the maximum swirl velocity). This, however, does not take into account the possible changes in the size of the phenomenon due to the adverse pressure gradient imposed on the breakdown region. It was shown (figure 4.7) that for two different chokes the core diameter after the burst changed by a factor of two, whereas the core diameter upstream of the burst was the same.

It should be admitted that the problem of a proper choice of reference length and velocity was not solved completely during the current investigations. The proposed frequency parameters are based on the observations of the development of the coherent structures in the breakdown wake. It was found that as the spiral

disturbance grows in size, the characteristic frequency of pressure disturbances related to the disturbance drops. Remarkably, the product of the characteristic frequency and the core diameter (based on the location of highest excitation, which overlaps both the inflection in the axial velocity profile and the location of the centres of the 'eddies' from the flow visualisation, as already noted) is approximately constant in both experiments. In these circumstances any 'reasonable' reference velocity produces a constant frequency parameter. Therefore, the length parameter based on the location of the highest excitation appears to be appropriate, however some more detailed research on the velocity controlling the phenomenon would be desirable.

The value of the frequency parameter for breakdown related fluctuations, based on the core diameter, is within a range of 0.2 to 0.4 (depending on what reference velocity is used). In addition, the well-pronounced peaks in the spectra, the clearly visible vortical structures downstream of the burst, and also some similarity between the burst and the flow around the body of revolution, may lead to some analogies between breakdown and flows past bluff bodies (and thus bluff body vortex shedding). On the other hand, it is interesting that the frequency parameter for maximum jet noise is 0.3 (Richards and Mead-1978). It has been suggested that there is an analogy between the generation of a high noise level, due to velocity shear in the jet, and the mechanisms responsible for fluctuations due to vortex breakdown (although the axial velocity profile downstream of the burst is wake-like, unlike in jets). However there is not enough evidence to support or refute any of these analogies.

The frequency parameter obtained from the delta wing experiments (n=0.3 to 0.4) is important from the viewpoint of early design studies of aircraft. The velocity profiles due to the vortex breakdown (and hence the point of their inflection) can be predicted reliably by relatively simple and efficient Euler calculations. The derived frequency parameter, together with the known aircraft velocity and calculated core diameter, can be used for predicting the frequency of the excitation imposed on the

airframe due to the bursting vortices. Similarly, inexpensive experiments conducted in wind tunnels, involving only the measurements of velocity profiles in the core region, can produce crude but quick estimates of the frequency of expected aerodynamic loads.

5.5. Excitation level and breakdown control

An interesting problem is the level of the excitation due to vortex breakdown imposed on a surface (be it a vortex tube wall or the suction side of the delta wing). Remarkably, in the experiments in the vortex tube no significant fluctuations were detected on the walls of the chokes or the test section. This is a clear indication that there are no 'far field' effects of the vortex breakdown and that no pressure waves propagate through the 'layer' of the outer flow (i.e. contained between the edge of the vortex and the wall of the test section). Similarly, for the delta wing experiment there is hardly any excitation detected on the wing's surface, as long as the burst region is separated from it by a 'layer' of the outer flow. The pressure fluctuations detected on the wing's surface become significant as incidence increases when the core gets wide enough to be in direct contact with the wing. This was shown in figure 4.66 and interpreted in figure 4.67. Two important conclusions can be drawn:

- The best way to diminish the adverse effects of the vortex breakdown excitation on the airframe components is to remove them from the direct vicinity of the burst region (ideally, say, about one core diameter). Clearly, this is not possible in every situation, but even minor changes (from the point of view of the overall aerodynamic performance) can significantly reduce the damage due to the fatigue processes.
- In the high-alpha flight regime, for slender wing configurations, there will always be the tendency of the vortex core to grow significantly (due to higher adverse

pressure gradients). Thus the wing's surface *will* have to experience the increased excitation, unless 'blowing' techniques are used which might delay the occurrence of breakdown. If, for example, axial blowing was applied at $\alpha=29^{o}$ (figure 4.67), so that the burst took place, say, at x/c=0.5 or later, there would be perhaps scarcely any burst-related excitation detected on the wing's surface. Of course, this might be unacceptable because of an associated increase in fin buffeting.

The vortex tube experiments with an oscillating blade (section 4.1.4) were conducted to check the possibility of breakdown control by imposing a small perturbation onto the flow upstream of the burst. (In real applications this might be, say, an oscillating leading-edge flap on the wing). Had the breakdown responded to the periodic perturbation by exhibiting any resonance phenomena (say, by an increase of excitation level downstream of the burst for a certain frequency range) there might have been a possibility of controlling its occurrence by a careful selection of the phase of the perturbations. Unfortunately, the tests gave inconclusive results.

For perturbations exceeding a certain level (a blade amplitude of 3^{o}) the structure of the breakdown was destroyed and the axial filament oscillated in an disorderly manner about the test section axis. At the same time the mean position of the burst was apparently displaced ahead of the choke. The spectral picture was also significantly changed.

Another, somewhat related, topic is the response of the breakdown flow field to increased turbulence levels (delta wing tests described in section 4.2.4). Here the 'perturbation' has a continuous spectrum corresponding to the spectrum of turbulence introduced. Therefore a *direct* comparison with the tube experiment is inappropriate. However, the results are qualitatively repeated. The character of the spectra (and also the burst appearance) does not change noticeably as long as the perturbation is not 'too high'. After turbulent fluctuations of a high level (i.e. of the order of the breakdown-related fluctuations) are introduced the structure of the flow is unclear. For example, it becomes difficult to judge where the burst takes place, due to rapidly

oscillating axial filament. The drastic change in the spectrum character (figure 4.85 vs. figures 4.82, 4.83 and 4.84) consisting of a shift to the lower frequencies and a much broader peak may suggest a more upstream location of the breakdown. This would be consistent with the vortex tube experiment.

CHAPTER 6

CONCLUSIONS

The following conclusions of a general nature can be drawn from the results and discussion presented:

1. Detailed investigations of the pressure fluctuations due to the phenomenon of vortex breakdown have been conducted. Spectral mapping of the pressure field has been well-documented for two experimental configurations: the vortex tube and the delta wing. The vortex breakdown wake was found to be a source of pronounced quasi-periodic fluctuations. These are of *local* radial range, but persist along the edge of the vortex core within a distance of several core diameters.
2. It is suggested that the immediate source of pressure (and velocity) fluctuations is the spiral vortical structure originating from the initial burst.
3. The highest level of excitation in the breakdown wake corresponds approximately to the point of inflection in the axial velocity profiles. It is recommended that the definition of the vortex core should be based on the radial location of this point, and the corresponding diameter should be used as a length scale for the frequency parameter studies.
4. The frequency parameter, based on the core diameter and the free stream

velocity, $n=f\,D_{core}\,/\,U$, is within the range of 0.3 to 0.4 for the delta wing configuration. This result is important for the early design studies of aircraft for rough estimates of the frequency of dynamic loads due to breakdown.

5. Due to the *local* character of the fluctuations, vortex breakdown can be a source of buffet excitation on airframe components only when closely approaching their surface. Thus reducing the buffet is possible in some situations, simply by making moderate changes in the airframe configuration. The required displacement of the core relative to the endangered components is of the order of one vortex core diameter.
6. Redesigning the airframe configuration may be insufficient for a high-alpha flight regime (say, $\alpha > 30^{o}$), due to large adverse pressure gradients causing a rapid vortex core expansion which makes contact with aircraft components more likely.
7. The vortex breakdown is not susceptible to small periodic perturbations, including the perturbations at the quasi-periodic frequency. Thus its control in this way is unlikely. Large perturbations induce premature bursts.

Recommendations for supplementary research:

1. More detailed measurements of the velocity field (possibly by LDV techniques) to find a reference velocity to unify the frequency parameter obtained from the vortex tube and the delta wing.
2. Tests on a larger family of delta wings to check the generality of the proposed frequency parameter based on the core diameter and also to explain the discrepancy between current measurements and frequency parameter proposed by Mabey (1995).
3. Detailed studies of the burst region (preferably by PIV techniques) to establish the origin and development of spiral structures responsible for quasi-periodic fluctuations.

LIST OF REFERENCES

[1] Agrawal S., Barnett R.M., Robinson B.A. (1990) Investigation of vortex breakdown on a delta wing using Euler and Navier-Stokes Equations, *AGARD-CP-494, Symposium of the Fluid Dynamics Panel in Scheveningen, The Netherlands, 1st to 4th October 1990*

[2] Agrawal S., Barnett R.M., Robinson B.A. (1992) Numerical Investigation of vortex breakdown on a delta wing, *AIAA Journal*, **30** (3), pp. 585-591

[3] Bean D.E., Greenwell D.I., Wood N.J. (1993) Vortex control technique for the attenuation of fin buffet, *Journal of Aircraft*, **30** (6), pp. 847-853

[4] Benjamin T.B. (1961) The explanation for the vortex breakdown phenomenon, *ARC, F.M. 3088 (22.802)*

[5] Benjamin T.B. (1962) Theory of the vortex breakdown phenomenon, *J. Fluid Mech.* **14** (4), pp. 593-629

[6] Benjamin T.B. (1967) Some developments in the theory of vortex breakdown, *J. Fluid Mech.* **28** (1), pp. 65-84

[7] Berger S.A., Erlebacher G. (1992) Vortex breakdown incipience: Theoretical considerations , *NASA-CR-189734*

[8] Bossel H.H. (1969) Vortex breakdown flowfield, *Phys. Fluids*, **12** (3), pp. 498-508

[9] Bossel H.H. (1971) Vortex computation by the method of weighted residuals using exponentials, *AIAA Journal*, **9** (10), pp. 2027-2034

[10] Brown D.,Lee B.H.K., Tang F.C. (1990) Some characteristics and effects of the F/A-18 LEX vortices, *AGARD-CP-494, Symposium of the Fluid Dynamics Panel in Scheveningen, The Netherlands, 1st to 4th October 1990*

[11] Brown G.L., Lopez J.M. (1990) Axisymmetric vortex breakdown Part 2. Physical mechanisms, *J. Fluid Mech.*, **221**, pp. 553-557

[12] Brücker C, Althaus W. (1992)) Study of vortex breakdown by particle tracking velocimetry (PTV) Part 1: Bubble-type vortex breakdown, *Experiments in Fluids*, **13**, pp. 339-349

[13] Brücker C. (1993) Study of vortex breakdown by particle tracking velocimetry (PTV) Part 2: Spiral-type vortex breakdown, *Experiments in Fluids*, **14**, pp. 133-139

[14] Brücker C., Althaus W. (1995) Study of vortex breakdown by particle tracking velocimetry (PTV) Part 3: Time-dependent structure and development of breakdown-modes, *Experiments in Fluids*, **18**, pp. 174-186

[15] Bryer D.W., Pankhurst R.C. (1971) Pressure-probe methosd for determining wind speed and flow direction. *National Physical Laboratory, Department of Trade and Industry. Published by Her Majesty's Stationery Office 1971*

[16] Canbazoglu S., Lin J.-C., Wolfe S., Rockwell D. (1995) Buffeting of fin, distortion of incident vortex, *AIAA Journal*, **33** (11), pp. 2144-2150

[17] Cassidy J.J, Falvey H.T. (1970) Observations of unsteady flow arising after vortex breakdown, *J. Fluid Mech.*, **41** (4), pp. 727-736

[18] Cunningham A.M., den Boer R.G. (1990) Steady and unsteady aerodynamics of a pitching straked wing model at high angles of attack, *AGARD-CP-494, Symposium of the Fluid Dynamics Panel in Scheveningen, The Netherlands, 1st to 4th October 1990*

[19] Darmofal D.L. (1993) A study of the mechanisms of axisymmetric vortex breakdown. *Doctoral Thesis, Dept. of Aeronautics and Astronautics, Massachusetts Institute of Technology*

[20] Delery J.M. (1994) Aspects of vortex breakdown , *Prog. Aerospace Sci.*, **30**, pp. 1-59

[21] Del Frate J.H., Fisher D.F., Zuniga F.A. (1990) In-flight flow visualisation and pressure measurements at low speeds on the NASA F-18 High Alpha Research Vehicle, *AGARD-CP-494, Symposium of the Fluid Dynamics Panel in Scheveningen, The Netherlands, 1st to 4th October 1990*

[22] Elle B.J. (1961) An investigation at low speed of the flow near the apex of thin delta wings with sharp leading edge, *ARC, R.&M. No. 3176 (19,780)*

[23] Erickson G.E., Gilbert W.P. (1983) Experimental investigation of forebody and wing leading-edge vortex interactions at high angles of attack, *AGARD Conference Proceedings, AGARD-CP-342, Fluid Dynamics Panel Symposium, 25-28 April 1983, Rotterdam, Netherlands*

[24] Escudier M. (1984) Observations of the flow produced in a cylindrical container by a rotating endwall, *Experiments in Fluids*, **2**, pp. 189-196

[25] Escudier M. (1987) Confined vortices in flow machinery, *Ann. Rev. Fluid Mech.*, **19**, pp. 27-52

[26] Escudier M. (1988) Vortex breakdown: observations and explanations, *Prog. Aerospace Sci.*, **25**, pp. 189-229

[27] Escudier M.P., Bornstein J., Zehnder N. (1980) Observations and LDA measurements of confined turbulent vortex flow, *J. Fluid Mech.*, **98** (1), pp. 49-63

[28] Escudier M.P., Keller J.J. (1983) Vortex breakdown: a two stage transition, *AGARD Conference Proceedings, AGARD-CP-342, Fluid Dynamics Panel Symposium, 25-28 April 1983, Rotterdam, Netherlands*

[29] Escudier M.P., Keller J.J. (1985a) Essential aspects of vortex breakdown, *Colloquium on vortex breakdown, February 11th-12th, 1985, Aachen*

[30] Escudier M.P., Keller J.J. (1985b) Recirculation in swirling flow: a manifestation of vortex breakdown, *AIAA Journal*, **23** (1), pp. 111-116

[31] Escudier M.P., Zehnder N. (1982) Vortex-flow regimes, *J. Fluid Mech.*, **115**, pp. 105-121

[32] Faler J.H., Leibovich S. (1977) Disrupted states of vortex flow and vortex breakdown, *Phys. Fluids*, **20** (9), pp. 1385-1400

[33] Faler J.H., Leibovich S. (1978) An experimental map of the internal structure of a vortex breakdown, *J. Fluid Mech.*, **86** (2), pp. 313-335

[34] Fraenkel L.E. (1967) On Benjamin's theory of conjugate vortex flows, *J. Fluid Mech.*, **28** (1), pp. 85-96

[35] Garg A.K., Leibovich S. (1979) Spectral characteristics of vortex breakdown flowfields, *Phys. Fluids*, **22** (11), pp. 2053-2064

[36] Gersten K., Kiske S., Pagendarm H.G. (1985) Vortex breakdown control by jet injection, *Colloquium on vortex breakdown, February 11th-12th, 1985, Aachen*

[37] Goldstein R.J. (1983) Fluid mechanics measurements, *Hemisphere Publishing Corporation 1983*

[38] Grabowski W.J. (1974) Solutions of the Navier-Stokes equations for vortex breakdown, *College of Engineering, University of California, Berkeley, Report No. FM-74-6*

[39] Grabowski W.J., Berger S.A. (1976) Solutions of the Navier-Stokes equations for vortex breakdown, *J. Fluid Mech.*, **75** (3), pp. 525-544

[40] Granger R.A. (1993) Some experimental observations of secondary motions in confined vortex flow, *J. Fluid Mech.*, **246**, pp. 653-674

[41] Greenwell D.I., Wood N.J. (1992) Determination of vortex burst location on delta wings from surface pressure measurements, *AIAA Journal*, **30** (11), pp. 2736-2739

[42] Gu W., Robinson O., Rockwell D. (1993) Control of vortices on a delta wing by leading-edge injection, *AIAA Journal*, **31** (7), pp. 1177-1186

[43] Gursul I. (1994) Unsteady flow phenomena over delta wings at high angle of attack, *AIAA Journal*, **32** (2), pp. 225-231

[44] Gursul I., Yang H. (1994) Vortex breakdown over a pitching delta wing, *AIAA 94-0536, 32nd Aerospace Sciences Meeting & Exhibit, January 10-13, 1994 Reno, NV*

[45] Gursul I.,Yang H. (1995) On fluctuations of vortex breakdown location, *Physics of Fluids*, **7** (1), pp. 229-231

[46] Hall M.G. (1961) A theory for the core of a leading-edge vortex, *J. Fluid Mech.*, **11**, pp. 209-228

[47] Hall M.G. (1966a) A numerical investigation of vortex breakdown, *Royal Aircraft Establishment, Technical Memoranda, Aero 926*

[48] Hall M.G. (1966b) The structure of concentrated vortex cores, *Prog. Aero. Sci.*, **7**, pp. 53-110

[49] Hall M.G. (1967) A numerical method for solving the equations for a vortex core, *ARC, R.&M. 3467 (27,150)*

[50] Hall M.G. (1972) Vortex breakdown, *Ann. Rev. Fluid Mech.*, **4**, pp195-218

[51] Hanff E.S., Ericsson L.E. (1990) Multiple roll attractors of a delta wing at high incidence, *AGARD-CP-494, Symposium of the Fluid Dynamics Panel in Scheveningen, The Netherlands, 1st to 4th October 1990*

[52] Harvey J.K. (1960) Analysis of the vortex breakdown phenomenon. Part II, *Imperial College of Science and Technology, Aeronautics Department, Report No. 103*

[53] Harvey J.K. (1962) Some observations of the vortex breakdown phenomenon, *J. Fluid Mech.*, **14** (4), pp. 585-592

[54] Hoeijmakers H.W.M. (1990) Modeling and numerical simulation of vortex flow in aerodynamics, *AGARD-CP-494, Symposium of the Fluid Dynamics Panel in Scheveningen, The Netherlands, 1st to 4th October 1990*

[55] Hubner J.P., Komerath N.M. (1994): Spectral mapping of quasi-periodic structures in a vortex flow, *AIAA, C-8286 (modified from AIAA 93-2914)*

[56] Hubner J.P., Komerath N.M. (1995): Spectral mapping of quasiperiodic structures in a vortex flow, *Journal of Aircraft*, **32** (3), pp.493-500

[57] Khorrami M.R. (1991) On the viscous modes of instability of a trailing line vortex, *J. Fluid Mech.*, **225**, pp.197-212

[58] Kirkpatrick D.L.I. (1965) Experimental investigation of the breakdown of a vortex in a tube, *ARC, C.P. No. 821*

[59] Kopecky R.M., Torrance K.E. (1973) Initiation and structure of axisymmetric eddies in a rotating stream, *Computers & Fluids*, **1**, pp. 289-300

[60] Krause E. (1983) A contribution to the problem of vortex breakdown, *AGARD Conference Proceedings, AGARD-CP-342, Fluid Dynamics Panel Symposium, 25-28 April 1983, Rotterdam, Netherlands*

[61] Krause E. (1985) Pressure variation in axially symmetric breakdown, *Colloquium on vortex breakdown, February 11th-12th, 1985, Aachen*

[62] Kribus A., Leibovich S. (1994) Instability of strongly nonlinear waves in vortex flows, *J. Fluid Mech.*, **269**, pp. 247-264

[63] Kücheman D. (1978) The aerodynamic design of aircraft, Pergamon Press.

[64] Lambourne N.C., Bryer D.W. (1962) The bursting of leading-edge vortices - some observations and discussion of the phenomenon, *ARC, R.&M. 3282 (22,775)*

[65] Lee B.H.K., Brown D., Zgela M., Poirel D. (1990) Wind tunnel investigation and flight tests of tail buffet on the CF-18 aircraft, *Paper 1, AGARD Specialists' Meeting on Aircraft Dynamic Loads due to Flow Separation, Sorrento, Italy, 1-6 April, 1990*

[66] Lee B., Brown D. (1990) Wind tunnel studies of F/A-18 tail buffet, *AIAA 90-1432, AIAA 16th Aerodynamic Ground Testing Conference, June 18-20, 1990/ Seattle, WA*

[67] Legendre R. (1966) Vortex sheets rolling-up along leading-edges of delta wings, *Prog. Aero. Sci.*, **7**, pp. 7-33

[68] Leibovich S. (1978) The structure of vortex breakdown, *Ann. Rev. Fluid Mech.*, **10**, pp. 221-246

[69] Leibovich S. (1983) Vortex stability and breakdown, *AGARD Conference Proceedings, AGARD-CP-342, Fluid Dynamics Panel Symposium, 25-28 April 1983, Rotterdam, Netherlands*

[70] Leibovich S. (1984) Vortex stability and breakdown: survey and extension, *AIAA Journal*, **22** (9), pp. 1192-1206

[71] Leibovich S. (1985) Attempts to assess the effects of azimuthal asymmetries in vortex breakdown, *Colloquium on vortex breakdown, February 11th-12th, 1985, Aachen*

[72] Leibovich S., Stewartson K. (1983) A sufficient condition for the instability of columnar vortices, *J. Fluid Mech.*, **126**, pp. 335-356

[73] Lessen M., Singh P.J., Paillet F. (1974) The stability of a trailing line vortex. Part 1. Inviscid theory, *J. Fluid Mech.*, **63** (4), pp. 753-763

[74] Lessen M., Paillet F. (1974) The stability of a trailing line vortex. Part 2. Inviscid theory, *J. Fluid Mech.*, **65** (4), pp. 769-779

[75] Lin J.-C. , Rockwell D. (1995) Transient structure of vortex breakdown on a delta wing, *AIAA Journal*, **33** (1), pp. 6-12

[76] Lopez J.M. (1990) Axisymmetric vortex breakdown Part 1. Confined swirling flow, *J. Fluid Mech.*, **221**, pp. 533-552

[77] Lopez J.M., Perry A.D. (1992) Axisymmetric vortex breakdown. Part 3. Onset of periodic flow and chaotic advection, *J. Fluid Mech.*, **234**, pp. 449-471

[78] Ma H.Y., Leibovich S. (1985) Modelling the spiral breakdown by the solitary waves, *Colloquium on vortex breakdown, February 11th-12th, 1985, Aachen*

[79] Mabey D.G. (1989) Some aspects of aircraft dynamic loads due to flow separation, *Prog. Aerospace Sci.*, **26**, pp. 115-151

[80] Mabey D.G. (1991) Measurements of fin buffeting on an 'F-18' model and a derived interpretative hypothesis, *DRA Bedford, Technical Memorandum Aero 2224*

[81] Mabey D.G. (1995) A review of the vortex shedding frequencies of aerofoils, flat plates and delta wings. *DRA Report No. DRA/AS/HWA/TR94064/1*

[82] Mager A. (1972) Dissipation and breakdown of a wing-tip vortex, *J. Fluid Mech.*, **55**, (4), pp. 609-628

[83] Magness C., Robinson O., Rockwell D. (1993) Laser-scanning particle image velocimetry applied to a delta wing in transient maneuver, *Experiments in Fluids*, **15**, pp. 159-167

[84] Maxworthy T., Mory M., Hopfinger E.J. (1983) Waves on vortex cores and their relation to vortex breakdown, *AGARD Conference Proceedings, AGARD-CP-342, Fluid Dynamics Panel Symposium, 25-28 April 1983, Rotterdam, Netherlands*

[85] Miau J.J., Chang R.C., Chou J.H., Lin C.K. (1992) Nonuniform motion of leading-edge vortex breakdown on ramp pitching delta wings, *AIAA Journal*, **30** (7), pp.1691-1701

[86] Nakamura Y., Leonard A., Spalart P.R. (1983) Numerical simulation of vortex breakdown by the vortex-filament method, *AGARD Conference Proceedings, AGARD-CP-342, Fluid Dynamics Panel Symposium, 25-28 April 1983, Rotterdam, Netherlands*

[87] Nelson R.C., Visser K.D. (1990) Breaking down the delta wing vortex. The role of vorticity in the breakdown process, *AGARD-CP-494, Symposium of the Fluid Dynamics Panel in Scheveningen, The Netherlands, 1st to 4th October 1990*

[88] Pagan D., Molton P. (1990) Etudes fundamentales sur l'eclatement tourbillonnaire et son controle, *AGARD-CP-494, Symposium of the Fluid Dynamics Panel in Scheveningen, The Netherlands, 1st to 4th October 1990*

[89] Peake D.J., Tobak M. (1983) On issues concerning flow separation and vortical flows in three dimensions, *AGARD Conference Proceedings, AGARD-CP-342, Fluid Dynamics Panel Symposium, 25-28 April 1983, Rotterdam, Netherlands*

[90] Peckham D.H. (1961) Low-speed wind-tunnel tests on a series of uncambered slender pointed wings with sharp edges, *ARC, R.&M. No. 3186 (20,727)*

[91] Peckham D.H., Atkinson S.A. (1957) Preliminary results of low speed wind tunnel tests on a gothic wing of aspect ratio 1.0, *ARC, C.P. No. 508 (19,632)*

[92] Polhamus E.C. (1966) A concept of the vortex lift of sharp-edge delta wings based on a leading edge suction analogy, *NASA TN D-3767*

[93] Polhamus E.C. (1984) Applying slender wing benefits to military aircraft, *Journal of Aircraft*, **21** (8), pp. 546-559

[94] Press W.H, Teukolsky S.A., Vetterling W.T., Flannery B.P. (1992) Numerical recipes in Fortran. The art of scientific computing. *Cambridge University Press 1992, 2nd edition.*

[95] Randall J.D., Leibovich S. (1973) The critical state: a trapped wave model of vortex breakdown, *J. Fluid Mech.*, **58** (3), pp. 495-515

[96] Rao D.M. (1990) Vortex control - further encounters, *AGARD-CP-494, Symposium of the Fluid Dynamics Panel in Scheveningen, The Netherlands, 1st to 4th October 1990*

[97] Rediniotis O.K., Stapountzis H., Telionis D.P. (1993) Periodic vortex shedding over delta wings, *AIAA Journal*, **31** (9), pp. 1555-1562

[98] Richards E.J., Mead D.J. (1968) Noise and acoustic fatigue in aeronautics, *John Wiley & Sons Ltd*

[99] Rizk Y.M., Gee K. (1992) Unsteady simulation of viscous flowfield around F-18 aircraft at large incidence, *Journal of Aircraft*, **29** (6), pp. 986-992

[100] Robinson B.A., Barnett R.M., Agrawal S. (1994) Simple numerical criterion for vortex breakdown, *AIAA Journal*, **32** (1), pp. 116-122

[101] Sarpkaya T. (1970) An experimental investigation of the vortex-breakdown phenomenon, *United States Naval Postgraduate School, Report NPS-59SL0071A, July 1970*

[102] Sarpkaya T. (1971) Vortex breakdown in swirling conical flows, *AIAA Paper No. 71-52, AIAA 9th Aerospace Sciences Meeting, New York, New York, January 25-27, 1971*

[103] Sarpkaya T. (1974) Effect of the adverse pressure gradient on vortex breakdown, *AIAA Journal*, **12** (5), pp. 602-607

[104] Sarpkaya T. (1995) Vortex breakdown and turbulence, *AIAA Paper No. 95-0433, 33rd Aerospace Sciences Meeting and Exhibit, January 9-12, 1995, Reno, NV*

[105] Shah G.H. *et. al.* (1990) Effects of vortex flow characteristics on tail buffet and high-angle-of-attack aerodynamics of a twin-tail fighter configuration, *High-Angle-of-Attack Technology Conference, October 30 - November 1, 1990, NASA Langley Research Center, Hampton, Virginia*

[106] Shi X. (1985) Numerical simulation of vortex breakdown, *Colloquium on vortex breakdown, February 11th-12th, 1985, Aachen*

[107] Signalysys (1991) ACP1 user manual & ACP1 software manual, *Signalysys Ltd. Buckland Village, Aylesbury HP22 5HU, U.K.*

[108] Soltani M.R., Bragg M.B. (1993) Early vortex burst on a delta wing in pitch, *AIAA Journal*, **31** (12), pp. 2284-2289

[109] Spall R.E., Gatski T.B., Grosch C.E. (1987) A criterion for vortex breakdown, *Phys. Fluids*, **30** (11), pp. 3434-3440

[110] Spohn A., Mory M., Hopfinger E.J. (1993) Observations of vortex breakdown in an open cylindrical container with a rotating bottom, *Experiments in Fluids*, **14**, pp. 70-77

[111] Squire H.B. (1960) Analysis of the 'Vortex Breakdown' phenomenon. Part I, *Imperial College of Science and Technology, Aeronautics Department, Report No. 102.*

[112] Squire H.B. (1962) Analysis of the 'Vortex Breakdown' phenomenon. Part I, *Miszellaneen der Angewandten Mechanik, Akademie-Verlag Berlin (1962)*

[113] Staufenbiel R., Helming Th. (1985) Experiments on the breakdown of vortices in pressure field, *Colloquium on vortex breakdown, February 11th-12th, 1985, Aachen*

[114] Stewartson K. (1982) The stability of swirling flows at large Reynolds number when subjected to disturbances with large azimuthal wavenumber, *Phys. Fluids*, **25** (11), pp. 1953-1957

[115] Stewartson K., Hall M.G. (1963) The inner viscous solution for the core of a leading-edge vortex, *J. Fluid Mech.*, **15**, pp. 306-318

[116] Suematsu Y., Ito T. (1981) Vortex breakdown phenomena in a circular pipe (1st Report, Modes of stationary breakdown), *Bulletin of JSME*, **24** (193), pp. 1137-1144

[117] Suematsu Y., Ito T., Niimi T., Nakamura T. (1982) Vortex breakdown phenomena in a circular pipe (2nd Report, Flow modes of unsteady type breakdown), *Bulletin of JSME*, **25** (199), pp. 38-45

[118] Suematsu Y., Ito T., Hayase T. (1986a) Vortex breakdown phenomena in a circular pipe (4th Report, Mechanisms of axisymmetric bubble type breakdown), *Bulletin of JSME*, **29** (253), pp. 2086-2094

[119] Suematsu Y.. Ito T., Hayase T. (1986b) Vortex breakdown phenomena in a circular pipe (5th Report, Axisymmetric breakdown in rotating conical pipe), *Bulletin of JSME*, **29** (258), pp. 4122-4129

[120] Titchener I.M., Taylor-Russell A.J. (1956) Experiments on the growth of vortices in turbulent flow, *ARC, F.M. 2379 (18,302)*

[121] Towfighi J., Rockwell D. (1993) Instantaneous structure of vortex breakdown on a delta wing via particle image velocimetry, *AIAA Journal*, **31** (6), Technical Notes, pp. 1160-1162

[122] Visbal M.R. (1994) Onset of vortex breakdown above a pitching delta wing, *AIAA Journal*, **32** (8), pp. 1568-1579.

[123] Visbal M.R. (1995) Numerical simulation of spiral vortex breakdown above a delta wing, *AIAA Paper No. 95-2309, 26th AIAA Fluid Dynamics Conference, June 19-22, 1995 San Diego, CA*

[124] Wentz W.H., Kohlman D.L. (1969) Vortex breakdown on slender sharp-edged wings, *AIAA 69-778*

[125] Wolfe S., Lin J.-C., Rockwell D. (1995) Buffeting at the leading-edge of a flat plate due to streamwise vortex: flow structure and surface pressure loading, *J. Fluids and Structures*, **9**, pp. 359-370

[126] Wood N.J., Bean D.E. (1993) A study of reduced frequency parameter for fin buffeting response on slender delta configurations", School of Mechanical Engineering, Report No. 2112/096/A

APPENDIX A

TECHNICAL DETAILS

A.1. Design of the vortex tube - additional information

The detailed dimensions of the fibre glass castings forming the radial air intake are given in figure A.1. The castings were held by 4 supports shown in figure A.2. The supports were made of steel tub-ing (1½" outer diameter), connected to a steel frame which in turn was bolted to the floor. The supports were bent at right angles and held the castings from the back, so that the air flowing into the intake was not directly disturbed by the supports. The intake was 2 feet above the floor level to reduce the ground effects. The accurate alignment between castings was maintained by an aluminium perforated sheet, rolled around the intake and screwed to both castings.

The swirl vanes or 'blades' were cast in resin and had a cross-section based on the NACA 65-(18)10 blower blade. Steel studs, 20 cm long, with an M4 thread, were permanently joined with each blade during the casting process and formed the shafts for rotating the blade. Twenty blades were placed between the castings forming the air intake, just before the final assembly (the studs were placed in prepared holes). Figure A.3 shows the way the blades were mounted in the intake. They were located every 18° in relation to the centre line of the apparatus (figure A.4), with the axes of the studs placed in the circle with the diameter of 600 mm (figure A.1).

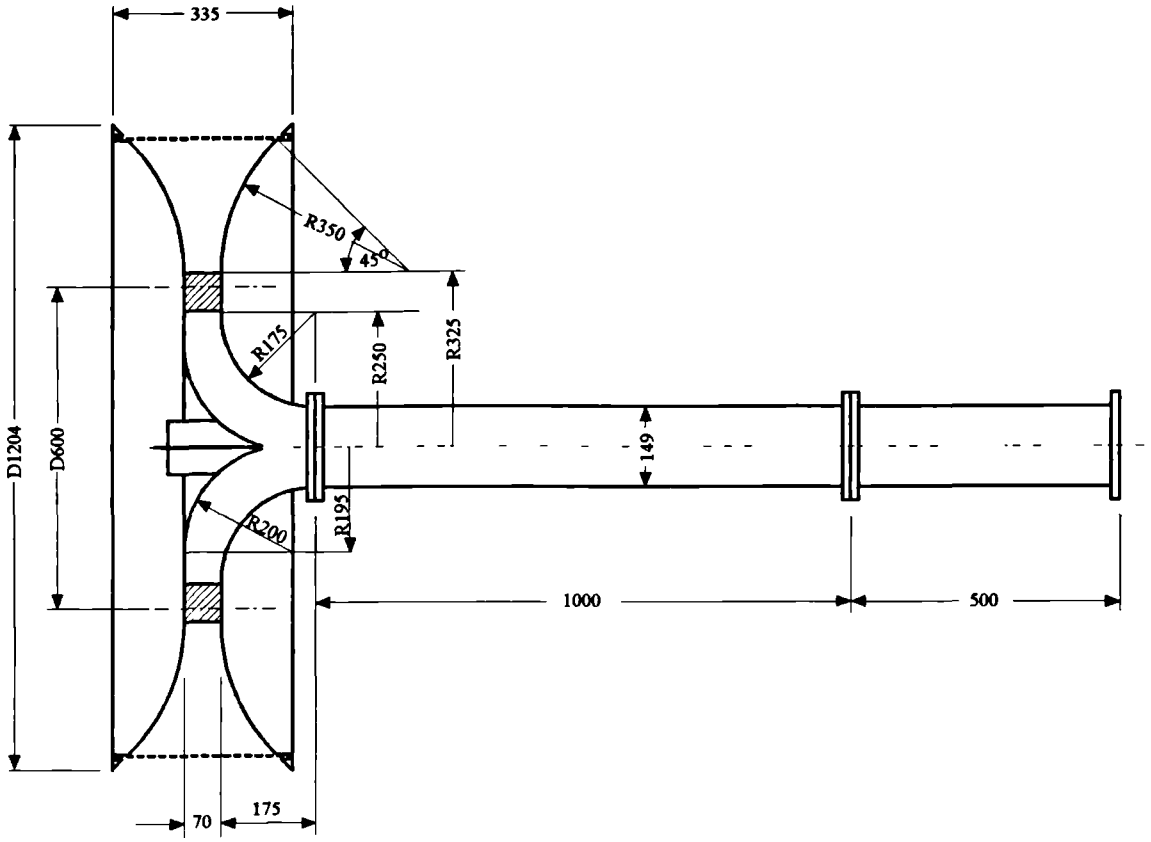

Figure A.1.General dimensions of the air intake and the test section.

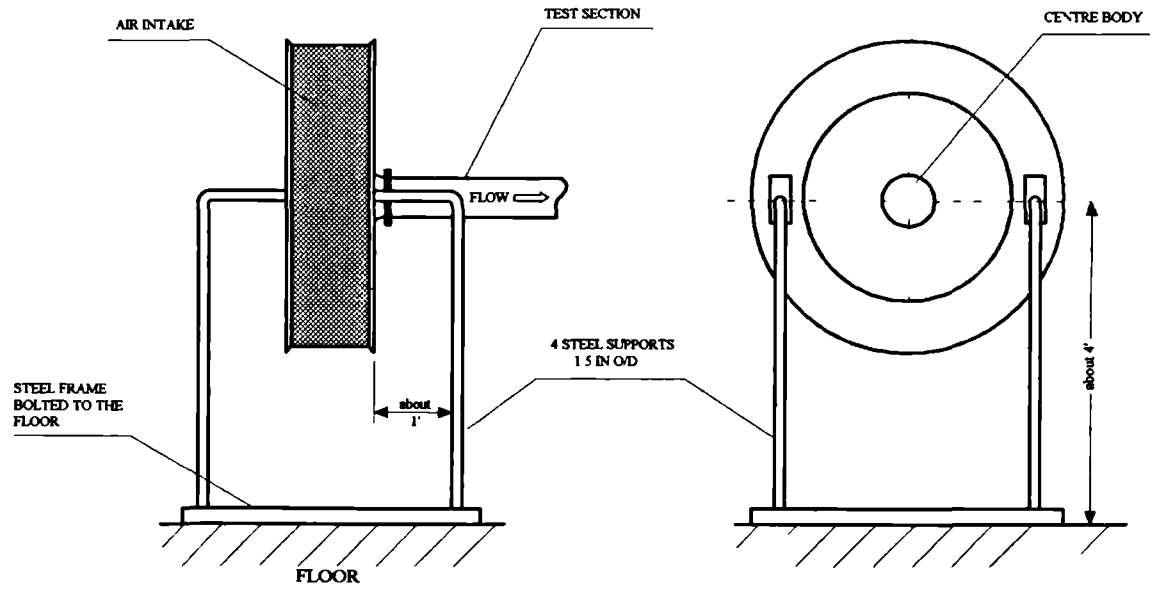

Figure A.2.Air intake supports.

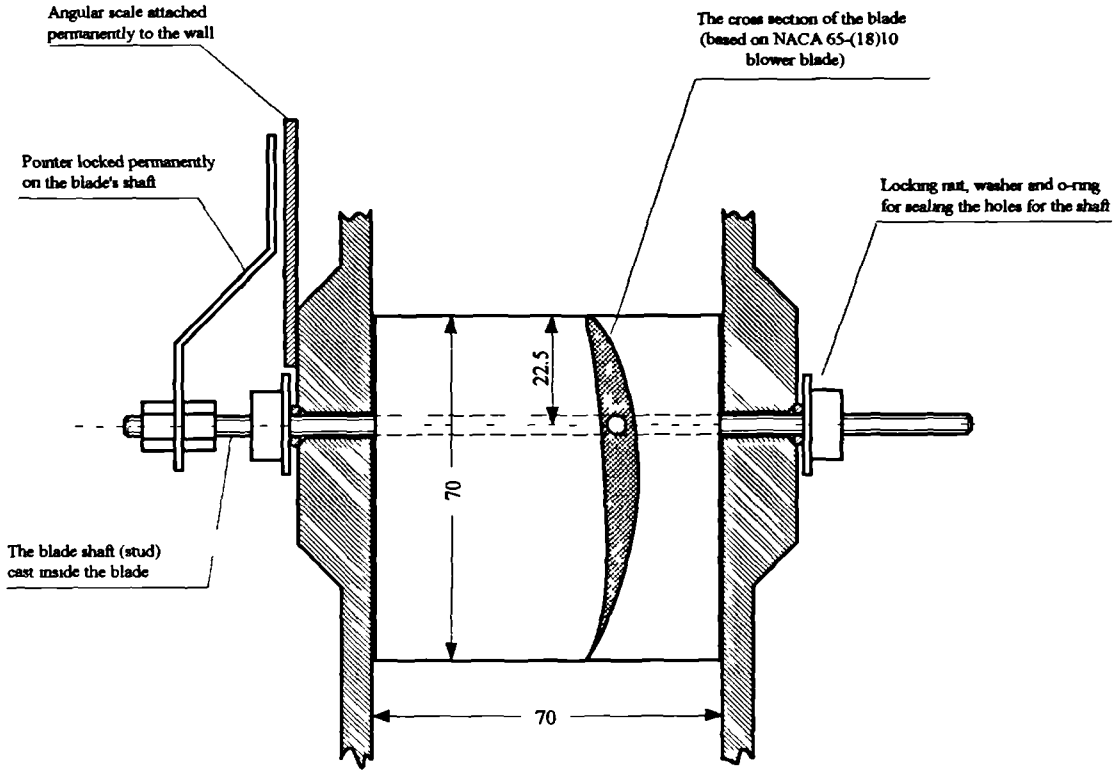

Figure A.3.A single blade mounted in the air intake.

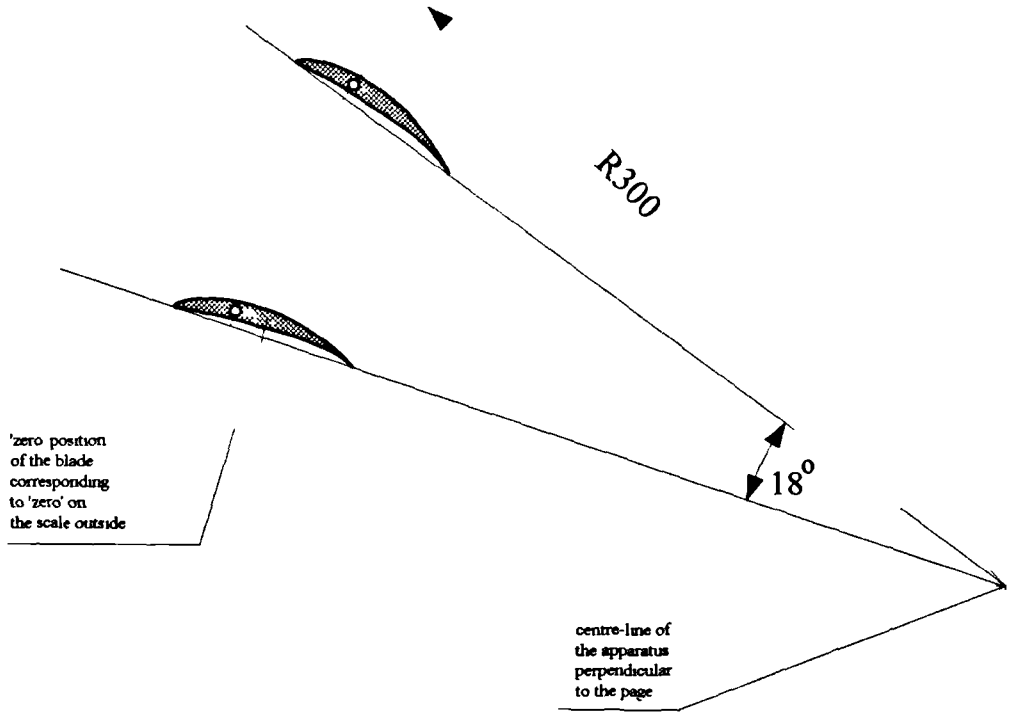

Figure A.4.Position of the blades relative to the axis of the apparatus.

To each shaft (outside the intake, on the side remote from the test section), a pointer was attached. This indicated the blade's angular position against a scale. By calibration it was possible to relate the 'zero' position of the blade (figure A.4) to the 'zero' on the scale. The estimated error in positioning the blades was about $\pm 0.1^{\circ}$.

The centre body was made in the form of an insert which slides into one of the castings (see figure A.5). The centre body was made mostly of wood, but had a brass insert inside to improve the strength of the tip. The insert was fixed to the centre body with a nut. The smoke injecting tube (¼" stainless steel hypodermic) was attached to the insert, which had a 2 mm hole bored in the centre. The curvature of the centre body matched the curvature of the fibre glass casting.

Figure A.6 shows the smoke generator. The 200W soldering iron was slid into the brass housing, which was connected directly to the smoke injecting tube. The medical syringe pump fed mineral oil through a thin (about 0.5 mm internal diameter) steel tube straight onto the soldering iron tip (a small hollow was machined on the iron tip). The oil dripping on the hot tip produced good quality, dense smoke. The oil flow was regulated to within an accuracy of 0.1 ml/hour. The required amount of oil varied between 5 to 15 ml/hour. The smoke was forced out into the apparatus through the smoke injecting tube by slight pressurisation of the housing (by using CO_2 from a gas cylinder)[13].

The test section of the apparatus, discussed somewhat in chapter 3, was made from a Perspex tube with the nominal internal diameter of 149 mm (5 7/8 in.) and a wall thickness of ¼". It was built in two parts, 1000 mm and 500 mm long, respectively (figure A.1). Figure A.7 shows the way the tubes were joined together. The rings made of Perspex were glued to the ends of each tube section forming the 'collars'. The location steps (either 'male' or 'female') required for exact alignment were turned in each of them. The joints were made air-tight by using o-rings placed

[13] The pressure difference between inside the rig and ambient was usually adequate to drive the smoke flow. However the smoke residue was likely to block the thin nozzle of the brass insert in the centre body. In addition CO_2 provided extra safety against fire. The flow rate due to the pressurisation was negligibly small and did not alter the phenomena in the test section.

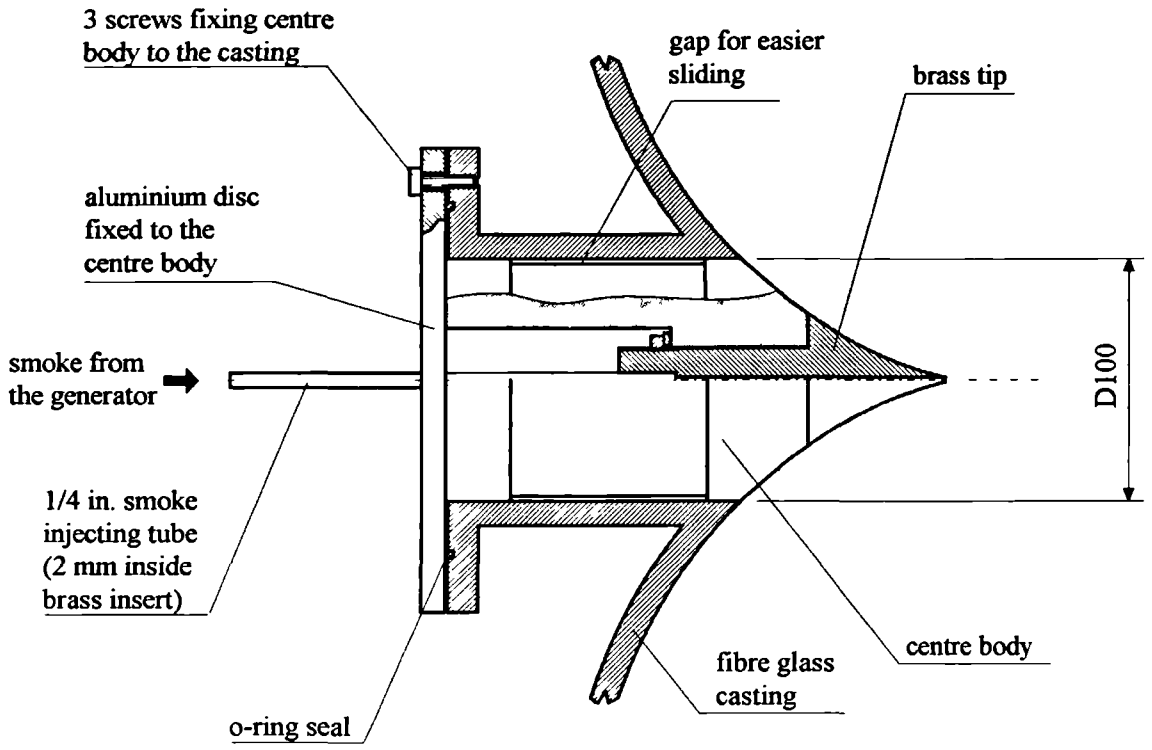

Figure A.5.Centre body

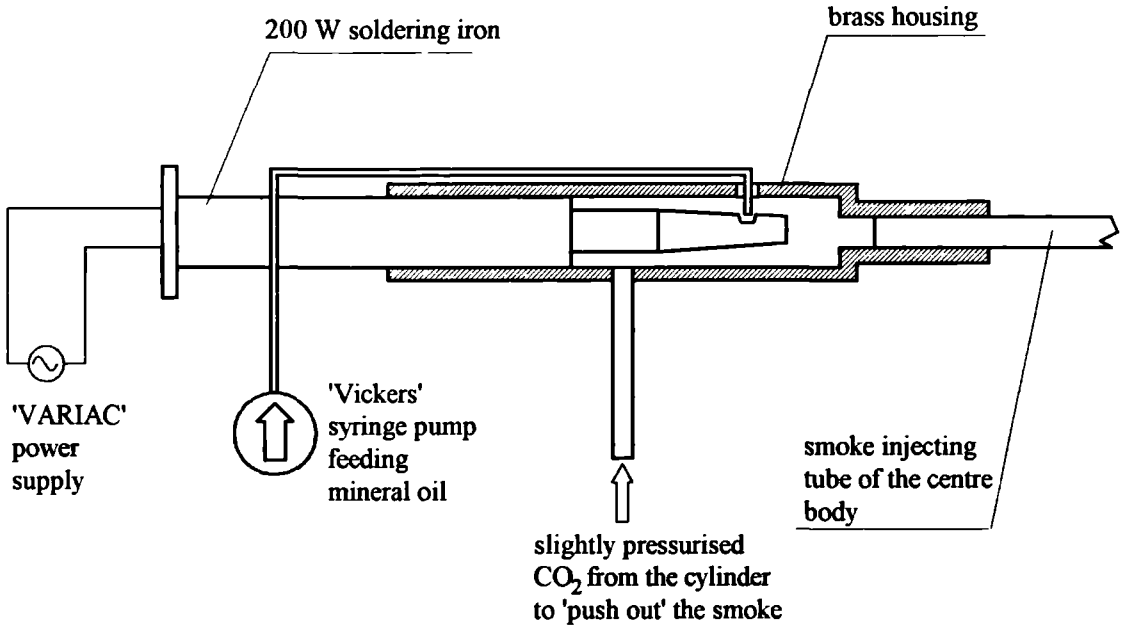

Figure A.6.Smoke generator

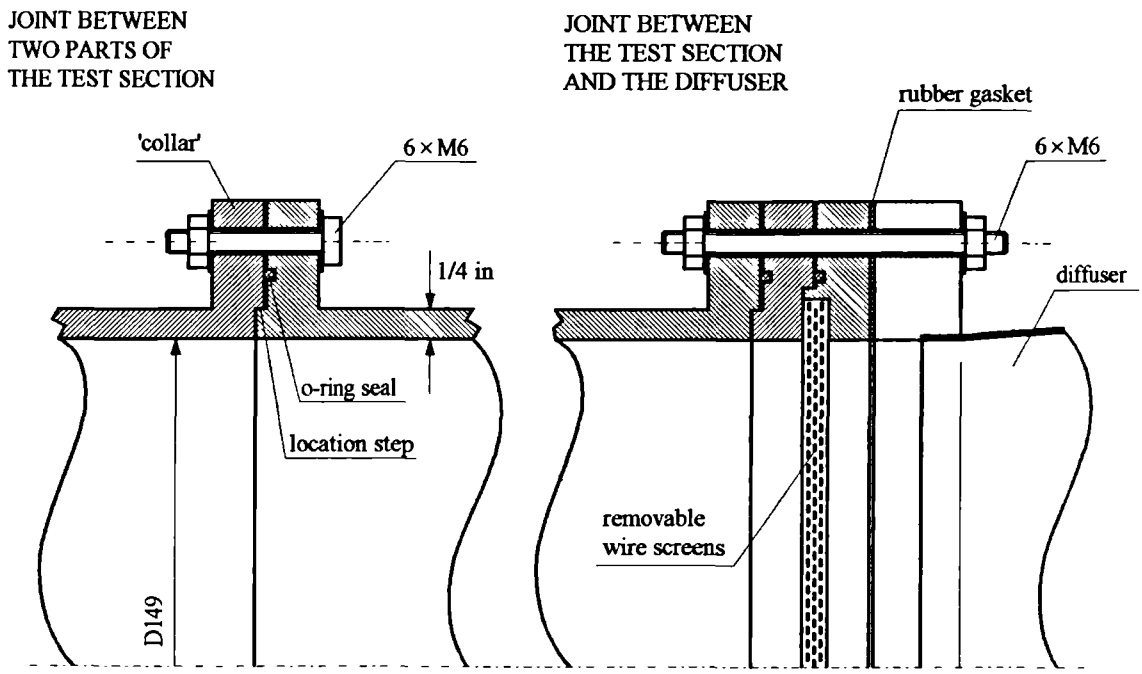

Figure A.7.Joints between parts of the test section.

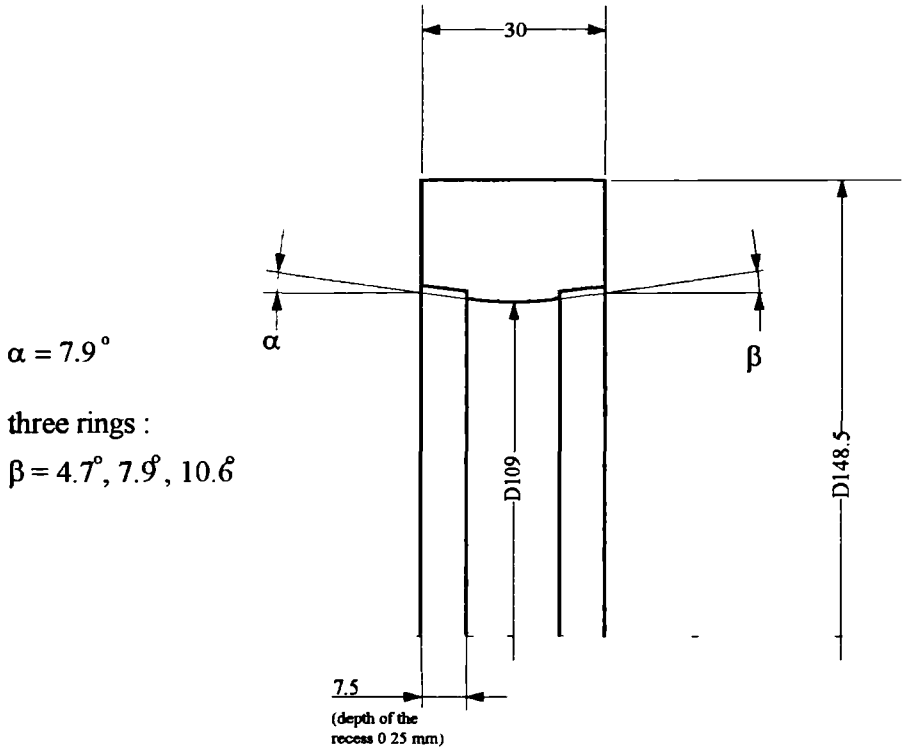

Figure A.8.Wooden ring for supporting the chokes.

in the grooves of the 'male' part of the joint. Six M6 screws placed evenly around the joint gave it the necessary strength. Exactly the same technique was used for the joint between the intake and the test section. The only difference was that for the air intake the 'collar' was made of aluminium and attached to the fibre glass 'shell' during the casting process. Figure A.7 also shows the joint between the downstream end of the test section and the diffuser, including the arrangement for holding a set of wire screens.

The probe ports, placed along the test section (see figure 3.2 in chapter 3) consisted of brass 'plugs' with a ¾" thread connecting them to the Perspex tube wall. The plugs had holes in the centre through which the probes were introduced into the flow (the diameters of the holes differed depending on the size of the probe). The position of a probe in the plug was fixed by a small (M2) locking screw. Unused ports were plugged with 'blank' plugs (without a hole for the probe).

Figure A.8 shows the details of wooden rings used to support the melanex cones in the middle of the choke (three values of β correspond to the different diffusers). The external diameter of the rings was slightly smaller than the internal diameter of the test section to allow for easier movement of the choke. Inside the choke a radius of about 110 mm was used to smooth the transition from contraction to diffuser. The internal walls of the rings sloped at angles corresponding to the semi-angles of the melanex cones (shown in figure 3.3 in chapter 3). A 0.25 mm deep recess was made on each side of the ring to accommodate the edge of the melanex cone. The cones were attached to the rings by means of small flat-headed wood screws; the seal was made air tight by using Araldite glue.

A.2. Pressure transducers, amplifiers and their calibration

The following piezoresistive miniature pressure transducers were used for measurements of fluctuating pressure:

- two of type EPIL 10-49-080B-15D (serial numbers 90C90C19-W08 and

90C90C19-W27) made by Entran. The operating pressure range was 15 PSI (differential). The transducers did not have temperature compensation units. They are referred to as W08 and W27 respectively or generally 'Entran' [14].

- one of type XSC-093-5D (serial number 4186-4-30), made by Kulite, with operating range 5 PSI (differential). The transducer was equipped with a temperature compensation unit. It is referred to as 'Kulite'

They were connected to the signal conditioning system consisting of 'Flyde' bridge units and amplifiers assembled as an 8-channel device. The bridge units provided excitation of 10V DC for the Entran pressure transducers and 12.8V DC (the highest available[15]) for the Kulite transducer. The signal was amplified usually 2000 or 5000 times, due to fairly low sensitivity of the transducers. The amplified signal was visible on a 2-channel oscilloscope and its RMS value was read from a DVM connected to the true RMS meter. The signal was then read and recorded by a PC operated data acquisition system.

Figure A.9 is a typical example of the frequency response of one of the bridge/amplifier units used, for two gains: 2000 and 5000. The amplitude characteristic was 'flat' up to about 1.5 kHz (the frequency range of interest was 0-1000 Hz). The phase characteristic was 'flat' only up to about 600 Hz. However, for the high frequencies the time lag, resulting from these small differences in phase, was negligible from the point of view of the correlations calculated.

The pressure transducers were calibrated both statically and dynamically. The static calibration was made by comparing the electrical output from the bridge/amplifier[16] while the pressure was applied to the transducer. The pressure was

[14] These transducers were borrowed by the Department from DRA Bedford, thanks to Professor Dennis G. Mabey. The Kulite transducer was purchased by the Department for this specific project by kind permission of Head of Department Professor Peter W. Bearman.

[15] The excitation recommended by the manufacturer is 15V. However different values are permitted, with proportionally reduced (increased) calibration coefficient.

[16] It was pointless in the author's opinion to calibrate the transducers separately from the signal conditioning system. It was more practical to calibrate them with the amplifiers' gains set to values used during the experiments. In addition it should be pointed out that each transducer was assigned to the particular channel of the bridge/amplifier.

Frequency response of Channel 1 of 'Fylde' bridge/amplifier unit

gain set to '5000'
gain set to '2000'

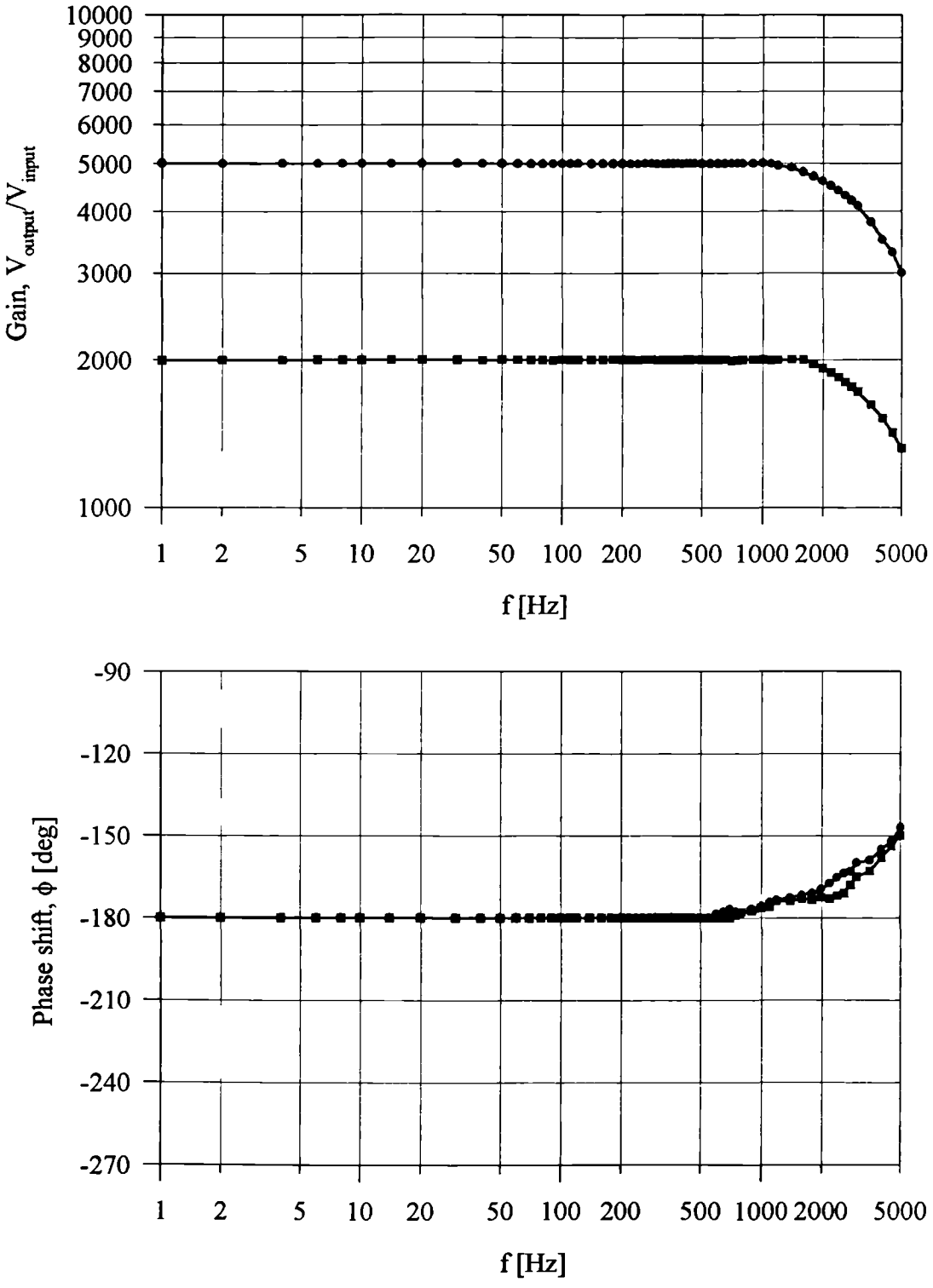

Figure A.9.An example of frequency response of a bridge/amplifier unit.

read by means of a Betz manometer with an accuracy of 0.01 mm H_2O (i.e. 1/10 of the elemental section on the scale). Both situations, i.e. with the positive and negative gauge pressure, were tested. However only the differences within the method's error were found. Figure A.10 shows schematically the calibration set-up (the transducer is not drawn to scale). A 1 litre vessel was introduced to stabilise the calibration with respect to the thermal effects of air compression. The vessel itself was immersed in a bucket of water at room temperature. Figure A.11 gives an example of a calibration chart for the three transducers together with calibration constants (obtained from linear regression).

The dynamic calibration was conducted in three stages. Firstly, each of the transducers was subjected to the sinusoidal changes of pressure created by a Brüel and Kjær *pistonphone*. The device is in principle a cylindrical chamber with a piston forming one endwall, with the transducer port in the other. The piston was driven by a small electric motor and its sinusoidal motion (at a frequency of 50 Hz) produced corresponding changes in pressure. The nearly sinusoidal pressure fluctuations were equivalent to a sound pressure level (SPL) of 124 dB (89.7 Pa in terms of peak-to-peak difference in pressure). This calibration gave an independent check as to whether the results of the static calibration (f = 0 Hz) matched the dynamic calibration for a given frequency (f=50 Hz). The results obtained from these tests were within 2% of the static values.

The transducers used in the investigations had, according to the manufacturers' specifications, a natural frequency of 70 kHz and thus a 'flat' frequency response well beyond the range of interest (which was up to 1 kHz). However there were no means available to calibrate the transducers against any master device. Instead they were dynamically 'calibrated' *against each other* in order to eliminate the one which might *not have* the 'flat' frequency characteristics[17]. The calibration device is shown in figure A.12. A 6 mm thick brass disk with the

[17] It was assumed unlikely that all three transducers are faulty. Besides they are of two different makes so that even the same fault *should not* appear in the same manner.

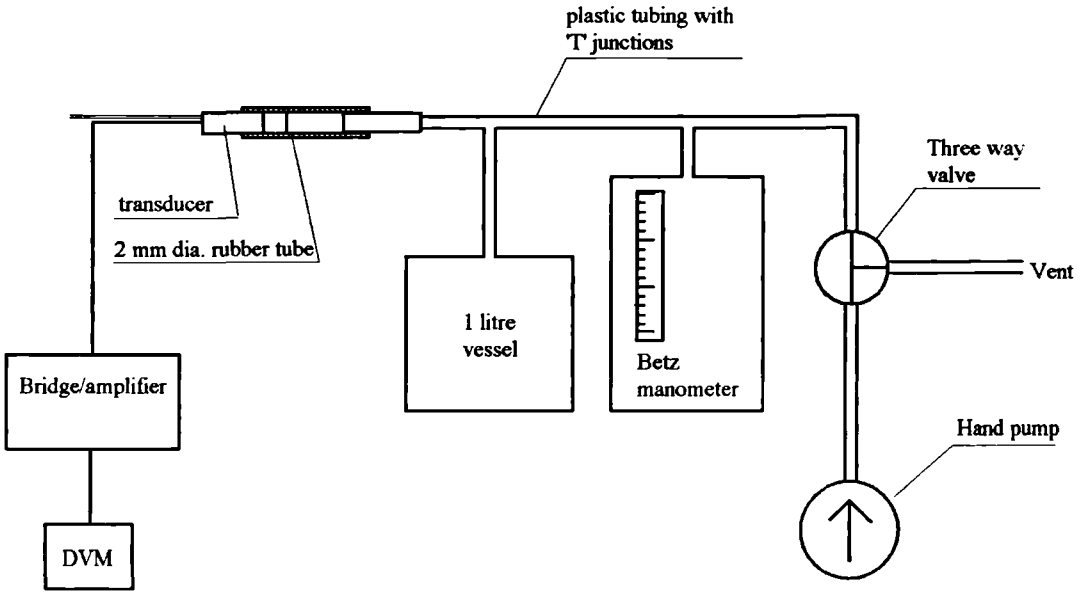

Figure A.10.The set-up for static calibration.

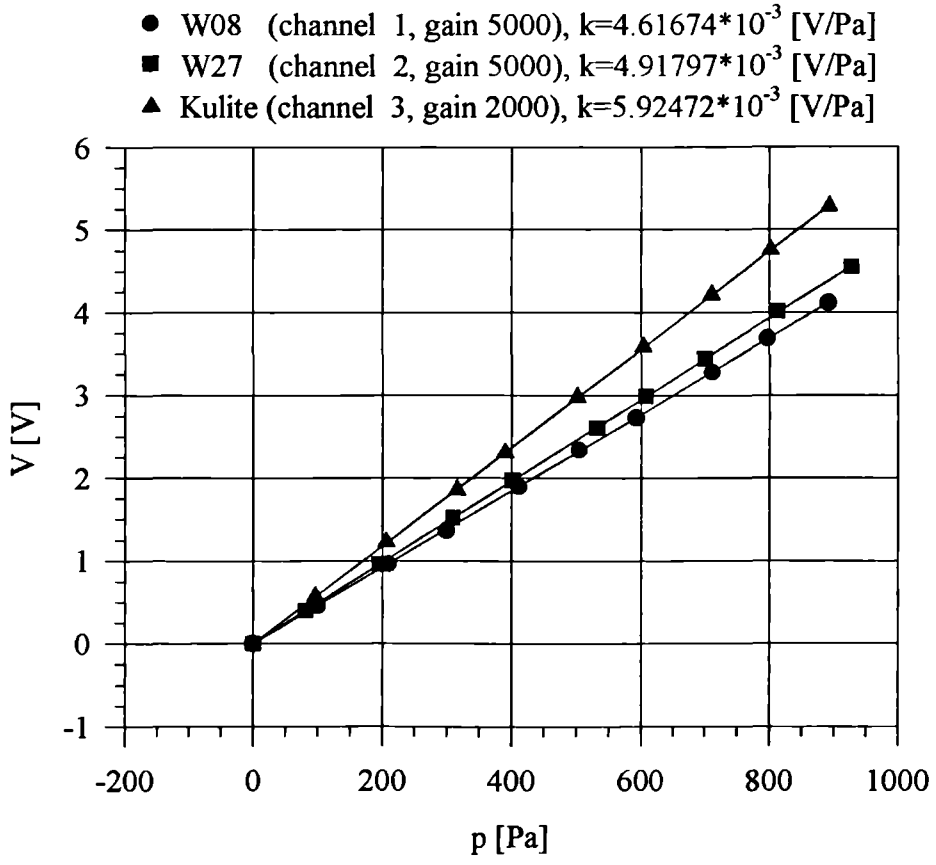

Figure A.11.A typical static calibration chart.

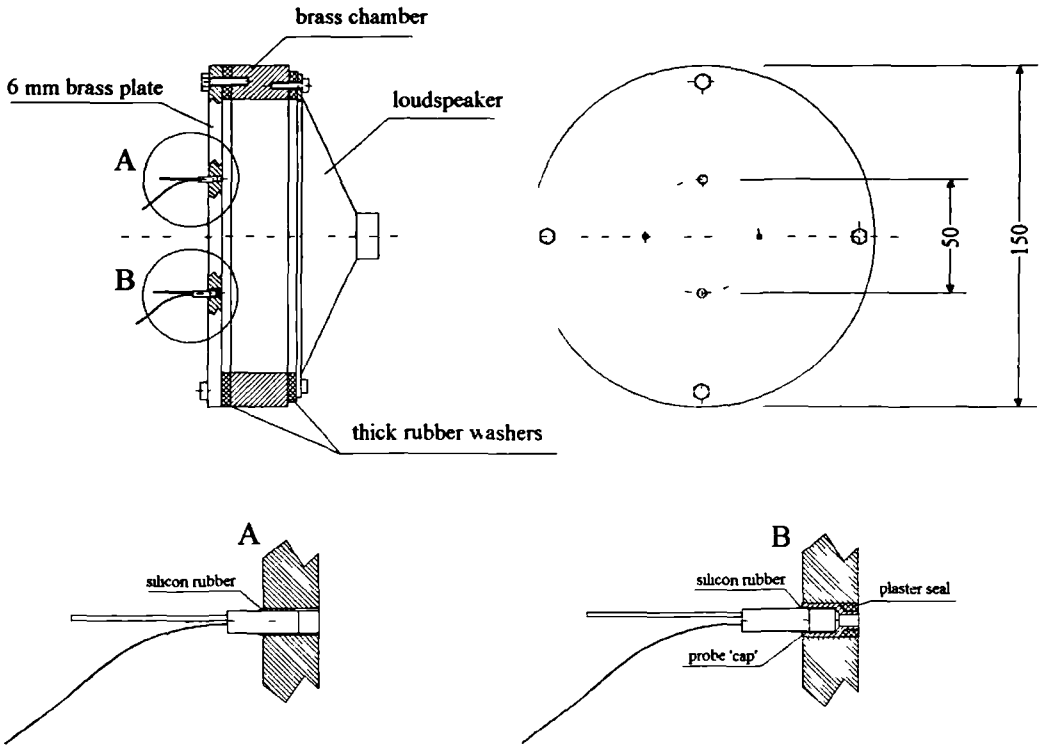

Figure A.12.The device for dynamic calibration.

transducer ports was located in front of a large diameter loudspeaker. The disk and the loudspeaker were fixed to the opposite ends of a cylindrical brass chamber. The loudspeaker was excited by a variable frequency sine-wave generator, via an audio amplifier. Both the 'shape' and the amplitude of pressure fluctuations generated depended on frequency, following the unknown characteristics of the audio amplifier and loudspeaker. However, a *pair* of transducers experienced the *same* fluctuations which allowed the comparison of both the level and the phase shift between the output signals.

The second stage of dynamic calibration consisted of the comparisons between each two of the transducers mounted *flush* to the disk surface (as shown in fragment A of figure A.12) with different settings of the amplifiers' gains[18]. Figure A.13 shows an example of this type of dynamic calibration.

[18] Generally there were much more tests performed with different settings than it is possible to place in the main text or appendices. Hence only some examples are given

Results of the dynamic calibration of two transducers:

FIRST: Channel 1, gain 5000, transducer W08 (flush) vs.
SECOND: Channel 2, gain 5000, transducer W27 (flush)

Upper graph shows (rms value from second channel)/(rms value from first channel)
Lower graph shows delay of first channel in relation to the second

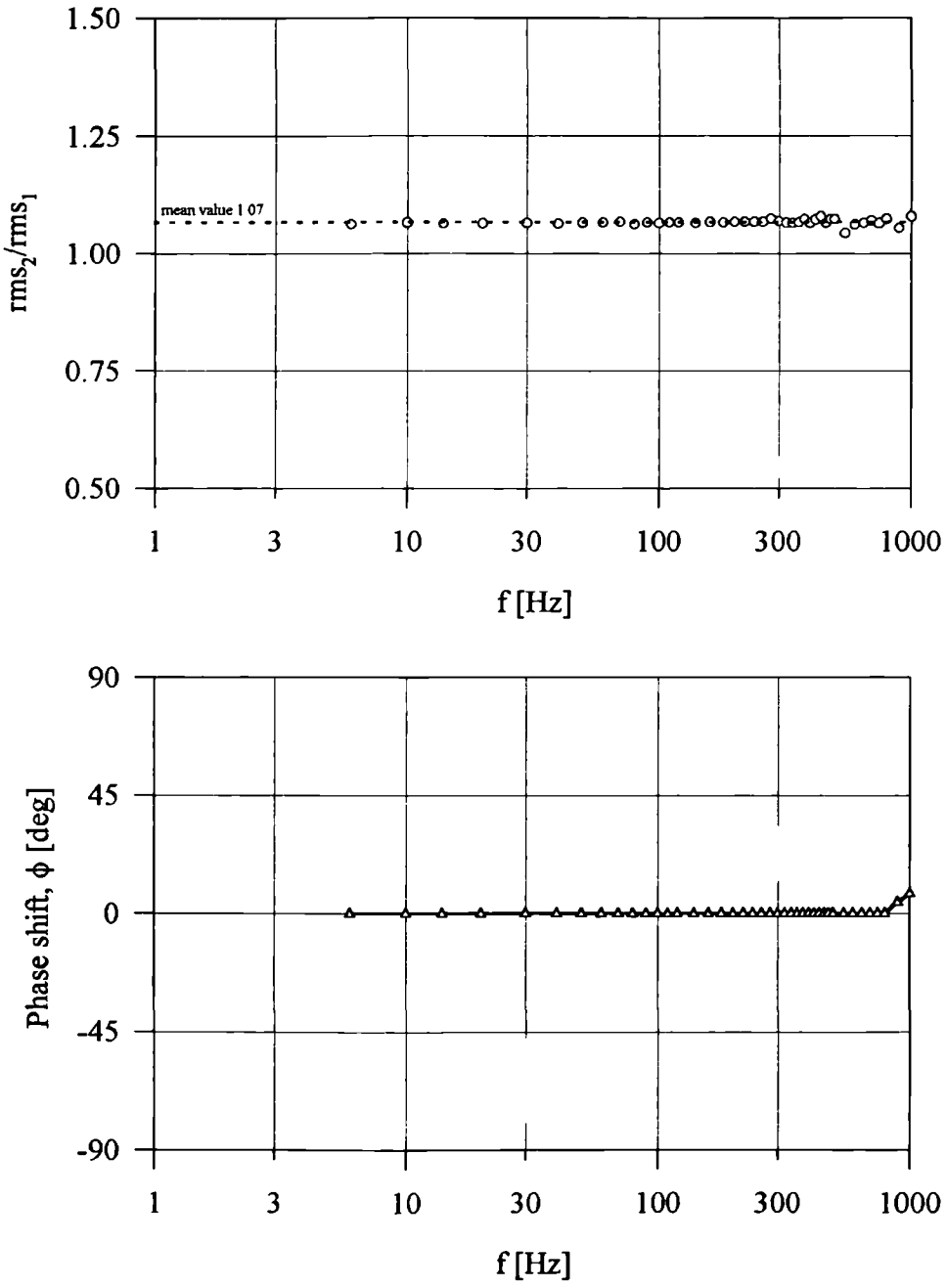

Figure A.13. Typical results of the second stage of dynamic calibration.

Results of the dynamic calibration of two transducers:

FIRST: Channel 1, gain 5000, transducer W08 (flush) vs.
SECOND: Channel 2, gain 5000, transducer W27 (probe)

Upper graph shows (rms value from second channel)/(rms value from first channel)
Lower graph shows delay of first channel in relation to the second

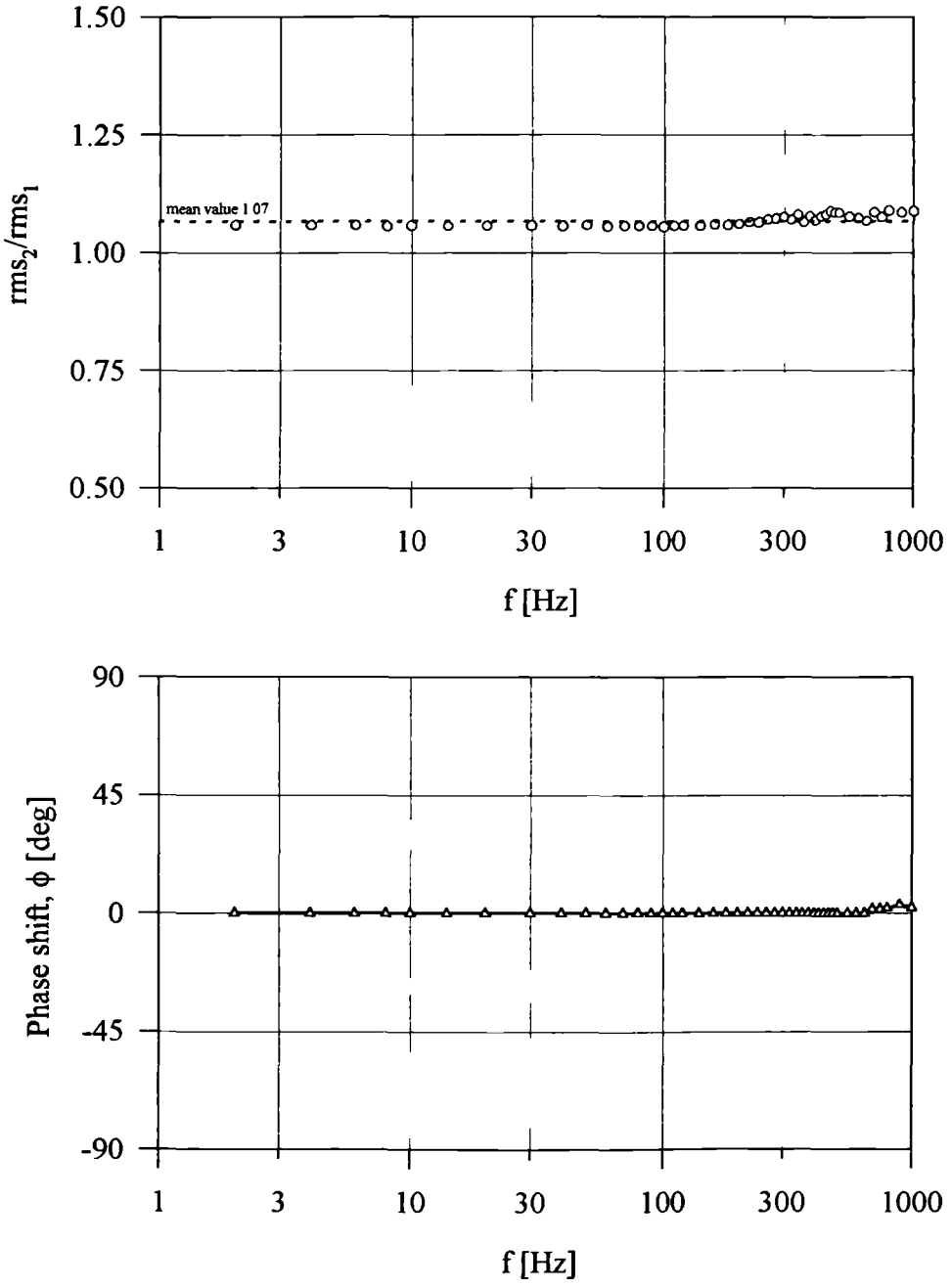

Figure A.14. Typical results of the third stage of dynamic calibration

The third stage compared the flush mounted transducer with the *probe-like* mounted one. In this case the transducer already fixed in the 'cap' was placed in its appropriate port (see fragment B in figure A.12), and compared with the flush transducer. The gap between the cap's end and the disk was filled with a plaster seal. The example of this type of calibration is given in figure A.14.

A.3. Calibration of a 3-tube probe

The 3-tube probe calibration against the Pitot-static tube is shown in figure A.15. For the range of speeds used, it was possible to find a single coefficient relating the dynamic head to the probe reading.

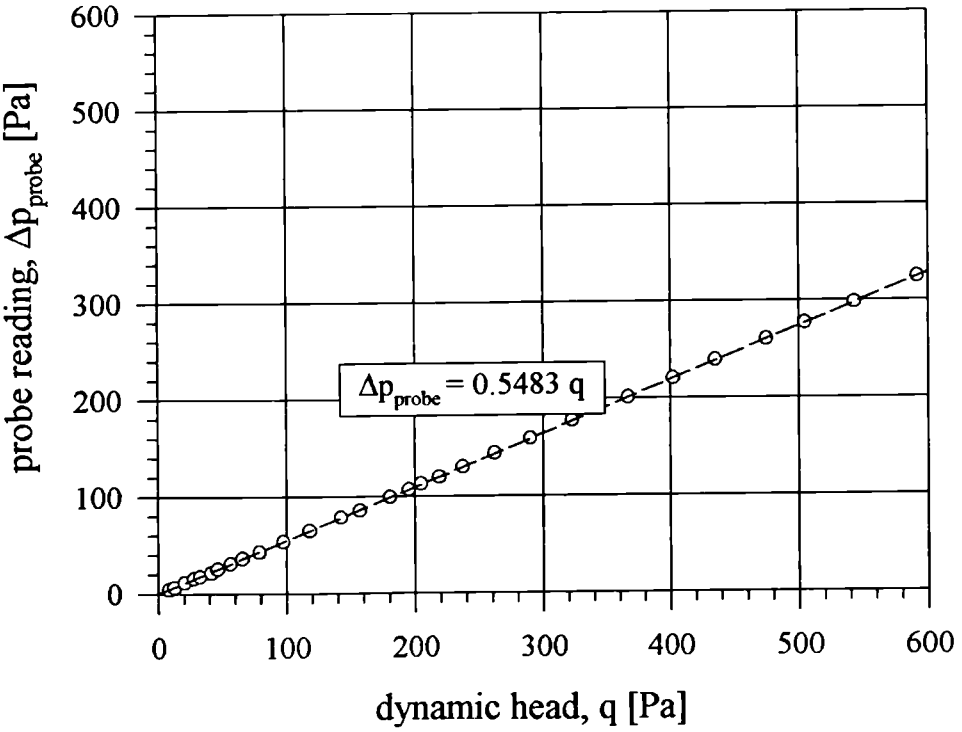

Note: Δp_{probe} is the pressure difference between
the centre tube and each of side tubes
of the 3-tube pressure probe,
q is the dynamic head read by a Pitot-static tube.

Figure A.15.Results of the calibration of the 3-tube probe agains the Pitot-static tube.

APPENDIX B

SOFTWARE TESTING USING SIMPLE MODELS

The performance of both the equipment and the software was checked directly by tunnel tests with two simple models: a circular cylinder and a slab.

The test on the circular cylinder is shown schematically in figure B.1. The cylinder 100 mm in diameter and 4 ft long was placed vertically in the middle of the Donald Campbell wind tunnel. The wind tunnel speed was 29 m/s, which gave the Reynolds number $Re=UD/\nu=2\times10^5$ (near critical flow). Two probes with pressure

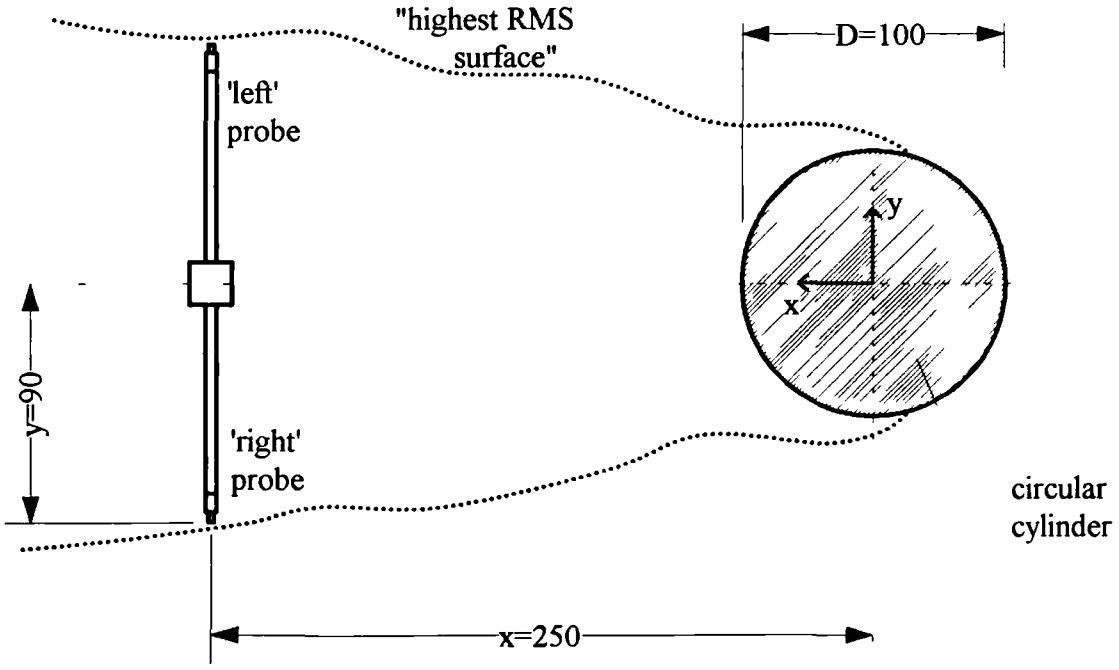

Figure B.1.Schematic view of the measurements behind the circular cylinder.

transducers were symmetrically mounted behind the cylinder in its wake (at a distance of $2D$, i.e. x=250 mm). They were traversed in a lateral direction until the maximum signal RMS level was achieved (this happened for y=90 mm). The signals from the pressure transducers were recorded at two sampling rates f_s=6.667 and 33.0 kHz.

The objectives of these measurements were twofold. Firstly, to check if the cylinder is shedding the vortices with a 'correct' frequency (i.e. giving the Strouhal number, based on the cylinder's diameter, about 0.2). Secondly, to investigate time-correlation between the two signals. This should be relatively high (say 70%) and should indicate 180° phase shift (asymmetric shedding).

Figures B.2 shows spectra of pressure fluctuations obtained from both probes ('left' and 'right') [1]. The frequency was normalised by the cylinder diameter, D, and the tunnel speed, U; the spectral density was normalised in turn by the square of a dynamic head (q^2). The spectra demonstrated practically no differences. The first, second and third harmonics are apparent in the figure. The Strouhal number estimated from the spectra was 0.194. Figure B.3 shows the correlation coefficient (c_{LR}) between the signals read by both probes (for the two sampling rates). The minimum for time lag t=0 indicates the 180° phase difference between signals. The maximum in correlation coefficient is about 0.67. The Strouhal number obtained from the 'periodic' behaviour of correlation function was 0.193 (in excellent agreement with the spectral values).

The second configuration tested (see figure B.4) consisted of a wooden slab 254×305×36 mm with two end plates, mounted horizontally on the sting (the same as for the delta wing). A series of holes was made in the middle of the slab in the streamwise directions, every 10 mm, to accommodate the transducers (the details of

[1] at the sampling rate of 6.667 kHz.

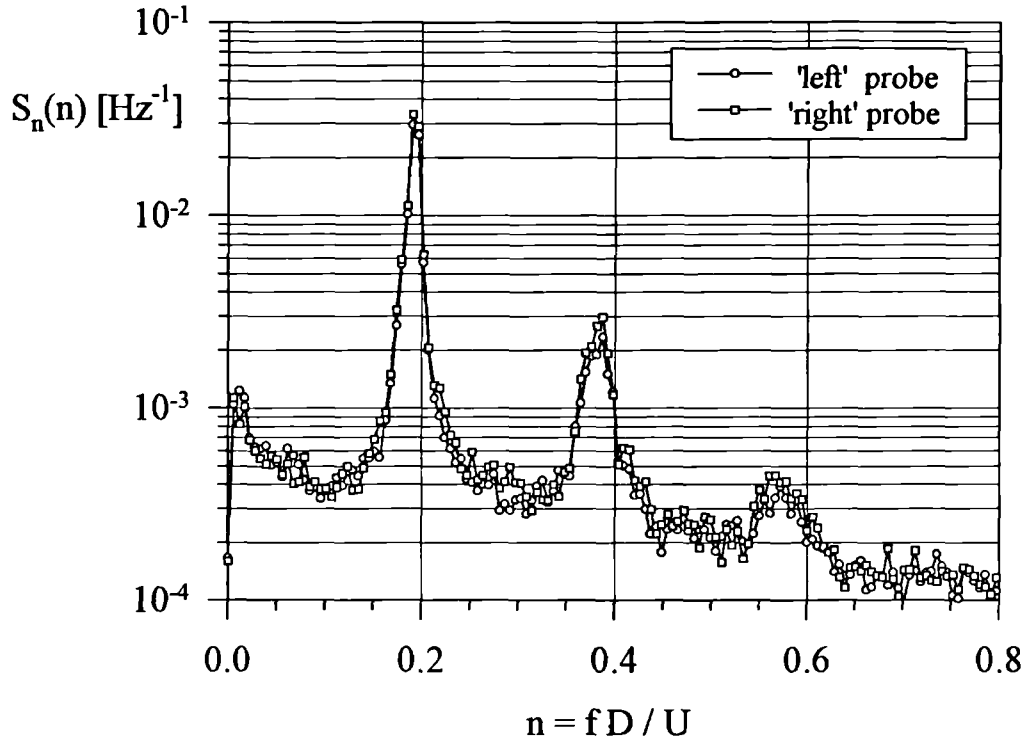

Figure B.2.Spectra of pressure fluctuations for situation shown in figure B.1.

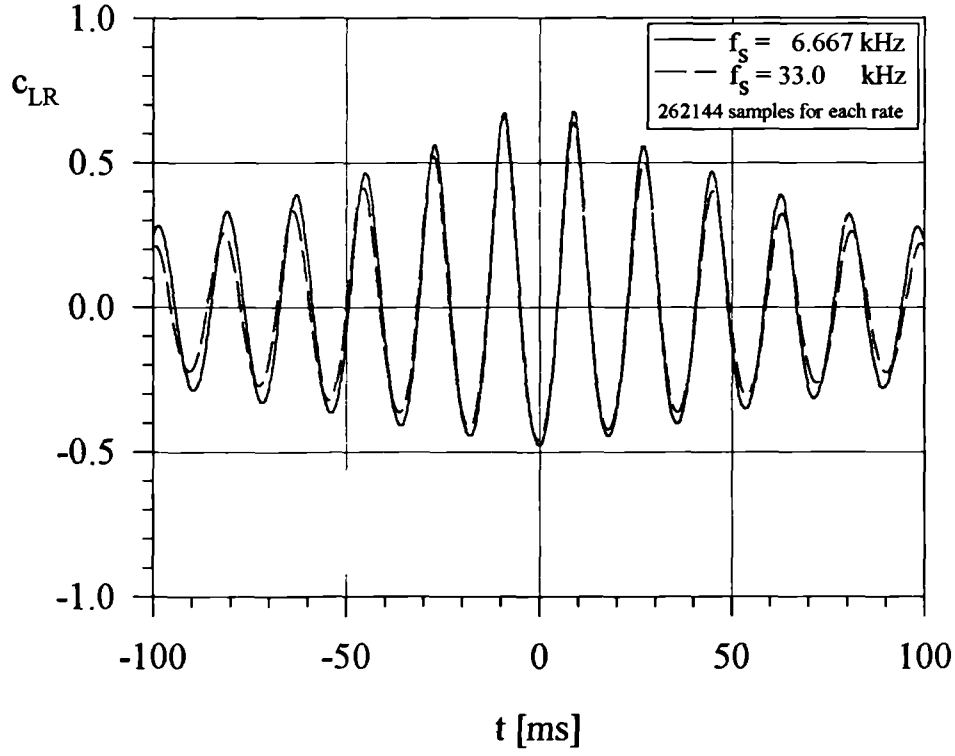

Figure B.3.Correlation between signals from 'left' and 'right' probes.

mountings are omitted here). The 'master' transducer was placed 54 mm from the 'trailing edge' of the slab, whereas the 'slave' was 10, 20, 30 or 40 mm downstream from the 'master'. The tunnel speed was 10 m/s [2], the sampling rate 10 kHz. The pronounced separations on the slab's 'leading edge' and the subsequent reattachment of the separated turbulent shear layer were the source of pressure fluctuations. Both the flow visualisation and the results in terms of RMS level and AGARD notation indicated that the reattachment point was just upstream of the 'master' transducer. The main objective of this test was to establish the propagation speed of the pressure disturbances within the boundary layer.

Figure B.5 shows the spectra of pressure fluctuations obtained from 'master' (x=0 mm) and 'slave' (x=10, 20, 30 and 40 mm). The variables were normalised similarly as figure B.2 [3]. The magnitude of the spectra is decreasing monotonically going downstream, however their character remains unchanged (mild slopes, maxima for $n \approx 0.16$). Figure B.6 shows the correlation functions for different distances between transducers (x=0 mm denotes autocorrelation for the 'master'). This thesis adopts the convention that the negative time lags correspond to the delay of 'slave' signal relative to 'master' (compare Press *et.al.*-1992). The marks in the correlation curves show every tenth data point. The characteristic frequency parameter obtained from the 'period' of correlation functions is between 0.144 and 0.167 (close to the value from the spectra). The propagation speed (U_{prop}) of pressure disturbances (see figure B.7) can be estimated from the time lag of maxima from the correlation functions together with the known distance between transducers. By plotting the distance vs. time lag, one gets from the regression technique $U_{prop} \approx 0.6\ U$.

[2] This low speed was dictated by a poor strength of the support in these tests.
[3] The plate thickness h was arbitrarily chosen as a characteristic dimension - this is not important here.

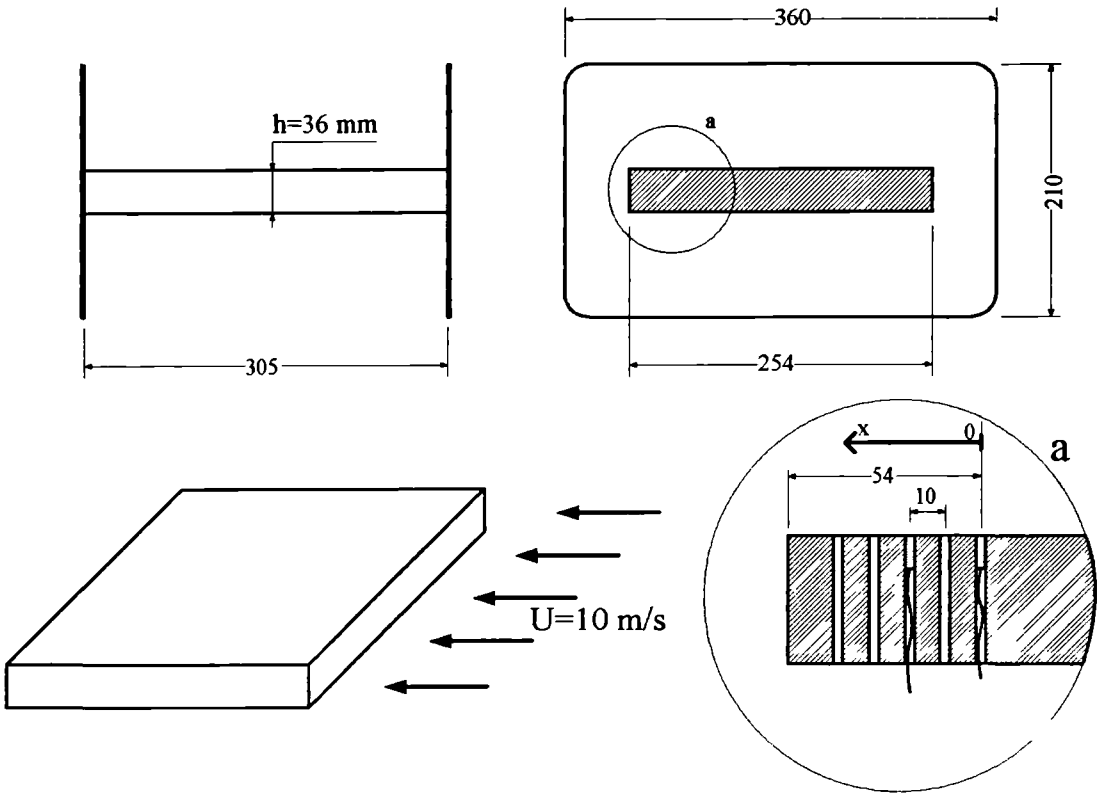

Figure B.4.Design and orientation of the slab.

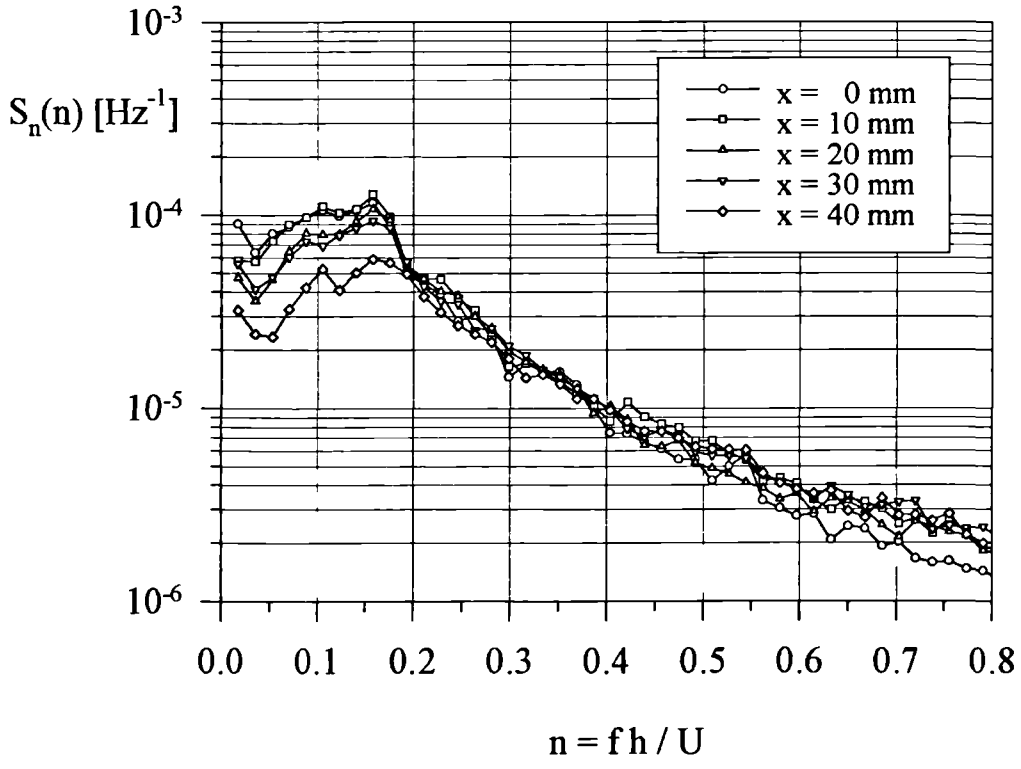

Figure B.5. Pressure spectra for different streamwise locations of the transducers.

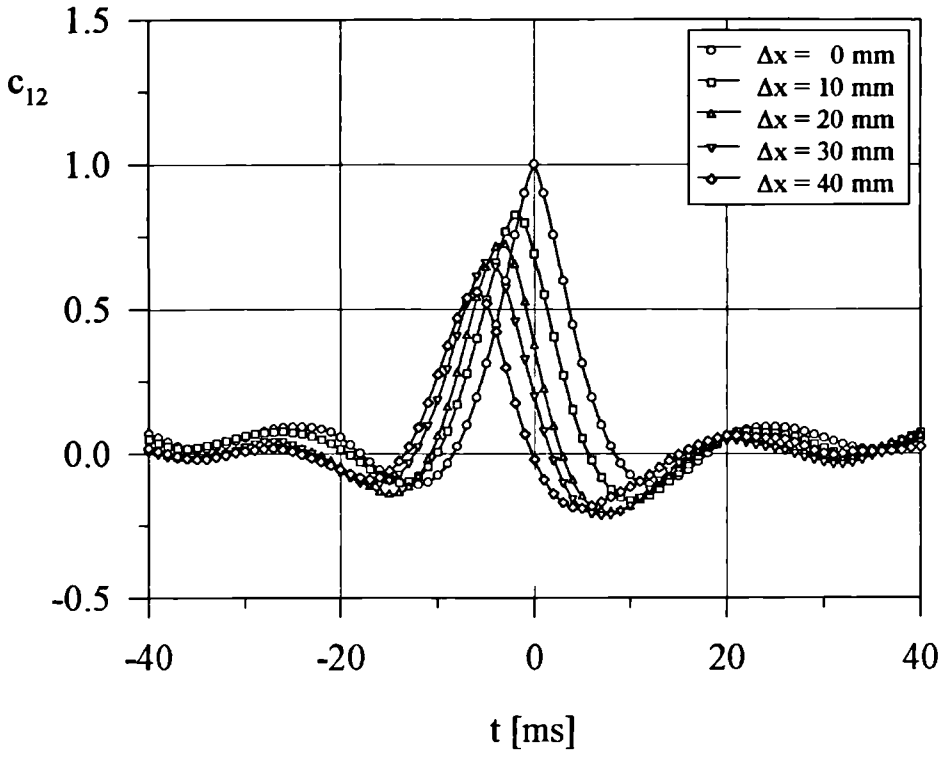

Figure B.6.Correlation functions between transducers with increasing distance.

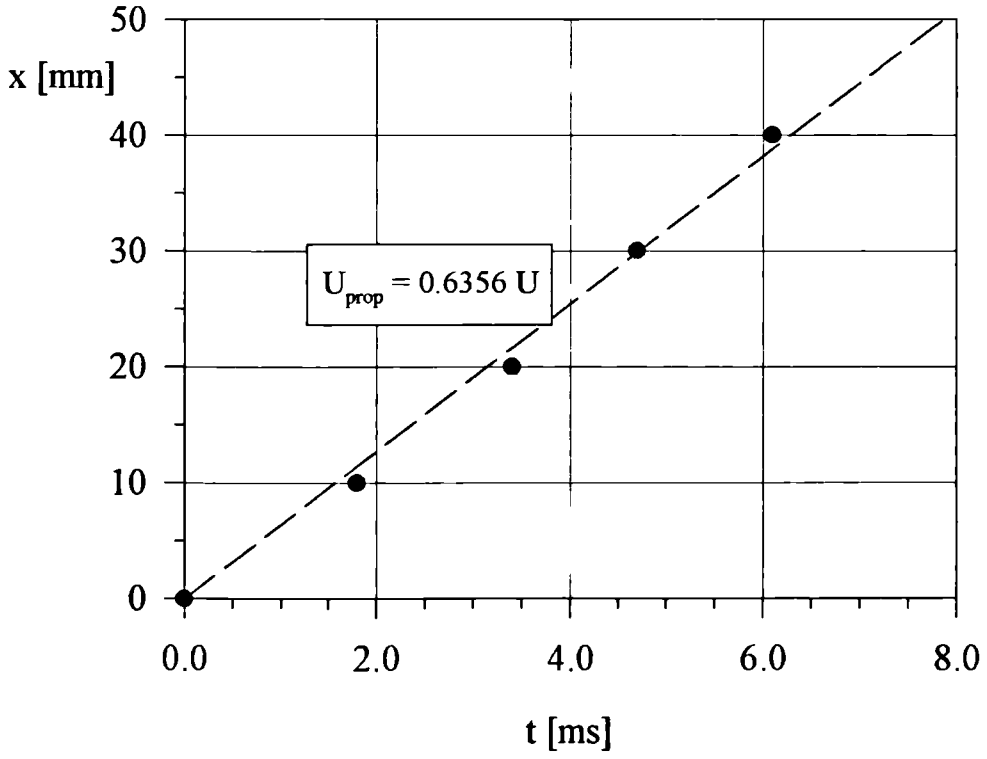

Figure B.7.Distance vs. time lag and the resulting propagation speed of pressure disturbances.

APPENDIX C

ADDITIONAL EXPERIMENTAL RESULTS

This appendix contains some more examples of measurements obtained in the vortex tube experiment, which supplement the results given in chapter 4.

Figures C.1 through C.5 show the sharpest pressure spectra for the following chokes and flow rates:

- Long choke, both flow rates. (figure C.1 and C.2).
- Medium choke, lower flow rate (figure C.3) - results for the higher one were shown in figure 4.14.
- Short choke, both flow rates (figures (C.4 and C.5).

The 'suddenness' of the quasi-periodic fluctuations both in space and frequency should be noted. The frequency of the quasi-periodic fluctuations 'scales' well with the flow rate (decrease in the flow rate to 0.6 of its maximum value is followed by a proportional decrease in the characteristic frequency). Similar trend can be observed in figures C.6 and C.7 (spectra of velocity fluctuations) which should be compared to figures 4.24 and 4.26, respectively.

Figures C.8 through C.13 show the velocity profiles in the medium choke, at the higher flow rate, with increasing streamwise co-ordinate: x=10, 17, 30, 40, 80 and 100 (x=60 was shown in figure 4.32), measured by the hot-wire. As already noted in chapters 4 and 5 the highest excitation corresponds approximately to the point of inflection in the velocity profiles (at least for x greater then 30 mm).

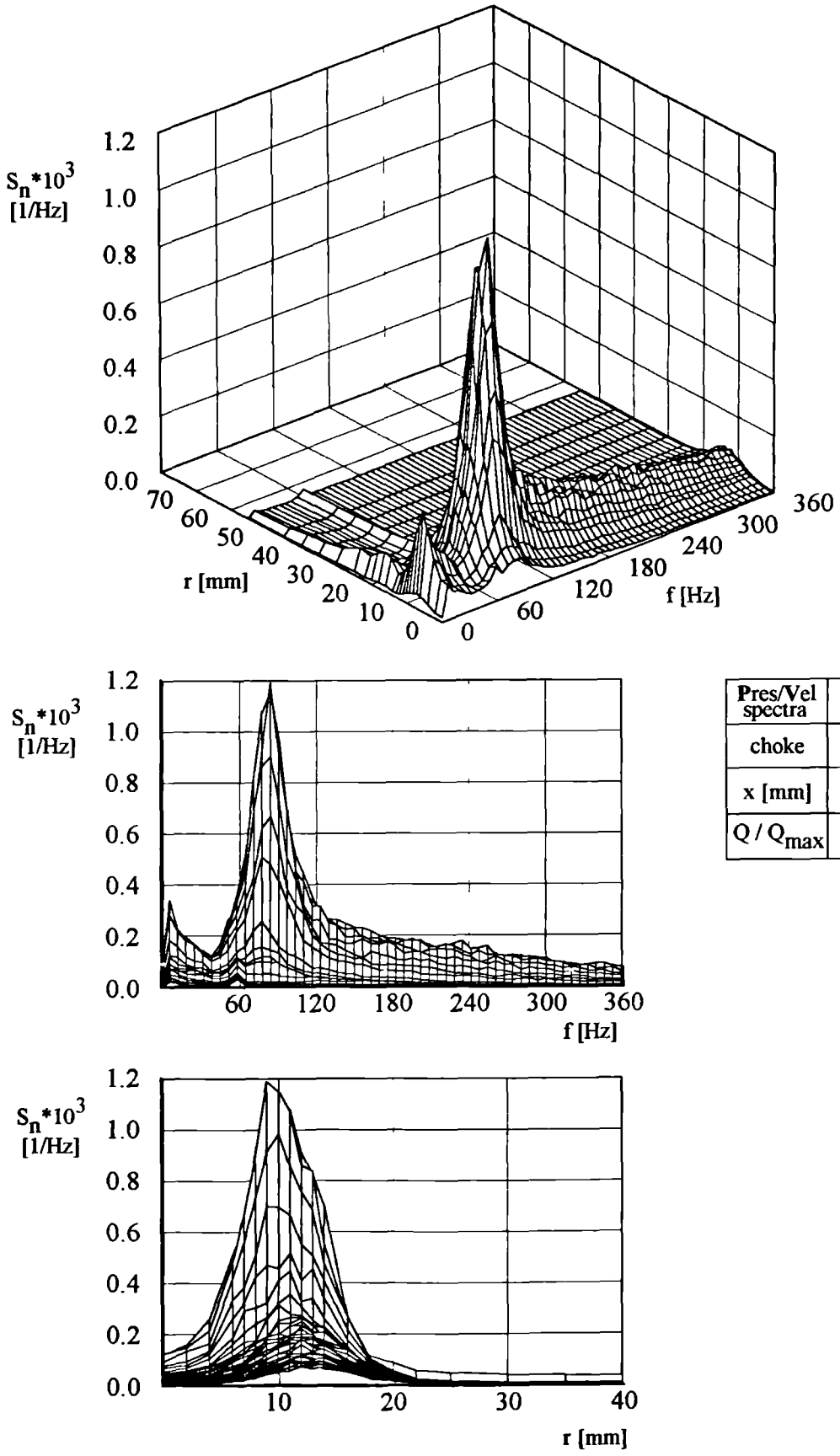

Pres/Vel spectra	P
choke	L
x [mm]	60
Q / Q_{max}	0.6

Figure C.1.Long choke, lower flow rate.

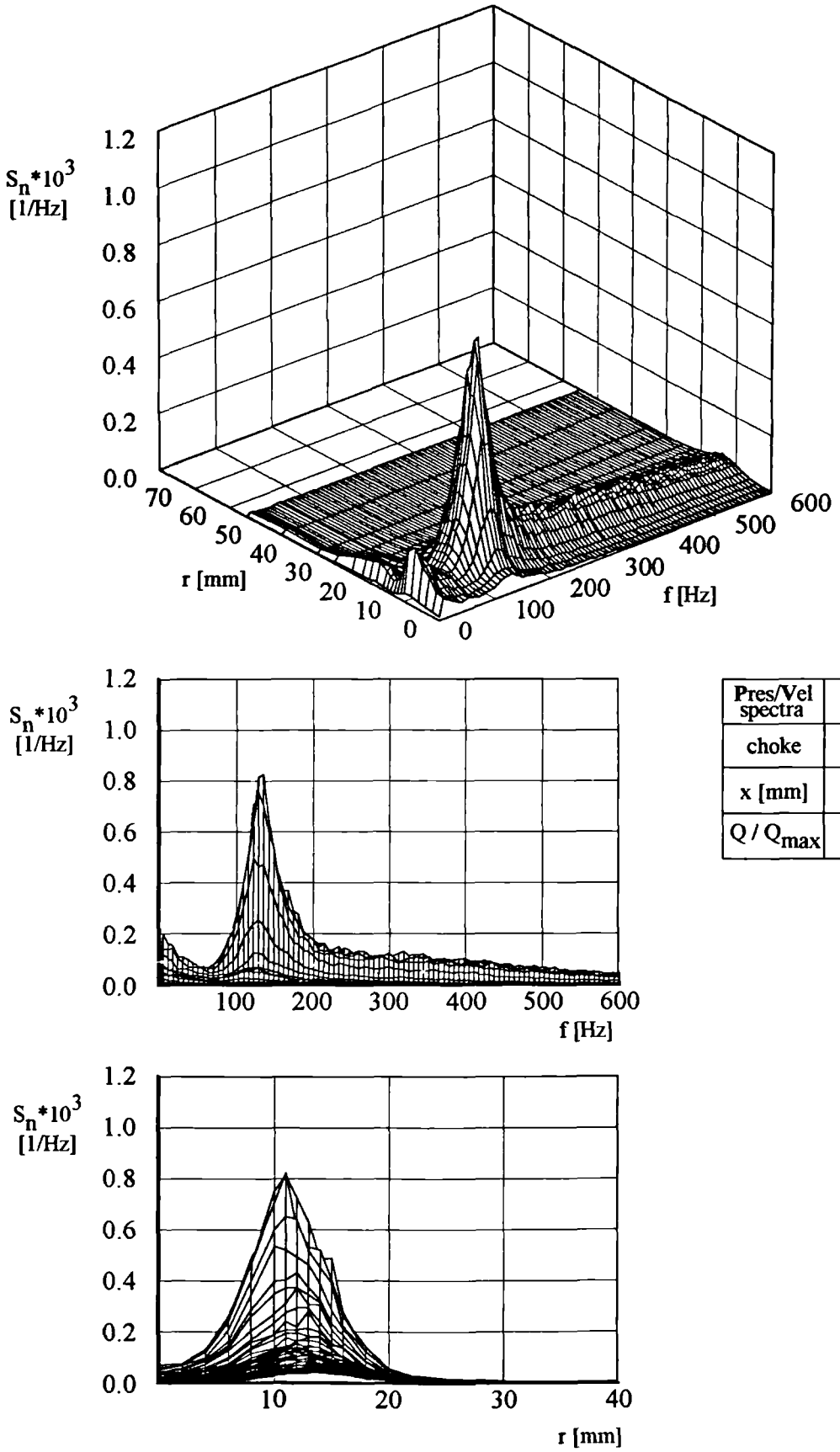

Pres/Vel spectra	P
choke	L
x [mm]	60
Q / Q_{max}	1.0

Figure C.2.Long choke, higher flow rate.

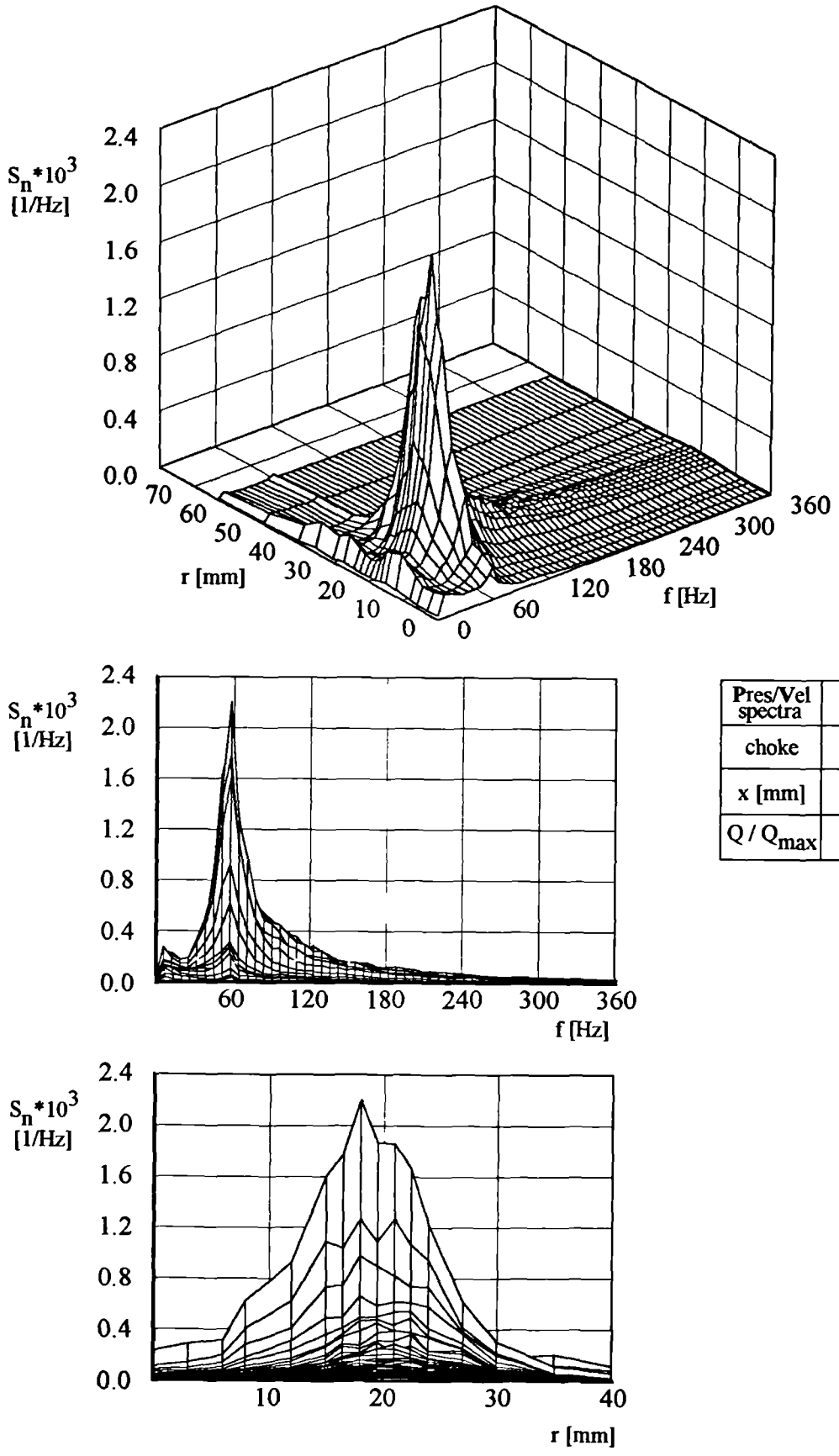

Pres/Vel spectra	P
choke	M
x [mm]	80
Q / Q_{max}	0.6

Figure C.3.Medium choke, lower flow rate.

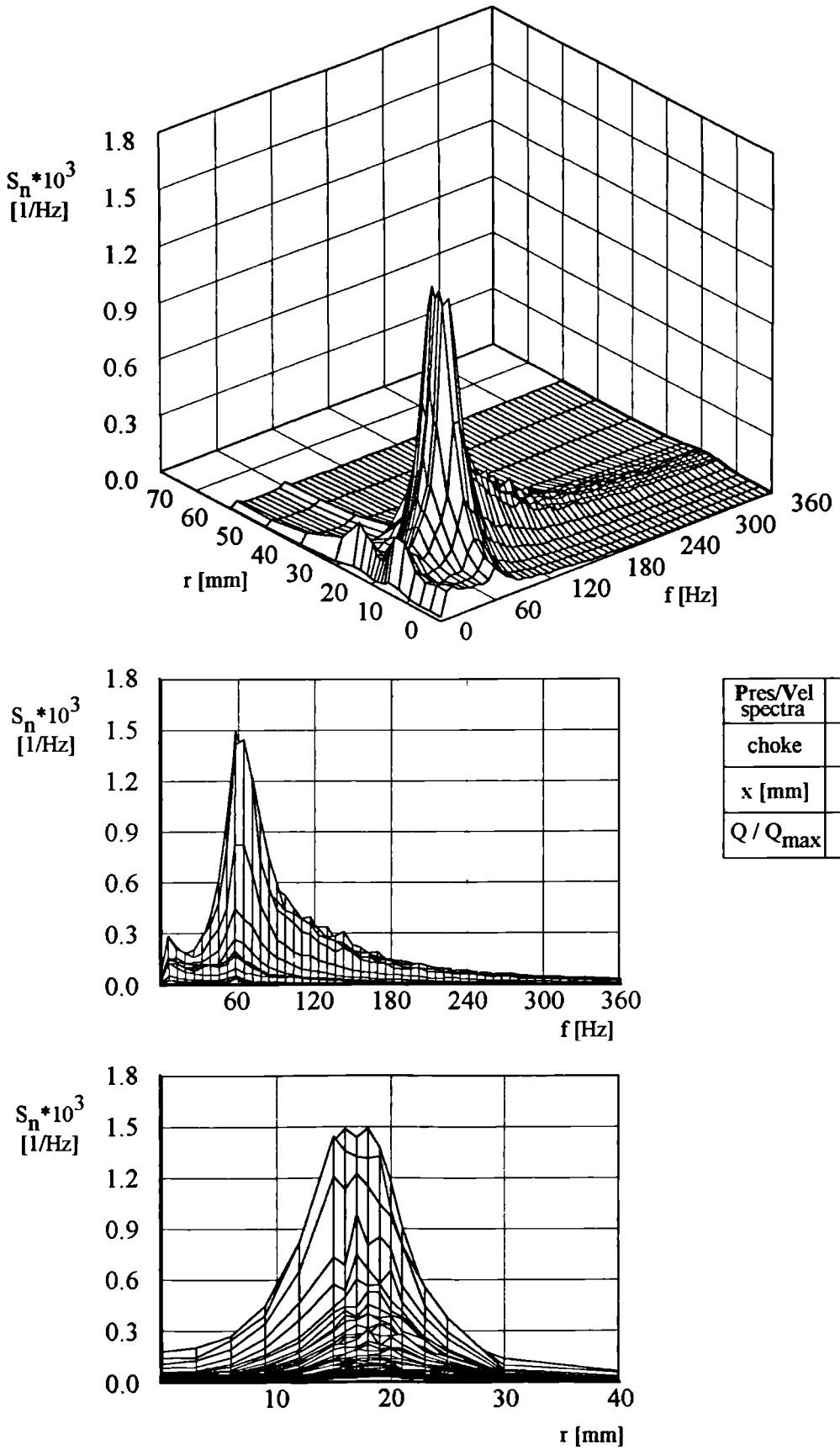

Pres/Vel spectra	P
choke	S
x [mm]	60
Q / Q_{max}	0.6

Figure C.4.Short choke, lower flow rate.

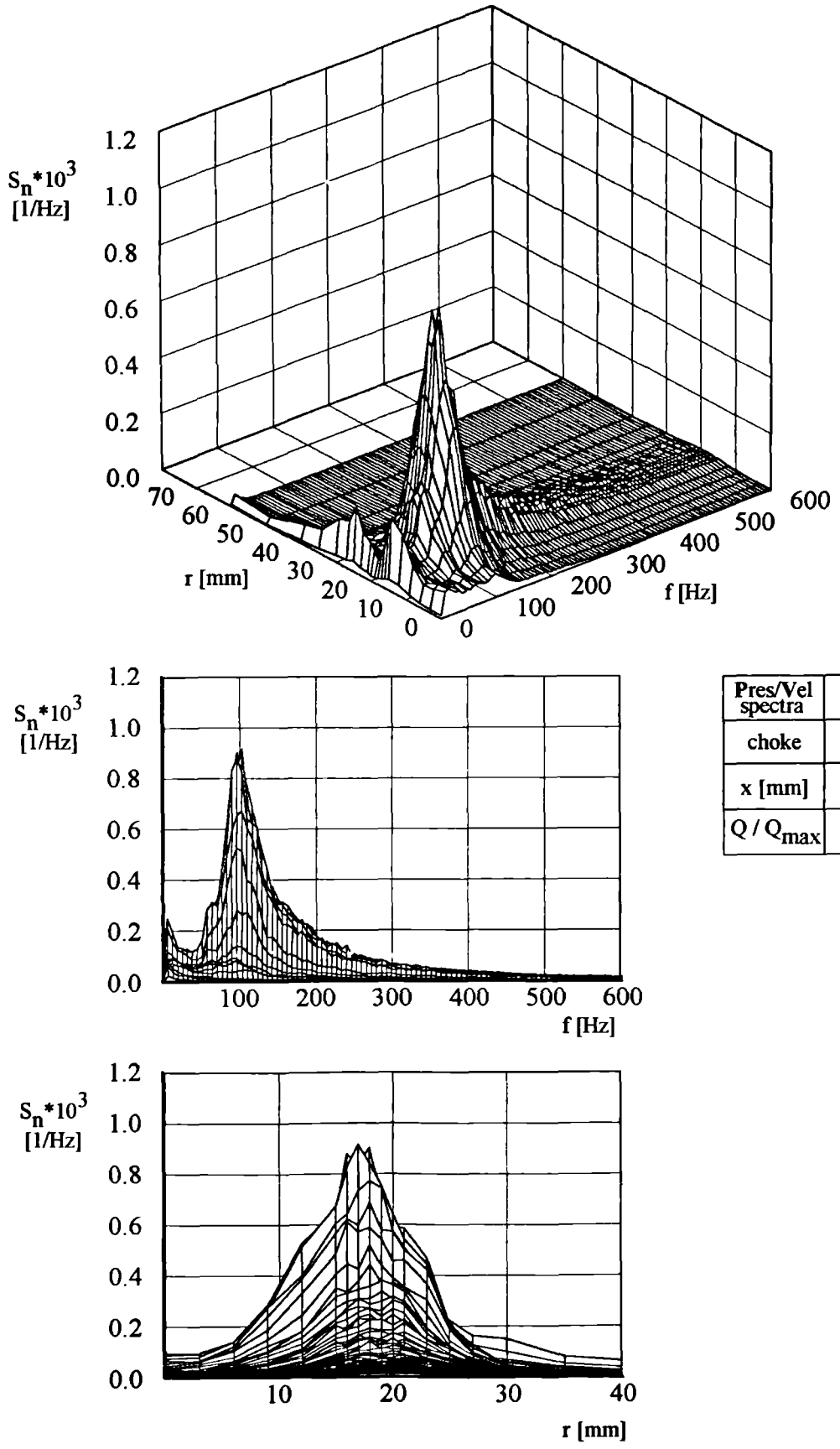

Pres/Vel spectra	P
choke	S
x [mm]	60
Q / Q_{max}	1.0

Figure C.5.Short choke, higher flow rate.

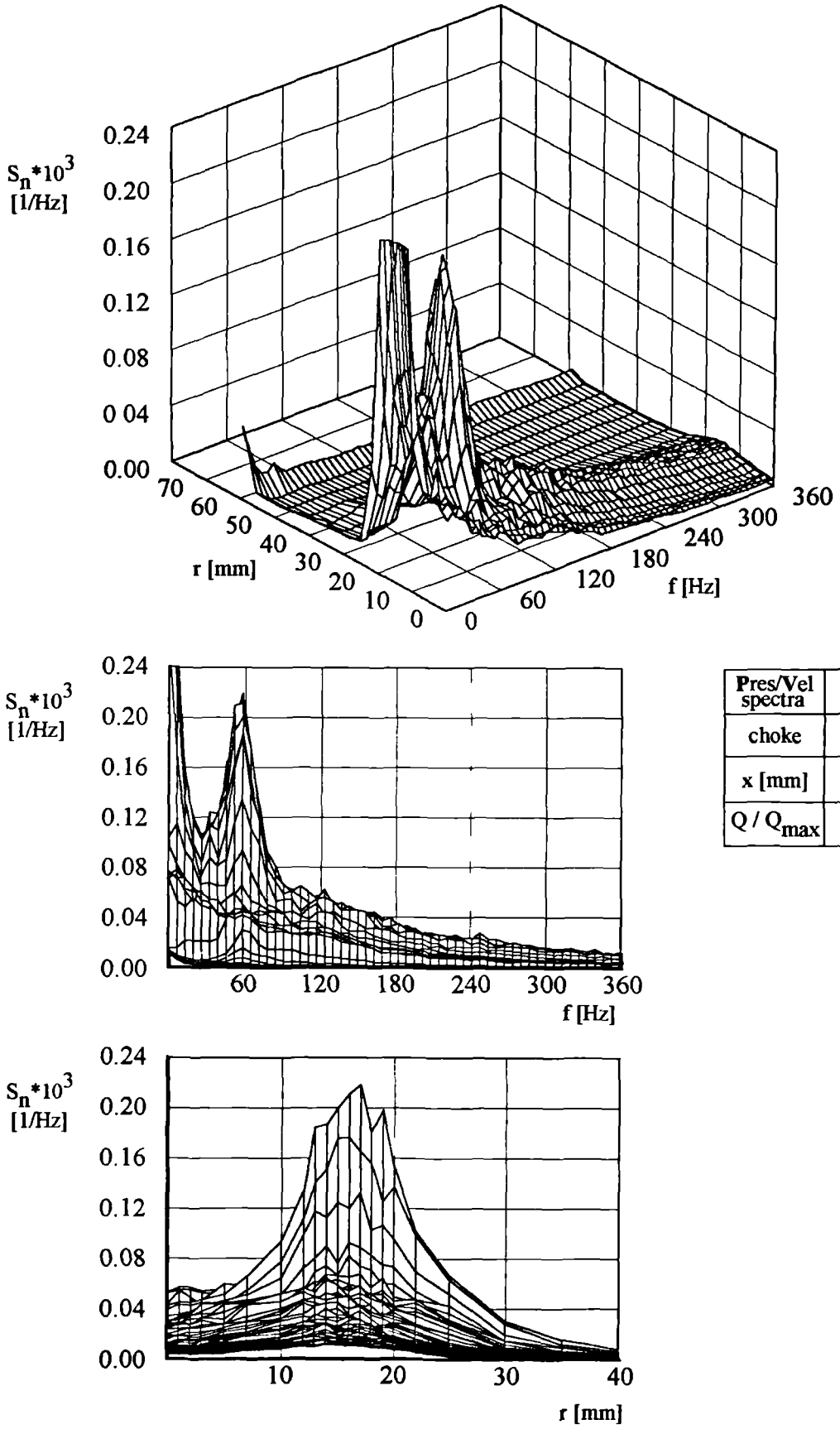

Pres/Vel spectra	V
choke	M
x [mm]	60
Q / Q_{max}	0.6

Figure C.6. Velocity spectra, long choke, lower flow rate, x=60 mm.

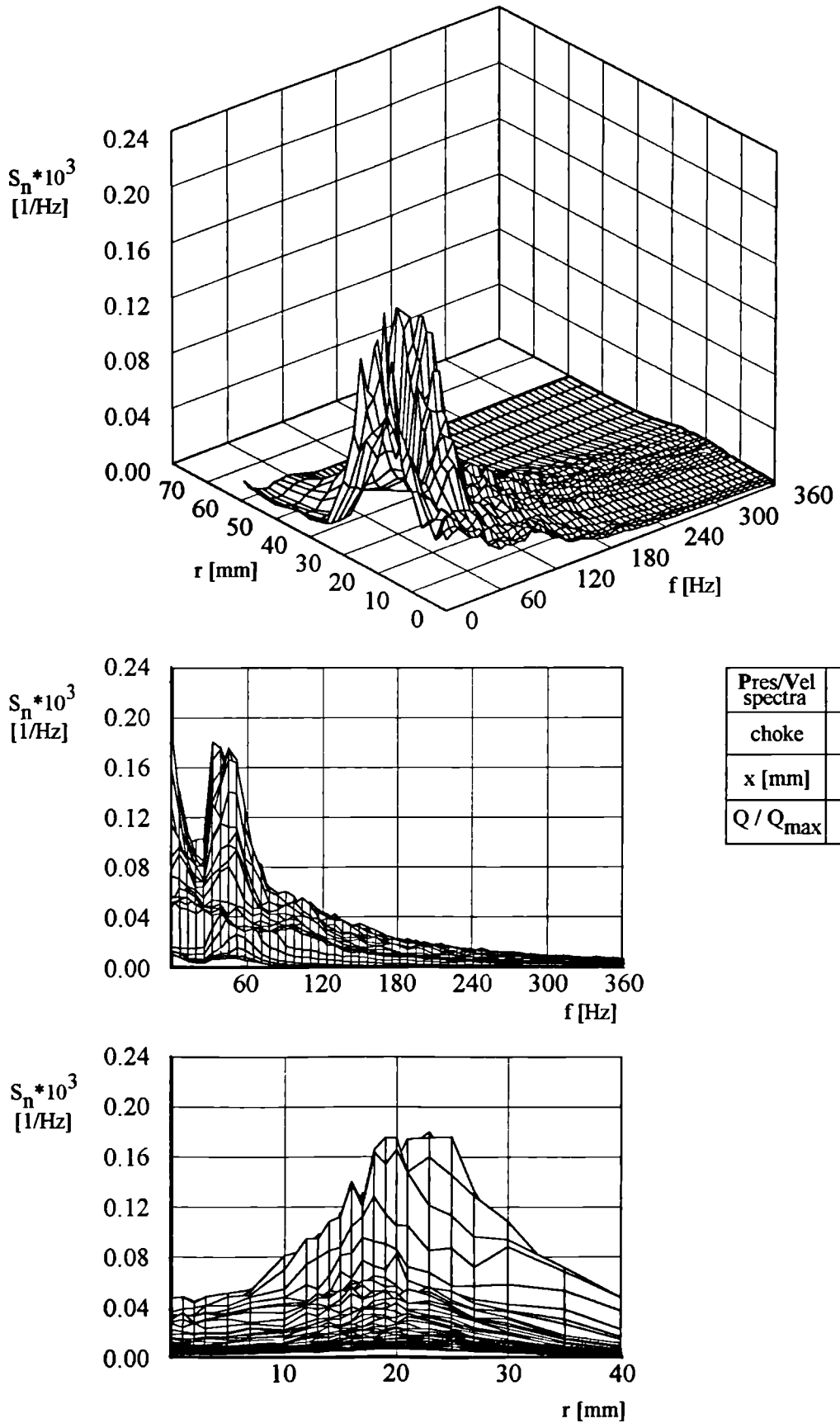

Pres/Vel spectra	V
choke	M
x [mm]	100
Q / Q_{max}	0.6

Figure C.7. Velocity spectra, long choke, lower flow rate, x=100 mm.

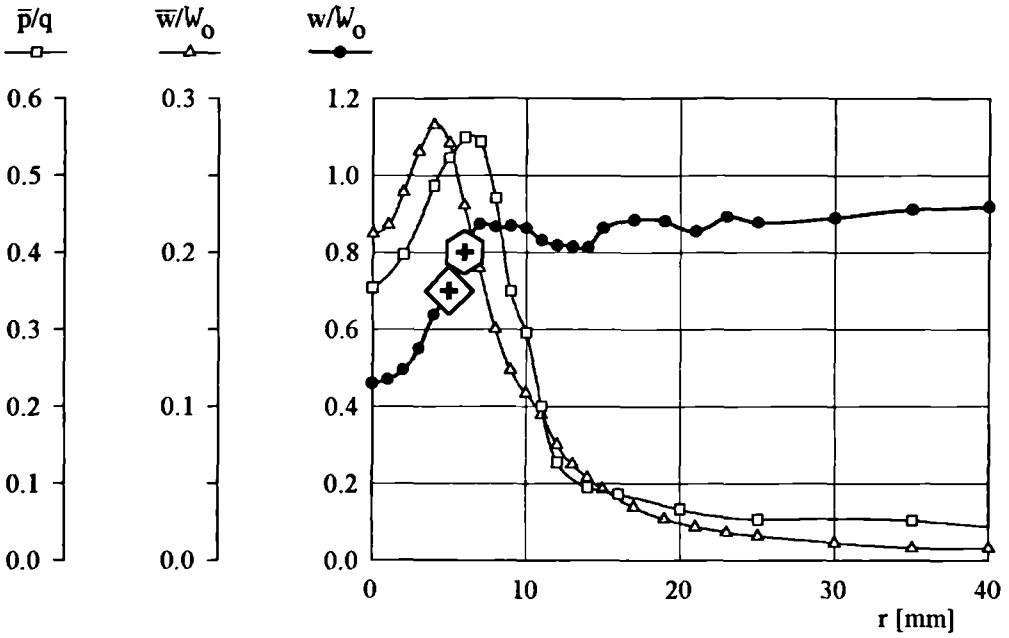

Figure C.8. Velocity profile, medium choke, higher flow rate, x=10 mm.

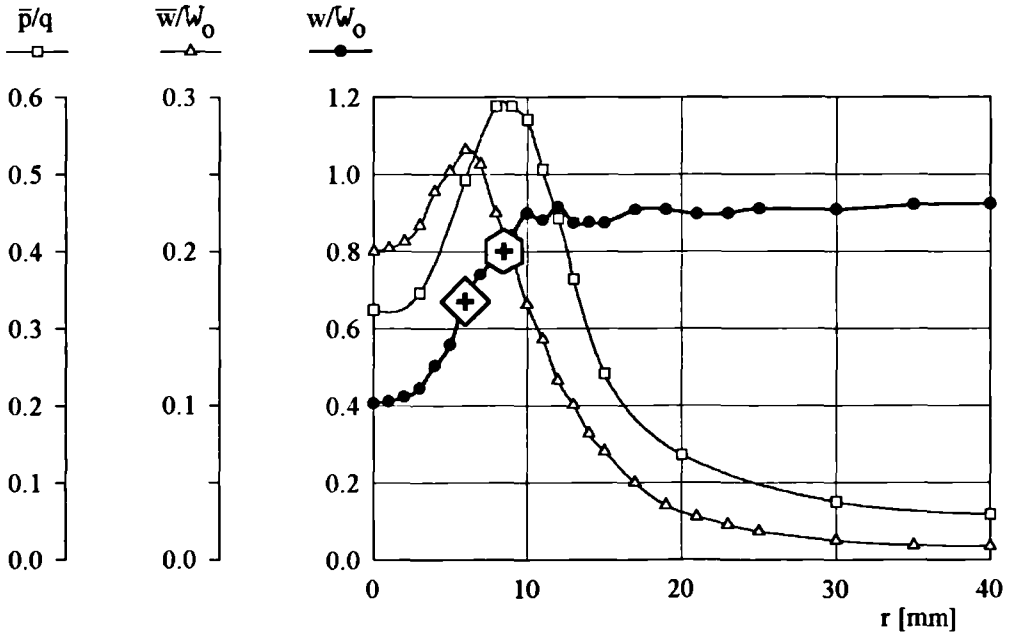

Figure C.9. Velocity profile, medium choke, higher flow rate, x=17 mm.

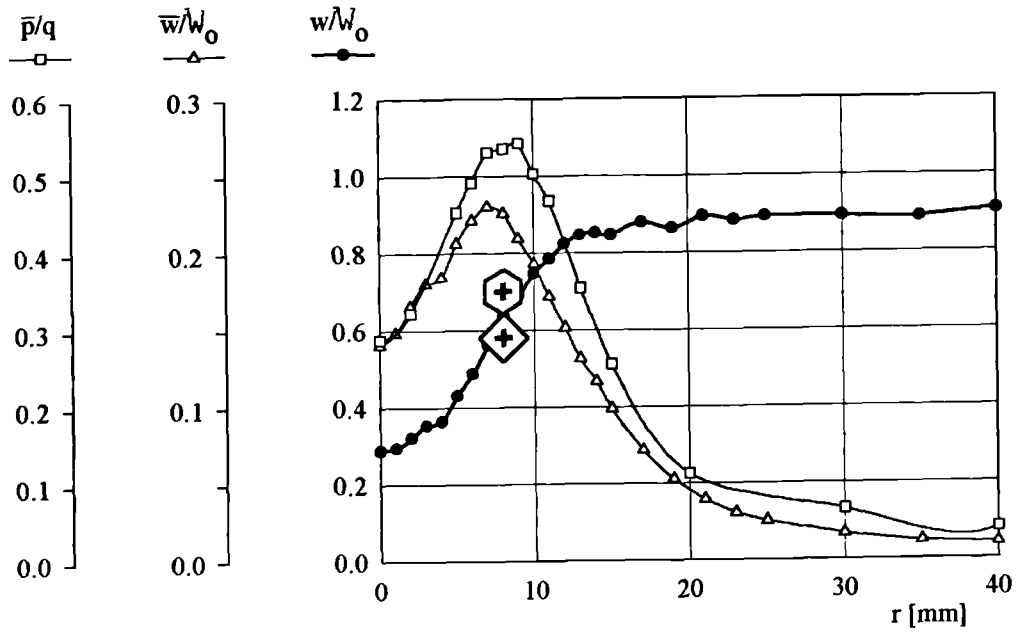

Figure C.10.Velocity profile, medium choke, higher flow rate, x=30 mm.

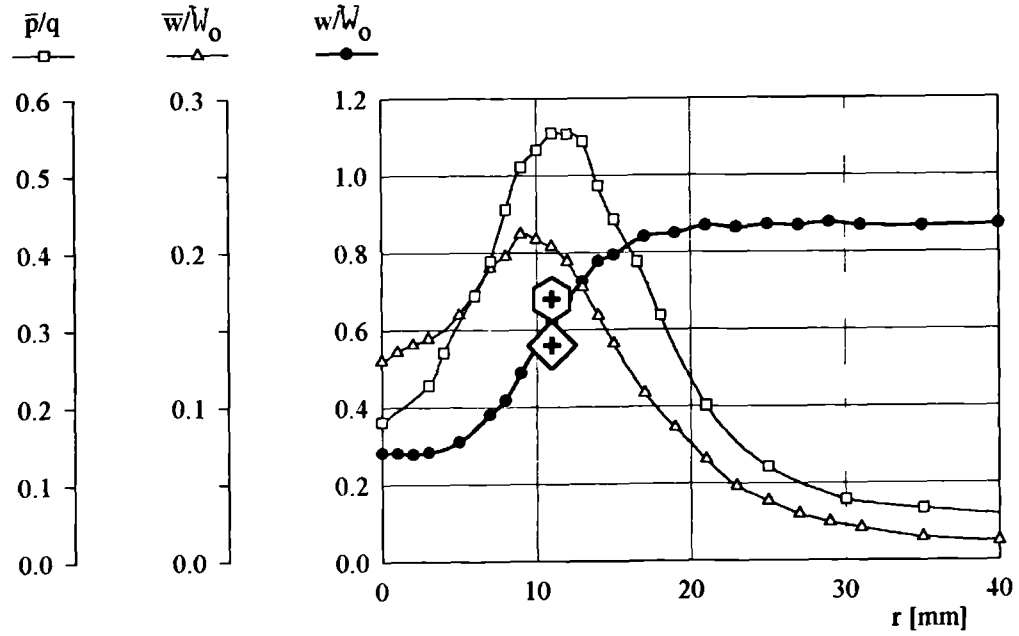

Figure C.11.Velocity profile, medium choke, higher flow rate, x=40 mm.

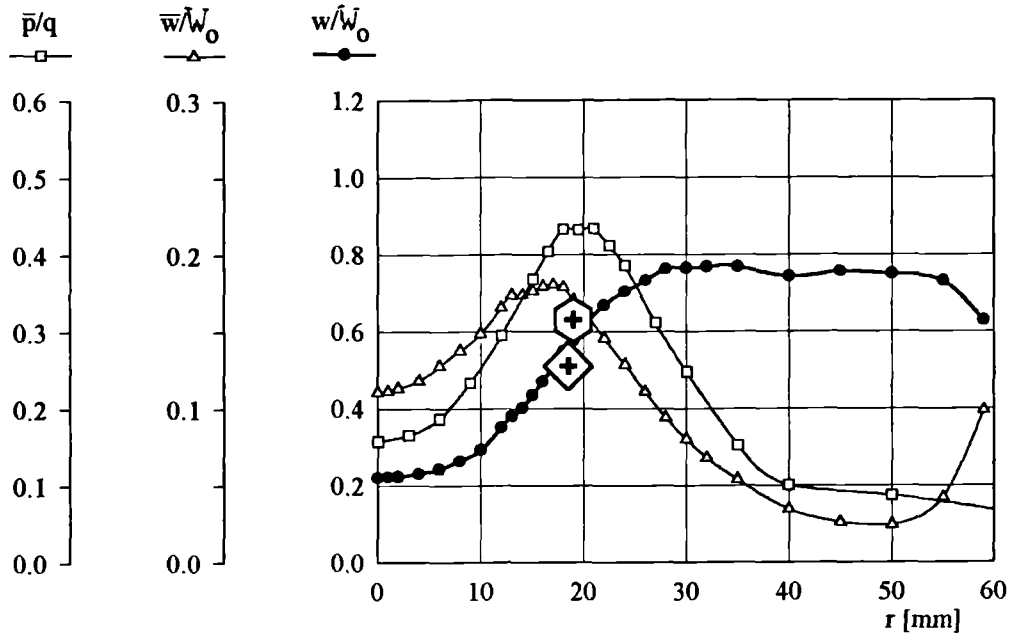

Figure C.12. Velocity profile, medium choke, higher flow rate, x=80 mm.

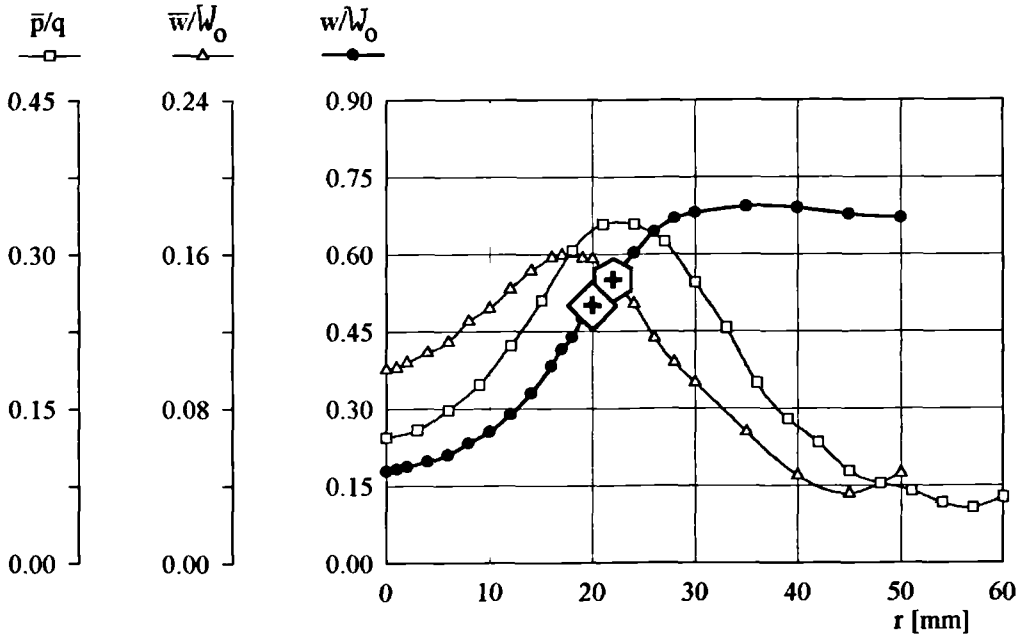

Figure C.13. Velocity profile, medium choke, higher flow rate, x=100 mm.